



HAL
open science

Aerodynamic and acoustic analysis of the tip-leakage flow past a single airfoil

Bo Li

► **To cite this version:**

Bo Li. Aerodynamic and acoustic analysis of the tip-leakage flow past a single airfoil. Other. Université de Lyon, 2016. English. NNT : 2016LYSEC042 . tel-01538111

HAL Id: tel-01538111

<https://theses.hal.science/tel-01538111>

Submitted on 13 Jun 2017

HAL is a multi-disciplinary open access archive for the deposit and dissemination of scientific research documents, whether they are published or not. The documents may come from teaching and research institutions in France or abroad, or from public or private research centers.

L'archive ouverte pluridisciplinaire **HAL**, est destinée au dépôt et à la diffusion de documents scientifiques de niveau recherche, publiés ou non, émanant des établissements d'enseignement et de recherche français ou étrangers, des laboratoires publics ou privés.

École Centrale de Lyon

École Doctorale de MEGA

THÈSE

Aerodynamic and acoustic analysis of the tip-leakage flow on a single airfoil

Soutenu publiquement le 07/12/2016 par

Bo LI

en vue d'obtenir le titre de

Docteur

spécialité

Mécanique des Fluides et Aéroacoustique

Composition du jury

Pr. Gérard BOIS	LML, Arts et Métiers ParisTech	<i>Rapporteur</i>
Pr. Nicolas BINDER	ISAE-SupAéro	<i>Rapporteur</i>
Pr. Régiane FORTES-PATELLA	LEGI, Grenoble INP	<i>Examinatrice</i>
Pr. Lipeng LU	Université Beihang	<i>Examineur</i>
Dr. Laurence VION	Safran Aircraft Engines	<i>Examineur</i>
Dr. Jérôme BOUDET	LMFA, École centrale de Lyon	<i>Co-directeur de thèse</i>
Pr. Marc C. JACOB	ISAE-SupAéro	<i>Directeur de thèse</i>

I would like to dedicate this thesis to my loving parents.

Acknowledgements

This thesis is supported by the China Scholarship Council (CSC), the French National Research Agency (ANR), the French National Center for Scientific Research (CNRS) and the National Computing Center for Higher Education (CINES). It is supervised by Prof. Marc C. Jacob from Institut Supérieur de l'Aéronautique et de l'Espace and Dr. Jérôme Boudet from LMFA at École Centrale de Lyon in France.

My first gratitude goes to my supervisors, Marc and Jérôme. I appreciate their constant encouragement, guidance and trust. They are always available for replying all my questions and for resolving all the technical problems that I encountered.

My sincere thanks goes to my college and friend Feng Gao for his constant and great help on the numerical simulation. I would like to thank Joëlle Caro, Michel Roger, Emmanuel Jondeau, Yannick Rozenberg, Alexis Giauque and Marc Michard for the discussions. This thesis would not have been possible without their help.

I would like to thank the whole research team at LMFA. It is a great pleasure to do research in this strong international group. It provides me freedom, equality and fraternity during the thesis. In particular, I would like to thank Philippe Eyraud for the help in the library.

I want to thank Prof. Gérard Bois and Prof. Nicolas Binder for accepting to review this manuscript. Their precious comments helped to improve the final manuscript. I would also like to thank Prof. Lipeng Lu, Prof. Régiane Fortes-Patella and Dr. Laurence Vion for accepting to be members of the jury.

I received generous support and encouragement from colleges and friends, I enjoy the best time with them. I want to thank Lu Zhang (Annabelle) and Benoit Hennebelle, Gang Huang and Changwei Zhou, Xu Chen, Zhe Li, Baolin Xie, Bo Qu, Yu Bai, Ming Xiao, Lei Jiang, Xiangkun Sun, Xingrong Huang, Yu Fan, Kaijun Yi . . .

Finally, and most importantly, I would like to thank my wife Lu Zhou. Her support, encouragement, quiet patience and unwavering love were undeniably the bedrock upon which the past three years of my life have been built. I thank my parents for their faith in me and allowing me to be as ambitious as I wanted. Also, I thank Lu's parents. They provided us with unending encouragement and support.

Abstract

The tip-leakage flow is a common flow feature in turbomachines. It originates from the relative motion between the blade tip and the end-wall, and the pressure difference across the blade. The tip-leakage flow is extremely complex for its three-dimensional unsteady nature, and its existence leads to many unfavourable effects, such as aerodynamic performance losses and noise emissions. These issues have motivated extensive experimental and numerical researches from both aerodynamic and aeroacoustic points of view.

In order to improve the understanding of the tip-leakage flow and its associated broadband noise, a research campaign has been carried out at LMFA. Regarding the tip-leakage flow, this research campaign includes an experiment with advanced measurement technologies, a zonal LES computation and a series of RANS/URANS computations. Both the experiment and the simulations consider a single-airfoil configuration at low Mach number. Experimental and numerical results are analysed systematically and thoroughly in the current study. Finally, efforts are put on the broadband noise modelling and prediction based on the experimental and numerical results.

A multi-vortex system with an intense tip-leakage vortex is observed in the experiment. The various analyses of the flow characteristics show a good agreement between the experiment and the ZLES in the blade tip region. The zonal (RANS-LES) approach proves itself to be a powerful tool to provide a detailed description of the tip-leakage flow, with a limited computational cost. However, the RANS and URANS computations globally over-estimate the diffusion of the tip-leakage vortex. Furthermore, the random oscillation of the tip-leakage vortex is investigated using PIV instantaneous flow fields and the wandering amplitude is evaluated. The dynamic response of the tip-leakage vortex is also studied with URANS at selected frequencies.

Two far-field noise prediction models, corresponding to two different acoustic sources, are reformulated and implemented with the near-field data from the numerical simulations. These predictions are compared to the far-field measurements. Using the ZLES data as input, the blade-tip self-noise model is found to over-estimate the noise generated in the blade-tip region. The trailing-edge noise model is implemented with the time-averaged ZLES and the RANS near-field data, and yields a very good prediction within a broad range of frequency.

Keywords: tip-leakage flow, zonal large-eddy simulation, Reynolds-averaged Navier-Stokes, vortex wandering, far-field noise modelling

Table of contents

List of figures	xi
List of tables	xiii
Nomenclature	xv
1 Introduction	1
1.1 Background	1
1.2 Motivations and objectives	2
1.3 Thesis outline	3
2 Review of research on tip-leakage flow	5
2.1 Review of aerodynamic research on tip-leakage flow	5
2.1.1 Tip-leakage flow modelling	6
2.1.2 Experimental research	9
2.1.3 Numerical research	15
2.2 Review of aeroacoustic research on tip-leakage flow	25
2.2.1 Experimental research	25
2.2.2 Noise prediction methods	27
2.3 Conclusions	28
3 Experimental and numerical methods	29
3.1 Configuration of the tip-leakage flow experiment	29
3.2 Coordinate system	31
3.3 Measurement technologies and experimental database	31
3.3.1 Velocity measurements	31
3.3.2 Pressure measurements	36
3.4 Numerical methods	36
3.4.1 ZLES	37

3.4.2	RANS/URANS	42
4	Mean aerodynamics of the tip-leakage flow	47
4.1	Inflow conditions	47
4.1.1	Mean velocity profile	48
4.1.2	Turbulent fluctuations	49
4.2	Post-processing strategy	50
4.3	Mean aerodynamics of the tip-leakage flow	52
4.3.1	Blade surface static pressure coefficient	52
4.3.2	Tip-leakage vortex	53
4.3.3	Mean velocity field	64
4.4	Conclusions	78
5	Turbulent characteristics of the tip-leakage flow	81
5.1	Instantaneous tip-leakage vortex visualization	81
5.2	Reynolds stresses	82
5.3	Near-field energy spectrum	84
5.4	Space-time correlations	91
5.4.1	Space-time correlations in the experiment	91
5.4.2	Space-time correlations in the ZLES	94
5.5	Tip-leakage vortex wandering	100
5.5.1	Tip-leakage vortex wandering in the experiment	100
5.5.2	Tip-leakage vortex wandering in the ZLES	103
5.6	An exploration of vortex wandering using URANS	104
5.6.1	Effects of grid coarsening	104
5.6.2	URANS convergence	105
5.6.3	Vortex wandering amplitude	105
5.6.4	Discussion	108
5.7	Conclusions	109
6	Far-Field Noise Prediction	111
6.1	Blade-Tip Self-Noise Model	111
6.2	Tip noise modelling from near-field ZLES data	116
6.2.1	Damping factor α	117
6.2.2	Wall pressure spectrum Φ_{pp}	118
6.2.3	Spanwise coherence length l_y	121
6.2.4	Longitudinal convection velocity U_c	123

6.2.5	Far-field noise prediction with ZLES data	125
6.2.6	Sensitivity of the blade-tip self-noise model	126
6.3	Trailing-edge noise model	127
6.4	TE noise modelling from near-field ZLES and RANS data	128
6.4.1	Wall pressure spectrum Φ_{pp}	129
6.4.2	Far-field noise prediction with ZLES and RANS data	130
6.5	Combined noise (TE+Tip) modelling from near-field ZLES data	132
6.6	Conclusions	133
7	Conclusions and perspectives	135
7.1	Conclusions	135
7.2	Perspectives	137
Appendix A	Blade-tip self-noise model - integration of Σ_Y	139
Appendix B	Trailing-edge noise model	141
Appendix C	Published papers	143
References		145

List of figures

1.1	Tip clearance in turbomachines.	1
2.1	Rains's tip-leakage flow model [92].	7
2.2	Idea used in Chen <i>et al.</i> 's model [27]: the evolution of the tip-leakage flow is treated as an unsteady process in the successive crossflow planes.	9
2.3	Wall pressure (C_p) distributions with tip clearance of 0% (left), 0.8% (middle) and 1.35% (right) chord, observed in Storer and Cumpsty's experiment [102].	11
2.4	Three-vortex structure, observed in Kang and Hirsch's experiment [67]. . .	12
2.5	Tip-leakage flow structure at design point, observed in Inoue and Furukawa's RANS computation [56].	14
2.6	Tip-leakage flow structure near stall, observed in Furukawa and Inoue's RANS computation [44].	17
2.7	Tip-leakage vortex and leakage streamlines at (a) peak efficiency condition (b) near stall condition, observed in Wu and Chu's RANS computation [111].	18
2.8	Multi-vortex structure, observed in You <i>et al.</i> 's LES computation [114]. . .	20
2.9	Generation and evolution of the end-wall vortical structures, observed in You <i>et al.</i> 's LES computation [115].	21
2.10	Tip-leakage flow and vortex for three different gap sizes, observed in You <i>et al.</i> 's LES computation [113].	22
2.11	Energy spectra of the pitchwise velocity fluctuations in the blade wake, observed in You <i>et al.</i> 's LES computation [115].	23
2.12	Flow structures for a clearance of (a) 2% chord (b) 10% chord, observed in Decaix <i>et al.</i> 's LES computations [33].	24
3.1	Experimental set-up.	30
3.2	Coordinate system.	31
3.3	Set-up for 2D-2C TR PIV measurements (view from top).	32

3.4	Positions and dimensions of the PIV measurement planes (a) $x - y$ view (b) $y - z$ view.	34
3.5	Set-up for the 2D-3C TR PIV measurements (view from top).	35
3.6	Effective AOA.	37
3.7	LES and RANS zones in the blade tip region ($x - y$ view at $z = 0.5h$).	38
3.8	Global view of the ZLES computational domain.	40
3.9	Detailed views of the ZLES mesh at (a) leading edge (b) trailing edge, with every two points plotted	41
3.10	Global view of the RANS/URANS computational domain.	43
3.11	Detailed views of the RANS/URANS mesh at (a) leading edge (b) trailing edge.	44
4.1	Mean velocity profiles inside the incoming boundary layer at $1.5c$, $1.0c$ and $0.5c$ upstream of the leading edge.	48
4.2	Turbulent fluctuations inside the incoming boundary layer at $1.5c$, $1.0c$ and $0.5c$ upstream of the leading edge.	49
4.3	Two coordinate systems	51
4.4	Comparison between the corrected results (rotated plane) and uncorrected results from the simulations, with respect to experimental data.	52
4.5	Mean pressure coefficient C_p at mid-span and close to the blade-tip.	53
4.6	Mean vortex system at 2mm downstream of the trailing edge, based on the function Γ_2 . View from downstream. (a) PIV (b) ZLES (c) RANS. The black dashed line indicates the position of the airfoil trailing edge.	56
4.7	Circulation of the TLV as a function of the integration radius, for three different PIV measurements.	57
4.8	Γ_2 of the time-averaged flow field, 2mm downstream of the trailing edge, from the experiment. (a) AXIOOM-2 (large window 2C-PIV) (b) AXIOOM-3 (small window 2C-PIV) (c) AXIOOM-7 (small window 3C-PIV) (d) AXIOOM-10 (small window 3C-PIV)	58
4.9	Γ_1 of the time-averaged flow field, 2mm downstream of the trailing edge. (a) 2C-PIV AXIOOM-2 (b) 2C-PIV AXIOOM-3 (c) 3C-PIV AXIOOM-7 (d) 3C-PIV AXIOOM-10 (e) ZLES (f) RANS	60
4.10	Solid and dashed lines: iso-contours of Γ_1 (positive and negative values, respectively), dotted line: iso-contour $\Gamma_2 = 2/\pi$, background: circumferential velocity levels, 2mm downstream of the trailing edge. (a) 2C-PIV AXIOOM-2 (b) ZLES (c) RANS	61

4.11	Tip-leakage vortex trajectory	62
4.12	K in Chen's model, calculated from ZLES data.	63
4.13	Γ_1 of the time-averaged flow field with different integration domains, for 2C-PIV AXIOOM-2. Integration box: (a) 3×3 (b) 5×5 (c) 7×7 (d) 9×9 (e) 11×11 (f) 13×13	65
4.14	Γ_2 of the time-averaged flow field with different integration domains, for 2C-PIV AXIOOM-2. Integration box: (a) 3×3 (b) 5×5 (c) 7×7 (d) 9×9 (e) 11×11 (f) 13×13	66
4.15	Mean streamwise velocity field U at $x=2\text{mm}$. (a) Experiment (b) ZLES (c) RANS	67
4.16	Mean horizontal velocity fields V . From left to right: PIV, ZLES, RANS. From top to bottom: $x = -40\text{mm}$, $x = -20\text{mm}$, $x = 2\text{mm}$	69
4.17	Mean vertical velocity fields W . From left to right: PIV, ZLES, RANS. From top to bottom: $x = -40\text{mm}$, $x = -20\text{mm}$, $x = 2\text{mm}$	70
4.18	Solid and dashed lines: iso-contours of Γ_1 (positive and negative values, re- spectively), dotted line: iso-contour $\Gamma_2 = 2/\pi$, background: circumferential velocity levels. From left to right: PIV, ZLES, RANS. From top to bottom: $x = -40\text{mm}$, $x = -20\text{mm}$, $x = 2\text{mm}$	71
4.19	Velocity profile comparison, $z = -5\text{mm}$. (a)(c)(e) $x = -20\text{mm}$ (b)(d)(f) $x = 2\text{mm}$	73
4.20	Velocity profile comparison, $z = 0\text{mm}$. (a)(c)(e) $x = -20\text{mm}$ (b)(d)(f) $x = 2\text{mm}$	74
4.21	Velocity profile comparison, $z = 10\text{mm}$. (a)(c)(e) $x = -20\text{mm}$ (b)(d)(f) $x = 2\text{mm}$	75
4.22	Velocity profile comparison, $z = 20\text{mm}$. (a)(c)(e) $x = -20\text{mm}$ (b)(d)(f) $x = 2\text{mm}$	76
4.23	Velocity profile comparison, $z = 30\text{mm}$. (a)(c)(e) $x = -20\text{mm}$ (b)(d)(f) $x = 2\text{mm}$	77
5.1	3D instantaneous view of the ZLES simulation. Iso-surface of Q-criterion, colored by the velocity magnitude.	82

5.2	PIV instantaneous flow fields at $x = 2\text{mm}$. The background is coloured by the normalized circumferential velocity magnitude $\sqrt{V^2 + W^2}/U_0$ in the plane. The arrows represent the 2D instantaneous velocity vectors. From left to right and from top to bottom: $t, t + \Delta t, t + 2\Delta t, t + 3\Delta t, t + 4\Delta t, t + 5\Delta t$, with $\Delta t = 0.33\text{ms}$	83
5.3	Normalized normal Reynolds stresses at $x = -20\text{ mm}$. The arrows represent the 2D mean velocity vectors. Left: PIV, right: ZLES, top to bottom: $u'u'/U_0^2, v'v'/U_0^2, w'w'/U_0^2$	85
5.4	Normalized shear Reynolds stresses at $x = -20\text{ mm}$. The arrows represent the 2D mean velocity vectors. Left: PIV, right: ZLES, top to bottom: $u'v'/U_0^2, u'w'/U_0^2, v'w'/U_0^2$	86
5.5	Normalized normal Reynolds stresses at $x = 2\text{ mm}$. The arrows represent the 2D mean velocity vectors. Left: PIV, right: ZLES, top to bottom: $u'u'/U_0^2, v'v'/U_0^2, w'w'/U_0^2$	87
5.6	Normalized shear Reynolds stresses at $x = 2\text{ mm}$. The arrows represent the 2D mean velocity vectors. Left: PIV, right: ZLES, top to bottom: $u'v'/U_0^2, u'w'/U_0^2, v'w'/U_0^2$	88
5.7	Probe locations and corresponding pressure (B, 21, 46) and velocity (102, 106) power spectral densities.	90
5.8	Locations of the LDV measurement points at $x = 2\text{mm}$	91
5.9	Velocity spectra obtained from LDV (solid line) and 2D-2C PIV measurements (dashed line) at $x = 2\text{mm}$. Left: PIV AXIOOM-2, 3000Hz, right: PIV AXIOOM-3, 7000Hz	92
5.10	Statistical error for the space-time velocity correlations at the vortex center. (a) R_{ww} (b) R_{uu}	93
5.11	Two-point two-time correlation map for the spanwise velocity fluctuations R_{ww} , for a point (\cdot) located at the vortex center (x). PIV AXIOOM-10. From left to right and top to bottom: $\tau = 0, \Delta t_{PIV}, 2\Delta t_{PIV}, 3\Delta t_{PIV}, 5\Delta t_{PIV}, 7\Delta t_{PIV}, 10\Delta t_{PIV}, 15\Delta t_{PIV}, 20\Delta t_{PIV}$	
5.12	Two-point two-time correlation map for the streamwise velocity fluctuations R_{uu} , for a point (\cdot) located at the vortex center (x). PIV AXIOOM-10. From left to right: $\tau = 0, \Delta t_{PIV}, 2\Delta t_{PIV}$	96
5.13	Two-point two-time correlation map for the spanwise velocity fluctuations R_{ww} , for a point (\cdot) located 3.5 mm left of the vortex centre (x). PIV AXIOOM-10. From left to right and top to bottom: $\tau = 0, \Delta t_{PIV}, 2\Delta t_{PIV}, 5\Delta t_{PIV}, 10\Delta t_{PIV}, 15\Delta t_{PIV}$	96

5.14	Two-point two-time correlation map for the streamwise velocity fluctuations R_{uu} , for a point (\cdot) located 3.5 mm left of the vortex centre (x). PIV AXIOOM-10. From left to right and top to bottom: $\tau = 0, \Delta t_{PIV}, 2\Delta t_{PIV}, 5\Delta t_{PIV}, 10\Delta t_{PIV}, 15\Delta t_{PIV}$.	97
5.15	Two-point two-time correlation map for the spanwise velocity fluctuations R_{ww} , for a point (\cdot) located at the vortex center (x). ZLES results. From left to right and top to bottom: $\tau = 0, \Delta t_{ZLES}, 2\Delta t_{ZLES}$.	98
5.16	Two-point two-time correlation map for the streamwise velocity fluctuations R_{uu} , for a point (\cdot) located at the vortex center (x). ZLES results. From left to right and top to bottom: $\tau = 0, \Delta t_{ZLES}, 2\Delta t_{ZLES}$.	98
5.17	Two-point two-time correlation map for the spanwise velocity fluctuations R_{ww} , for a point (\cdot) located 3.5 mm left of the vortex centre (x). ZLES results. From left to right and top to bottom: $\tau = 0, \Delta t_{ZLES}, 2\Delta t_{ZLES}$.	99
5.18	Two-point two-time correlation map for the streamwise velocity fluctuations R_{uu} , for a point (\cdot) located 3.5 mm left of the vortex centre (x). ZLES results. From left to right and top to bottom: $\tau = 0, \Delta t_{ZLES}, 2\Delta t_{ZLES}$.	99
5.19	Probability density function (PDF) of the tip-leakage vortex centre distribution at $x = 2\text{mm}$, PIV AXIOOM-2.	101
5.20	Evolution of the half vortex wandering amplitudes σ_y and σ_z , with different integration domain sizes, PIV AXIOOM-2.	102
5.21	Probability density function (PDF) of the tip-leakage vortex centre distribution at $x = 2\text{mm}$, ZLES.	103
5.22	Comparison of Γ_1 and Γ_2 between RANS (left) and time-averaged URANS (right) results, 2mm downstream of the trailing edge.	106
5.23	Comparison of velocity components U , V and W between RANS (left) and time-averaged URANS (right) results, 2mm downstream of the trailing edge.	107
5.24	Transverse velocity time histories close to the blade tip - trailing edge corner, from URANS computations.	108
6.1	Coordinate system for the blade-tip self-noise model [80].	112
6.2	Numerical probes on the suction surface.	117
6.3	PSD of wall pressure at probes 29 ($y = 1.5\text{mm}$), 28 ($y = 3\text{mm}$) and 27 ($y = 6\text{mm}$).	119
6.4	Original and modelled PSD of wall pressure [50], blue lines: original EXP results; red lines: modelled EXP results (Eq.6.30).	120
6.5	Original and modelled PSD of wall pressure, solid lines: original ZLES results; dashed lines: modelled ZLES results; dot-dashed line: modelled EXP result for $z = 1.5\text{mm}$.	120

6.6	Original and modelled coherence function γ^2 , solid lines: original ZLES results; dashed lines: modelled ZLES results; dot-dashed line: modelled EXP results for $\eta = 1.5\text{mm}$	121
6.7	Comparison of coherence length l_y between ZLES and EXP, for different values of K_2	123
6.8	Original and modelled convection velocity U_c , solid blue line: original ZLES results; dashed blue line: modelled ZLES results; dot-dashed red line: modelled EXP results.	125
6.9	Power spectral density of the far-field pressure.	126
6.10	The sensitivity of the blade-tip self-noise model to α , U_c , Φ_{pp} and l_y . “+” denotes +10% and “-” denotes -10% to each individual input parameter.	127
6.11	Power spectral density of the far-field pressure.	131
6.12	Power spectral density of the far-field pressure.	132
6.13	Power spectral density of the far-field pressure.	133

List of tables

3.1	Details of the 2D-2C TR PIV database.	33
3.2	Details of the 2D-3C TR PIV database.	35
5.1	Half vortex wandering amplitudes in y and z directions.	100
5.2	Vortex wandering amplitudes in y and z directions.	100
5.3	Half vortex wandering amplitudes with different integration domain sizes, PIV AXIOOM-2.	102
5.4	Half vortex-wandering amplitudes in y and z directions, ZLES & PIV AXIOOM-2.	104
5.5	Vortex-wandering amplitudes in y and z directions, ZLES & PIV AXIOOM-2.	104
5.6	Calculated vortex wandering amplitudes for PIV and URANS.	108
6.1	Boundary layer parameters at $97.5\%c$ from ZLES and RANS.	130

Nomenclature

Roman Symbols

\bar{S}_{ij}	filtered rate-of-strain tensor
c	blade chord
C_p	mean pressure coefficient
h	clearance height
k	turbulence kinetic energy
M	Mach number
Re	Reynolds number
Re_c	chord-based Reynolds number
T_u	turbulent intensity
U	streamwise velocity component (x direction)
u'	streamwise velocity fluctuation (x direction)
U_0	free-stream velocity
V	horizontal velocity component (y direction)
v'	horizontal velocity fluctuation (y direction)
W	vertical velocity component (z direction)
w'	vertical velocity fluctuation (z direction)
x	streamwise coordinate

x_{LE} leading edge streamwise coordinate

y normal coordinate

z spanwise coordiante

Greek Symbols

β zonal parameter in ZLES

Γ_1 vortex center detection function

Γ_2 vortex core detection function

ν molecular viscosity

ν_t turbulent eddy viscosity

ν_{mod} eddy viscosity in ZLES

ν_{sgs} subgrid-scale eddy viscosity

ψ angle between coordinate systems (x, y, z) and (x', y', z')

σ_y half vortex wandering amplitude in the horizontal direction

σ_z half vortex wandering amplitude in the vertical direction

Acoustic Models

α damping factor

\bar{k} normalized acoustic wavenumber

Φ_{pp} wall pressure spectrum

b half chord

c blade chord

c_0 sound speed

e blade thickness

h clearance height

k acoustic wavenumber

K_1	streamwise wavenumber
K_2	spanwise wavenumber
L	double blade span for blade-tip self-noise model, blade span for trailing-edge noise model
l_y	spanwise correlation length
M	Mach number
U_0	incident mean flow speed
U_c	convection velocity
X	normalized streamwise coordinate
x	streamwise coordinate
x_1	observer coordinate in x direction
x_2	observer coordinate in y direction
x_3	observer coordinate in z direction
Y	normalized normal coordinate
y	normal coordinate
Z	normalized spanwise coordinate
z	spanwise coordinate

Acronyms / Abbreviations

2D-2C TR PIV Two-Dimensional Two-Component time-resolved Particle image velocimetry

2D-3C TR PIV Two-Dimensional Three-Component time-resolved Particle image velocimetry

AOA angle of attack

CFD computational fluid dynamics

FWH Ffowcs-Williams Hawkins acoustic analogy

HWA Hot-Wire Anemometers

LDV Laser Doppler Velocimetry

LE leading edge

LES large eddy simulation

PIV Particle Image Velocimetry

PSD pressure spectral density

RANS Reynolds-averaged Navier-Stokes

SISM shear-improved Smagorinsky model

TE trailing edge

TLV tip-leakage vortex

URANS unsteady Reynolds-averaged Navier-Stokes

ZLES zonal large eddy simulation

Chapter 1

Introduction

1.1 Background

In turbomachines like compressors and turbines, the clearance between a rotor and its surrounding casing is necessary for the operation, as shown in Fig.1.1. The clearance is quite small, typically about one percent of the blade span for compressors and less than one percent for the turbines [81]. However, the relative motion between the blade tip and the end-wall, and the pressure difference across the blade, create a tip-leakage flow, and this flow eventually rolls up, forming a tip-leakage vortex.



Fig. 1.1 Tip clearance in turbomachines.

The tip-leakage flow is extremely complex for its three-dimensional unsteady nature. Both viscous and inviscid interactions occur between the tip-leakage flow, other secondary flows and the boundary layers on both the blade and the end-wall. In a multistage turbomachine, the flow structures formed from the tip clearance not only influence the adjacent blades of the same stage, but also convect to the downstream blade rows and interact with the downstream flow features, making it even more complex.

The tip-leakage flow has been a subject of interest in turbomachinery and aeroacoustic research for a long time [25]. It has been shown from these studies that the unsteady tip-leakage flow has a large effect on the performance of the machine. For the aerodynamic part, it influences blade loading, stage efficiency, heat transfer and stall margin. While for the acoustic part, it has been recognized as an important source of noise. Furthermore, recent studies have shown that the tip-leakage vortex can develop large-scale oscillations, referred to as “vortex wandering”, which can also contribute to the noise emissions.

1.2 Motivations and objectives

Funded by the European Community as part of the Sixth Framework Project PROBAND n° AST4-CT-2005-012222, a successful research campaign on the tip-leakage flow has been carried out at Laboratoire de Mécanique des Fluides et d’Acoustique (LMFA), and numerous remarkable results have been achieved:

1. An experiment about the tip-leakage flow past a single non-rotating airfoil has been conducted under low Mach number condition [59]. Through velocity and pressure measurements in the near and far field, an extensive data set has been obtained.
2. A RANS computation on the same configuration as the experiment has been performed, providing a numerical database for the broadband noise modelling [17].
3. A detailed wavelet analysis of wall pressure and velocity measured in the experiment has been performed [23].
4. A new trailing-edge noise model has been developed [85, 93]. This model is an extension of Amiet’s trailing-edge noise model [2, 3] by taking into account the effects due to the limited chord length. It makes it possible to infer the far-field radiation off the mid-span plane.
5. A method to predict the fan blade trailing-edge noise using RANS simulations has been proposed by Rozenberg *et al.* [94, 96], based on the new trailing-edge noise model.

6. An empirical model of wall pressure spectra, considering the adverse pressure gradient effects, has been developed [95].
7. A new tip-clearance noise model has been developed by extending Amiet's trailing-edge noise model to the blade tip region [50]. It has been compared with the experimental data.

In 2012-2016, a new research campaign on the tip-leakage flow has been carried-out, in the frame of the Sino-French project AXIOOM and the present PhD. The PROBAND configuration has been investigated again with a thinner incoming boundary layer and more advanced measurement technologies. At the same time, a zonal LES simulation has been performed. As a part of the project AXIOOM, the objectives of the current research include:

1. to evaluate the capabilities of new advanced measurement technologies;
2. to evaluate the capabilities of zonal LES (ZLES), providing a direct description of the largest turbulent eddies in the region of interest at the blade-tip;
3. to exploit the advanced experimental and numerical description of the flow, for an in-depth analysis of the tip-leakage vortex dynamics and associated noise emissions;
4. to implement and evaluate the far-field noise prediction models with experimental and numerical near-field data.

1.3 Thesis outline

Chapter 2 reviews previous works on tip-leakage flow, for both the aerodynamics and the aeroacoustics.

In **Chapter 3**, the flow configuration considered in both the experiment and the numerical simulations is introduced. Then the measurement technologies and the experimental database are presented. Finally, the numerical methods are introduced, including the ZLES and (U)RANS approaches, the meshes, the turbulence/subgrid-scale modelings, the boundary conditions, etc.

Chapter 4 concerns the mean aerodynamics of the tip-leakage flow. The time-averaged ZLES results and the RANS results are analyzed in comparison with the experimental results.

The turbulent characteristics of the tip-leakage flow are analyzed in **Chapter 5**, using the ZLES, the URANS and the experimental results.

In **Chapter 6**, the blade-tip self-noise model and the trailing-edge noise model are reformulated and implemented with the experimental, the RANS and the ZLES near-field data.

Finally, the conclusions and perspectives are drawn in **Chapter 7**.

Chapter 2

Review of research on tip-leakage flow

In this chapter, some previous works on tip-leakage flow will be reviewed. These works are classified by the aerodynamic research and the aeroacoustic research. The review of aerodynamic research put emphasis on tip-leakage flow modelling, experimental research and numerical research. And the review of aeroacoustic research put emphasis on experimental research and noise prediction methods.

2.1 Review of aerodynamic research on tip-leakage flow

At early stages of the research on tip-leakage flow, the modelling and the experience are the main research approaches, because of the lag in the computational capabilities. For the modelling, most of the tip-leakage flow models are dedicated to predict the overall efficiency loss due to the tip clearance and others can even predict some detailed flow features. However, these models can hardly be identified as universal, since they are all deduced on specific assumptions and the parameters used are semi-empirical, which makes them not very reliable during the turbomachinery design. The experiment becomes more and more popular among the tip-leakage flow researchers since 1980s. The rapid development of the experimental measurement technology, for example, from Hot-wire anemometers (HWA) to Laser Doppler velocimetry (LDV) and Particle image velocimetry (PIV), makes it possible to extract more information in the flow field with better accuracy. The experimental researches on tip-leakage flow mainly focus on linear and annular cascades, isolated and multistage axial rotors. Compared with the modelling, the experiment overcomes the restriction of various assumptions used in the models, but it is sometimes not feasible for some complex problems. There is still some working conditions that the experimental technology can not reach for the moment. However, the repeatability of the experiment makes it extremely suitable for the parametric analysis. The numerical simulation by solving the 3D Navier-Stokes

equations is more and more widely used since the late 1990s, thanks to the development of the computational capabilities. The numerical method based on Reynolds-averaged Navier-Stokes equations (RANS) has been accepted as a powerful tool for some industrial purposes, such as the turbomachinery design. In recent years, some researchers employ the large-eddy simulation (LES) to investigate the tip-leakage flow and obtain more detailed spatial and temporal information within a wider range of turbulence scales than RANS. Compared with the experiment, the numerical simulation is theoretically easier to solve a complex problem. And the flow field information is complete and available for some further processing and analysis. The disadvantage of the numerical simulation is also obvious: the computational cost is generally proportional to the amount of the resolved flow field information, which makes it sometimes “expensive” to resolve a flow field with satisfactory accuracy. Some researchers also use a combination of the three methods mentioned above, such as modelling/experiment and experiment/simulation.

Following is a review of the previous tip-leakage research, with emphasis on tip-leakage flow modelling, experimental research and numerical research, respectively.

2.1.1 Tip-leakage flow modelling

The first widely accepted tip-leakage flow model should be the one proposed by Rains [92]. Rains finds that the pressure difference across the blade tip is dominant compared with the pressure gradient along the blade chord on both surfaces. The gap exit jet flow could be considered as a simple mixing of two flows, as shown in Fig.2.1: one is the jet driven by the dominant pressure difference across the blade tip, in the direction normal to the blade camber line. Given the pressure difference across the blade tip, the jet velocity could be calculated by the Bernoulli's principle. The kinetic energy of this jet will be subsequently dissipated through mixing, which results in the overall efficiency loss due to the tip clearance. The other flow is the original longitudinal inlet flow. Rains assumes that the viscous effect could be neglected during the formation of the tip-leakage flow, so that the longitudinal momentum component is conserved through the gap. Note that Rains's model has nothing to do with the spanwise direction, so it is actually a 2D analytical model. This model can predict the mean exit jet velocity and the mass flow rate of the tip-leakage flow. However, the loss due to the tip clearance is somewhat under-estimated, which is probably because this model ignores the flow perturbations due to the presence of the tip-leakage vortex when calculating the overall loss. And this model provides no information on the essential details of the passage flow field. Despite the defect in many aspects, Rains's model opened the gate of the tip-leakage flow modelling.

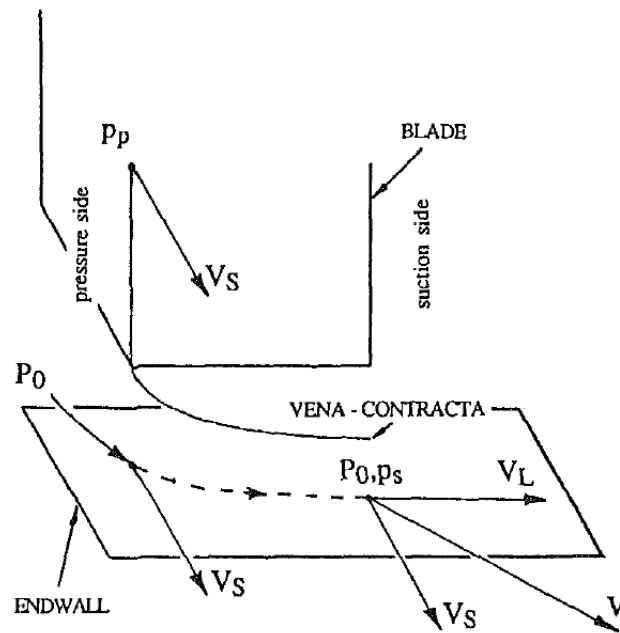


Fig. 2.1 Rains's tip-leakage flow model [92].

Another early attempt to predict the effects of the tip clearance in turbomachines is made by Lakshminarayana and Horlock in their successive researches [72, 73]. They are inspired by Betz's earlier research [14], which considers the velocities induced at the lifting line by the bound vortices shed all along the blade span, and proposes a potential vortex model based on the lifting line theory. It is assumed in this model that the lift is uniform all along the span, and the boundary condition at the end-wall is satisfied by the use of image vortices. At the blade tip region, a part of the bound vortex is shed off into the tip-leakage vortex, and the rest is retained inside the tip region. The model introduces a factor to express the percentage of the bound vorticity retained inside the tip region. This factor is determined empirically through some experimental data, and is formulated as a function of the clearance-to-chord ratio. The potential vortex model is only dedicated to predict the overall effects of the tip clearance, such as the efficiency loss and induced drag, and is inadequate to describe the detailed flow, such as the exit jet flow angle. The detailed flow pattern observed in the experiment, with a loss core in the clearance region, does not resemble to what the potential vortex model describes: the shed vortex is assumed to be distributed uniformly across the passage and sinusoidally across the wall boundary layer. So Lakshminarayana developed a new theoretical model [71] based on many flow visualizations and vorticity measurements to predict the blade-to-blade flow details. According to this new model, the tip-leakage flow produces shear layers which roll up into a spiral to form a core of rotating fluid, which is validated by many experimental observations. Some important parameters in

the model, for example, the radius, the angular rotation and the location of the vortex core, are determined from Rains's theory. Lakshminarayana's models predict the effects of tip clearance with acceptable accuracy in many cases. However, a major drawback of this model is its semi-empirical nature. The empirical relationships involved in the model makes it not universal.

Although more and more researchers chose to use experiment and numerical simulation to investigate the tip-leakage flow since the late decades of last century, the attempt of improving old models or developing new models of the tip-leakage flow never stopped. Chen *et al.* [27] were probably the first ones to model the evolution of the tip-leakage vortex. Following the same idea as Rains: the pressure difference across the blade tip is much larger than the pressure gradient along the blade chord, Chen *et al.* decompose the tip clearance velocity field into independent throughflow and crossflow. As for the slender bodies in external aerodynamics, the 3D steady flow field of interest could be reconstructed from the point of view of a 2D unsteady flow, because the translation along the streamwise direction is analogous to moving in time. In this way, the evolution of the tip-leakage flow could be treated as an unsteady process in the successive crossflow planes which are normal to the blade camber, as shown in Fig.2.2. The fluid during the evolution of the tip-leakage flow is taken as inviscid, so there is a conservation of momentum of the throughflow at each crossflow plan. As for the crossflow, a similarity scaling is employed and a generalized tip-leakage vortex trajectory is obtained. Chen *et al.* find that this generalized tip-leakage vortex trajectory is almost a straight line and the tip clearance does not affect the trajectory of the vortex core in the blade passage. This result agrees very well with a wide range of experimental data, which implies that the behaviour of the tip-leakage flow is essentially inviscid and is dominated by the vortical structure.

Nikolos *et al.* [89] examined the basic theoretical models and proposed some modifications to Rains's gap flow model and Lakshminarayana's vortex model. For Rains's gap flow model, Nikolos *et al.* add a simple modelling of the loss production mechanism inside the gap by using different velocity profiles at the gap exit, which ensures a more accurate prediction of the overall loss due to the tip clearance and the gap exit jet velocity. For Lakshminarayana's vortex model, Nikolos *et al.* deny the validity of the retained lift theory used in Lakshminarayana's model and propose a new way to describe the process of the rolling-up of the jet issued from the gap. Incorporated with a modelled vorticity diffusion, the new model predicts well the shed out vorticity and the total pressure loss. In addition to the new models, Nikolos *et al.* conclude that the key factor for both the shed vorticity and the mechanics of the tip-leakage vortex formation is the mass flow rate through the tip gap. The mass flow rate through the tip gap is affected not only by the tip gap size and the pressure

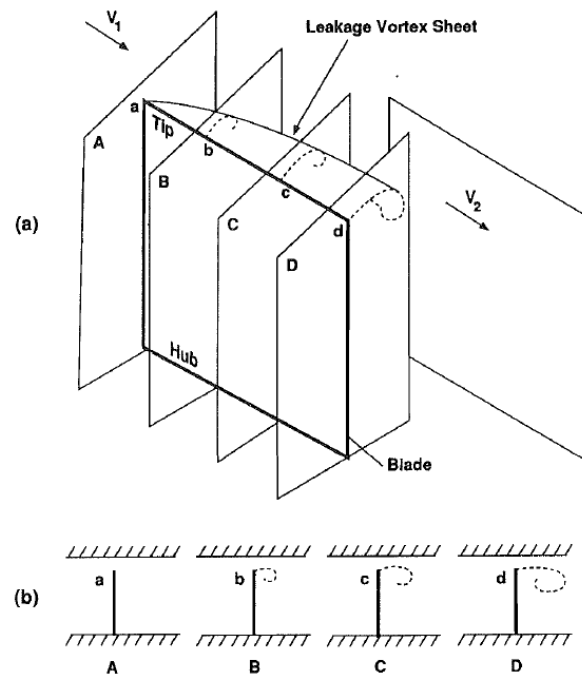


Fig. 2.2 Idea used in Chen *et al.*'s model [27]: the evolution of the tip-leakage flow is treated as an unsteady process in the successive crossflow planes.

difference across the blade tip, but also by the relative motion of the end-wall. However, neither of the models mentioned above consider the relative wall motion. So Nikolos *et al.* investigated the relative wall motion effects on tip-leakage flow in a later research paper [88]. The previous basic gap flow model without wall motion is extended and a new theoretical model is deduced to predict the relative wall motion effects on the mass flow rate through the tip gap for compressors and turbines respectively. The relative wall motion increases the strength of the tip-leakage vortex for a compressor and decreases it for a turbine. For both cases, the effect of the relative wall motion extends over almost the whole gap height, and the vortex center is moving towards the direction of the wall motion. However, the effect seems relatively larger for the turbine, because the pressure driven flow and the moving wall driven flow have opposite directions in the turbine. In addition, Nikolos *et al.* draw the same conclusion as Chen: the tip clearance size has little effect on the trajectory of the tip-leakage vortex core in the blade passage.

2.1.2 Experimental research

Compressor cascades

Most of the early basic experimental research on the tip-leakage flow is restricted to cascades, since they have lower requirements for the measurement technology. Storer and Cumpsty [102] investigated the tip-leakage flow in a linear compressor cascade comprising five blades with stationary walls, focusing on the blade surface pressure distribution, tip gap exit flow field and the loss due to the clearance. The cascade inlet velocity is 24 m/s, corresponding to a Mach number of 0.03. The chord based Reynolds number is 5×10^5 . The tip gap is adjusted to 2% and 4% chord, compared with the no clearance case. The measurements are conducted using pressure tappings and five-hole probes. Results show that for a typical compressor-type blade, the tip-leakage flow separates from the blade tip and does not reattach along the majority of the chord. The trajectory of the tip-leakage vortex coincides with a trough of pressure measured on the end-wall. The origin of the trough is close to the lowest pressure contour on the end-wall, which is located close the blade tip. With the increase of the tip gap, the position of the minimum pressure on the end-wall moves progressively downstream of the leading edge: it is located at about 25% chord from the leading edge for a 2% chord tip gap, and moves to near 42% chord for a 4% chord tip gap. From this point of view, the size of tip gap does have an influence on the tip-leakage vortex trajectory. The pressure measurements reveal that the pressure distribution at the blade tip, as shown in Fig.2.3, is different from that at the mid-span, and the blade loading is smaller at the blade tip. The tip clearance vortex substantially alters the static pressure field near the tip on the suction side, moving the minimum pressure back along the chord as the clearance is increased. The position of the vortex relative to the suction surface is very important in determining the pressure distribution near the blade tip and the blade force. As for the losses, a non-linear rise of total pressure loss is observed in spite of a linear relationship of the tip-leakage flow to clearance gap height. A very high loss is produced in a thin layer separating the two high-speed flows near the exit of the tip gap where intense shearing is caused by the difference in flow direction. Store and Cumpsty also performed a numerical simulation to explore the aspects of tip-leakage flow less accessible by the experiment alone. Despite a relatively coarse mesh, especially near the tip, and a rather unsophisticated turbulence modelling, the results agree well with the experiment on many aspects. The analysis led Store and Cumpsty to conclude that the tip-leakage flow is controlled by a primarily inviscid mechanism.

In Store and Cumpsty's experiment, the ratio of blade thickness to clearance height is low, and the flow leaving the tip gap may not be fully mixed out. Things may be different for other typical compressor blades with higher ratio of blade thickness to clearance height, such as the NACA 56 series profiles. Kang and Hirsch [67, 68] conducted an experiment in a linear compressor cascade of seven NACA 65-1810 blades with stationary walls. The main

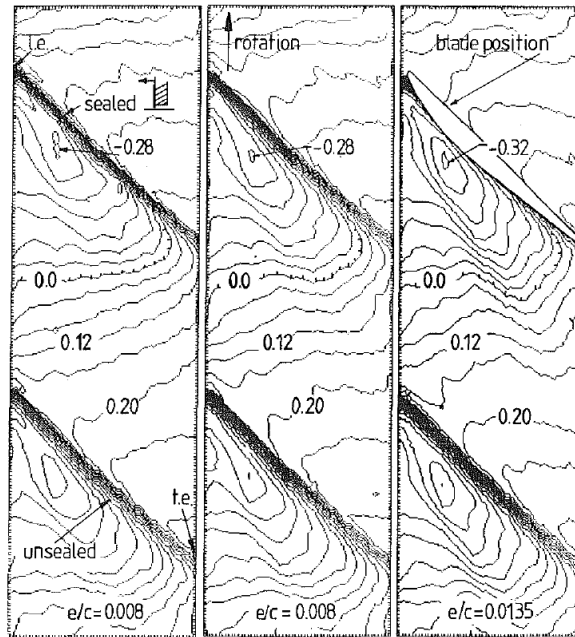


Fig. 2.3 Wall pressure (C_p) distributions with tip clearance of 0% (left), 0.8% (middle) and 1.35% (right) chord, observed in Storer and Cumpsty's experiment [102].

purpose of this research was to investigate the flow nature existing inside the clearance over the whole chord. The tip gap is adjusted to 1%, 2% and 3.3% chord, compared with the no clearance case. The Reynolds number is about 3×10^5 based on the chord. Measurements are conducted with five-hole probes inside and downstream of the blade passage. Surface flow visualizations are performed on the end-wall and the blade surface to reveal the flow patterns. In the experiment, Kang and Hirsch observe a three-vortex structure in the blade tip region, as shown in Fig. 2.4: A large tip-leakage vortex, which starts a little downstream of the leading edge, grows in size along the chord and progressively dominates the end-wall region; A small tip separation vortex formed by the fluid close to the tip surface at the pressure side, diverging from about the middle of the blade profile. It has the same rotation sense as the tip-leakage vortex; A small secondary vortex, which rolls up at the suction side edge. It has an opposite rotation sense to the tip-leakage vortex. Contrary to Rains's 2D model, the flow inside the tip gap is strongly three-dimensional almost over the whole chord length. For the small clearance cases, a weak horseshoe vortex is also observed to be formed from the blade leading edge. Kang and Hirsch conclude that the generation of the tip-leakage vortex results in the passage vortex moving close to the end-wall and to the suction side of the passage. The motion of the tip-leakage vortex arouses a strong reloading by which the leakage flow is reinforced. The size of the tip gap does have an effect on the tip-leakage vortex trajectory: the tip-leakage vortex deviates from the blade suction side with the increase of the tip gap. In

this experiment, the mixing process is found not fully completed at the gap exit, since the gap exit velocity shows a wakelike profile close to the tip.

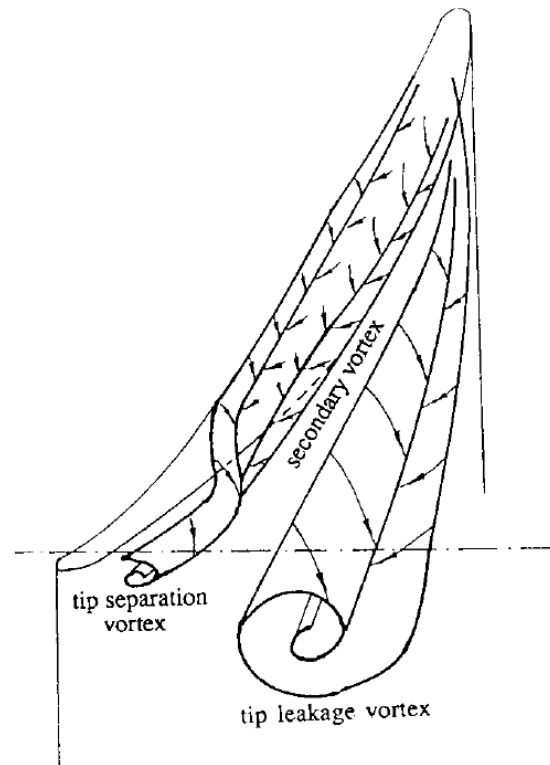


Fig. 2.4 Three-vortex structure, observed in Kang and Hirsch's experiment [67].

In recent years, a series of experiments [87, 104] have been carried out at Virginia Polytechnic Institute and State University, for the purpose of understanding the structure of the vortex-dominated endwall flows found in aircraft engine fans and compressors. A compressor cascade with different tip gaps and with/without moving endwall was used to investigate the tip-leakage flow dynamics under different flow conditions. It was found that the tip-leakage vortex dynamics are dominated by the streamwise mean-velocity deficit it produces. Mean velocities associated with the deficit are more than twice as strong as those associated with the rotating motion and decay more slowly with downstream distance. Turbulent kinetic energy in the vortex is produced almost entirely by velocity gradients associated with the deficit. By comparing the flow fields with and without the moving endwall, it is found that, many critical features of the tip-leakage vortex are almost unaffected by the endwall motion: the vortex produces almost the same magnitude of the streamwise mean-velocity deficit, and the deficit still dominates both the mean velocity field and the production of turbulence. Thus, the moving endwall does not fundamentally alter the mechanisms that govern the development of mean tip-leakage flow and its turbulence

structure. Another experiment [58] conducted at Virginia Polytechnic Institute and State University concerns the initial formation of the tip-leakage vortex and the interaction between the vortex and inflow disturbances. The mechanism of the tip leakage vortex formation is found to be independent of the tip gap setting. The vortical structure is initially generated and attached to the blade tip, progressively picks up circulation shed from the blade tip and the endwall boundary layer, and finally moves across the passage resulting in a reduction in its rotational strength as the cross sectional area of the vortex increases, but little circulation is added. Inflow disturbances are found to cause small-scale responses and large-scale responses upstream and downstream of the vortex shedding location, respectively.

Compressor rotors

There are substantial differences in the structure of tip-leakage flow in the cascades and the rotors. The differences result not only from the moving end-wall, but also from the inlet boundary layer. Compared with the cascades, the flow field of the rotors is more complex and more similar to the real turbomachine, that's why the compressor rotors attract more attention among tip-leakage flow researchers.

Inoue *et al.* [57] performed an experimental research on an isolated axial compressor rotor of NACA 65 series profile. The purpose of the research is to investigate the clearance effect on the end-wall flow development and the behaviour of the tip-leakage flow. The tip gap is set from 0.5 mm (0.4% chord) to 5 mm (4.3% chord) by changing the radius of the casing. The flow rate is adjusted to yield the same incidence angle of the rotor blade at mid-span for different clearances, in order to get rid of the effect of incident variation caused by boundary layer blockage. The averaged phase-locked flow field inside the tip clearance and behind the rotor is measured by a constant temperature hot-wire anemometer and a periodic multisampling and averaging technique. Inoue *et al.* find that an increase of the clearance size reduces the efficiency, resulting in a decrease of the stage performance. When the tip clearance is small, the leakage jet flow interacts violently with the through flow near the leading edge, and a rolling-up tip-leakage vortex decays downstream. The circulation of the tip-leakage vortex increases with larger tip clearance, and the position of the rolling-up deviates from the blade suction side. Moreover, the intense vortex causes reverse flow in the axial direction near the casing wall.

Foley and Ivey [41] investigated the behaviour of the tip-leakage flow under the effects of stator-rotor interactions. The experiment was conducted with a large-scale low-speed four-stage axial compressor, with a tip gap of 1.2% and 3% chord. Detailed measurements are performed upstream and downstream of the third stage rotor, as well as on the rotor blade surface, using pneumatic probe traverses, blade static pressure tappings and 3D laser

transit anemometry. At the rotor inlet, a two-dimensional flow region is observed from approximately 40% to 85% annulus span. Outside of this region, reduced total pressure is measured due to the leakage jet losses from the upstream stages and the three-dimensional end-wall effects. This reduced pressure results in a higher incidence angle at the rotor inlet close to the blade root and tip. At the blade tip, the peak suction pressure point is found to occur closer to the leading edge compared with the mid-span region. This is believed to be caused by fluid travelling radially up the suction surface as it is entrained into the leakage jet. At the rotor exit, the contours of the total pressure are generally pitchwise uniform due to the developing wall boundary layer and the mixed-out effects of the upstream rotor tip-leakage flows. The increase of the rotor tip clearance height is found to reduce the loading distribution at the blade tip.

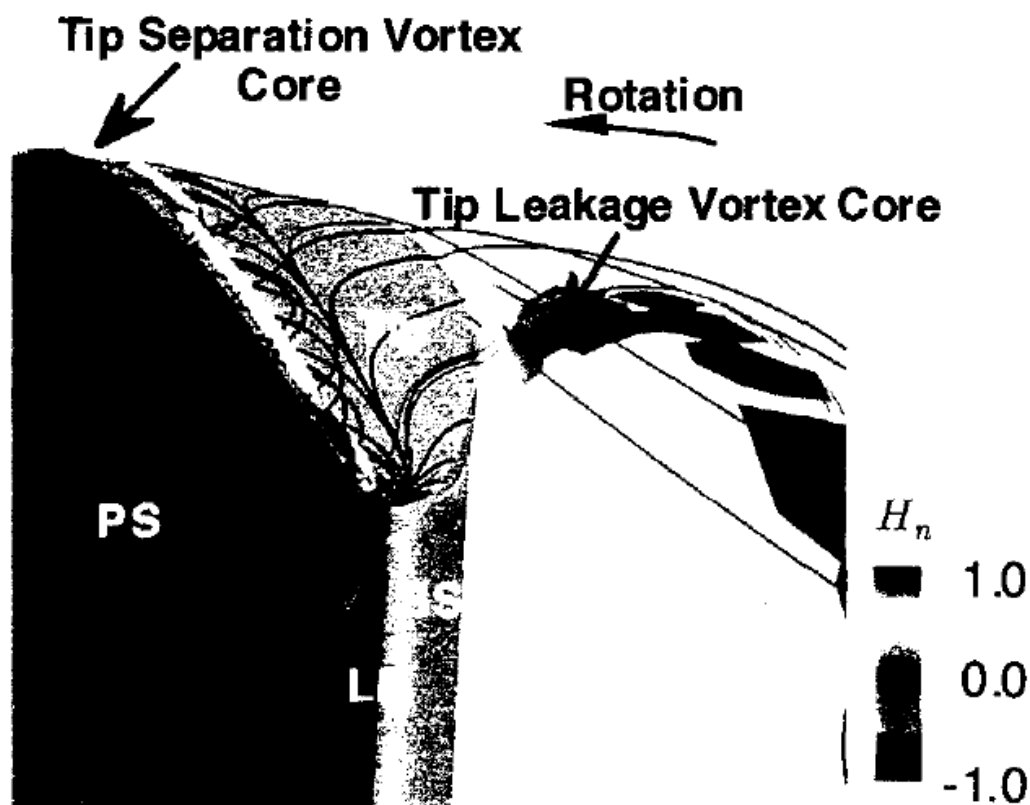


Fig. 2.5 Tip-leakage flow structure at design point, observed in Inoue and Furukawa's RANS computation [56].

The blade tip region of the turbomachine rotors is extremely complex, because of the interaction between the tip-leakage flow and the boundary layers on both the end-wall and the blade surface. So various flow behaviours may occur here. Lakshminarayana *et al.*'s experimental research [74] shows that the tip-leakage jet may not necessarily roll up into a

vortex. The experiment is conducted with a compressor stage consisting of an inlet guide vane, a rotor row and a stator row. The blade section at the rotor tip is a NACA 65 series, and the average tip clearance is 2.27% chord. The inlet flow velocity is about 25.4 m/s and the boundary layer thickness on the casing is about 8% blade span. A rotating five-hole probe is employed to measure the flow field downstream of the rotor. Lakshminarayana observes that the tip-leakage jet emerging from the tip clearance is of high velocity and mixes quickly with the main stream, producing intense shearing and flow separation. The tip-leakage jet does not roll up into a vortex, probably because the inlet swirl, the high turbulence intensity and the high blade loading in this experiment cause an intense mixing of the tip-leakage jet before it has a chance to roll up into a discrete vortex. Lakshminarayana *et al.* conclude that the formation of the tip-leakage vortex depends on various parameters: in addition to the widely accepted ones, such as the tip clearance height, Reynolds number and blade loading, it may also depend on the configuration of the facility, inlet flow turbulence, annulus wall boundary layer thickness, velocity difference between the tip-leakage jet and the main stream, and blade speed.

Another specific phenomenon is observed in the experiment of Stauter [101]. Stauter investigated the development of the tip-leakage flow in a two-stage axial compressor with a tip gap of about 1.25% chord. A two-color, five-beam LDV system is employed to simultaneously measure the three velocity components of the flow field inside the blade passage and downstream of the second stage rotor. The measurements are performed at 18 axial positions, from 42% to 130% chord, and five of them are reported in details. The clear evidence of the tip-leakage vortex roll-up could be observed through the vector plots at the axial positions of 42%, 63% and 115% chord. However, the tip-leakage vortex seems too weak to be captured at the axial positions of 90% and 130% chord. Stauter concludes that the strength of the tip-leakage vortex decays through the passage until aft of the trailing edge, at which point it starts increasing again, reaching a peak at 115% chord, after which, it starts decreasing again. Stauter does not provide an explanation of this phenomenon. This behaviour of the tip-leakage vortex is generally different from that observed in other experiments, and it has never been observed again by other researchers.

2.1.3 Numerical research

Reynolds-averaged Navier-Stokes equations (RANS)

Most of the numerical studies on the tip-leakage flow are based on Reynolds-averaged Navier-Stokes (RANS) simulations, since they have a moderate computational cost compared with experiments and other numerical methods. Inoue and Furukawa performed a series of numerical simulations to investigate the behaviour of the tip-leakage flow at design point

[56] and at near-stall conditions [44] of an isolated low-speed axial compressor rotor. The configuration of this axial compressor rotor is the same as their previous experiment [57] mentioned above. The blade is of NACA 65 series profile and the tip clearance is set to 1.7% chord. The flow field is simulated by the three-dimensional compressible Reynolds-averaged Navier-Stokes equations based on a high-resolution upwind scheme using the TVD formulation. The eddy viscosity is estimated by the algebraic turbulence model of Baldwin and Lomax [10]. The computational domain consists of 518,144 cells and the grid spacing on the solid walls is small enough ($y^+ < 1$) to describe the viscous sublayer. The inlet boundary layer is given by the experimental results. The flow field is displayed and analysed in terms of vortex-core identification, helicity, flow topology, etc. At the design point of the compressor rotor, a two-vortex structure is captured in the blade tip region, as shown in Fig.2.5: one large tip-leakage vortex and one small tip separation vortex. The tip-leakage flow starts to roll up at a position a little downstream of the blade leading edge. The streamlines reveal that the vortex core is mainly composed of fluid particles formerly included in the shear layer and the fluid passing through the clearance coils around the vortex core. As for the vortex-lines, it is found that the vortex-lines in the suction surface boundary layer link to either the tip-leakage vortex core, either to the pressure surface boundary layer, or to the casing wall boundary layer, depending on the issuing position. Inoue and Furukawa also investigate the effects of the relative motion of the casing wall. It is found that the flow topology changes with the moving casing wall. In this configuration, the moving wall increases the circulation of the tip-leakage vortex and reduces the leakage flow losses, mainly due to lower friction losses. At the near-stall conditions, a tip-leakage vortex breakdown is observed inside the rotor passage at a lower flow rate than the peak pressure rise operating condition, as shown in Fig.2.6. The occurrence of the breakdown causes some significant changes in the nature of the vortex: the vortex core rapidly decelerates, followed by a bubble-like recirculation region. In the flow topology, a stagnation point is observed just in front of the recirculation region. The vortex breakdown leads to an expansion of the tip-leakage vortex, which has an extremely large blockage effect, resulting in a large loss region. Downstream of the breakdown region, a weak tip-leakage vortex rolls up, but decays and disappears rapidly. So there is no tip-leakage vortex observed downstream of the rotor. The same behaviour of the tip-leakage vortex is observed by Wu and Chu [111] in an isolated high-speed axial compressor rotor, as shown in Fig.2.7. Wu and Chu also find that the tip-leakage vortex exerts little influence on the development of the blade suction surface boundary layer even at near-stall conditions.

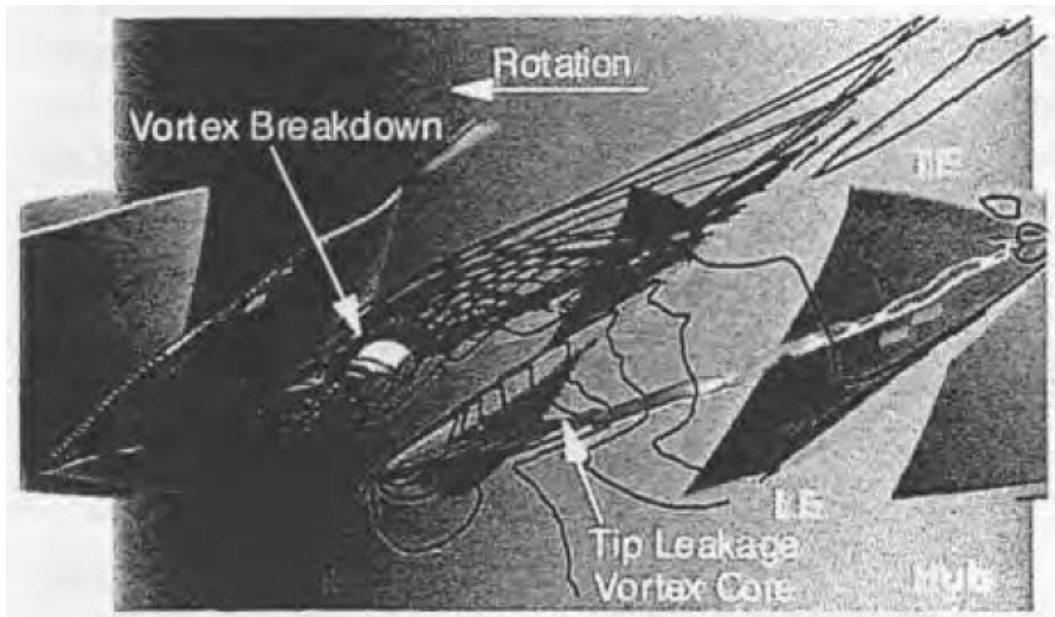
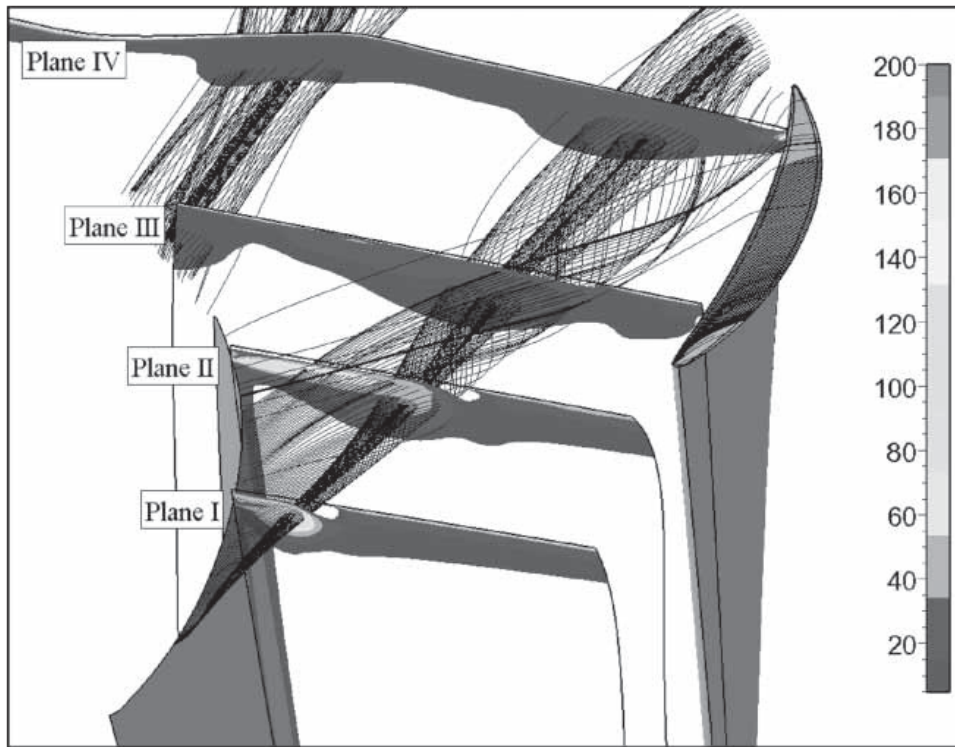
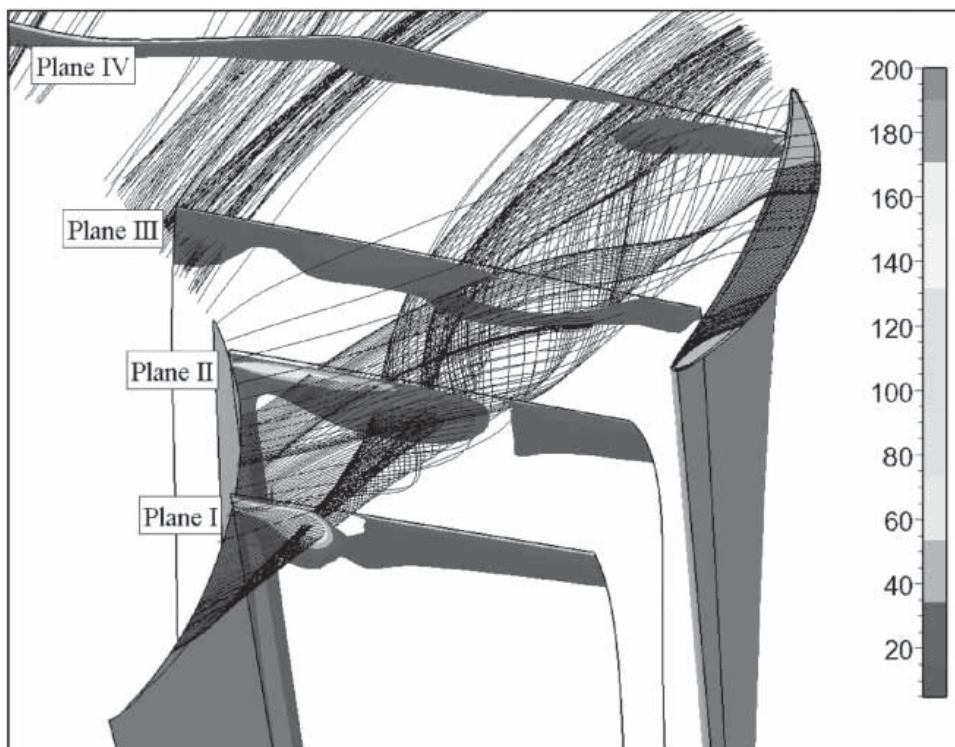


Fig. 2.6 Tip-leakage flow structure near stall, observed in Furukawa and Inoue's RANS computation [44].

RANS resolves the steady mean flow field, so only the steady flow features can be captured and studied by RANS. There are still some unsteady flow phenomena related to the tip-leakage flow, such as the oscillation of the tip-leakage vortex, also referred to as vortex wandering. Zhang *et al.* [116] investigated the tip-leakage flow unsteadiness in an isolated axial compressor rotor by solving the unsteady Reynolds-averaged Navier-Stokes equations (URANS). The tip gap is set to 2%, 3.4% and 5% chord, compared with the no clearance case. A standard $k - \epsilon$ turbulence model and a non-equilibrium wall function are employed. Steady boundary conditions are imposed at both the inlet and the outlet of the computational domain. The unsteadiness of the tip-leakage flow is clearly revealed by the static pressure evolution in the blade passage. It is found that this unsteadiness only exists in the blade tip region and has its own frequency. Zhang *et al.* explain this periodic oscillation of the tip-leakage flow as a result of a dynamic balance between two counter-acting driving "forces": one "force" is the aerodynamic loading of the blade, which results from the pressure difference across the blade; the other "force" is the unloading of the blade, which originates from the tip-leakage flow balancing the pressure difference. The unsteadiness begins to emerge when the originally static balance is broken and replaced by the dynamic balance. It is found that the trajectory of the tip-leakage vortex can be used as an indicator of the onset of the dynamic balance between the two "forces": if these two "forces" are strong enough to push the tip-leakage vortex across the blade passage and stamp a low pressure spot on



(a)



(b)

Fig. 2.7 Tip-leakage vortex and leakage streamlines at (a) peak efficiency condition (b) near stall condition, observed in Wu and Chu's RANS computation [111].

the pressure side of the neighboring rotor blade, the static balance will be broken and the unsteady oscillation results.

Large-eddy simulation (LES)

Despite the progresses made with RANS approaches in the computational interpretation of the tip-leakage flow, the unsteady nature of the tip-leakage flow limits the applicability of RANS approaches in further investigations of the flow physics. In recent years, with increasing computing power, the large-eddy simulation (LES) technique, in which resolved and subgrid-scale motions are defined by a spatial filter applied to the Navier-Stokes equations, has emerged as a promising tool to complement RANS computations [112].

You *et al.* performed a series of comprehensive analyses of the tip-leakage flow based on large-eddy simulation (LES) results, with emphasis on the effects of the tip gap size [113], the mechanisms for viscous losses [114] and the unsteady characteristics [115], along with the mean flow features. The flow configuration is a linear cascade with a moving end-wall. The tip gap is set to 1.53%, 3.06% and 6.11% of the axial chord. With the periodic boundary conditions used, only one single-blade passage is considered in the simulation. The computational mesh consists of more than 25 million cells. In wall units, the blade surface resolution in the region of primary interest is within the range $\Delta x^+ \leq 50$, $\Delta y^+ \leq 3$ and $\Delta z^+ \leq 30$. A Lagrangian dynamic subgrid-scale (SGS) model [83] is employed to estimate the subgrid-scale eddy viscosity. The inlet boundary layer is generated by a separate LES of a turbulent boundary layer on a stationary flat plate. In the mean flow field, a multi-vortex structure is observed in the end-wall region, as shown in Fig.2.8: a dominant tip-leakage vortex, a tip-separation vortex and several small induced vortices with the same or opposite rotation sense as the tip-leakage vortex. These vortices are found to decay continuously as they convect downstream, as shown in Fig.2.9. Inside the blade passage, the trajectory of both the tip-leakage vortex and the tip-separation vortex is strongly affected by the moving end-wall. Downstream of the trailing edge, the tip-leakage vortex core is lifted from the end-wall, which is probably an effect of the moving end-wall, and since then its trajectory is mostly influenced by the main stream. The comparison of the Reynolds stresses reveals that the normal-stress components are always larger than the shear-stress components throughout the cascades. Inside the blade passage, $\overline{u'u'}$ dominates among the three normal-stress components, while they are of the same magnitude downstream of the trailing edge. The tip-leakage vortex and the tip-leakage jet are found to generate most of the turbulent kinetic energy in the end-wall region. In addition, the tip-leakage vortex is found to experience a pitchwise wandering motion, which is demonstrated by a peak in the energy spectra of the pitchwise velocity fluctuations, as shown in Fig.2.11. With the increase of the

tip gap size, the strengths of the tip-leakage vortex and the induced vortex increase, while the tip-separation vortex decreases, as shown in Fig.2.10. The trajectory of the tip-leakage vortex also deviates from the blade suction surface with larger clearance. However, the mechanisms for the generation of vorticity and turbulent kinetic energy are mostly unchanged by the tip gap size variation.

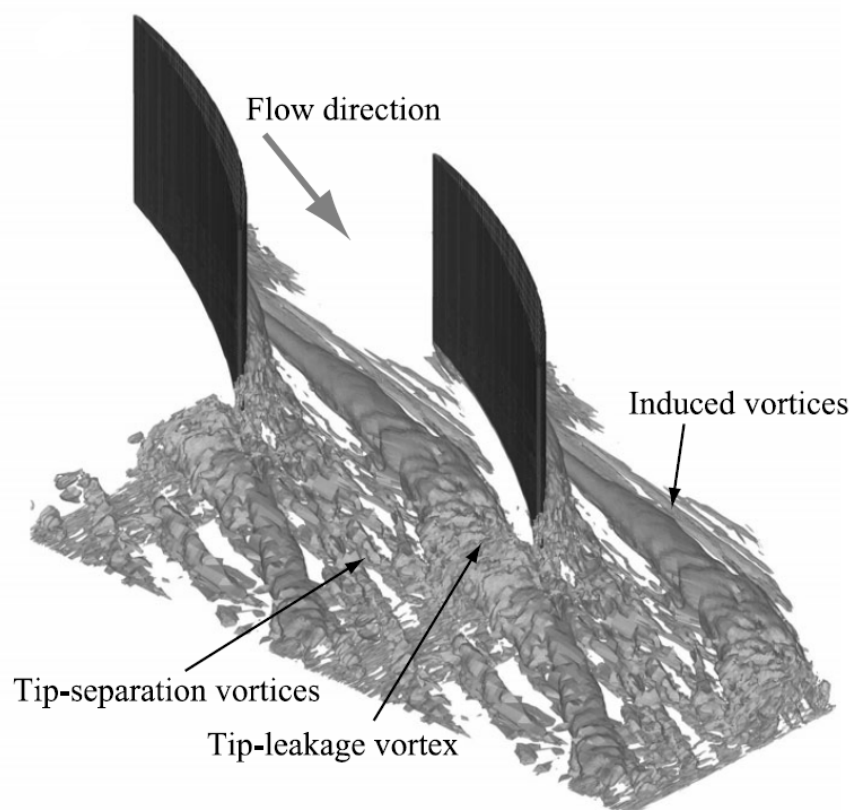


Fig. 2.8 Multi-vortex structure, observed in You *et al.*'s LES computation [114].

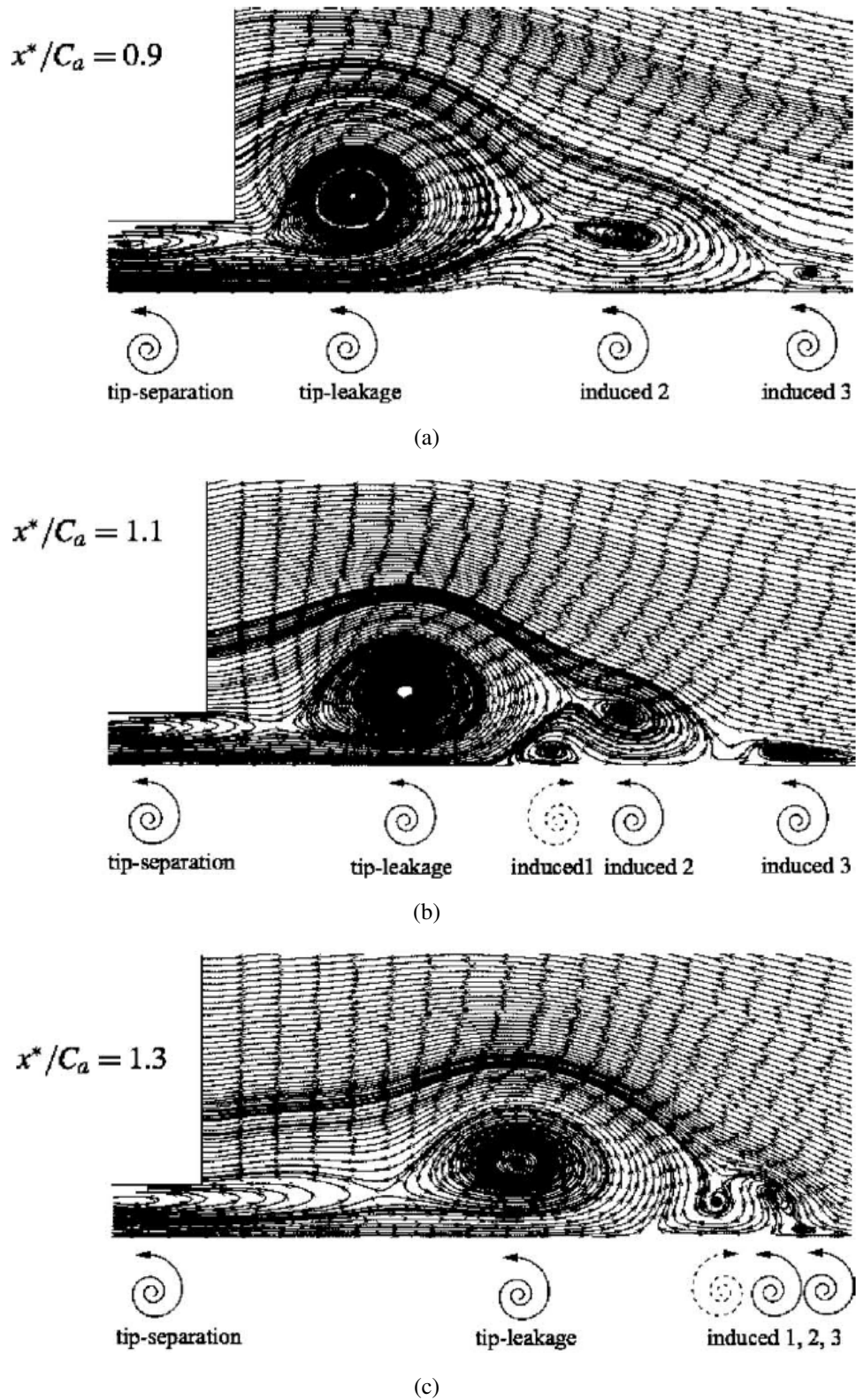


Fig. 2.9 Generation and evolution of the end-wall vortical structures, observed in You *et al.*'s LES computation [115].

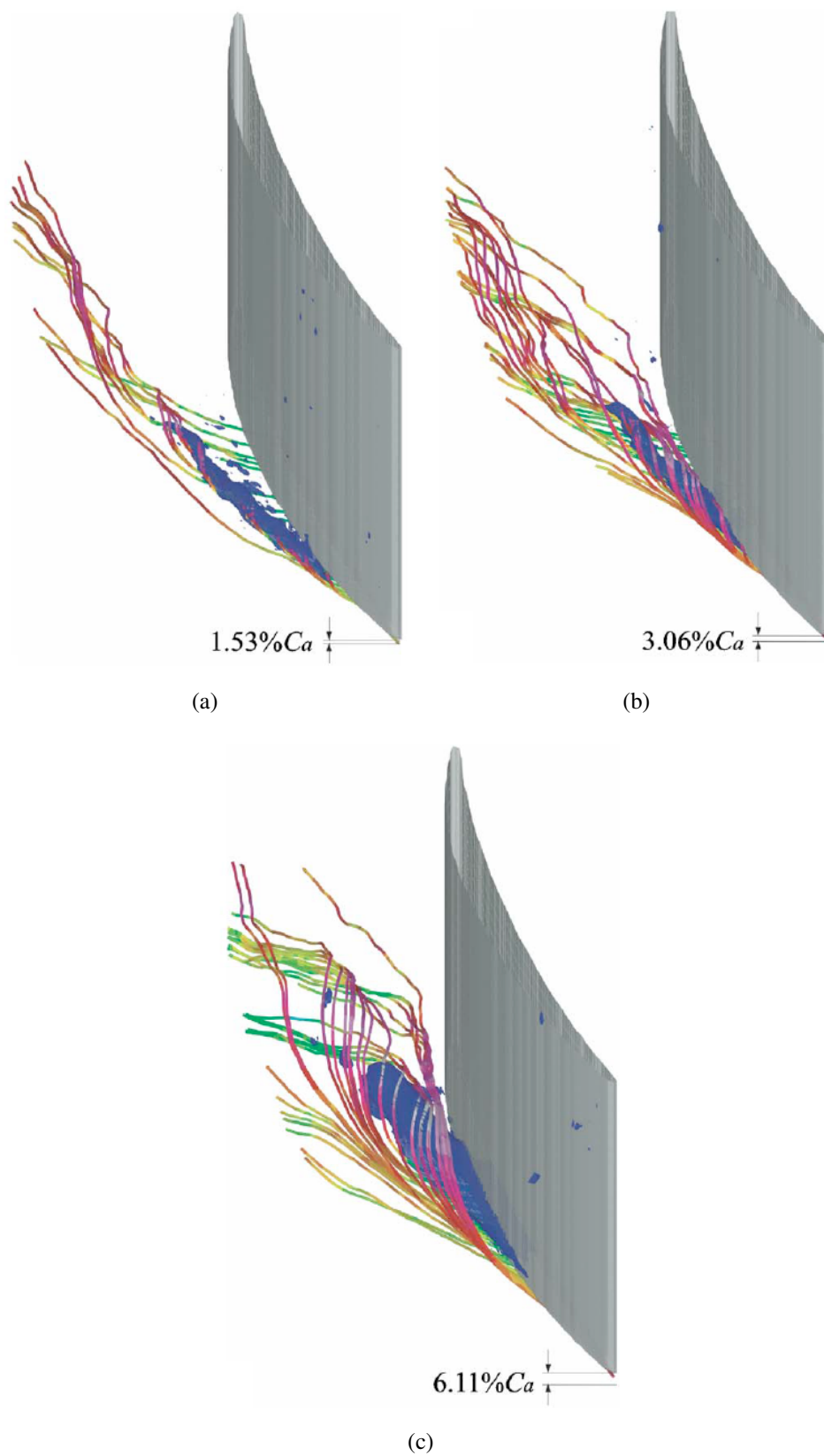


Fig. 2.10 Tip-leakage flow and vortex for three different gap sizes, observed in You *et al.*'s LES computation [113].

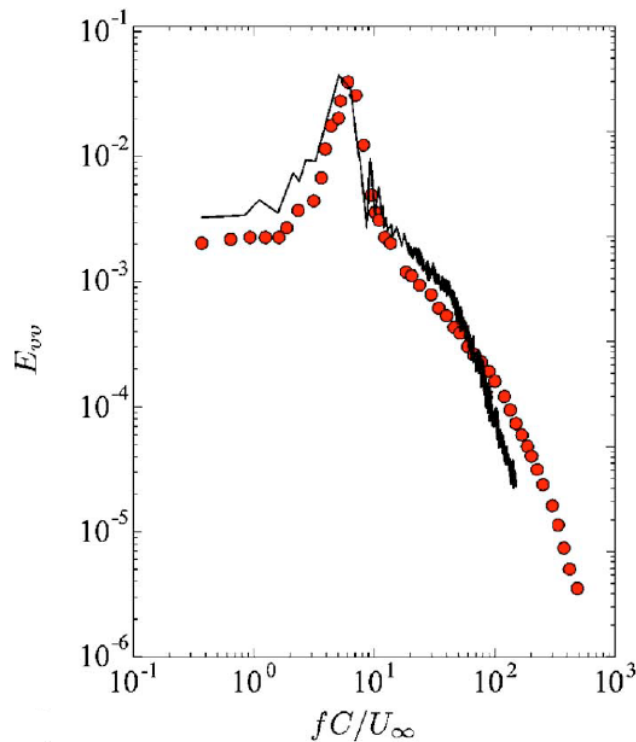
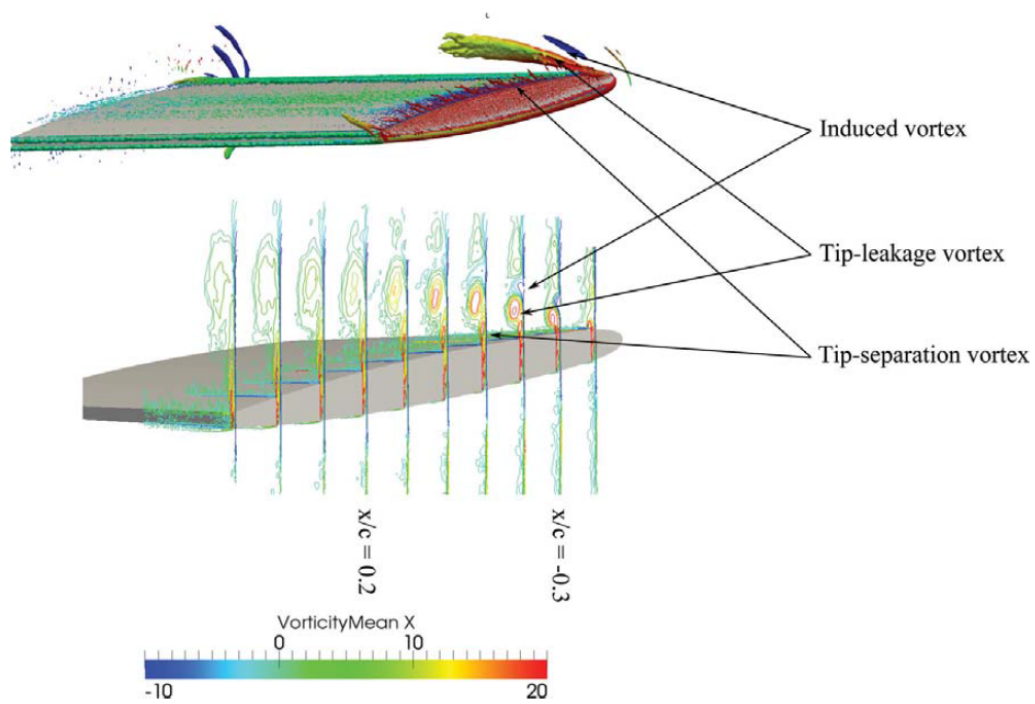
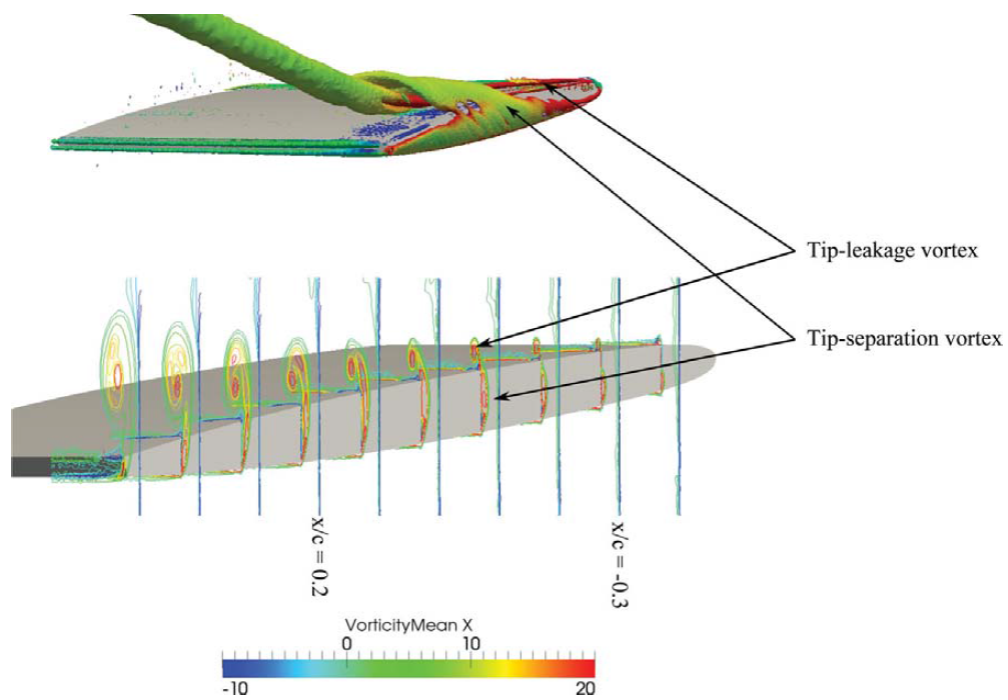


Fig. 2.11 Energy spectra of the pitchwise velocity fluctuations in the blade wake, observed in You *et al.*'s LES computation [115].

The tip-leakage flow topology under the condition of a relative large clearance is investigated in a very recent numerical research with RANS and LES performed by Decaix *et al.* [33]. The flow configuration is an isolated NACA0009 airfoil with a relatively large tip clearance, 10% chord, as well as a smaller one, 2% chord. The computational mesh for LES is non-structured with 200 million elements for the 10% chord case and 300 million elements for the 2% chord case. While the mesh for RANS is structured with approximately 2.8 million nodes for both cases. The LES subgrid-scale eddy viscosity is estimated by a localised dynamic Smagorinsky model [47] and RANS turbulent viscosity is evaluated by the $k - \omega$ SST model [84]. As shown in Fig.2.12, for the small-clearance case, the tip-leakage vortex, the induced counter-rotating vortex and the tip-separation vortex are all captured, though the evidence of the tip-separation vortex is not clear. For the large-clearance case, the induced vortex disappears and a fusion between the tip-leakage vortex and the tip-separation vortex is depicted. The formation of the tip-leakage vortex is not delayed with the larger gap and the vortex core is found to be sustained all along the vortex.



(a)



(b)

Fig. 2.12 Flow structures for a clearance of (a) 2% chord (b) 10% chord, observed in Decaix *et al.*'s LES computations [33].

2.2 Review of aeroacoustic research on tip-leakage flow

As one of the five fundamental airfoil noise mechanisms identified by Brooks *et al.* [20], the tip clearance noise in the axial flow fans has been a major concern, since turbo-jet engines have been introduced on aircrafts to replace propellers on a commercial scale. One of the most important objectives of the studies is to identify the mechanisms of the noise generation and to relate the strength of the sources to the physical parameters. This was usually achieved through the measurements and observations in the experiments in the early stages. Based on the adequate knowledge, some appropriate noise-suppression devices have been designed and many noise prediction methods have been developed.

Considering the main interest of the current research, a review of the aeroacoustic research on the tip-leakage flow is presented, with emphasis on experimental research and noise prediction methods, respectively.

2.2.1 Experimental research

As early as the 1960s, Sharland [98] investigated the various possible mechanisms of noise generation in axial flow fans, as well as the key factors on which the strength of the noise sources depends. Sharland concludes that the noise from the axial fans is of a dipole nature and the broadband noise arises from the vortex shedding at the blade trailing edge. He also proposes a simple model for the noise prediction, which is fundamental for many subsequent studies. However, no specific attention is paid on the noise from the tip-leakage flow.

Mugridge and Morfey [86] reviewed the experiments and theories relating to the fan noise sources for both subsonic and supersonic axial flow machines. They conclude that secondary flows associated with the tip clearance and the duct boundary layer are sources of turbulence and hence broadband noise. Because of their opposing effects on the secondary flow, the tip clearance and the boundary layer thickness can be optimized to reduce the additional noise radiation. The optimal tip clearance is found to be 5% of the blade chord in Mugridge and Morfey's tests. The authors also add that the removal of the wall boundary layer may actually increase the radiated broadband noise for a given tip clearance, owing to an increase in the leakage losses.

Longhouse [79] conducted a series of experiments with different clearance sizes to investigate the tip clearance noise and its control in axial flow fans. He concludes that the tip clearance noise is caused by an unsteady interaction of the tip-leakage vortex with the blade trailing edge and with the leading edge of the following blade. The tip clearance noise contributes up to 15 dB(A) to the fan noise for the large clearances (>3-4% of the blade

chord). It is also dominant for the small clearances, when the fan is heavily loaded. In order to control the tip clearance noise, Longhouse proposes a rotating ring attached to the tips of the blades and a noise reduction of as much as 12 dB is achieved, in spite of a little performance loss.

Kameier and Neise [64, 65] explain the tip clearance noise as a result of a rotating flow instability. In the experiment, Kameier and Neise find that the tip clearance noise is measured in the acoustic far field only if the rotating flow instability components are present simultaneously in the near field. The rotating instability occurs if a strong reversed flow exists in the tip clearance gap. The tip clearance noise is generated when the rotating instability interacts with the impeller blades. When the tip clearance is enlarged, besides the higher broadband levels, the sound pressure level increases significantly within limited, almost narrow frequency bands in a region below the blade passing frequency. With a turbulence generator installed in the tip gap, the tip clearance noise component in the far field is found to be diminished by more than 30 dB, and the fan efficiency is also increased by 7%. Another comprehensive investigation of the tip-leakage flow and the rotating instability is made by März *et al.* [82]. However, only the aerodynamic aspect is considered in this research.

Fukano *et al.* [43] investigated the effects of the tip clearance on the characteristics of noise by using three kinds of low pressure axial flow fans and a mixed flow fan. It is found that when the tip clearance is reduced, a lower level of noise is observed at both the design and off-design conditions. If the rotor shaft is not co-axial with the duct axis, a discrete frequency noise is generated by the interaction of the blades with the duct wall, which should be avoided. In a more recent study, Fukano and Jang [42, 62] find that the increase of noise due to the tip clearance at low flow rate conditions is mainly caused by the high velocity fluctuations in the vortical flow. The noise due to the peak frequency of the velocity fluctuations can be an important noise source, at high rotational speed.

In most of the experimental researches, a clear trend towards better aerodynamic efficiency and quieter fans with decreasing tip clearance could be observed, such as in the experiment of Karstadt *et al.* [69]. In Hughes, Woodward *et al.*'s aeroacoustic wind tunnel test program [54, 55, 109], they find that the optimal tip clearance with minimal broadband noise level depends on the fan speed. The broadband noise level is the lowest for the nominal clearance at the fan speeds below 75%. Above that speed, a tip clearance of 0.02 inch shows the lowest broadband noise levels. This phenomenon may be explained by that, at lower speeds, the amount of the tip-leakage flow and its interaction with the fan tip are driving the noise. At larger speeds, a very small gap may cause a scraping vortex to be formed, and to interact with the fan tip, generating more broadband noise.

2.2.2 Noise prediction methods

Most of the efforts on the noise prediction are addressed to the trailing-edge noise, because the trailing-edge noise is the only remaining broadband noise contribution when a subsonic fan operates in a homogeneous stationary flow and it defines the minimum achievable noise of a fan [110]. Some of the prediction methods used for the trailing-edge noise are also available for the prediction of the tip-clearance noise.

The most direct way to predict the tip clearance noise should be the Ffowcs-Williams and Hawkings (FWH) acoustic analogy [107]. FWH is an extension of the Lighthill's theory [77, 78]. The turbulence is treated as a volume distribution of moving quadrupoles and the surfaces as dipole and monopole distributions, when both the bounding surfaces and the turbulence are compact relative to the radiated wavelengths. This approach is based on the ideal assumption of separating the sound generation mechanisms from its pure propagation, so its biggest advantage is that the computational cost is independent of the distance between the source and the observer. According to this method, the far-field noise can be computed by the hypersurface integrals of the unsteady near-field flow data, such as the pressure fluctuations on the blade surface, if the source field and surface-boundary conditions are known in space and time. So the FWH cooperates well with the unsteady simulations, such as the large-eddy simulation. Some of recent efforts to predict the tip clearance noise with FWH and the unsteady simulations are made by Zhu and Carolus [117], where the flow field is simulated by an unsteady Scale-Adaptive Simulation (SAS), and by Knacke and Thiele [70], where the flow field is simulated by a compressible Detached-Eddy-Simulation (DES). There are also many extensions of this method, such as Casalino's advanced time formulation [24], which allows the computation of the acoustic field as the CFD simulation is processed.

Another way to predict the tip-clearance noise is the traditional computational aeroacoustic (CAA) approach: solving the linearized Euler equations (LEE) coupled with an acoustic source term. The acoustic source term may be derived from an unsteady computation, or synthetic from a stochastic model based on the statistical quantities. There are two widely used stochastic models to set up the turbulence velocities for broadband sound sources: Stochastic Generation and Radiation (SNGR) model and Random Particle Mesh (RPM) method. The SNGR model [6, 7] provides a stochastic turbulent field generated by a sum of unsteady random Fourier modes based on the turbulent kinetic energy and the length-scale distribution from a RANS simulation. This model has been evaluated for the prediction of turbulence mixing noise [8, 9] and trailing edge noise [11, 63]. The RPM method [36, 40] generates the fluctuating quantities by spatially filtering convective white-noise. The discrete realization of convective white-noise is based on random particles. The generated fluctuations reproduce very accurately the autocorrelation and integral length-scale provided by RANS.

This method has been used in the prediction of the slat noise [37], the trailing edge noise [38, 39], the turbulence interaction noise [34] and the sweeping noise in jets [99]. Compared with FWH, the CAA approach needs high-accuracy numerical schemes, and consequently the reasonable cost solutions are generally restricted to near-field predictions.

There are also some analytical models based on the induced wall pressure, such as the model developed by Amiet [2, 3] and by Brooks and Hodgson [19]. This kind of model considers the incident aerodynamic wall pressure as the equivalent acoustic source. Recently, Roger and Moreau extended Amiet's model to predict the trailing-edge noise [85, 93] and the tip-clearance noise [50]. More details of these analytical models will be presented in Chapter 6.

2.3 Conclusions

In this chapter, some previous research works on the tip-leakage flow were reviewed. We started from the tip-leakage flow modelling, which is mainly dedicated to predicting the overall efficiency loss due to the tip clearance. These models can hardly be identified as universal, since they are all deduced on specific assumptions and the parameters used are semi-empirical, which makes them not very reliable during the turbomachinery design. Then we talked about some experimental and numerical researches on the aerodynamics of tip-leakage flow. most of these works put emphasis on the flow structures of the tip-leakage flow, and others also investigate some specific phenomena related to the tip-leakage vortex, such as the TLV beakdown and TLV wandering. From these works, we can find that the tip-leakage flow is extremely complex: it is governed by various parameters, such as the clearance height and the Reynolds number, and both viscid and inviscid interactions occur in the flow field. After that, we talked about the noise emissions from the tip-leakage flow. It is found that the tip clearance noise is closely related to the tip-leakage vortex. Finally, we discussed some far-field noise prediction methods, and some analytical models are chosen to be the investigation tools for the current research.

Chapter 3

Experimental and numerical methods

In this chapter, the flow configuration considered in both the experiment and the numerical simulations will be introduced, followed by a brief description of the coordinate system. Next, the measurement technologies and the experimental database will be introduced. Finally, the numerical methods used in this thesis will be described.

3.1 Configuration of the tip-leakage flow experiment

The experiment was conducted in the large anechoic room (10m × 8m × 8m) of Ecole Centrale Lyon. As shown in Fig.3.1, a simplified tip-leakage flow configuration is considered: an isolated airfoil is set in the potential core of a rectangular open jet (0.45m × 0.2m), the flow is enclosed between two end-plates, and a clearance is arranged between the airfoil and the lower end-plate. A NACA 5510 airfoil is used in the experiment. According to the naming convention of the NACA 4-digit series, this airfoil is generated with 5% maximum camber, 50% maximum camber position and 10% thickness, all percentages being expressed with respect to the chord length, which is $c = 200\text{mm}$. The angle of attack (AOA) is set to $16.5^\circ \pm 0.5^\circ$. The free-stream velocity at the nozzle outlet is $U_0 = 70\text{m/s}$. The Mach number is $M \sim 0.2$. Although this Mach number is quite small, the corresponding chord based Reynolds number $Re_c \sim 9.3 \times 10^5$ is close to that of an approaching aircraft for which the fan broadband noise is a major sound source. The turbulence level in the main flow at the jet nozzle is $u'/U_0 \sim 0.5\%$. Two cases with different clearance heights are considered in the experiment: $h = 10\text{mm}$ ($5\%c$) and 0mm (without clearance). The sum of the clearance height and the blade span is 200mm, which equals to the channel height.

This configuration should be the simplest tip-leakage flow configuration, where there are no effects of cascade and moving end-wall. However, this simplest configuration does have some practical applications in the real life: the flow at the slat fuselage junction is very

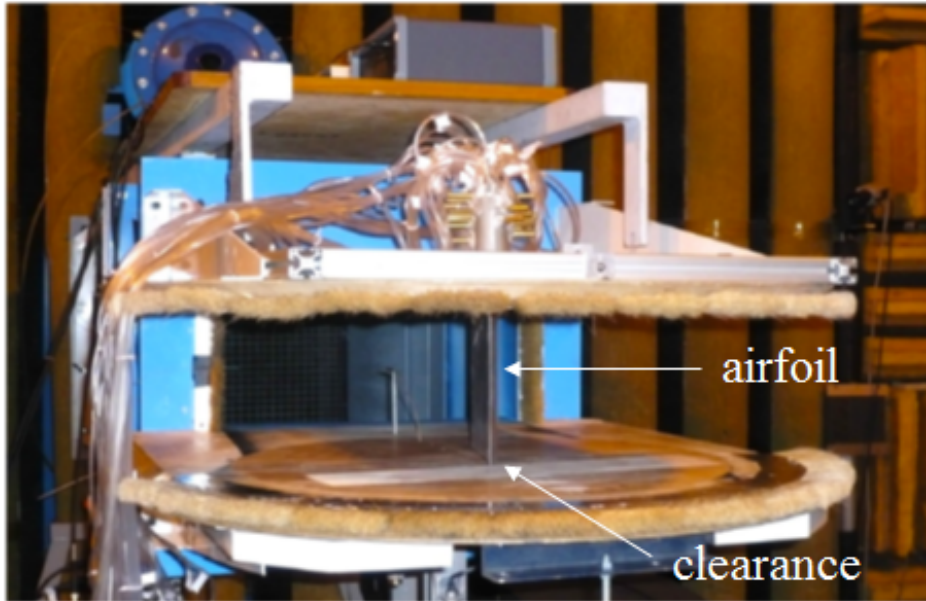


Fig. 3.1 Experimental set-up.

similar to that in the current configuration. In the future, by comparing the current results and those in a more complex configuration, we will be able to determine the influence of some isolated factors, such as cascade or end-wall motion effects. On the other hand, for numerical simulations, especially for LES, a validation in such a simple configuration is required in order to gain confidence in more complex situations.

It should be emphasized that this recent experiment (ANR-NSFC project AXIOOM) is actually an improvement of a previous experiment conducted about 10 years ago (European project PROBAND [59]). A device perturbing the incoming wall flow has been removed to obtain an incoming boundary layer thinner than the tip gap, in order to limit the interaction between the incoming boundary layer and the blade leading edge. The rig has been modified in order to increase the signal-to-noise ratio of the tip-leakage noise, and more advanced measurement technologies are employed. The angle of attack is adjusted in this recent experiment in order to recover the same blade loading as in the former experiment, where $AOA=15^\circ \pm 0.5^\circ$.

A detailed parametric study has been carried out by Grilliat [50] during the project PROBAND. In this thesis, the experimental results are used to investigate the mean and turbulent flow features of the tip-leakage flow at several cross-stream planes, and to validate the numerical results.

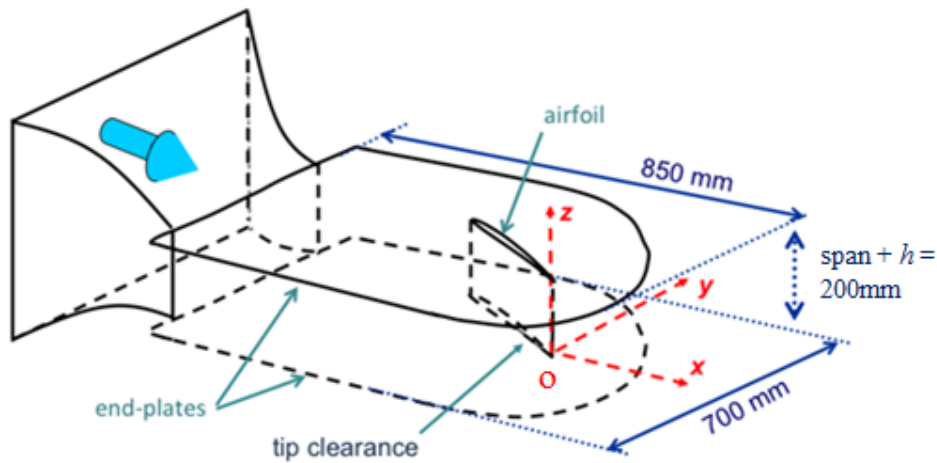


Fig. 3.2 Coordinate system.

3.2 Coordinate system

Fig.3.2 shows the coordinate system used in this thesis. The origin locates at the trailing edge / tip corner. The x -axis is aligned with the main flow direction and is oriented from upstream to downstream. The y -axis is the cross-stream direction and is oriented from the pressure side to the suction side. The z -axis is the spanwise direction and is oriented from the lower end-plate to the upper end-plate. In the following chapters, all the results will be shown in this coordinate system, unless indicated otherwise.

3.3 Measurement technologies and experimental database

The measurements have been carried out in 2012 by Y. Liu, E. Jondeau and M. Jacob in the large anechoic chamber of ECL, during the ANR-NSFC project AXIOOM. The data obtained have been processed and analysed in the frame of this PhD work.

3.3.1 Velocity measurements

In the experiment, the time-resolved Particle Image Velocimetry (TR PIV) and the Laser Doppler Velocimetry (LDV) technologies are employed to measure the velocity field.

For the PIV measurements, the flow is seeded with vaporized glycerine at the inlet of the wind tunnel blower, far upstream of the test section: thus the particles are homogeneously distributed in the flow, except at the TLV centre, where the centrifugal forces cause a particle defect.

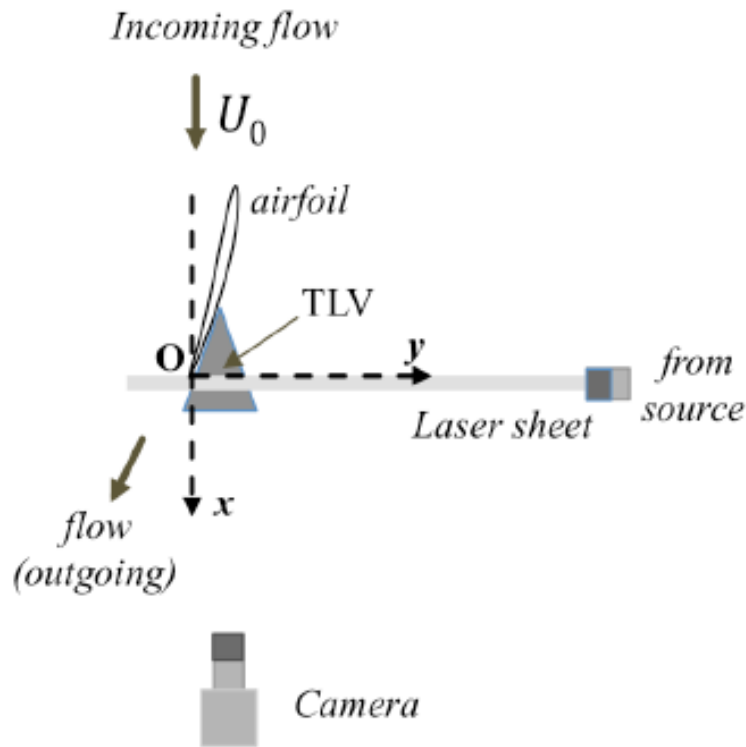


Fig. 3.3 Set-up for 2D-2C TR PIV measurements (view from top).

2D-2C TR PIV

Two-Dimensional Two-Component Time Resolved PIV measurements (2D-2C TR PIV) are carried out in the tip-leakage vortex region at various streamwise positions. The horizontal velocity component V and the vertical velocity component W in the cross-stream plane are measured.

As shown in Fig. 3.3, the laser sheet is parallel to the cross-stream plane ($y-z$ plane). The source is a Quantronix Dual Cavity Laser. It is placed on the suction side pointing towards the airfoil. In order to minimize light reflections, the airfoil is painted in black. The seeding material is vaporised paraffin injected into to wind-tunnel fan inlet, thus ensuring a homogeneous mixing throughout the flow. A Phantom V12 high speed camera is employed to receive the signals downstream of the airfoil, making the views oriented from downstream to upstream. The camera is equipped with a 100mm lens, which has to be cleaned every 5 s, that is, every 14000 to 37000 snapshots, because of the paraffin condensation. The velocity is computed on 12×12 px spots by an iterative algorithm with 50% overlap.

The measurement planes include three small planes with the same dimensions, located respectively at 80% c (Axioom-6, $x=-40$ mm), 90% c (Axioom-5, $x=-20$ mm) and 101% c (Axioom-3, $x=2$ mm), and a much larger plane at $x=2$ mm (Axioom-2). Fig. 3.4 shows the

relative positions and dimensions of these measurement planes in a $x - y$ view (Fig.3.4 (a)) and a $y - z$ view (Fig.3.4 (b)). Details of the 2D-2C TR PIV database are summarized in Tab.3.1.

Table 3.1 Details of the 2D-2C TR PIV database.

database	Axioom-2	Axioom-3	Axioom-5	Axioom-6
axial position (mm)	2	2	-20	-40
sampling frequency (HZ)	3000	7000	7000	7000
resolution (pixel)	1280 × 800	608 × 600	608 × 600	608 × 600
physical resolution (mm)	0.57	0.57	0.57	0.57
measurement points ($y \times z$)	160 × 100	76 × 75	76 × 75	76 × 75
database size (series × files)	5 × 2780	5 × 7300	5 × 7300	5 × 7300

2D-3C TR PIV

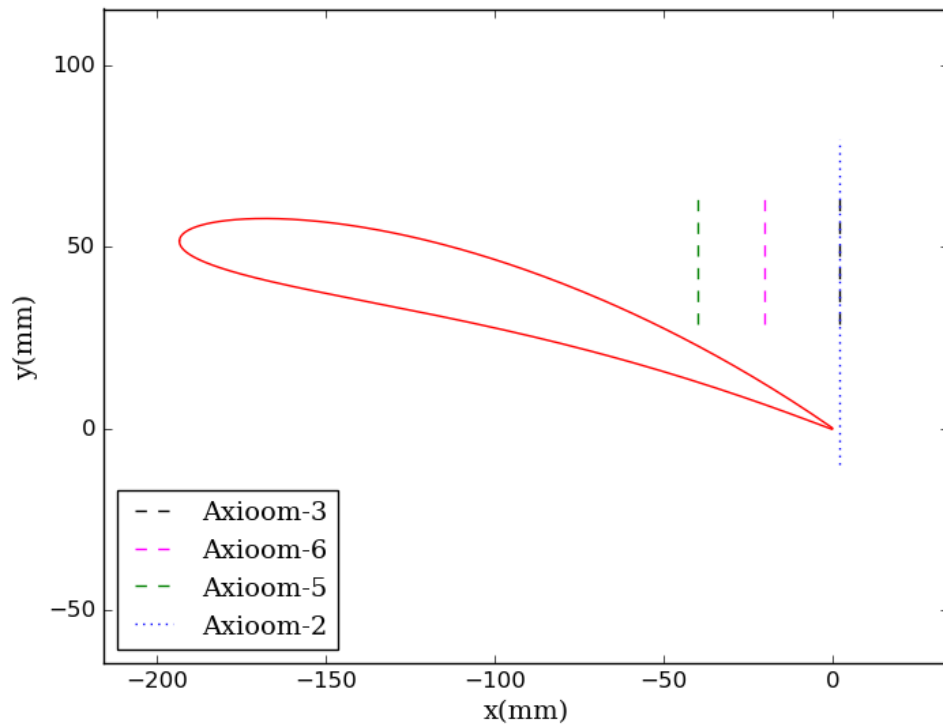
Two-Dimensional Three-Component Time Resolved PIV measurements (2D-3C TR PIV) are carried out in the tip-leakage vortex region at the axial position $x=2\text{mm}$.

Similar to the 2D-2C TR PIV, the Quantronix Dual Cavity Laser source is placed beneath the casing plate equipped with a glass window, in order to minimise light reflections on the airfoil. Two Phantom V12 high speed cameras equipped with 135mm lenses are employed to measure the three velocity components, including the component u normal to the cross-stream plane. As shown in Fig.3.5, the two cameras are placed on the suction side, downstream and upstream of the airfoil, pointing towards the TLV region, with a 45° angle on each side of the measurement plane. Each camera is equipped with a Scheimpflug support to compensate for angular distortion. The original views are oriented from upstream to downstream, but it is modified to be the same as 2D- 2C TR PIV through a coordinate system transformation during the post-processing. The flow is seeded in the same way as 2D-2C TR PIV. The velocity is computed on 12×12 px spots by an iterative algorithm with 50% overlap.

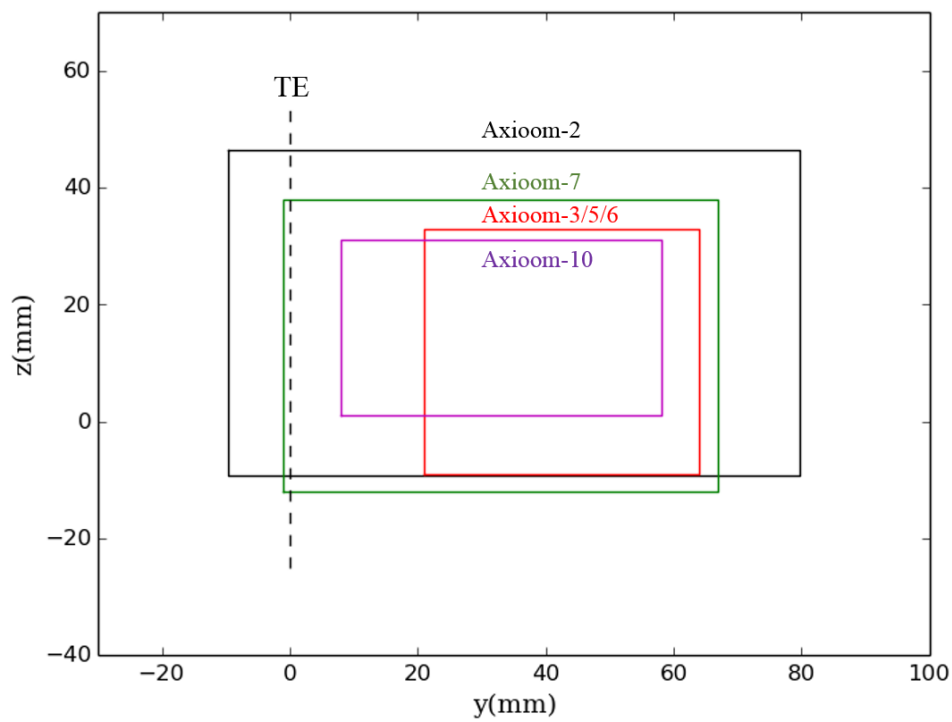
Two measurement planes of different sizes are employed (Axioom-7 & Axioom-10). Fig.3.4(b) indicates the relative positions and dimensions of these measurement planes in a $y - z$ view. Details of the 2D-3C TR PIV database are summarized in Tab.3.2.

LDV

LDV measurements are also carried out in the same region as the PIV measurements. The mean values and the fluctuations of the axial velocity component u and the vertical



(a)



(b)

Fig. 3.4 Positions and dimensions of the PIV measurement planes (a) $x-y$ view (b) $y-z$ view.

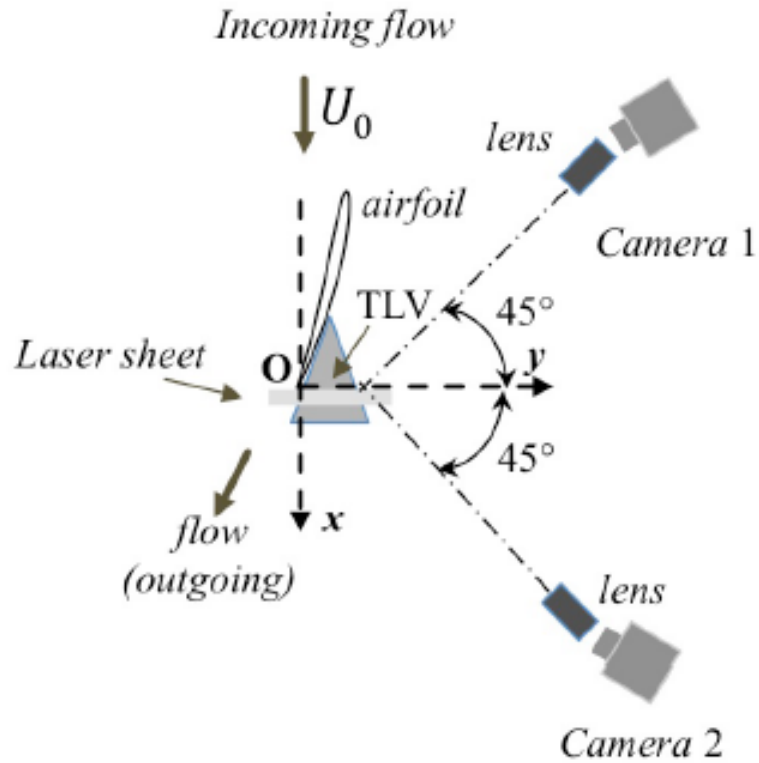


Fig. 3.5 Set-up for the 2D-3C TR PIV measurements (view from top).

Table 3.2 Details of the 2D-3C TR PIV database.

database	Axiom-7	Axiom-10
axial position (mm)	2	2
sampling frequency (HZ)	3000	7000
resolution (pixel)	800×800	608×600
physical resolution (mm)	1.28	1.28
measurement points ($y \times z$)	55×40	41×29
database size (series \times files)	5×3900	5×7200

velocity component w are measured at various streamwise and spanwise positions in the tip-leakage vortex region. They provide a useful comparison for the PIV measurements as well as spectral information.

A Dantec backscatter Laser Doppler Velocimetry (LDV) system is employed. The velocity measurements are conducted with two pairs of beams, supplied by the green line of wavelength 514nm and the blue line of wavelength 488nm from two coherent DPSS (Diode Pumped Solid State) 1 W Laser sources. The beams of each pair undergo a relative frequency shift of 40 MHz in a Bragg cell. The four beams are guided to the flow with an optical fibre, which is terminated by a focusing lens with a focal length of 400 mm for the gap region. The beams of each pair have a mutual angle of 5.6° . In the gap region the size of the measurement area is about $119 \mu\text{m}^2$ in the measurement plane, whereas its length in the cross-stream direction is about 2.4 mm. The Fringe spacing is $5.286 \mu\text{m}$ for the green line and $4.992 \mu\text{m}$ for the blue line. The backscattered beams are focused by the same lens and sent through an optical fibre onto photomultipliers. The signals are then treated by two Dantec real-time signal analysers and post-processed on a personal computer. The flow is seeded in the same way as the PIV measurements.

3.3.2 Pressure measurements

Numerous unsteady pressure probes are used to measure the pressure fluctuations on the blade surface. The measurement method is described in details in the article of Perennes and Roger [90], and the calibration in the thesis of Arguillat [4]. In the current configuration, the measurements mainly focus on the blade tip region ($z=1.5\text{mm}$), the trailing edge ($x=-5\text{mm}$) and mid-span ($z=100\text{mm}$) on both the suction and pressure surfaces. They provide a useful database for the validation of the numerical simulations and the noise modelling. Some probe locations will be introduced in Chapter 5 and Chapter 6. More details of the pressure measurements in the current configuration can be referred to the article of Jacob *et al.* [59].

3.4 Numerical methods

The same tip-leakage configuration is simulated by two numerical methods: zonal large-eddy simulation (ZLES) and (unsteady) Reynolds-Averaged Navier-Stokes approach (RANS/URANS). The flow solver employed for the simulations is the in-house solver *Turb'Flow* [16] developed in LMFA at Ecole Centrale Lyon. Since the simulations have been initiated simultaneously with the second experimental campaign, the original angle of attack (15°) is used. The influence of the AOA difference between the experiment and the

numerical simulations is in fact quite small, which is demonstrated by the good agreement of the obtained blade loadings, as shown in section 4.3.1. This small influence can also be explained by the effective AOA. During the project PROBAND, to obtain the same blade loading, the equivalent AOA in the uniform flow was found to be about 7° , as shown in Fig.3.6. From this point of view, the 1.5° AOA difference in the current configuration is equivalent to about 0.7° effective AOA difference, which is very small.

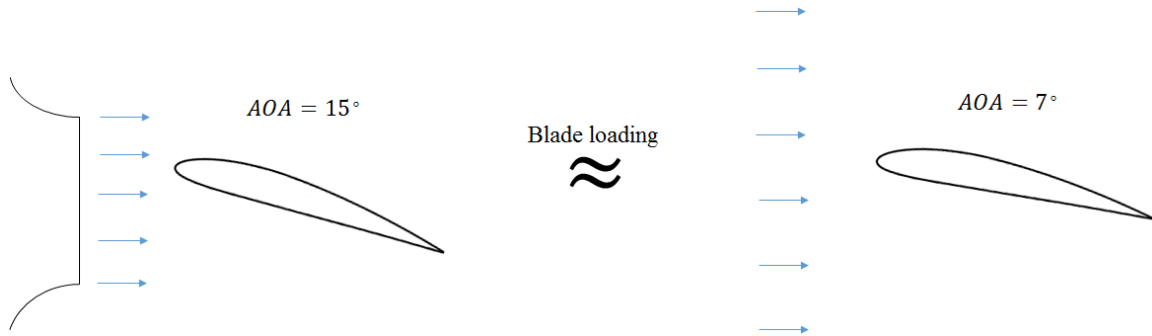


Fig. 3.6 Effective AOA.

3.4.1 ZLES

The ZLES simulation has been set-up and run by J. Caro and J. Boudet, but the post-processing has been carried out in the frame of this PhD.

In this thesis, the ZLES results are used to investigate the mean and turbulent flow features of the tip-leakage flow, and to implement the acoustic models. The ZLES simulation is also a good complement to the unsteady PIV, such as the high-frequency spectral contents.

Zonal strategy

In order to reduce the computational cost, a zonal strategy is employed in this simulation. The flow field is described partly by LES, partly by RANS:

LES is employed to describe the flow in the blade-tip region, including the tip-leakage jet, the boundary layers on both the blade and the end-wall, and the wake, where the flow is strongly unsteady. As shown in Fig.3.7, the extent of the LES region at the blade-tip is defined so that it covers almost all the main jet width (in the cross-stream direction). Spanwise, the LES region extends over $5h$ above the end-plate. Besides, the incoming boundary layer is also simulated by LES in a slice with a narrow cross-stream extent. Using cross-stream periodicity, this narrow boundary layer is duplicated in the cross-stream direction to feed the tip flow at $x - x_{LE} = -0.5c$.

RANS is applied in the peripheral regions where the flow is steady and weakly turbulent, and at the lateral and downstream boundaries where the grid is stretched in order to damp outgoing waves and minimize reflections.

Between the LES and RANS zones, there is a transition zone to ensure a smooth coupling of LES and RANS. The position of this transition zone is indicated by the grey lines in Fig.3.7. In this zone, the eddy viscosity ν_{mod} used in the simulation is evaluated by a linear combination of LES' subgrid-scale eddy viscosity ν_{sgs} and RANS' turbulent viscosity ν_t :

$$\nu_{mod} = (1 - \beta)\nu_{sgs} + \beta\nu_t, 0 \leq \beta \leq 1 \quad (3.1)$$

The zonal parameter β is prescribed to evolve smoothly (polynomial) between 0 (LES region) and 1 (RANS region), over a distance of $0.1c$.

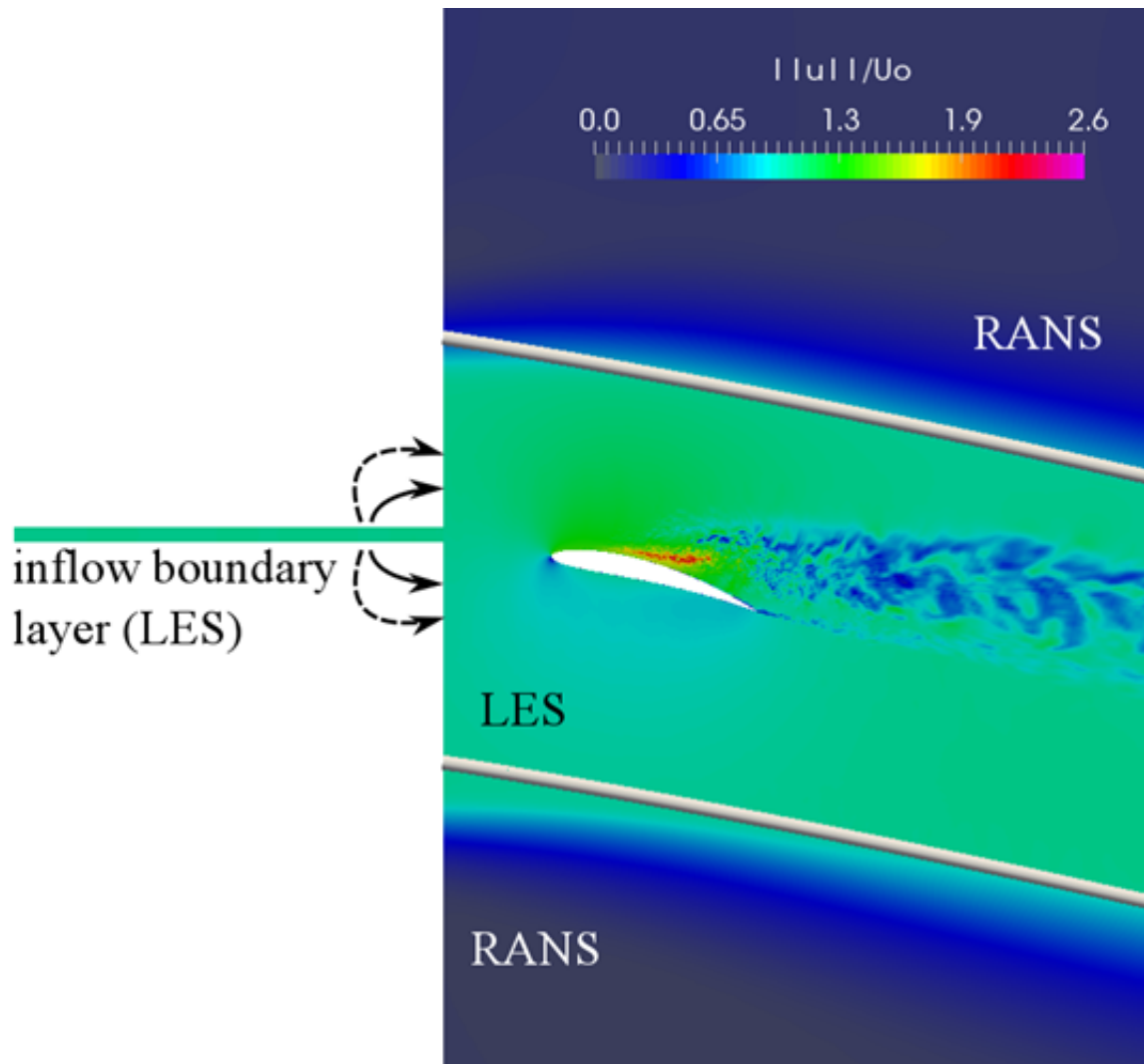


Fig. 3.7 LES and RANS zones in the blade tip region ($x - y$ view at $z = 0.5h$).

SGS model (LES)

In the LES zone, the shear-improved Smagorinsky (SISM) model [75] is employed to evaluate the subgrid-scale eddy viscosity. In order to account for the shear effects in wall-bounded turbulence [103], the original Smagorinsky model is modified by subtracting the magnitude of the mean shear $|\langle \bar{S} \rangle|$ from the magnitude of the instantaneous resolved strain-rate tensor $|\bar{S}|$:

$$\nu_{sgs} = (C_s \Delta)^2 (|\bar{S}| - |\langle \bar{S} \rangle|), \quad (3.2)$$

where $|\bar{S}| = (2\bar{S}_{ij}\bar{S}_{ij})^{1/2}$. $C_s = 0.18$ is the standard Smagorinsky constant and Δ denotes the grid spacing. The brackets $\langle \rangle$ would a priori denote an ensemble average. In practice, an exponential smoothing in time [21] is used in the present simulation, with cut-off frequency: $1.8U_0/c$.

This model, in addition of being physically sound, has a low computational cost and already yielded good results in complex non-homogeneous turbulent flows, as shown by Cahuzac [22] and Gao [45, 46].

Turbulence model (RANS)

In the RANS zone, the $k - \omega$ model of Wilcox [105, 106] is employed to evaluate the turbulent viscosity, as

$$\nu_t = c_\mu \frac{k}{\omega}, \quad (3.3)$$

where k and ω are modelled by solving the two turbulent transport equations:

$$\frac{\partial \langle \rho \rangle k}{\partial t} + \frac{\partial \langle \rho \rangle k u_j}{\partial x_j} = P_k - c_k \langle \rho \rangle \omega k + \frac{\partial}{\partial x_j} \left((\langle \mu \rangle + \frac{\mu_t}{\sigma_k}) \frac{\partial k}{\partial x_j} \right), \quad (3.4)$$

$$\frac{\partial \langle \rho \rangle \omega}{\partial t} + \frac{\partial \langle \rho \rangle \omega u_j}{\partial x_j} = c_{\omega 1} \frac{\omega}{k} P_k - c_{\omega 2} \langle \rho \rangle \omega^2 + \frac{\partial}{\partial x_j} \left((\langle \mu \rangle + \frac{\mu_t}{\sigma_\omega}) \frac{\partial \omega}{\partial x_j} \right), \quad (3.5)$$

and $c_\mu = 1.0$, $\sigma_k = 2.0$, $\sigma_\omega = 2.0$, $c_k = 0.09$, $c_{\omega 1} = \frac{5}{9}$ and $c_{\omega 2} = \frac{3}{40}$.

Mesh

Fig.3.8 gives a global view of the ZLES computational domain. The inlet plane is positioned $0.5c$ upstream of the leading edge, where the flow parameters of the incoming boundary layer are measured in the experiment. The LES slice of the incoming boundary layer is upstream. Including the incoming boundary layer, the whole computational domain

extends over $29c$ in the streamwise direction and $37c$ in the cross-stream direction. These large dimensions are chosen to limit the influence of the external boundaries on the tip-leakage flow. The spanwise extent is $1c$.

The grid has 150 million points, evenly distributed into 524 blocks for the parallel computation. In the LES zone, the cell dimensions on both the blade and the end-wall follow the standard practice of wall-resolved LES: $\Delta x^+ < 80$, $\Delta y^+ < 1.5$ and $\Delta z^+ < 30$. The grid expansion ratio is less than 1.2 in the wall normal direction. Views of the grid near the leading edge and the trailing edge are shown in Fig.3.9.

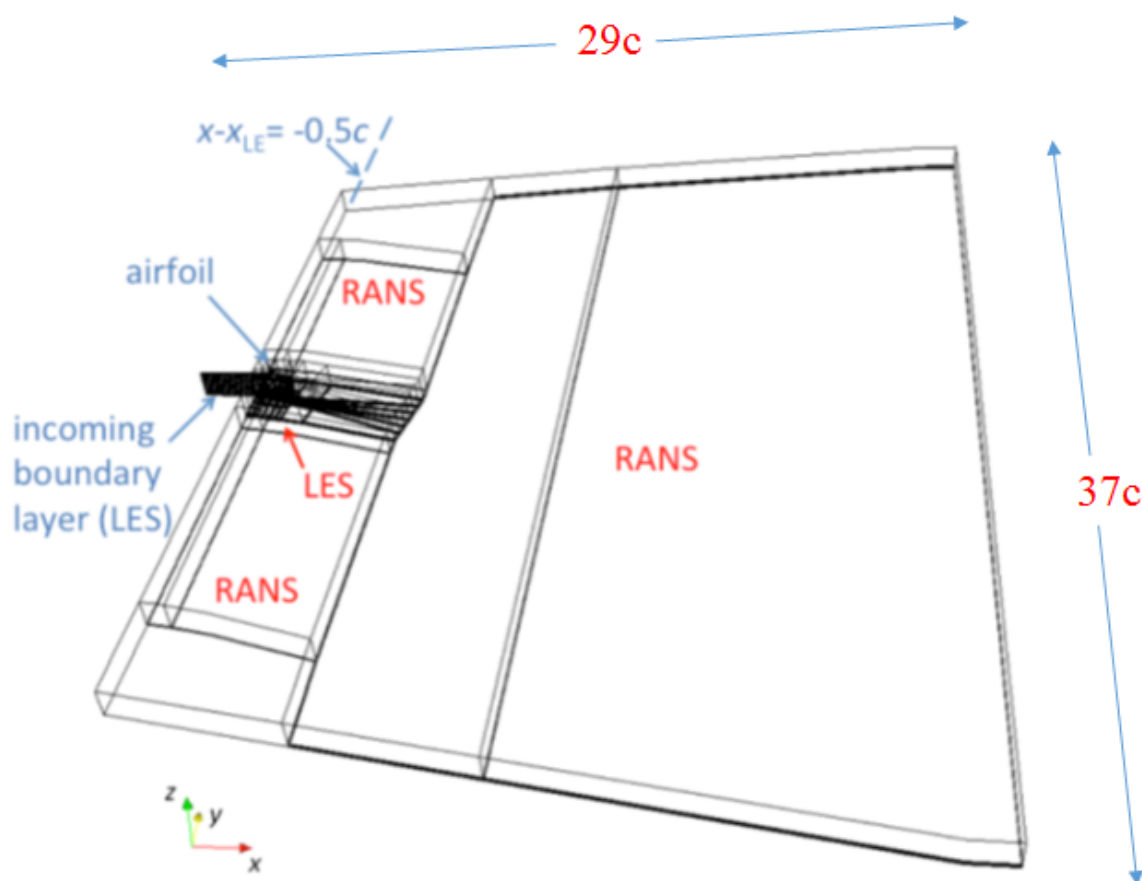
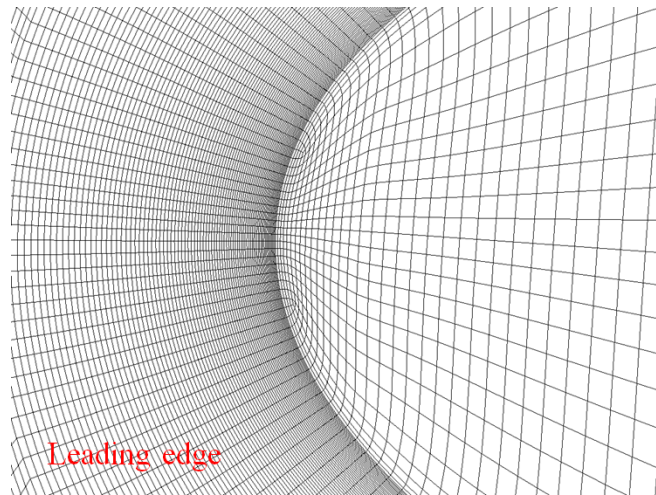
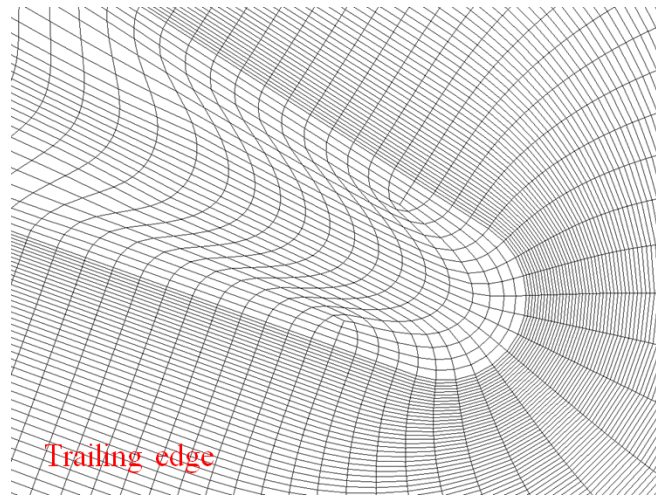


Fig. 3.8 Global view of the ZLES computational domain.



(a)



(b)

Fig. 3.9 Detailed views of the ZLES mesh at (a) leading edge (b) trailing edge, with every two points plotted

Boundary conditions

At the inlet boundary ($x - x_{LE} = 0.5c$), the LES of the incoming boundary layer provides the unsteady subsonic inflow conditions, whose statistics meet the experimental data, over a lateral extent of 450mm. This region corresponds to the jet flow in the experiment. The similar method is used by Lewin [76] and Gao [45]. Outside this region, a very small velocity ($\sim 1\text{m/s}$) is imposed with a very small inflow angle ($\sim 1^\circ$) inclining to the blade side.

The lateral boundaries are also treated as subsonic inlet. A very small velocity ($\sim 1\text{m/s}$) is again imposed with a very small inflow angle ($\sim 1^\circ$) inclining to the blade side.

At the outlet boundary, a mixed pressure outlet condition is employed. It combines the pressure outlet condition and the non-reflection outlet condition. Moreover, the grid is coarsened and the artificial viscosity is increased in a buffer layer upstream of the boundary.

Both the blade surface and the lower end-wall are treated as non-slip adiabatic walls. At the upper end-wall, a symmetry condition is employed.

The ZLES flow field is initialized by interpolating a pre-calculated RANS result to the ZLES mesh.

Numerical schemes

The inviscid fluxes are interpolated by the Jameson four-point centered spatial scheme [61]. A fourth-order artificial viscosity is employed to stabilize the computation. Its coefficient (cf. Boudet *et al.* [18]) is set to 0.003 on the plate below the airfoil, and increases up to 0.03 near the LES/RANS border and 0.3 in the RANS zone.

The viscous fluxes are interpolated by a second order centered scheme.

A three-step Runge-Kutta scheme with a global constant time step of $5.6 \cdot 10^{-6} c/U_0$ is employed for the temporal discretization. The maximum CFL number over the domain is close to 1.

3.4.2 RANS/URANS

In this thesis, the RANS results are used to investigate the mean flow features of the tip-leakage flow, and to implement the acoustic models. The URANS computations are also used to investigate the dynamic response of the tip-leakage flow to a harmonic inflow fluctuation.

Turbulence model

In RANS/URANS, the $k - \omega$ model of Wilcox is employed to evaluate the turbulent viscosity. More details about this model can be found in 3.4.1.

Mesh

Fig.3.10 gives a global view of the RANS/URANS computational domain. Although this computational domain is smaller than that of ZLES, the stretching mesh extends over $10c$ downstream of the airfoil and in the lateral directions. The inlet plane is positioned $1.8c$ upstream of the leading edge. The whole computational domain extends over $12c$ in the streamwise direction, $20c$ in the cross-stream direction and $1c$ in the spanwise direction.

The grid for RANS has 5.4 million points, evenly distributed into 62 blocks for the parallel computation. The height of the first cell on the blade surface and the lower end-wall is set to $\Delta y = 1 \cdot 10^{-5} \text{m}$, yielding $\Delta y^+ \approx 3$. The grid expansion ratio is less than 1.2 in the wall normal direction. In the TLV region, about 50 points in the horizontal direction (y) and 40 points in the vertical direction (z) are used to resolve the tip-leakage vortex at the trailing edge.

The grid for URANS is a coarsened version of the RANS grid (every second point in each direction), in order to reduce the computational cost. It has about 1 million points. The effect of the coarsening will be studied in Chapter 5.

Closer up views of the grid near the leading edge and the trailing edge are shown in Fig.3.11.

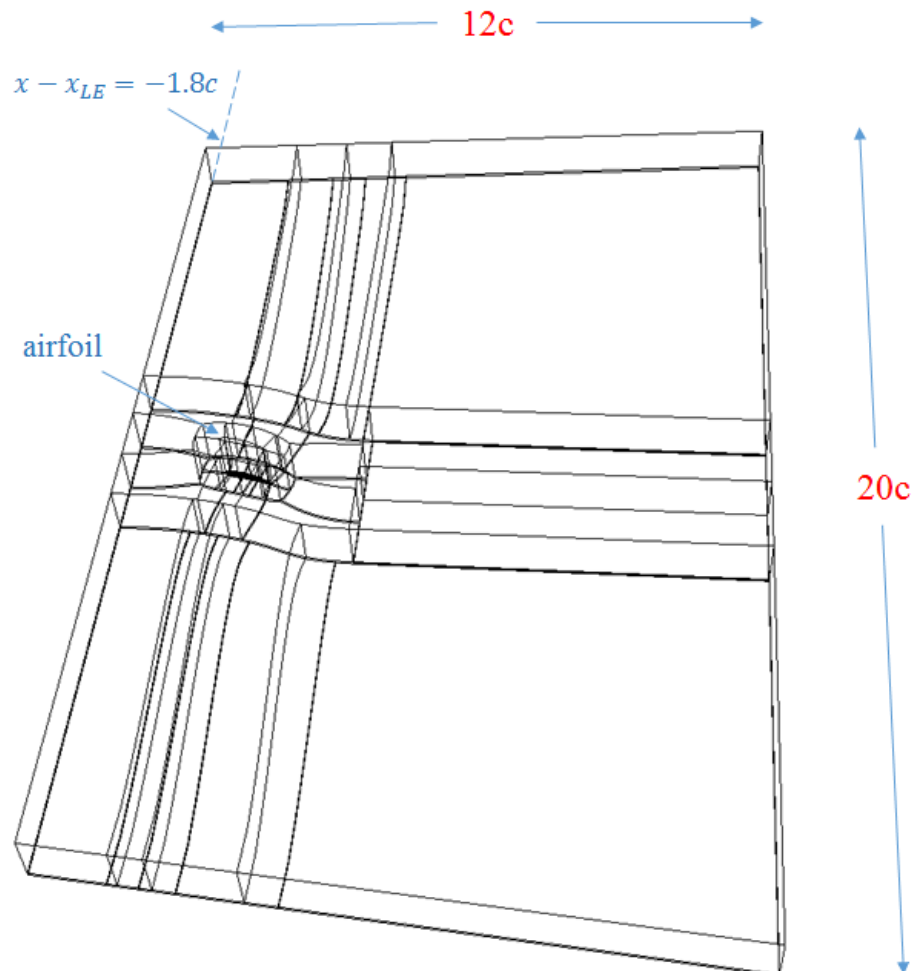


Fig. 3.10 Global view of the RANS/URANS computational domain.

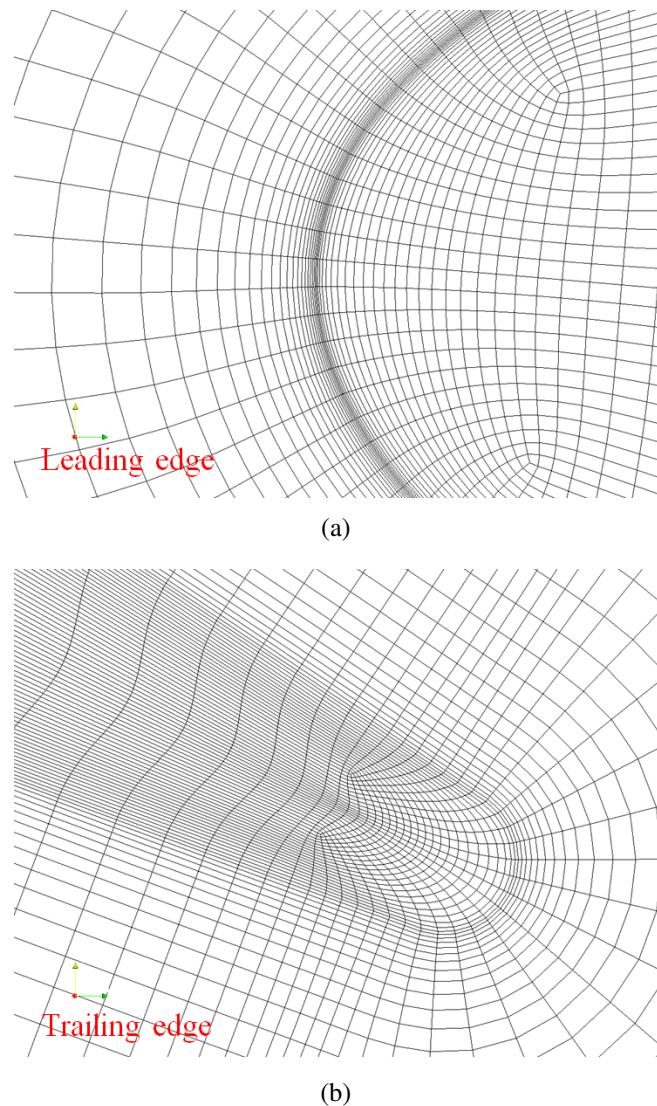


Fig. 3.11 Detailed views of the RANS/URANS mesh at (a) leading edge (b) trailing edge.

Boundary conditions

The boundary conditions for RANS/URANS are the same as for ZLES, as described in section 3.4.1, except at the inlet boundary.

The RANS inlet is positioned at the jet nozzle exit ($x - x_{LE} = -1.8c$). Consequently, the end-plate boundary layer is neglected. A steady uniform velocity U_0 is imposed at the inlet boundary within the region corresponding to the jet flow. Outside this region, a very small velocity ($\sim 1\text{m/s}$) is imposed with a very small inflow angle ($\sim 1^\circ$) inclining to the blade side. The turbulence intensity at the inlet boundary is set to 0.5% in accordance with the

experiment. The turbulence kinetic energy k is initialized by assuming isotropy and ω is initialized to ensure $v_t/v = 10$, which is a standard value in the external aerodynamics.

For URANS, an additional inflow angle fluctuation is imposed at the inlet plane. The objective is to test the dynamic response of the flow to a set of frequencies. In the current study, the fluctuation is only imposed in the horizontal (pitchwise) direction, because a larger wandering motion in the pitchwise direction than the spanwise direction is reported in nearly all the researches related to the vortex wandering. This seems to indicate that the vortex wandering is more sensitive to the flow fluctuations in the pitchwise direction. In this direction, the flow is more affected and controlled by the AOA. The amplitude of the fluctuation is calibrated on the measured turbulent intensity T_u , with $\Delta i = \arctan(2 \cdot T_u)$. The frequency of the fluctuation is chosen within the frequency range [0.7kHz, 7kHz] reported by Jacob *et al.* [60], over which the tip-leakage flow contributes essentially to the far-field noise. Finally, three frequencies, 1000Hz, 3000Hz and 5000Hz are chosen.

Numerical scheme

The inviscid fluxes are interpolated by the Jameson two-point centered spatial scheme. A second-order artificial viscosity is used with coefficient 0.02.

The viscous fluxes are interpolated by a second order centered scheme.

A three-step Runge-Kutta scheme with a global constant time step of $1.2 \cdot 10^{-6} c/U_0$ is employed for the temporal discretization. The maximum CFL number over the domain is close to 0.3.

Chapter 4

Mean aerodynamics of the tip-leakage flow

In this chapter, we will discuss the mean flow features. The inflow conditions (i.e. the incoming boundary layer) will be firstly presented for the experiment and the numerical simulations. Then, the post-processing strategy will be stated, taking into account the small AOA difference between the experiment and the simulations. Finally, the time-averaged zonal LES (ZLES) results as well as the RANS results will be analyzed by comparisons of various flow features with the experiment.

4.1 Inflow conditions

In the experiment, the mean velocity profiles and the turbulent fluctuations inside the incoming boundary layer on the lower end-plate are measured with hot-wire anemometry (HWA) at three axial locations upstream of the leading edge: $x - x_{LE} = -1.5c$, $-1.0c$, and $-0.5c$. In the ZLES, the incoming boundary layer is simulated simultaneously, but isolated from the corresponding main flow region. At each iteration, the flow variables are extracted and fed into the main flow, at the location where the simulated boundary layer coincides with the experimental data. In the RANS simulations, the incoming boundary layer is assumed to start to develop at $1.8c$ upstream of the leading edge. This assumption is reasonable, because in the experiment this position corresponds to the jet nozzle outlet and the upstream contraction of the flow should make the boundary layer thickness at this position nearly zero.

4.1.1 Mean velocity profile

Fig.4.1 shows the mean velocity profiles inside the incoming boundary layer for the experiment, ZLES and RANS at $1.5c$, $1.0c$ and $0.5c$ upstream of the leading edge. $\Delta z = z + h$ denotes the height measured from the lower end-plate. The growth of the boundary layer is clearly visible. In the experiment, the measured thickness increases from about $0.5h$ at $x - x_{LE} = -1.5c$ to about $0.8h$ at $x - x_{LE} = -0.5c$. So we can infer that when it reaches the blade leading edge, the boundary layer thickness is almost the same as the clearance height. It will certainly influence the tip-leakage flow. For the RANS computation, a close agreement with the experiment is observed at $x - x_{LE} = -1.5c$, but the thickening of the boundary layer is over-estimated downstream. As a result, the tip gap is fully embedded in the boundary layer and the leading edge corner lies in a highly turbulent region (see next subsection). One possible effect is that the low-speed fluid inside the boundary layer will reduce the intensity of the tip-leakage flow and thus reduce the tip-leakage flow self-noise. Another effect might be that the impingement of the highly turbulent flow onto the airfoil leading edge corner will significantly increase the boundary layer-airfoil interaction noise. For the ZLES, the velocity profiles are properly simulated. The boundary layer thickness is only slightly over-estimated compared to the experiment.

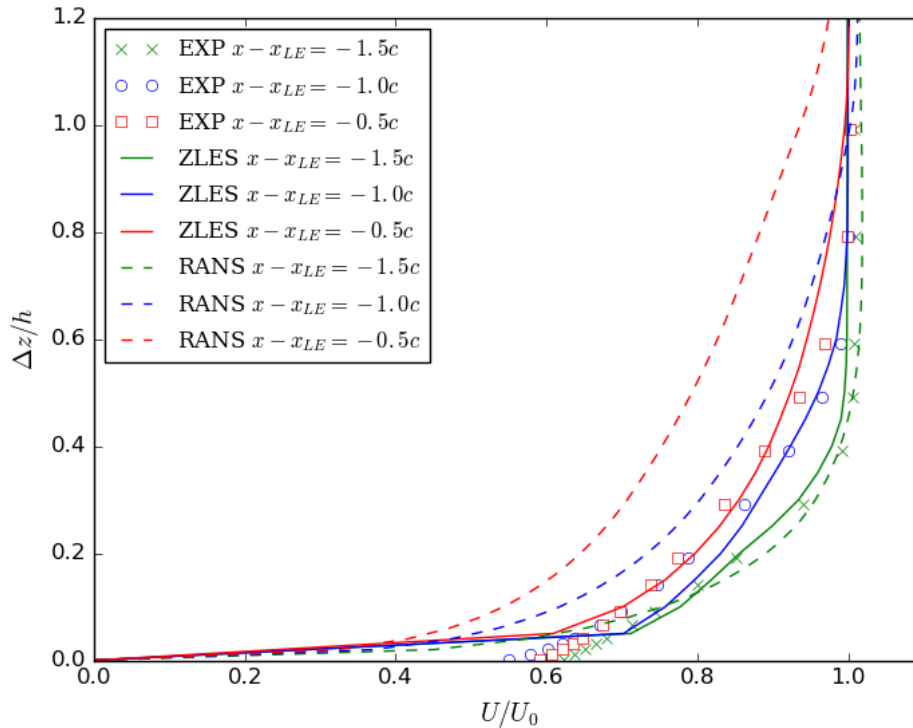


Fig. 4.1 Mean velocity profiles inside the incoming boundary layer at $1.5c$, $1.0c$ and $0.5c$ upstream of the leading edge.

4.1.2 Turbulent fluctuations

Fig.4.2 shows the turbulent fluctuations inside the incoming boundary layer for the experiment, ZLES and RANS at $1.5c$, $1.0c$ and $0.5c$ upstream of the leading edge. In the experiment, the peak of the turbulent intensity is smooth and locates under $0.2h$. The levels of the turbulent intensity inside the boundary layer globally increase along the downstream direction and its peak reaches 8% at $0.5c$ upstream of the leading edge. For the RANS simulation, the turbulent fluctuations are calculated from the turbulent kinetic energy with the assumption of isotropy. The peak is found to be over-estimated by RANS in the first section, but the shape is fairly well reproduced. However, the decrease away from the wall is too slow in the most downstream section ($x - x_{LE} = -0.5c$), resulting in a more than 100% over-estimate near the airfoil leading edge corner ($\Delta z/h = 1$, $x - x_{LE} = -0.5c$). This over-estimate of the diffusion is closely related with the over-estimate of the boundary layer thickening.

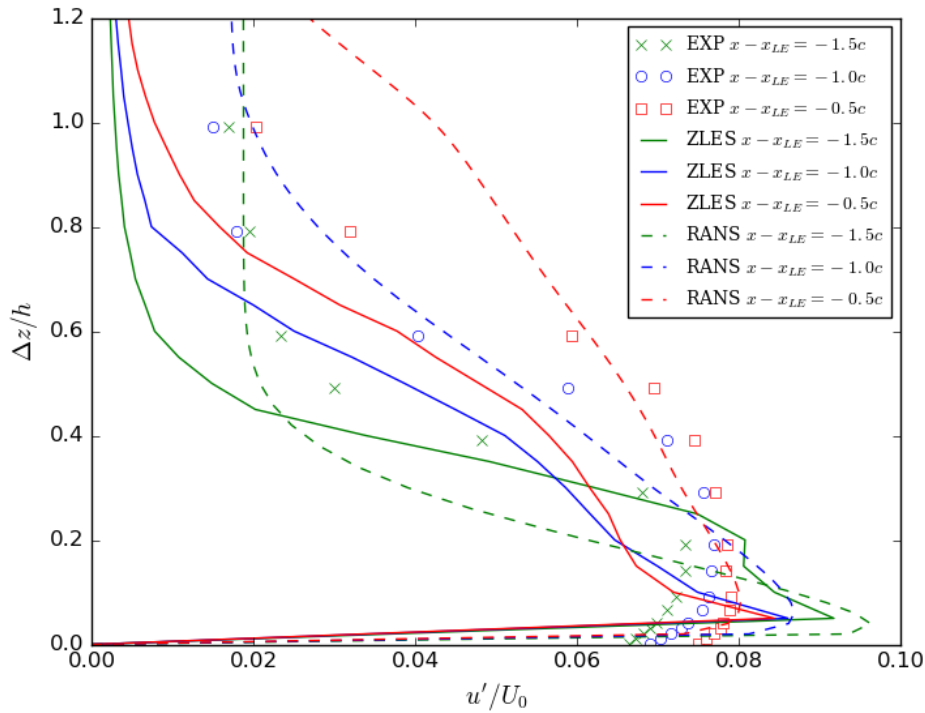


Fig. 4.2 Turbulent fluctuations inside the incoming boundary layer at $1.5c$, $1.0c$ and $0.5c$ upstream of the leading edge.

The ZLES globally under-estimates the turbulent fluctuations and their diffusion, especially close to the leading edge. In the vicinity of the end-plate, the ZLES results present the classical peak of fluctuations, as reported by DeGraaf and Eaton [32], while the evolution

of the fluctuations in the experiment is smooth. This uneven evolution in the ZLES results may be due to the shorter axial development. In other words, the longer development of the boundary layer in the experiment, upstream of the nozzle, may explain the smoothing of the fluctuation peak. On the other hand, in the experiment, the length of the hot wire may not be sufficient to fully describe the turbulent structures in the vicinity of the end-plate.

4.2 Post-processing strategy

As presented in the previous chapter, the configuration chosen in the numerical simulations slightly differs from the experimental one. The angle of attack is 15° in ZLES and RANS, while it is set to $16.5^\circ \pm 0.5^\circ$ in the experiment. This difference was introduced because the ZLES and the second experimental campaign started simultaneously. The simulations have been configured with the AOA of the first experimental campaign, while the second experimental campaign has been tuned afterwards to recover the same blade loading, and it appeared it required a slightly different AOA. In other words, the flow conditions have been tuned on the pressure distribution, which will be presented thereafter, instead of the AOA. In order to minimize the effect of this AOA difference during the comparison of the results, different coordinate systems are introduced for the post-processing.

The two coordinate systems, along with the experimental/numerical set-ups, are shown in Fig.4.3. The experiment is represented in blue, and the numerical simulation in red. The small difference in the angle of attack is clearly visible on this sketch. The coordinate system (x, y, z) is used in the experiment for both LDV and PIV measurements. Its origin is located at the trailing edge/tip corner. The $x - y$ plane is horizontal (parallel with the end-plate). The x -axis is aligned with the inflow direction and the y -axis is oriented from pressure side to suction side. The vertical axis z is oriented from the lower plate to the upper plate. In this way, $z < 0$ represents the region of clearance and $z > 0$ represents the region of the blade. In the experiment, the LDV and PIV measurements are carried out in several cross-stream planes. These planes are all normal to the inflow direction (x -axis) and parallel with each other. The coordinate system (x', y', z') is obtained by rotating the coordinate system (x, y, z) along the z -axis in the anti-clockwise direction with an angle ψ . The two coordinate systems share the same origin and vertical axis. ψ is equal to 1.5° , which is the difference of the angle of attack between the experiment and the simulations. All the measurement planes in the experiment follow the same rotation and the obtained planes are used as extraction planes in the numerical simulations, so that the relative positions between the airfoil and

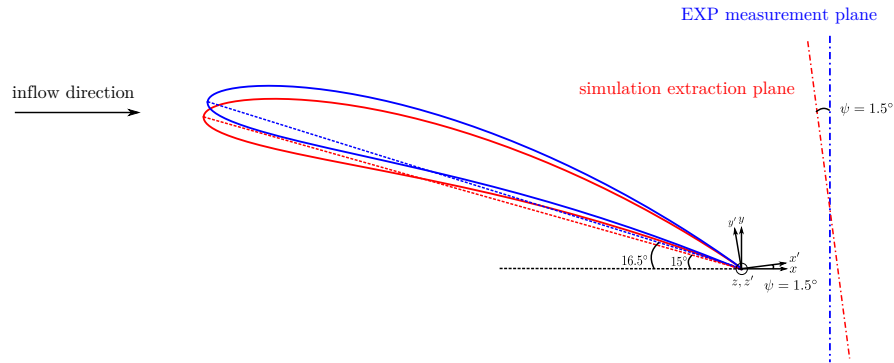


Fig. 4.3 Two coordinate systems

these planes remain unchanged. The velocity components U', V', W' in the system (x', y', z') are obtained by the following formula:

$$\begin{aligned}
 U' &= U \cdot \cos\psi + V \cdot \sin\psi \\
 V' &= V \cdot \cos\psi - U \cdot \sin\psi \\
 W' &= W
 \end{aligned}
 \tag{4.1}$$

For the ZLES and RANS simulations, the post-processing is performed in the coordinate system (x', y', z') with the corresponding velocity components U', V', W' . Fig.4.4 shows a comparison of the velocity components, U (no correction) and U' (corrected), along a line at $x = 2$ mm and $z = 10$ mm. It is obvious that the numerical results with correction are better aligned with the experimental data, thanks to the proper orientation with respect to the airfoil. This correction process has little effect on the magnitude of the various quantities, since the angle of rotation ψ is quite small. But it does affect the value distribution, especially along the y -axis. In the following analyses, all the numerical results are obtained in the system (x', y', z') , unless otherwise specified.

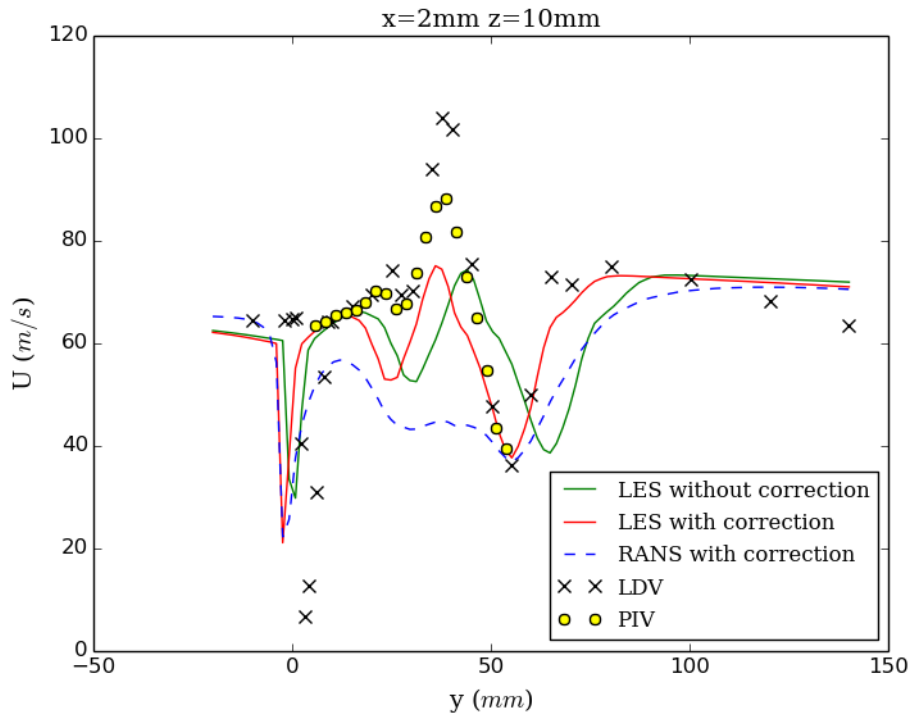


Fig. 4.4 Comparison between the corrected results (rotated plane) and uncorrected results from the simulations, with respect to experimental data.

4.3 Mean aerodynamics of the tip-leakage flow

4.3.1 Blade surface static pressure coefficient

The pressure distribution on the blade surface indicates the blade loading and is a very important indicator of the performance of simulations. The mean pressure coefficient at mid-span ($z = 90\text{mm}$) and close to the blade tip ($z = 1\text{mm}$) is shown in Fig.4.5. At mid-span, RANS and ZLES give almost the same prediction: compared with the experimental results, the pressure distribution on the pressure surface is perfectly predicted, while it is underestimated on the suction surface, resulting in a slightly larger blade loading at mid-span. In the blade-tip region, the blade loading is globally reduced, because the tip-leakage flow partly balances the pressure difference between the pressure side and the suction side. Both in the experiment and in the LES, a low-pressure hump can be observed on the suction side from $x/c = 0.2$ to 0.6 . This region may be associated with the tip-leakage flow. As reported by Jacob *et al.* [59], in this region the tip leakage flow leaves the gap in a jet-like manner, before rolling-up into the TLV. This structure is less visible in RANS, whose pressure distribution on the suction side is smoother. Overall, a fairly good agreement is achieved between the experiment and the simulations.

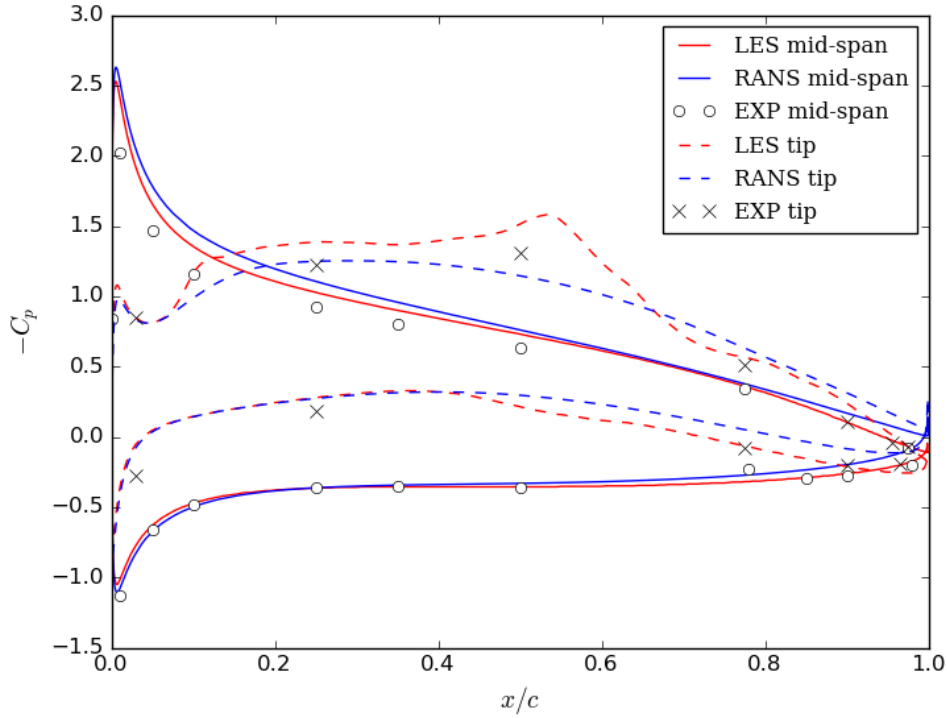


Fig. 4.5 Mean pressure coefficient C_p at mid-span and close to the blade-tip.

4.3.2 Tip-leakage vortex

Vortex detection algorithm

Various vortex-detection algorithms have been proposed, such as the widely-used Q and λ_2 criteria. However, the Q and λ_2 criteria are sometimes too sensitive to the small-scale turbulence (intermittency) and can have difficulties to identify the large-scale vortices with satisfactory accuracy, especially in instantaneous flow fields. In this study, we use the vortex identification functions Γ_1 and Γ_2 introduced by Graftieaux *et al.* [49] to estimate the tip-leakage vortex center and size, respectively. Contrary to the Q and λ_2 criteria, functions Γ_1 and Γ_2 are non-local functions, which “filter out” the small-scale turbulence to some extent. These functions are defined on a 2D space, and applied to cross-stream planes in the present study.

The vortex center identification function Γ_1 at a fixed point P is defined as:

$$\Gamma_1(P) = \frac{1}{S} \int_{M \in S} \frac{(PM \wedge U_M) \cdot \mathbf{n}_S}{\|PM\| \cdot \|U_M\|} \cdot dS \quad (4.2)$$

where S is a two-dimensional area surrounding the point P . It corresponds to the filter size and should be chosen to be centrosymmetric to the point P . So in the real application of

this function, a round or square area might be a good choice. \mathbf{n}_S is the unit vector normal to the area S . $|\Gamma_1|$ is a dimensionless scalar bounded by 1, and the sign of Γ_1 indicates the direction of rotation. $\Gamma_1 = \pm 1$ is reached at the center of ideal vortices. In real flows, the vortex centers are located by the extrema of Γ_1 .

The vortex size identification function Γ_2 could be considered as a relative form of Γ_1 , since it uses the relative velocity field by taking into account a local convection velocity \tilde{U}_P around P :

$$\Gamma_2(P) = \frac{1}{S} \int_{M \in S} \frac{[PM \wedge (U_M - \tilde{U}_P)] \cdot \mathbf{x}}{\|PM\| \cdot \|U_M - \tilde{U}_P\|} \cdot dS \quad (4.3)$$

$\tilde{U}_P = \frac{1}{S} \int_S U dS$ is the averaged velocity inside the area S . According to Graftiaux *et al.* [49], the vortex core region boundary can be determined by the iso-value contour $\Gamma_2 = 2/\pi$.

Because the velocity fields for both the experimental measurements and the numerical simulations are sampled at discrete spatial locations, we use discrete forms of Γ_1 and Γ_2 in our study:

$$\Gamma_1(P) = \frac{1}{N} \sum_s \frac{(PM \wedge U_M) \cdot z}{\|PM\| \cdot \|U_M\|} \quad (4.4)$$

$$\Gamma_2(P) = \frac{1}{N} \sum_s \frac{[PM \wedge (U_M - \tilde{U}_P)] \cdot z}{\|PM\| \cdot \|U_M - \tilde{U}_P\|} \quad (4.5)$$

where N is the number of discrete points inside S .

In this study, before applying the two functions, the simulation results will be firstly interpolated on the PIV grid, which is uniform. A square area S is chosen on the cartesian grid, with P located at its center. This area is characterized by the number of points used in each direction, such as 9×9 . A constant size of the integration domain S is used all over the domain, except close to the boundaries, where the integration domain is reduced to remain square. In the following part, we will also investigate the sensitivity of the results to this size of the integration domain S .

Vortex system in the blade-tip region

The vortex system in the blade tip / trailing edge corner region is firstly investigated. The vortex detection function Γ_2 is employed here to reveal these vortices. Fig.4.6 shows the mean vortex system at 2mm downstream of the trailing edge, based on the function Γ_2 . The positive value of Γ_2 indicates the region of anticlockwise vortex, while the negative value corresponds to the region of clockwise vortex. From these figures, we can observe

a multi-vortex system from both the experiment and the simulations. This system consists of one large tip-leakage vortex ($30\text{mm} < y < 50\text{mm}$, $0\text{mm} < z < 20\text{mm}$), one small tip-separation vortex ($0\text{mm} < y < 20\text{mm}$, $z < 0\text{mm}$) and several small induced vortices ($y > 60\text{mm}$, $z < 15\text{mm}$). The tip-leakage vortex, which is predominant, is formed by the roll-up of the tip-leakage jet. The ZLES simulation nicely predicts both the position and the size of the tip-leakage vortex. In the RANS computation, however, the position of the tip-leakage vortex is well captured, but its size is over-estimated. The tip-separation vortex is formed by the flow separation underneath the blade tip. This vortical structure is well reproduced by both the ZLES and RANS. On the right-hand side of the tip-leakage vortex viewed from the downstream direction, some induced vortices are also generated. These induced vortices are generated by the interaction between the tip-leakage vortex and the end-plate boundary layer. A part of the boundary layer vorticity is entrained by the tip-leakage vortex to the outer region and forms the induced vortices. In the experiment, we can observe a relatively large induced vortex with an opposite sense of rotation to the tip-leakage vortex ($\Gamma_2 < 0$), and also a small region with the same sense of rotation as the TLV ($\Gamma_2 > 0$). The induced vortex in the ZLES is distorted and its intensity is smaller. This difference between the experiment and the ZLES may be due to a larger dissipation or an imperfect statistical convergence of the ZLES. In the RANS simulation, the induced vortex is not detected by the function Γ_2 within the analysis window. Obviously, the RANS computation fails to reproduce the TLV - boundary layer interaction properly, because the TLV is much larger than in the experiment or the ZLES. The RANS approach, which replaces turbulence by an eddy viscosity, and the use of low-order numerical schemes, yield a more diffusive behaviour.

Tip-leakage vortex size

The tip-leakage vortex size is investigated at 2 mm downstream of the trailing edge. In this study, the circulation is calculated at different radii for PIV AXIOOM-2, 3 and 7, and the radius is measured with respect to the vortex center determined by Γ_1 . The vortex size is roughly estimated by the the radius where the circulation reaches the maximum. The circulation - radius plots are shown in Fig.4.7, and the corresponding Γ_2 plots are shown in Fig.4.8.

From the circulation - radius plots, we can see that the circulation reaches the maximum at a radius about $17 \pm 1\text{mm}$ for all the three series of PIV measurements. The decrease of the circulation after the maximum is due to the neighbouring counter-rotating induced vortex. Thus, the tip-leakage vortex size at 2 mm downstream of the trailing edge can be estimated to be 17 mm. In addition, the uncertainty of the vortex size between different PIV measurements, 1 mm, is smaller than the maximal PIV grid size. So we can consider there

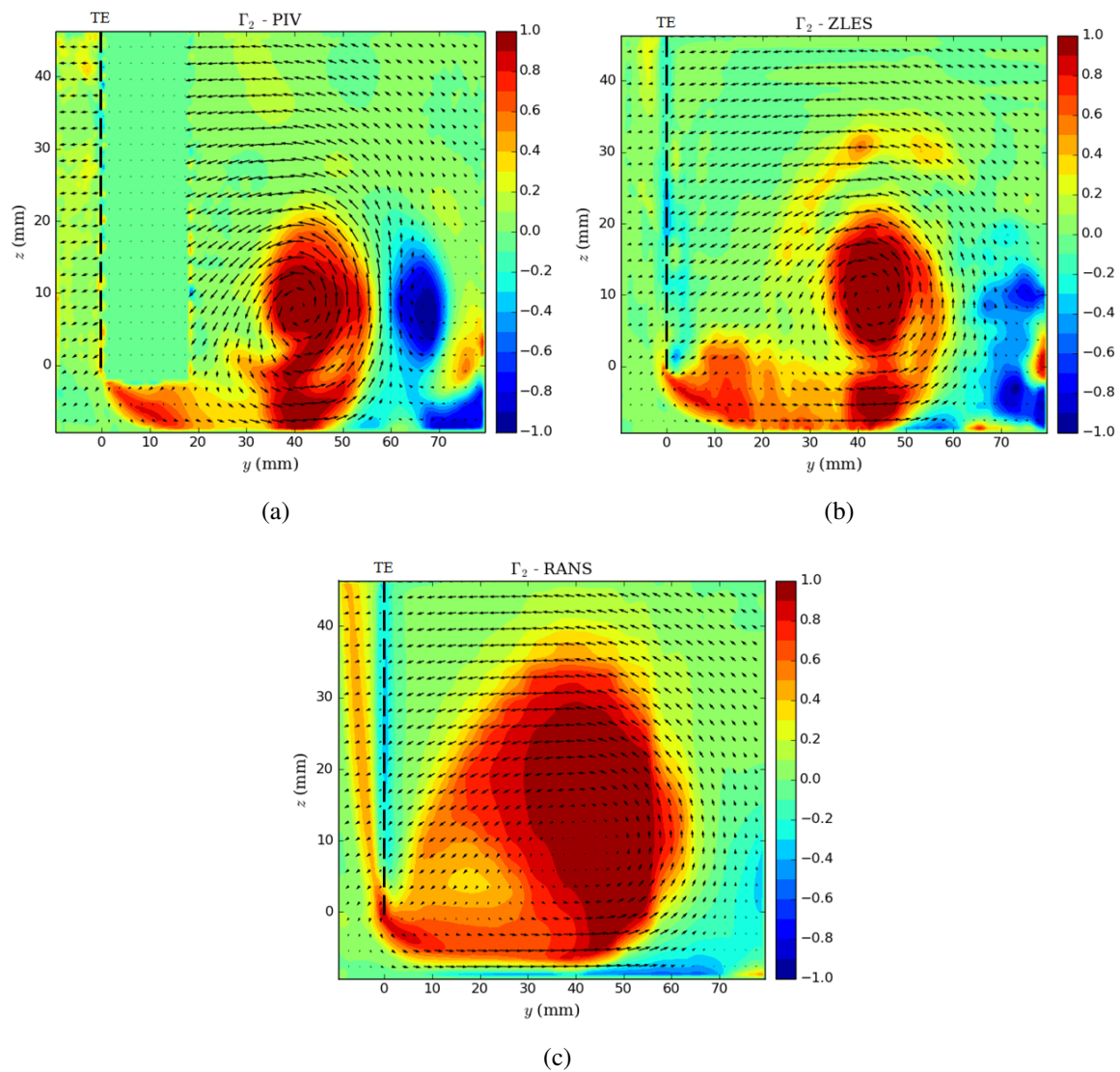


Fig. 4.6 Mean vortex system at 2mm downstream of the trailing edge, based on the function Γ_2 . View from downstream.

(a) PIV (b) ZLES (c) RANS.

The black dashed line indicates the position of the airfoil trailing edge.

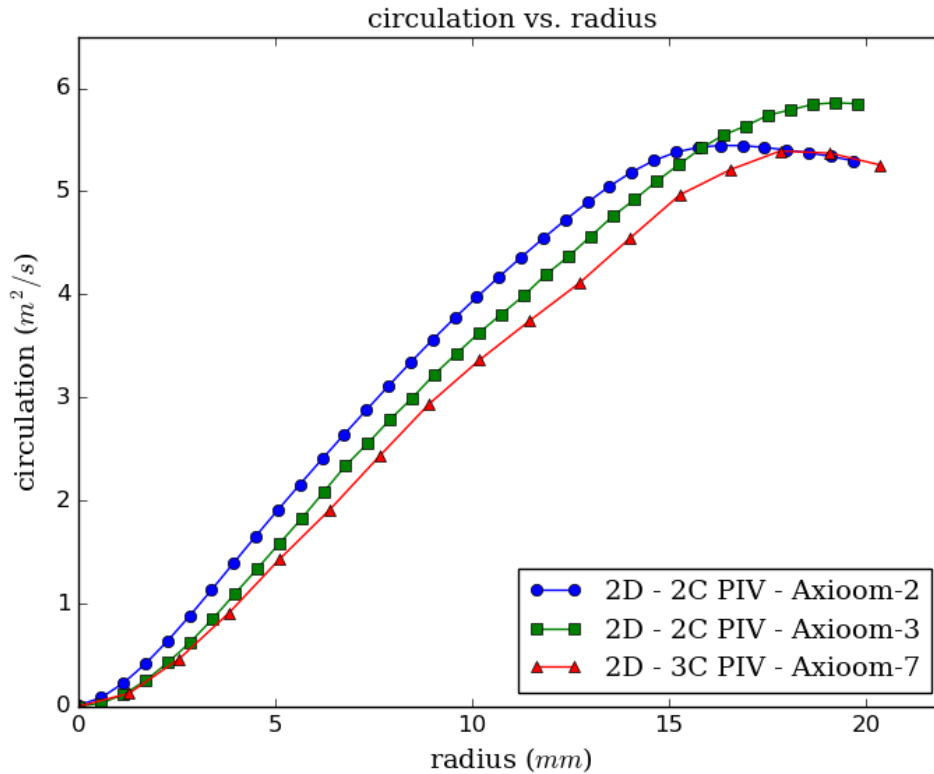


Fig. 4.7 Circulation of the TLV as a function of the integration radius, for three different PIV measurements.

is a good agreement among the three series of PIV measurements within a reasonable error range, which is consistent with the Γ_2 plots in Fig.4.8.

Tip-leakage vortex center

The function Γ_1 is used to locate the vortex center. Fig.4.9 shows the results of 4 series of PIV measurements, as well as ZLES and RANS. Similarly to Γ_2 , a positive value of Γ_1 indicates an anticlockwise vortex, while a negative value corresponds to a clockwise vortex. The extrema of Γ_1 are considered as vortex centers and marked with crosses in these figures. For the 4 series of PIV data, the difference of the vortex center positions is smaller than the PIV grid size. A good agreement is achieved between the 4 series of PIV measurements with a reasonable error range. Both the ZLES and RANS computations give a good prediction of the tip-leakage vortex center, but the counter-rotating induced vortex is much less visible. This phenomenon may be partly attributed to the filtering mechanism of the function Γ_1 . The small-scale vortices are filtered out by the function and the center of the large vortex is

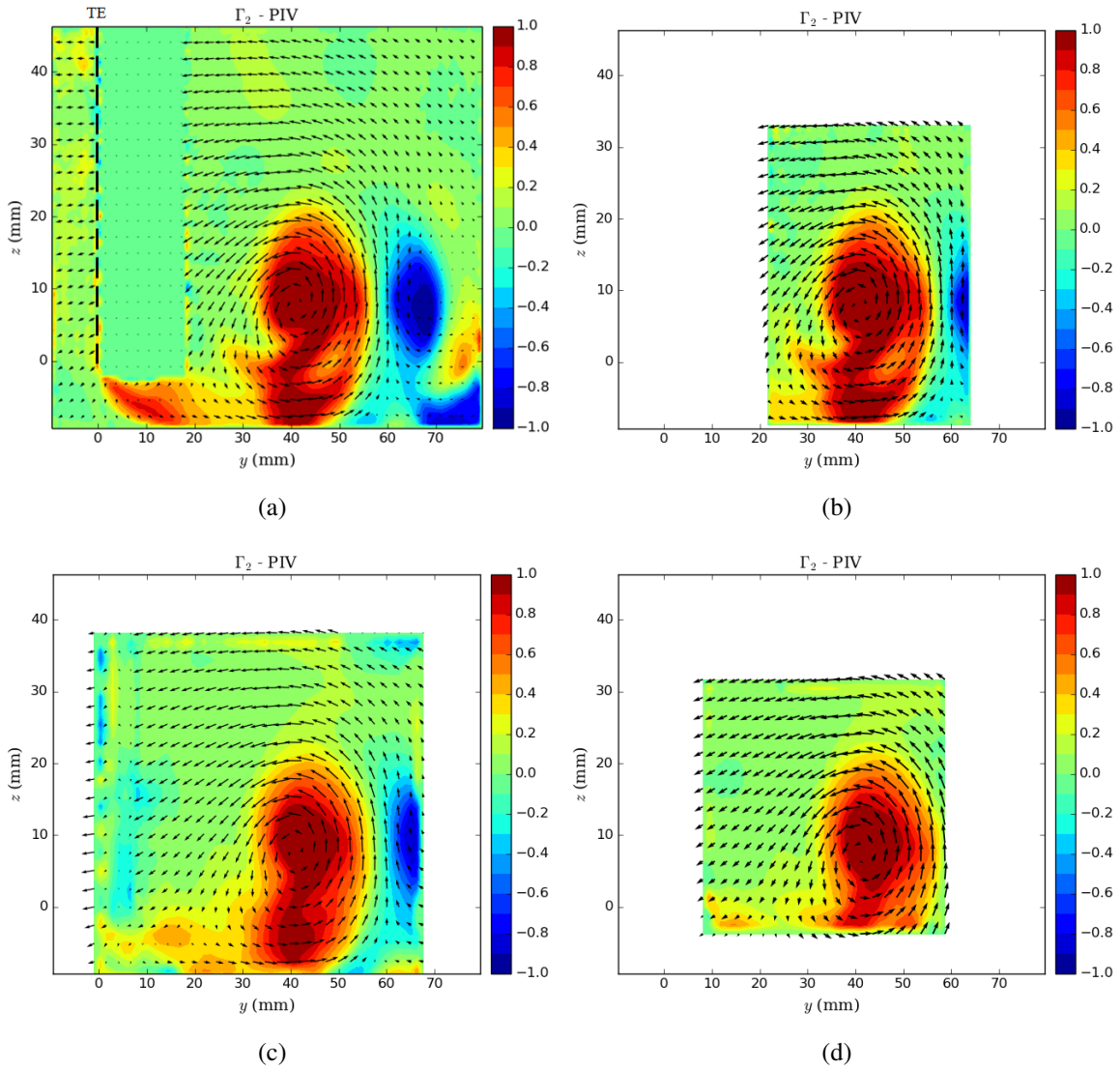


Fig. 4.8 Γ_2 of the time-averaged flow field, 2mm downstream of the trailing edge, from the experiment.

(a) AXIOOM-2 (large window 2C-PIV) (b) AXIOOM-3 (small window 2C-PIV)
(c) AXIOOM-7 (small window 3C-PIV) (d) AXIOOM-10 (small window 3C-PIV)

revealed. The induced vortex in the simulations is not intense enough to be detected by the Γ_1 function.

The iso-contours of Γ_1 are plotted in Fig.4.10, and the extrema are marked with crosses. The positive values are presented by solid lines and the negative values by dashed lines. The background is coloured by the normalized circumferential velocity magnitude $\sqrt{V^2 + W^2}/U_0$ in the plane. The iso-contour of $\Gamma_2 = 2/\pi$ is also plotted with a dotted line to indicate the vortex core region. It is interesting to observe that the vortex centers determined by Γ_1 just coincide with the minima of the circumferential velocity. Overall, the iso-contours of Γ_1 show a good consistency with the circumferential velocity field. Finally, the iso-contour $\Gamma_2 = 2/\pi$, used to determine the vortex core, coincides closely with the regions of maximal circumferential velocity.

Tip-leakage vortex trajectory

Based on the function Γ_1 , we calculate the tip-leakage vortex center at several axial positions, from 50% c upstream of the trailing edge to 25% c downstream of it, and we obtain the trajectory of the tip-leakage vortex. Fig.4.11 shows the results for ZLES, RANS and the experiment. The position of the airfoil and its chord are also indicated, in order to reveal the relative position between the vortex and the airfoil. We can see that there is a very good agreement between the experiment and the numerical simulations at the positions 20mm upstream and 2mm downstream of the trailing edge, which validates the results of the ZLES and RANS computations. The deviation of the experimental result from the numerical results at 40mm upstream of the trailing edge is probably due to measurement errors: indeed, at this position, the PIV measurement plane is too close to the blade surface and some measurement errors are caused by laser reflections. The TLV trajectories predicted by ZLES and RANS are not aligned with the inflow direction. They are slightly inclined towards the blade-side. Their angle with respect to the inflow direction is smaller than the angle of attack, that is to say, the TLV slowly deviates from the suction surface. If we extend linearly the trajectory upstream (blue dashed-line), the TLV is found to start in the front part of the blade. Downstream of the trailing edge, the ZLES trajectory remains straight, while the RANS result slightly deviates to the inflow direction. From the previous comparisons, we found that the intensity of the TLV in the RANS computation is under-estimated. So the TLV in the RANS computation mix more quickly with the main flow. Due to the finer grid downstream of the trailing edge, the ZLES result is more reliable here.

Many efforts have been made to model the tip-leakage vortex trajectory. The first recognized model is that of Chen [28], and this model has been improved by many other researchers, such as Song [100].

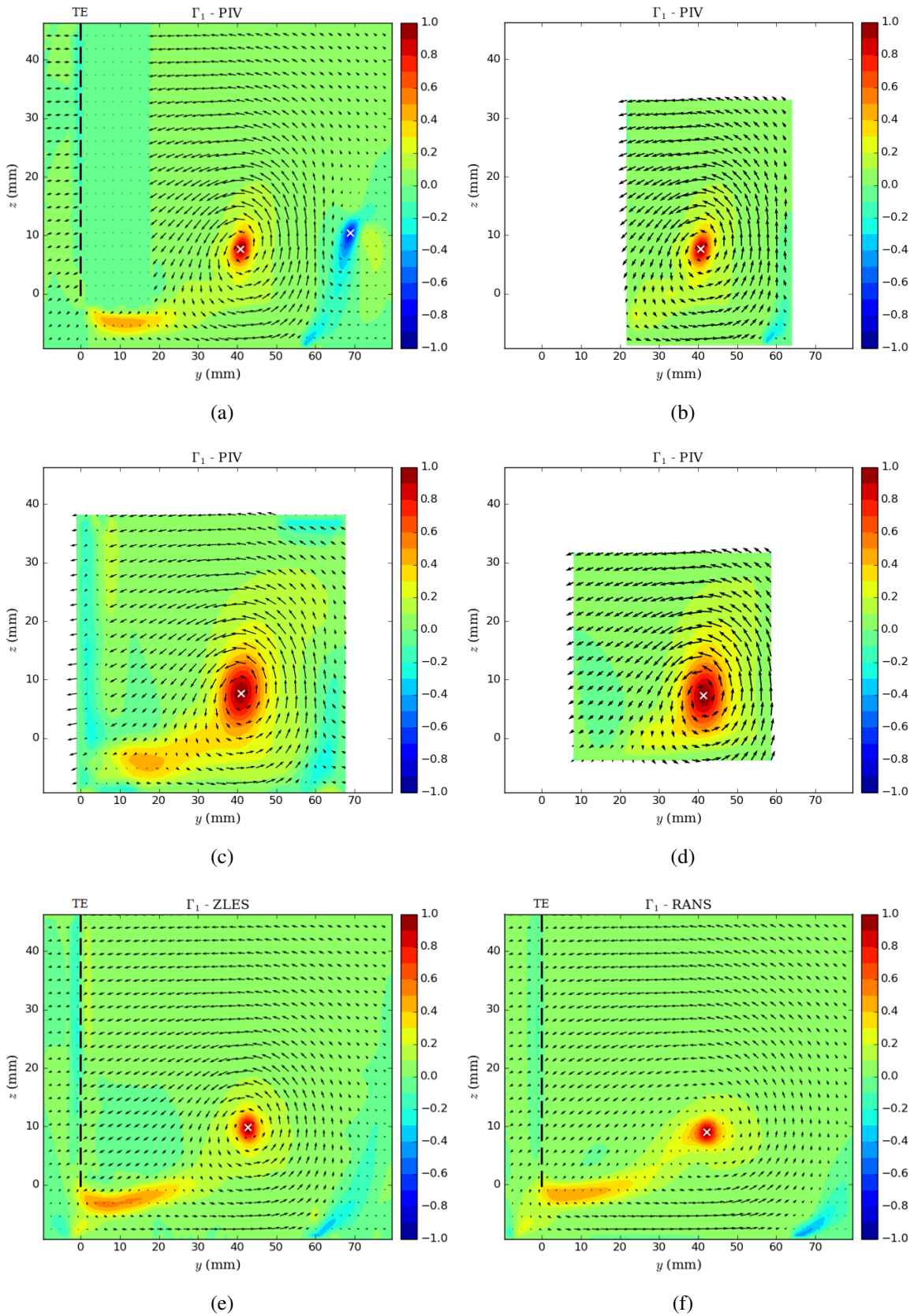
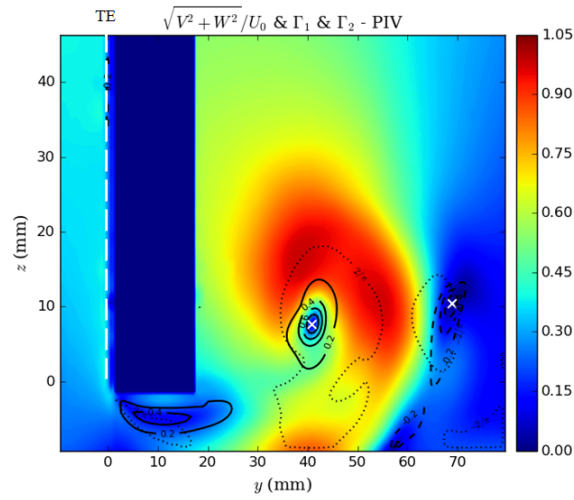
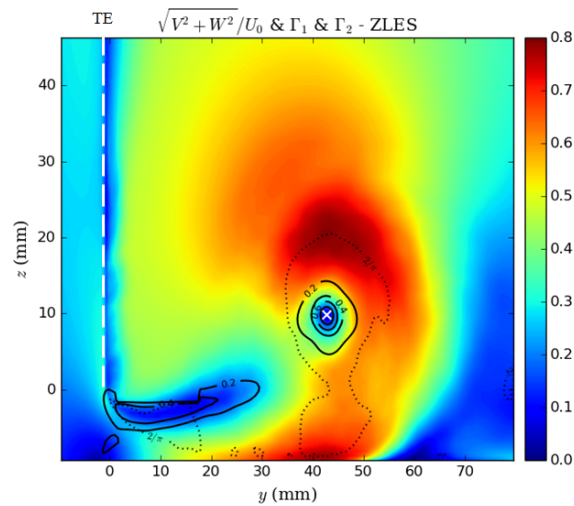


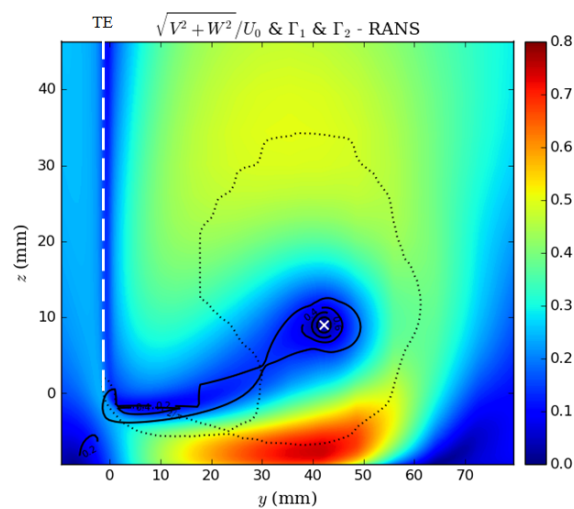
Fig. 4.9 Γ_1 of the time-averaged flow field, 2mm downstream of the trailing edge.
 (a) 2C-PIV AXIOOM-2 (b) 2C-PIV AXIOOM-3 (c) 3C-PIV AXIOOM-7
 (d) 3C-PIV AXIOOM-10 (e) ZLES (f) RANS



(a)



(b)



(c)

Fig. 4.10 Solid and dashed lines: iso-contours of Γ_1 (positive and negative values, respectively), dotted line: iso-contour $\Gamma_2 = 2/\pi$, background: circumferential velocity levels, 2mm downstream of the trailing edge.
 (a) 2C-PIV AXIOOM-2 (b) ZLES (c) RANS

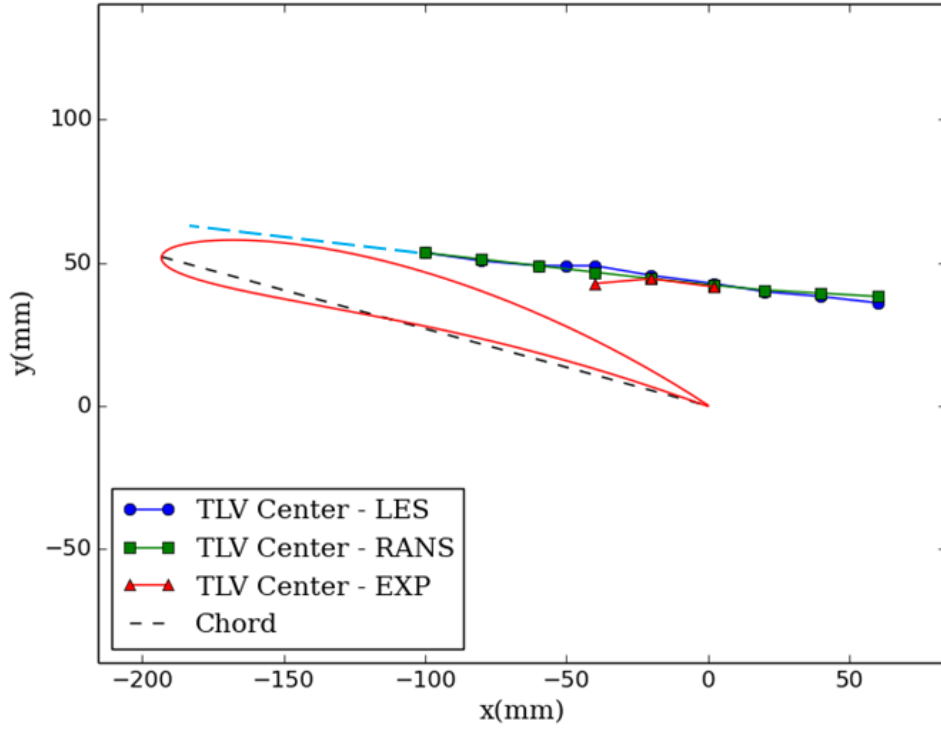


Fig. 4.11 Tip-leakage vortex trajectory

In Chen's model, the tip-leakage vortex trajectory is described in a coordinate system $x_1 - y_1$ defined as follows: the origin locates at the blade leading edge; x_1 is the streamwise position measured from the leading edge; the pitchwise position y_1 is the distance between the vortex center and the blade chord. In this coordinate system, the tip-leakage vortex trajectory may be approximated by:

$$y_1 = K \sqrt{\frac{Cp_m}{2}} x_1 \quad (4.6)$$

where Cp_m is the mean pressure difference coefficient $Cp_m = \frac{\overline{\Delta p}}{1/2 \rho u_x^2}$. K is a constant and is proposed to be 0.46 by Chen and 0.19 by Kang [66]. This model does not account for the influence of the tip clearance onto the TLV trajectory.

First, the linear evolution of the TLV proposed by the model agrees with the present results. Then, we use ZLES data to investigate the value of K in the present case. Cp_m is evaluated by a surface integration in the blade-tip region and we obtain $Cp_m \approx 0.907$. The value of K is calculated at different axial positions and it is found to vary from 0.34 to 0.42, as indicated in Fig.4.12. This value is in fairly good agreement with Chen's value ($K=0.46$). However, the tip-leakage vortex trajectory in the present case does not pass the blade leading

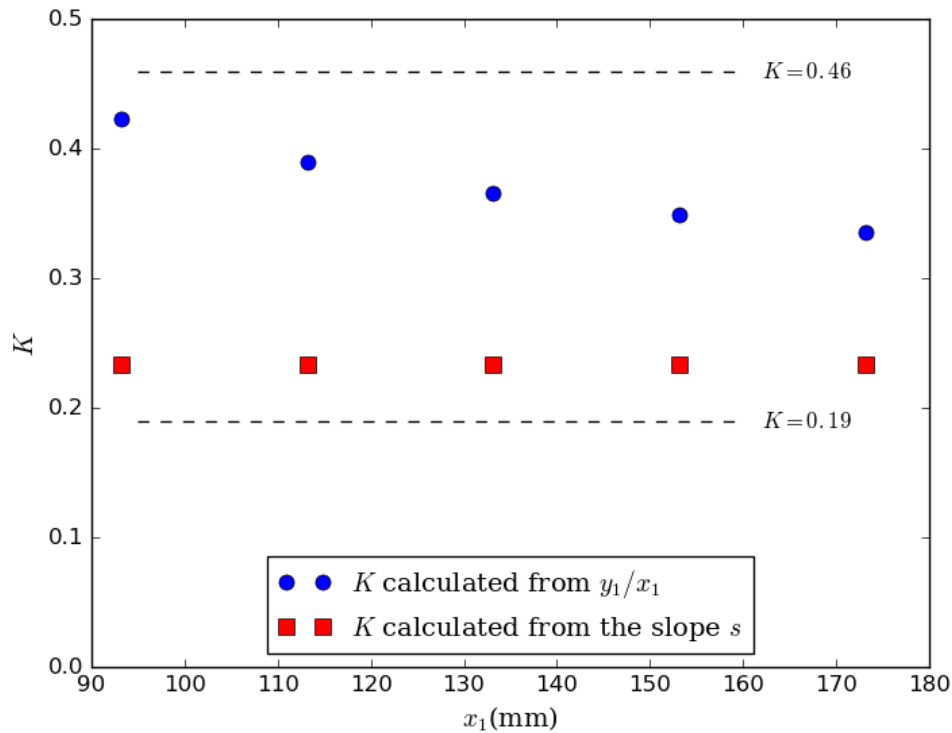


Fig. 4.12 K in Chen's model, calculated from ZLES data.

edge, which is different from the assumption of Chen's model. Based on this understanding, we may correct this model by interpreting y_1/x_1 as the slope s of the tip-leakage vortex trajectory in the $x_1 - y_1$ coordinate system. And we obtain $s \approx 0.157$ and a constant $K \approx 0.23$, as shown in Fig.4.12. This value is close to Kang's value ($K=0.19$).

As shown in the previous sections, RANS is more diffusive and globally under-estimates the intensity of the tip-leakage flow. But the TLV center is well predicted by RANS, which can be explained by Chen's model. According to this model, the TLV center depends mostly on the blade loading. Since the RANS computation yields a satisfactory prediction of the blade loading, as shown in section 4.3.1, and the diffusion does not affect the blade loading, it can be expected that the TLV center and the trajectory will be well predicted in RANS.

Sensitivity of vortex detection functions

In all the figures above, Γ_1 and Γ_2 are computed on an integration domain of 9×9 points around the central point. So we have interest in investigating the sensitivity of the two vortex detection functions to the size of the integration domain.

The sensitivity of the function Γ_1 to the size of the integration domain is illustrated in Fig.4.13. The region of vortex center becomes larger with the increase of the integration

domain. But when we compare the positions of the extreme values, that is, the vortex center, we find that there is nearly no difference between them. So it seems that the integration domain has little effect on the position of the vortex center, though the region of vortex center becomes larger with larger integration domain, because the Γ_1 integration smears out the core region.

This is not the case with the non-dimensional angular momentum Γ_2 . Fig.4.14 shows the results of Γ_2 for PIV AXIOOM-2 with different integration domains, from 3×3 to 13×13 points. From these figures, we can hardly find any difference between the different integration domains. So we can conclude that the integration domain has nearly no effect on Γ_2 within the range of values examined herein.

Theoretically, the integration involved in functions Γ_1 and Γ_2 serve to smooth the flow field and remove the small-scale turbulent structures. The larger the integration domain is, the larger the filtered scales will be. In the current case, an integration domain of 7×7 or 9×9 points is found to be a good compromise between the smoothing, the precision of the vortex characterisation for the mean field and the computational cost. Since the mean flow field is already smooth, an even larger integration domain has few benefits but increase the computational cost. On the other hand, a smaller domain is more appropriate for characterising small-scale instantaneous vortices.

4.3.3 Mean velocity field

In this section, the 2D velocity field at several cross-stream planes will be firstly presented for the time-averaged PIV, time-averaged ZLES and RANS computations. This 2D velocity field will give us a general comparison of the flow patterns. Then the velocity profiles on some lines in the field will be plotted, to ensure a more detailed comparison.

2D streamwise velocity field

The streamwise velocity component U is investigated at the plane $x = 2\text{mm}$ downstream of the trailing edge, as shown in Fig.4.15. For easier comparison, the same space and amplitude scales are chosen for all plots. The blank area in the experimental result Fig.4.15(a) comes from the smaller measurement window of the 2D-3C TR PIV.

In the experiment, a large excess of the streamwise velocity is found in the core region of the tip-leakage vortex. The maximal streamwise velocity reaches about 1.4 times the free-stream velocity close to the vortex center. This experimental result is consistent with former measurements [59] and with the tip-leakage vortex structure proposed by Bindon [15]. On the contrary, RANS predicts a deficit of the streamwise velocity in the same region. The

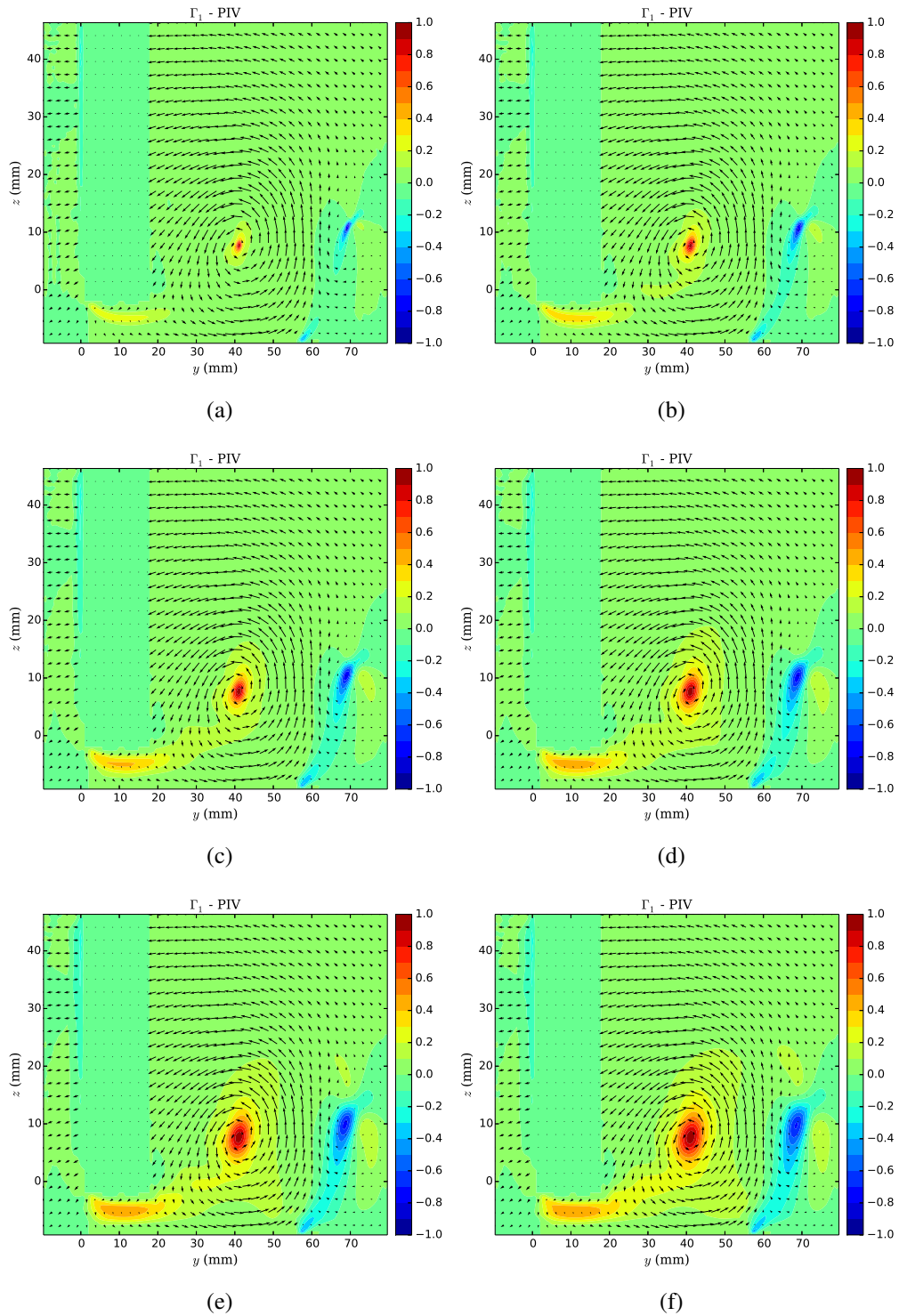


Fig. 4.13 Γ_1 of the time-averaged flow field with different integration domains, for 2C-PIV AXIOOM-2.

Integration box: (a) 3×3 (b) 5×5 (c) 7×7 (d) 9×9 (e) 11×11 (f) 13×13

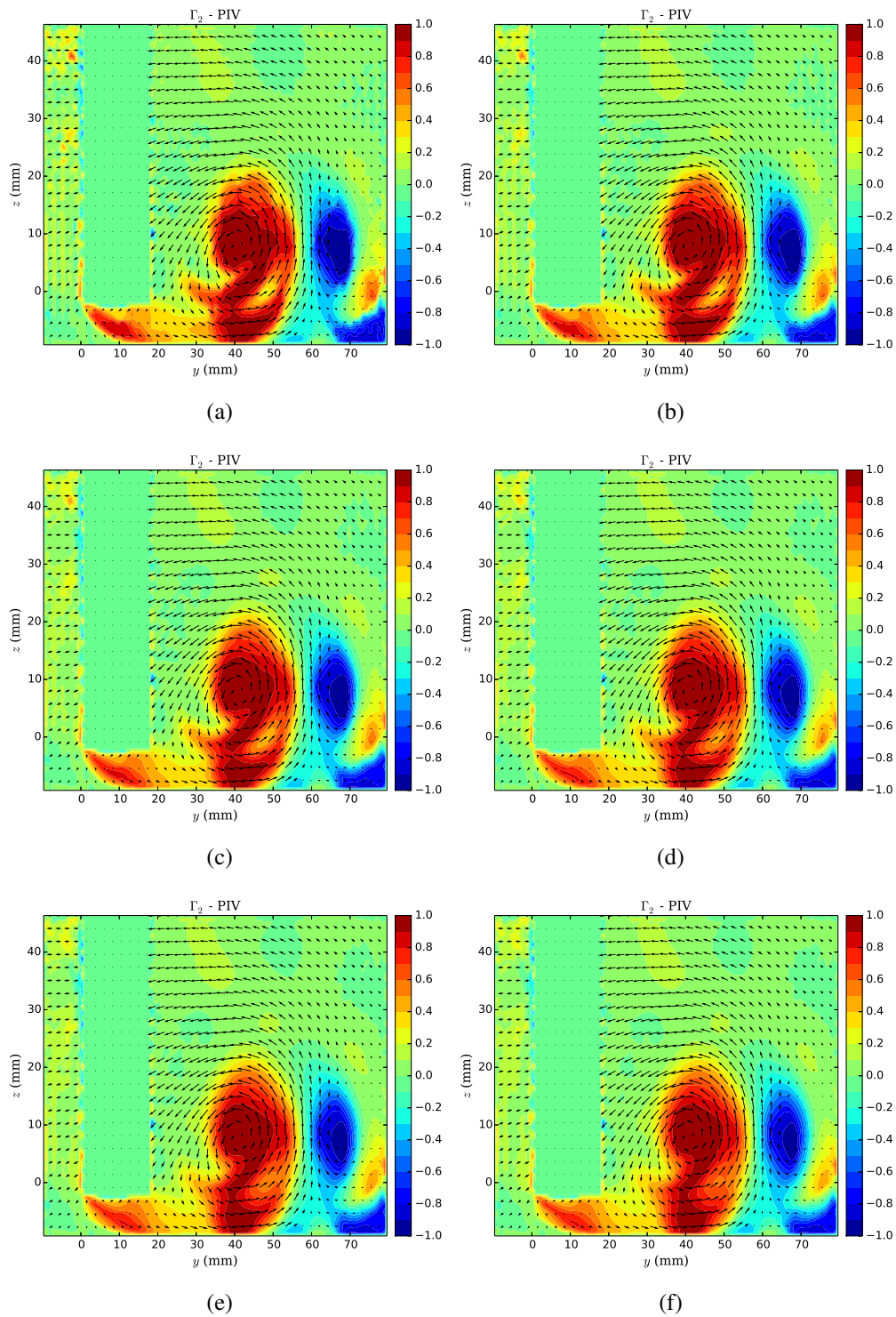


Fig. 4.14 Γ_2 of the time-averaged flow field with different integration domains, for 2C-PIV AXIOOM-2.

Integration box: (a) 3×3 (b) 5×5 (c) 7×7 (d) 9×9 (e) 11×11 (f) 13×13

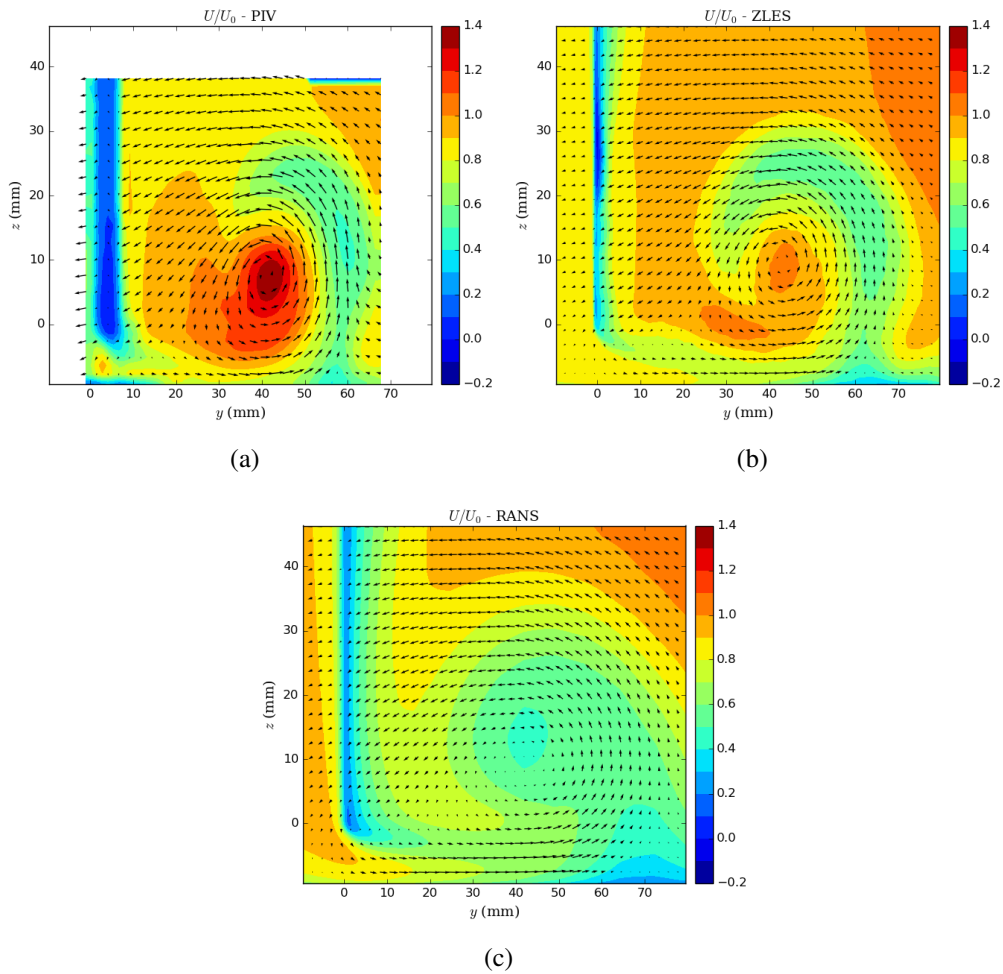


Fig. 4.15 Mean streamwise velocity field U at $x=2\text{mm}$.
 (a) Experiment (b) ZLES (c) RANS

ZLES reproduces the experimental topology. The velocity excess at the TLV center is less pronounced, but the low-velocity region on the right-hand side of the TLV is well described. This region is formed by the fluid entrained by the TLV from the end-plate boundary layer to the outer region. It is also associated with the induced counter-rotating vortex observed in the previous section.

2D cross-stream velocity field

The mean cross-stream velocity fields are investigated at $x = -40\text{mm}$, -20mm and 2mm . Fig.4.16 and Fig.4.17 show the mean horizontal velocity component V and the mean vertical velocity component W , respectively, for the experiment, ZLES and RANS. Again, these figures are all plotted with the same scale in order to directly compare their amplitudes.

In the experiment (first column), we can observe some regions with zero velocity on the left-hand side of the window at $x = -40\text{mm}$ and -20mm . They are actually measurement errors due to laser reflections, because these planes are close to the blade surface.

Through the velocity vector field, the TLV roll-off is clearly visible. The horizontal mean velocity component V is positive below the TLV and negative above. The vertical mean velocity component W is negative on the left-hand side of the TLV and positive on the right-hand side. In the experiment, when the vortex rolls off, both the mean horizontal velocity and the mean vertical velocity reach about 1.2 times the free stream velocity at $x = -40\text{mm}$. The tip-leakage vortex is very intense.

For the mean horizontal velocity component V , the elongated area at $z < 0\text{mm}$ corresponds to the tip-leakage jet, where V is intense and positive. The maximum value of V is found near the end-plate ($z = -10\text{mm}$), where the fluid should be inside the end-plate boundary layer and should decelerate. This phenomenon may be explained by the combined effect of two mechanisms: the tip-leakage jet locates very close to the end-plate, so it will accelerate the fluid near the end-plate, that is, increase V ; the boundary layer is kept very thin on the end-plate, because of the strong tip-leakage jet. As for the mean vertical velocity component W , the fluid in the inner area (left-hand side of the TLV) is found to undergo a stronger horizontal gradient than in the outer region (right-hand side of the TLV), which is due to the deceleration of the fluid in the vicinity of the blade. As the tip-leakage vortex moves downstream, it moves away from the blade, as demonstrated in the previous section, and the fluid is allowed to decelerate within a longer distance between the vortex center and the blade, contributing to the expansion of TLV. Concerning the fidelity of the simulations, a very good description is achieved by the ZLES. Both the size of the TLV and its intensity are well reproduced. RANS appears more diffusive, with a larger TLV and smoother gradients.

The mean circumferential velocity is plotted in Fig.4.18, as well as iso-contours of Γ_1 and Γ_2 . We can observe that there is a damping in the magnitude of the circumferential velocity for both the experiment and the simulations from $x = -40\text{mm}$ to $x = 2\text{mm}$. This damping of velocity magnitude results from the expansion of the tip-leakage vortex when it moves downstream, which is revealed by the expansion of the iso-contour $\Gamma_2 = 2/\pi$. In addition, the dissipation may also contribute.

Considering the topology of the flow, there is a good agreement between the experiment and the ZLES, except the magnitude is a little smaller for the ZLES, probably due to a slightly larger dissipation. The RANS computation is much more dissipative than the ZLES. The tip-leakage vortex predicted by the RANS computation is obviously less intense. Its velocity amplitude is much lower than that of the experiment and the ZLES, especially in the vertical direction.

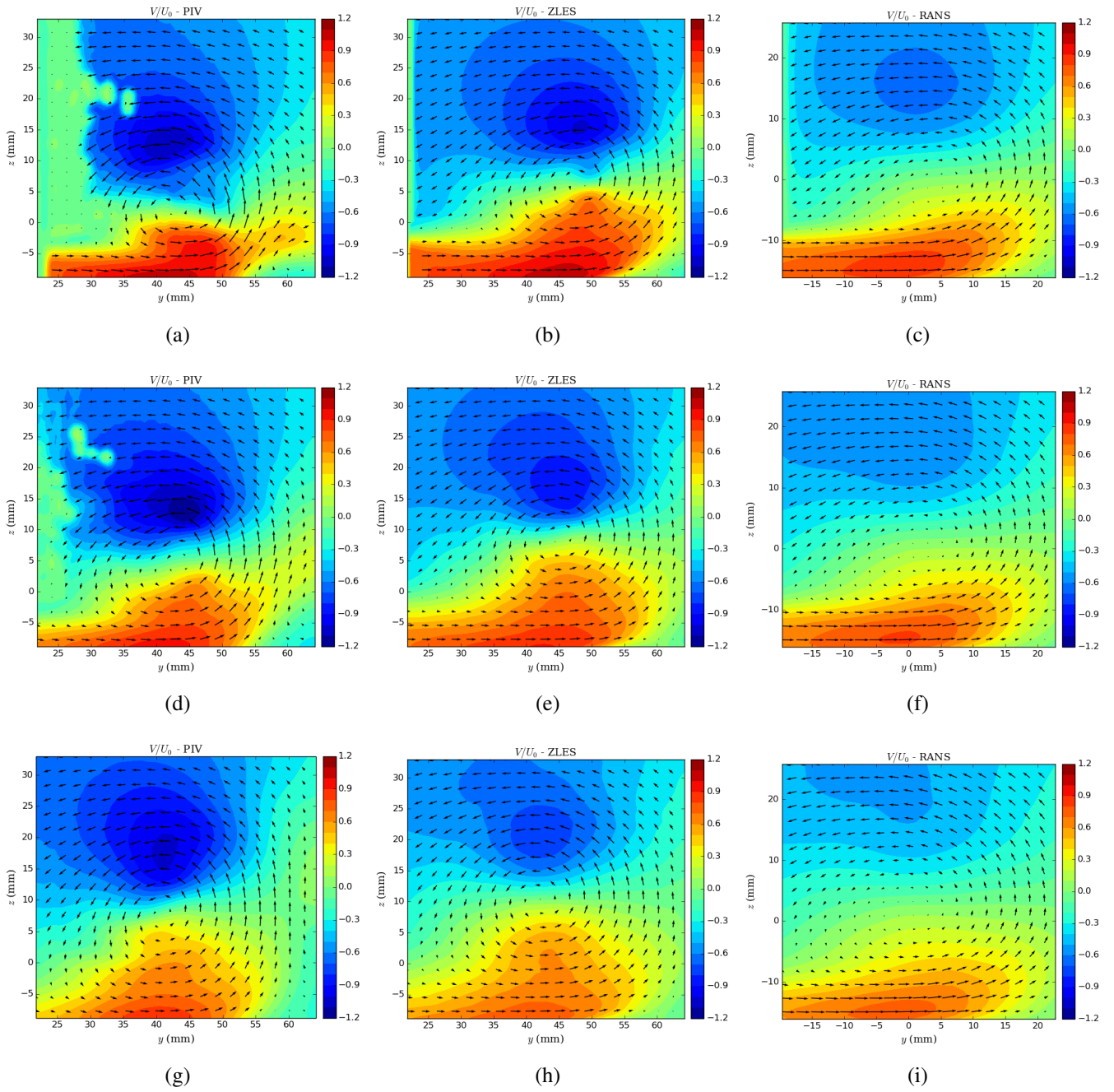


Fig. 4.16 Mean horizontal velocity fields V .
 From left to right: PIV, ZLES, RANS.
 From top to bottom: $x = -40\text{mm}$, $x = -20\text{mm}$, $x = 2\text{mm}$.

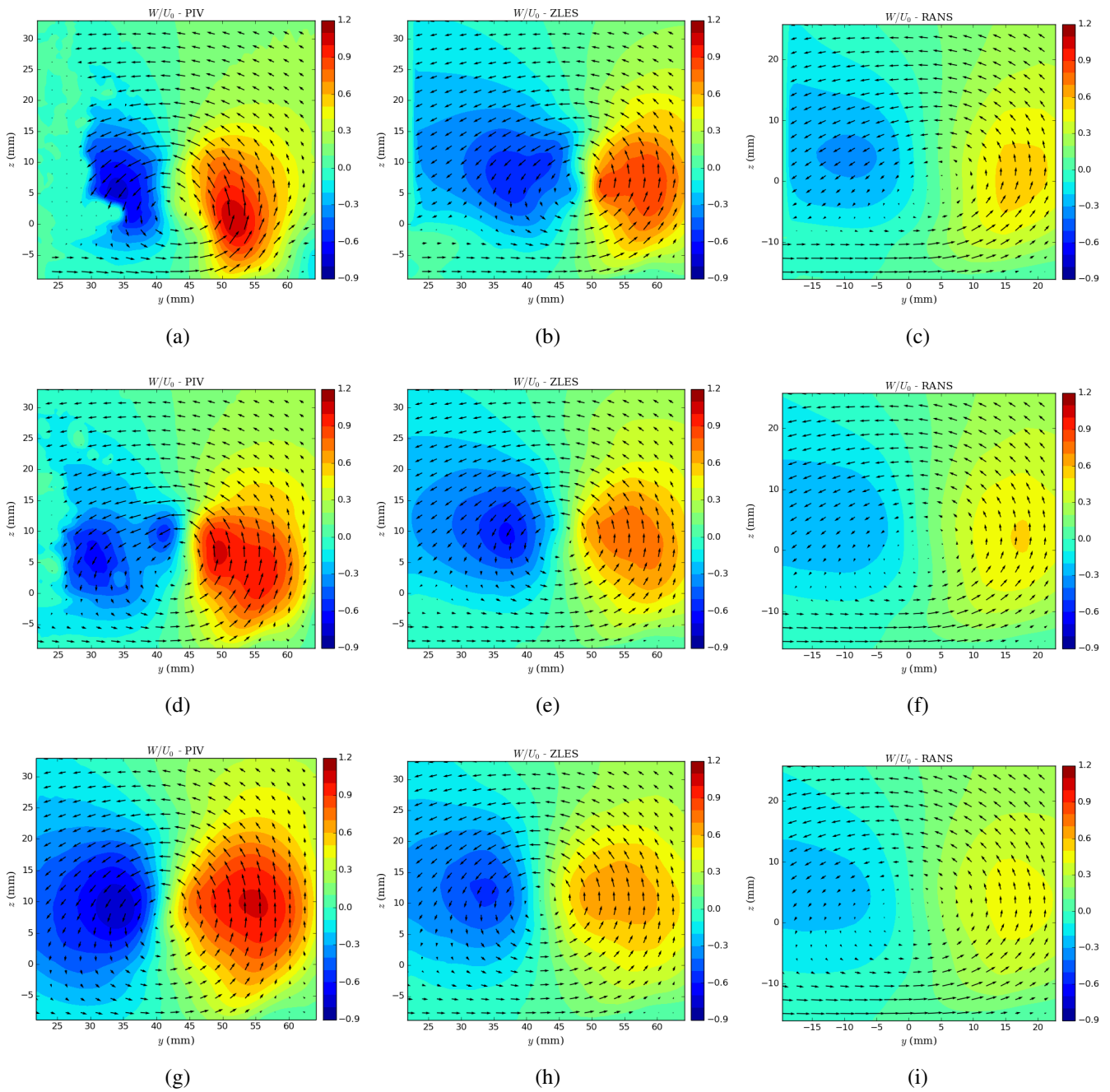


Fig. 4.17 Mean vertical velocity fields W .
 From left to right: PIV, ZLES, RANS.
 From top to bottom: $x = -40$ mm, $x = -20$ mm, $x = 2$ mm.

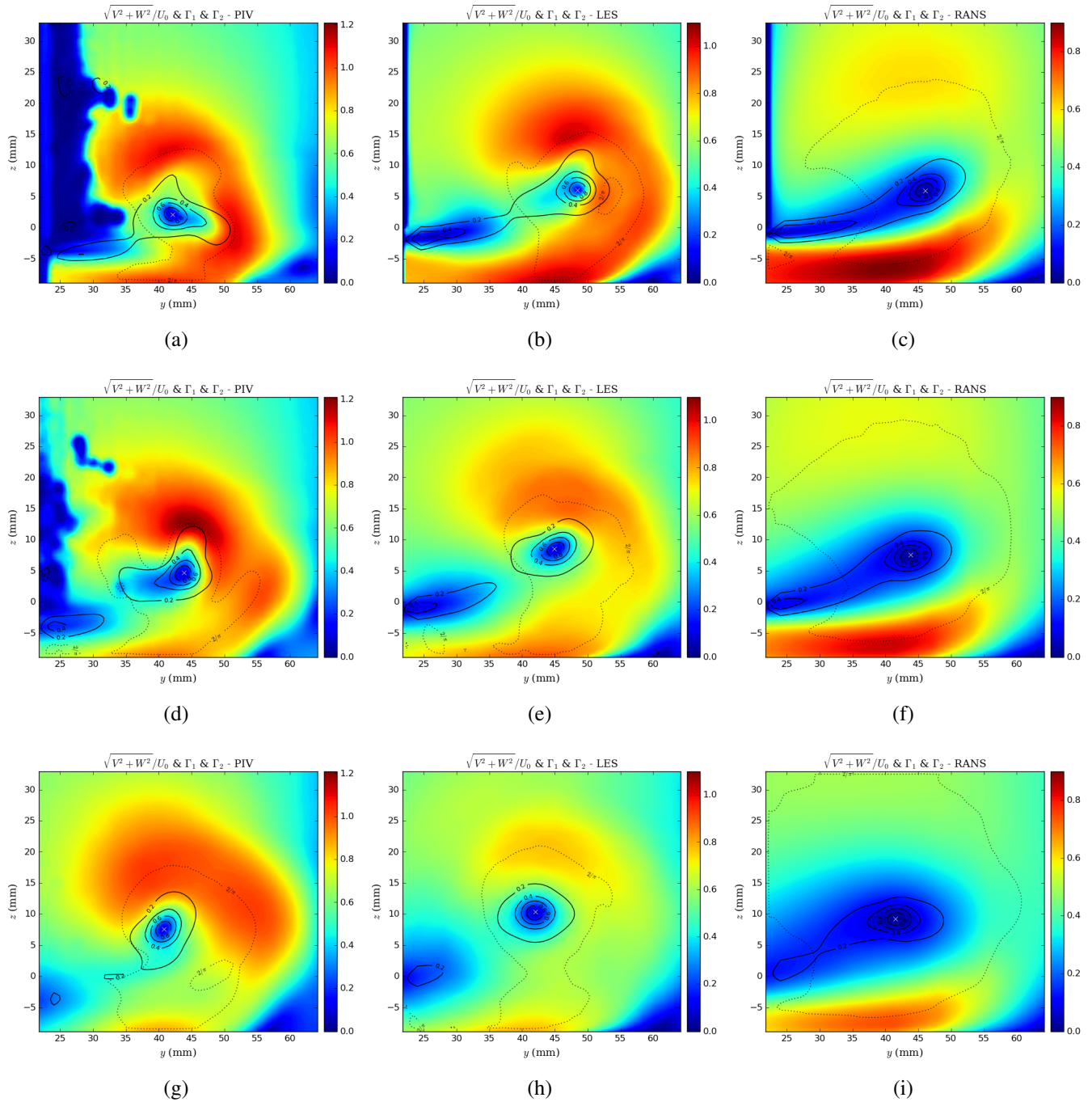


Fig. 4.18 Solid and dashed lines: iso-contours of Γ_1 (positive and negative values, respectively), dotted line: iso-contour $\Gamma_2 = 2/\pi$, background: circumferential velocity levels.
 From left to right: PIV, ZLES, RANS.
 From top to bottom: $x = -40$ mm, $x = -20$ mm, $x = 2$ mm.

1D velocity profiles

In the experiment, the streamwise velocity component U is only measured by PIV within a window of very limited size at $x = 2\text{mm}$, using 2D-3C TR PIV. In order to complement the experimental database, LDV measurements are also performed at 4 streamwise locations $x = -60\text{mm}$, -40mm , -20mm and 2mm and 6 spanwise locations $z = -5\text{mm}$, 0mm , 10mm , 20mm , 30mm and 40mm . Both the streamwise velocity component U and the vertical velocity component W are measured by LDV. In this section, PIV and LDV data are compared with each other, along with the ZLES and RANS results. ZLES and RANS results are extracted and corrected as described in the previous section. Here we only display the results at $x = -20\text{mm}$ and 2mm , because the PIV measurements are less affected by laser reflections at these two positions.

Results are shown in Figs.4.19-4.23. A good agreement is achieved between PIV and LDV at most of the positions. The deviation of the peaks in some figures, such as Fig. 4.19(e) and 4.22(e), could be partly explained by differences in the coordinate systems of the two measurement techniques. Large discrepancies between LDV and PIV are observed at some positions and might be due to an inappropriate PIV seeding in some parts of the TLV. Finally, it is interesting to observe 3C-PIV achieves a description of the velocity component U , normal to the plane, in fairly good agreement with LDV.

The prediction of ZLES is similar to the measurements. At some locations, their results even collapse, as can be seen on Figs. 4.20(d) and 4.22(c). At some other locations, such as Fig.4.20(e) and 4.22(e), a shift of peaks can be observed between the experimental results and the ZLES results. The vortex structure predicted by ZLES locates a little further away from the blade side, though the extension of the TLV in y direction is well captured. The RANS simulation gives a rather good prediction of the three velocity components close to the mid-span. At the other locations, the normal velocity component V is acceptable, but U and W differ from the experimental and ZLES results. The vortex structure predicted by the RANS computation spreads more: the peak of positive W locates at larger y coordinate at the outer side of the vortex, as seen in Fig.4.21(e) at $x = -20\text{mm}$. This effect is no more observed at $x = 2\text{mm}$ (Fig.4.21(f)). For both ZLES and RANS simulations, the velocity magnitude of the peaks is under-estimated at most locations. Some peaks even vanish for RANS, as can be seen on Figs.4.19(a)(b), Figs.4.20(a)(b) and Fig.4.22(b). This is again a sign of excessive diffusion.

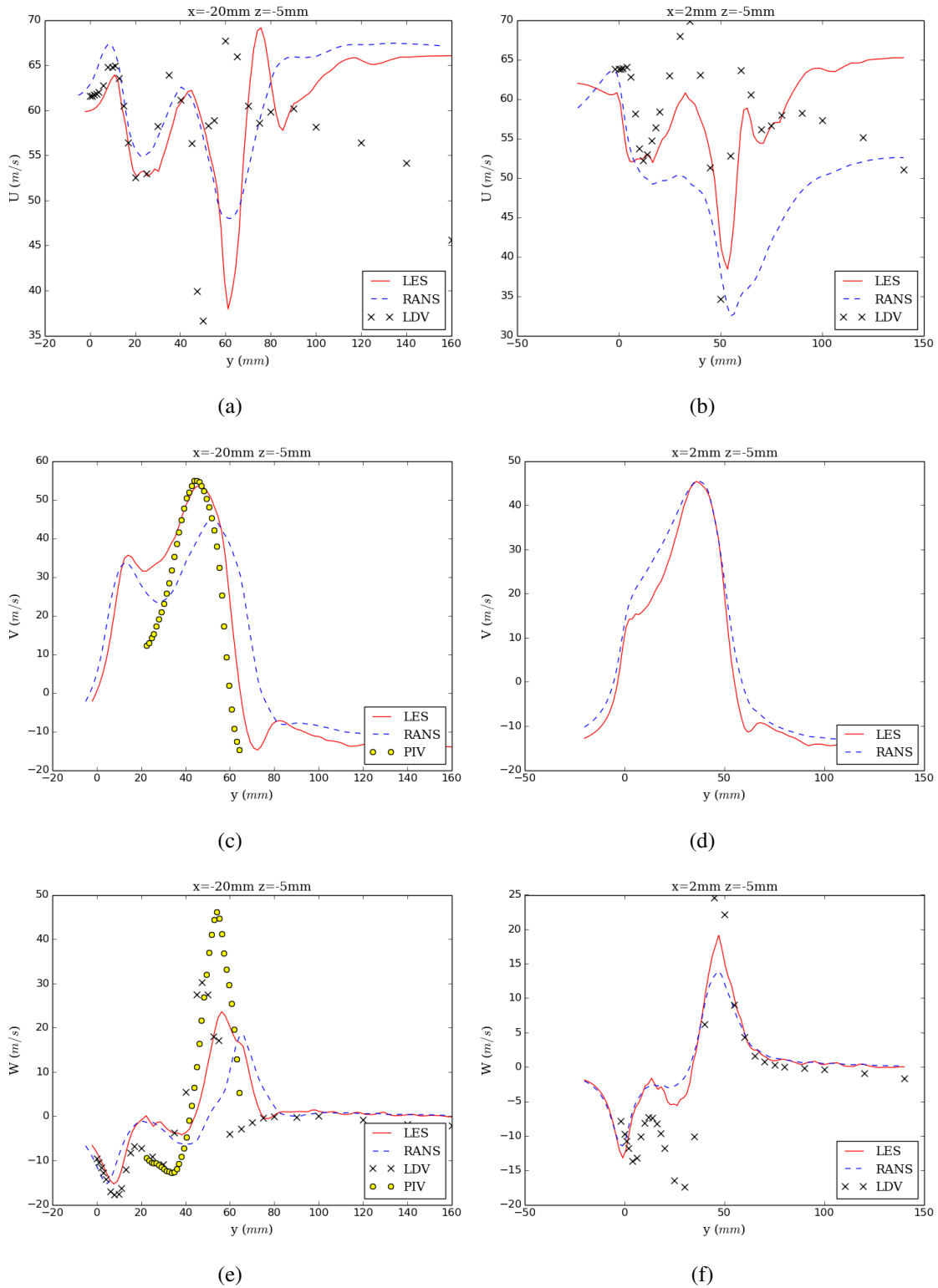
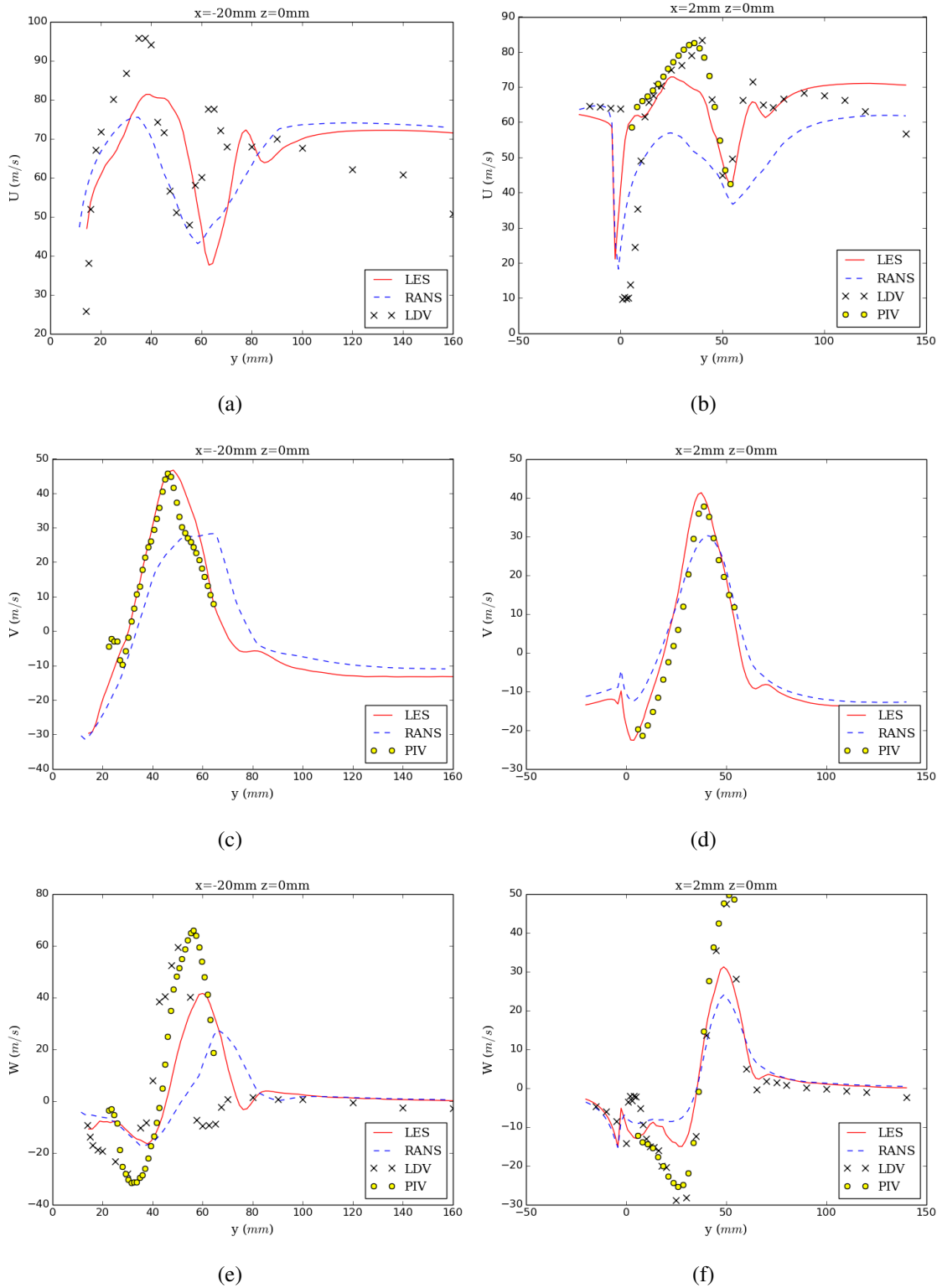


Fig. 4.19 Velocity profile comparison, $z = -5\text{mm}$.
 (a)(c)(e) $x = -20\text{mm}$ (b)(d)(f) $x = 2\text{mm}$

Fig. 4.20 Velocity profile comparison, $z = 0\text{ mm}$.(a)(c)(e) $x = -20\text{ mm}$ (b)(d)(f) $x = 2\text{ mm}$

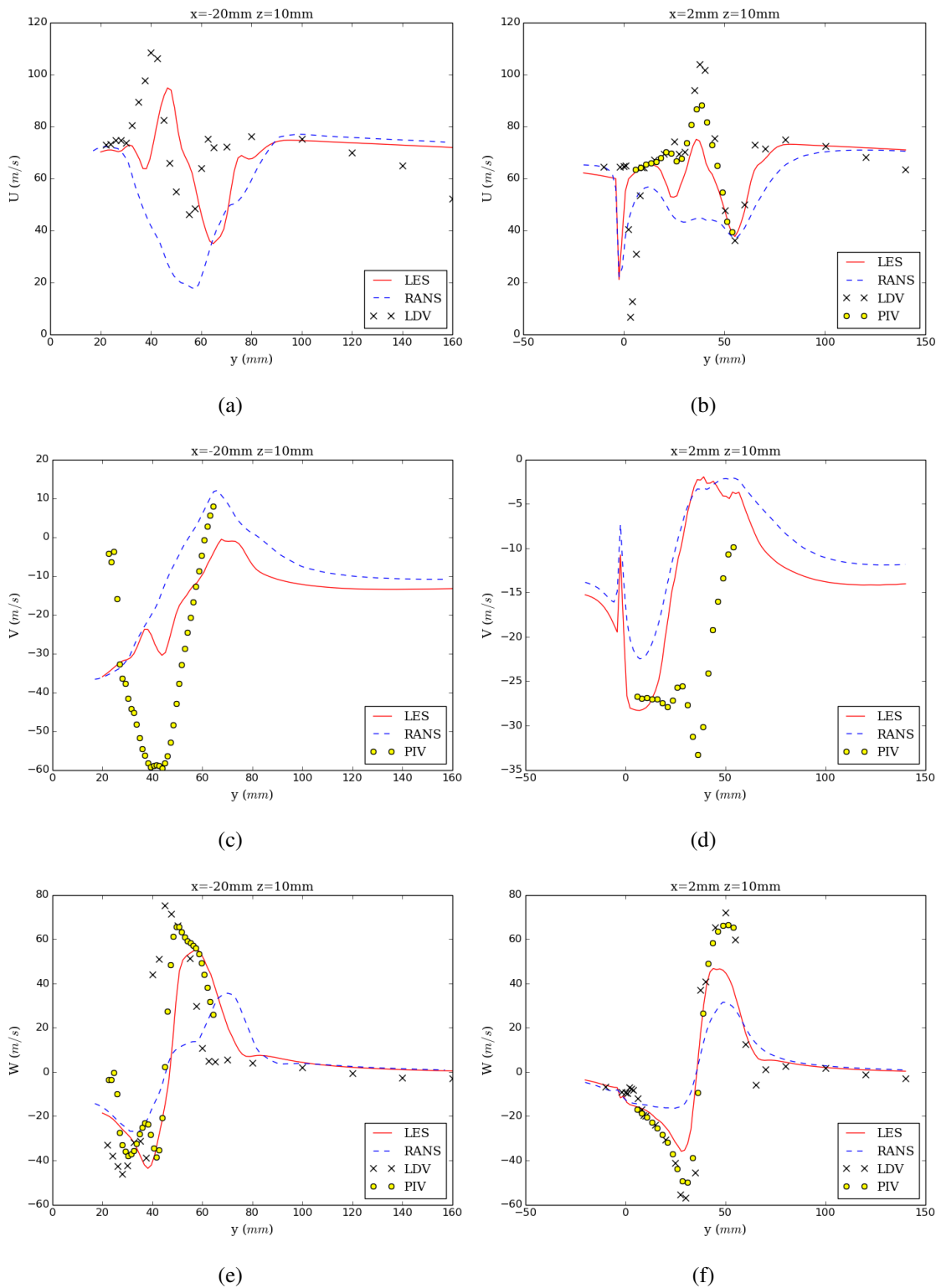


Fig. 4.21 Velocity profile comparison, $z = 10\text{mm}$.
 (a)(c)(e) $x = -20\text{mm}$ (b)(d)(f) $x = 2\text{mm}$

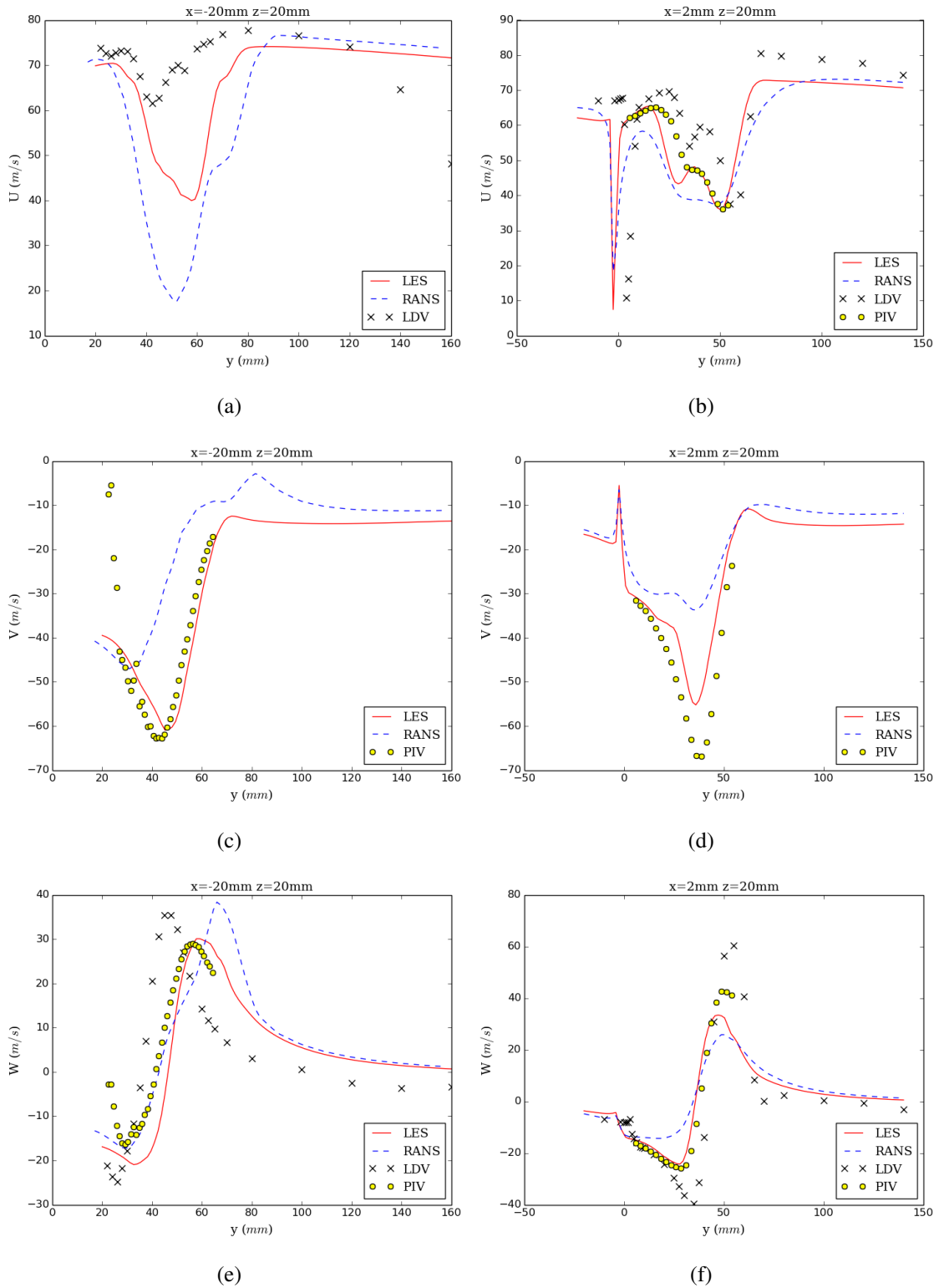


Fig. 4.22 Velocity profile comparison, $z = 20\text{mm}$.

(a)(c)(e) $x = -20\text{mm}$ (b)(d)(f) $x = 2\text{mm}$

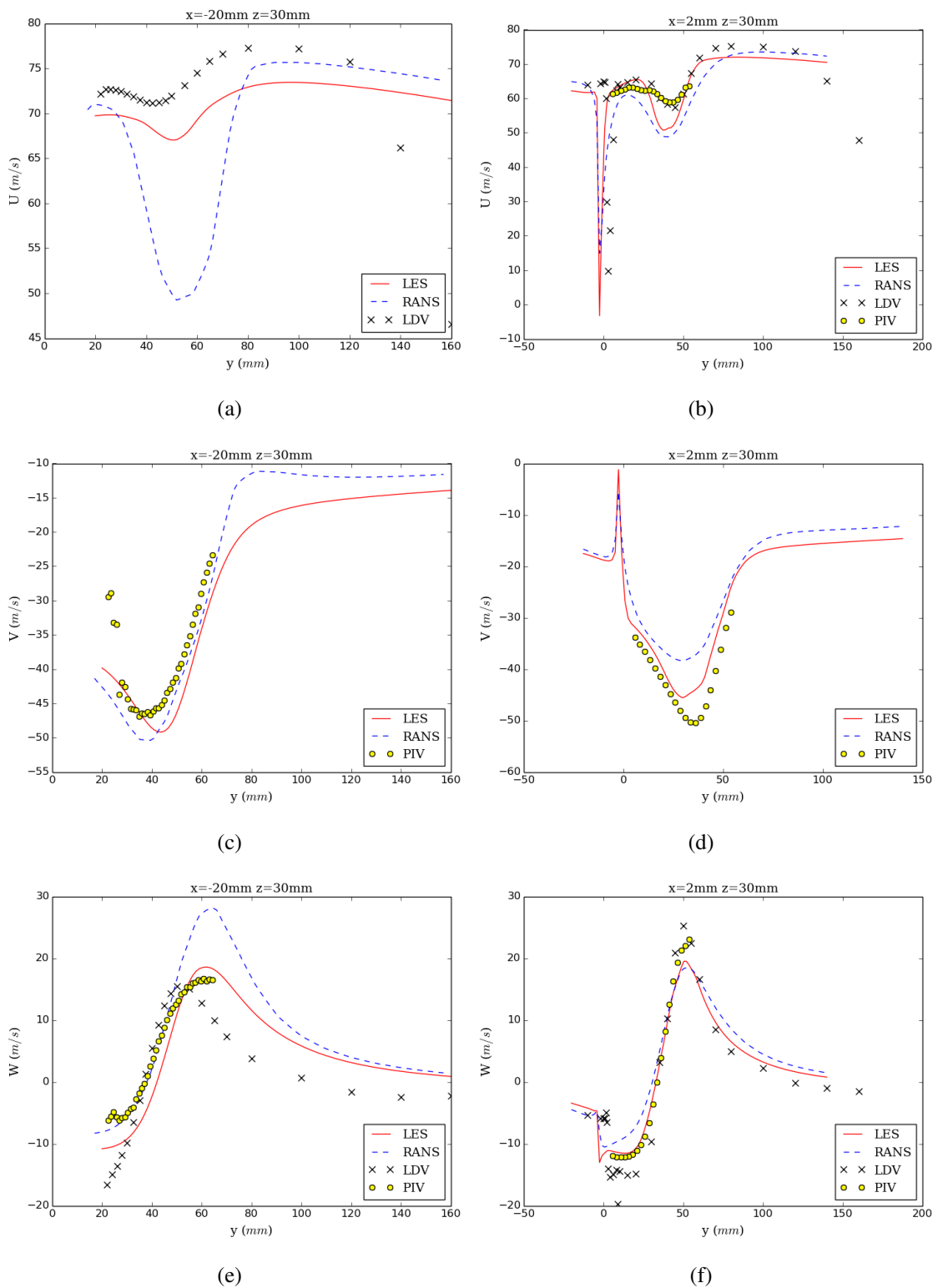


Fig. 4.23 Velocity profile comparison, $z = 30\text{mm}$.
 (a)(c)(e) $x = -20\text{mm}$ (b)(d)(f) $x = 2\text{mm}$

4.4 Conclusions

In this chapter, firstly, we have carefully validated the inflow conditions of the ZLES and the RANS simulations with the experiment. Secondly, the post-processing strategy has been introduced, in order to minimize the effect of the AOA difference between the experiment and the numerical simulations. Finally, the time-averaged ZLES results and the RANS results have been compared with the experimental ones. Analyses have been carried out during the comparisons. The main conclusions of this chapter are drawn below:

1. The velocity profiles within the incoming boundary layer are properly simulated by the ZLES, but the thickening of the incoming boundary layer is over-estimated by the RANS computation. Considering that the boundary layer thickness is almost the same as the clearance height, it will certainly influence the tip-leakage flow.
2. The ZLES globally under-estimates the turbulent fluctuations and their diffusion within the incoming boundary layer, especially close to the leading edge. On the contrary, the over-estimate of the diffusion by the RANS computation is closely related with its over-estimate of the boundary layer thickening.
3. Both the ZLES and the RANS simulations yield satisfactory predictions of the pressure distribution at mid-span. The blade loading is only slightly over-estimated. In the blade-tip region, the blade loading is globally reduced, because of the tip clearance. A low-pressure hump can be observed on the suction side in the experiment and the ZLES, associated with the tip-leakage flow. Overall, a fairly good agreement is achieved between the experiment and the simulations.
4. Vortex detection functions Γ_1 and Γ_2 have been implemented for the characterization of the vortex centers and core sizes. A sensitivity test has shown that the size of the integration domain has little effect on the predicted vortex characteristics in the current case.
5. A multi-vortex system can be observed from the experiment and the simulations. This system consists of one large tip-leakage vortex, one small tip-separation vortex and one or several small induced vortices.
6. For the tip-leakage vortex, the ZLES simulation yields good predictions for both the position and the size, while the RANS computation over-estimates its size. The induced vortices are well captured by the experiment and the ZLES, though the main induced vortex in the ZLES results is distorted and obviously less intense. The induced vortices totally vanish in the RANS results.

7. A very good agreement is achieved for the TLV trajectory between the experiment and the simulations. The trajectory is found not aligned with the inflow direction, but slightly inclined towards the blade-side.
8. Considering the topology of the flow field, there is a fairly good agreement between the experiment and the ZLES. The RANS computation is more diffusive and underestimates the intensity of the tip-leakage vortex.
9. 3C-PIV was shown to yield a description of the velocity component U , normal to the measurement plane, in good agreement with LDV.

Chapter 5

Turbulent characteristics of the tip-leakage flow

In this chapter, an instantaneous tip-leakage vortex visualization will be firstly given. Then, the turbulent characteristics of the tip-leakage flow and the relevant flow features will be investigated and discussed using the experimental and numerical results, including the Reynolds stresses, the spectral contents, the space-time correlations and the tip-leakage vortex wandering. Finally, the URANS computations are employed to investigate the oscillation of the tip-leakage vortex.

5.1 Instantaneous tip-leakage vortex visualization

Fig.5.1 shows an instantaneous view of the tip-leakage flow after the convergence of the ZLES. In this figure, the iso-surface of Q-criterion is coloured by the velocity magnitude. The tip-leakage vortex is clearly visible. It starts just a little downstream of the blade leading edge and grows rapidly.

Fig.5.2 shows a few consecutive snapshots of TR PIV measurements at $x = 2\text{mm}$. They are obtained at a 3kHz sampling frequency. The background is coloured by the normalized circumferential velocity magnitude $\sqrt{V^2 + W^2}/U_0$ in the plane, and the arrows represent the 2D instantaneous velocity vectors. The flow field in the dark area is not available because of laser reflections. The vortex rotation can be observed when comparing these successive snapshots. The fluctuations are strong and change rapidly in the tip-leakage vortex region. The instantaneous velocity magnitude reaches about $1.5U_0$, which is consistent with the findings of Jacob *et al.* [59]. Besides, the vortex centre is located in the region of the deep blue spot (vanishing velocity) that is visible inside the tip-leakage vortex. The position of

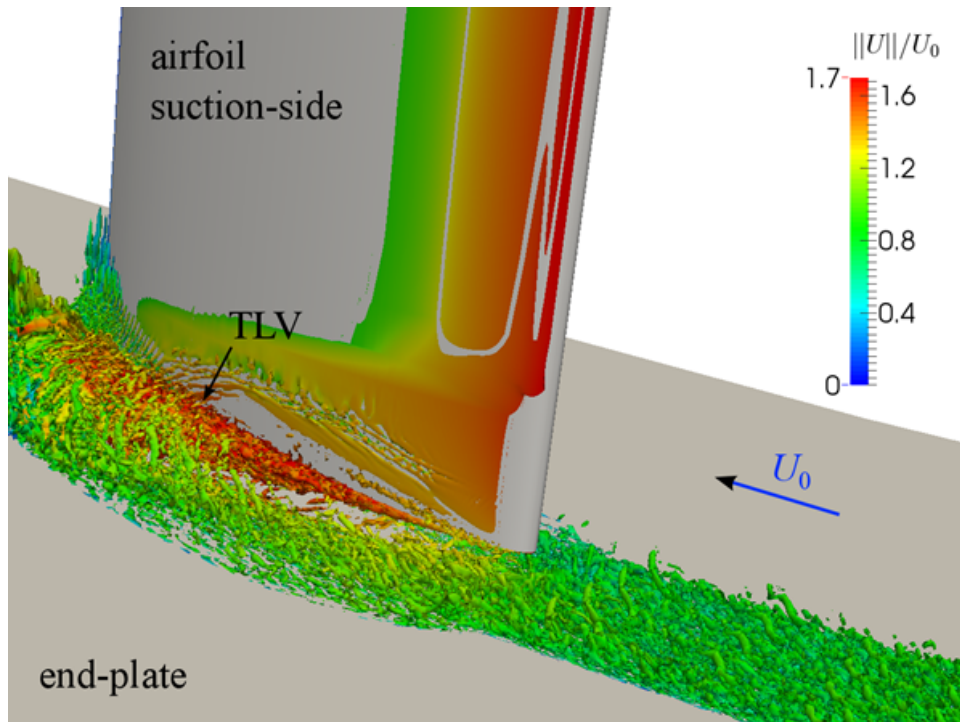


Fig. 5.1 3D instantaneous view of the ZLES simulation. Iso-surface of Q-criterion, colored by the velocity magnitude.

vortex center is not fixed. It undergoes a small-amplitude oscillatory motion, which will be hereafter referred to as “vortex wandering” and will be investigated in details in section 5.5.

5.2 Reynolds stresses

Reynolds stresses are compared at $x = -20$ mm and $x = 2$ mm between the experiment and the ZLES. At $x = -20$ mm, only the components $v'v'$, $w'w'$ and $v'w'$ are available in the experiment, because the velocity component u and its fluctuation u' are not measured at this position. At $x = 2$ mm, the velocity component u and its fluctuation u' are measured by 2D-3C TR PIV with a smaller measurement window.

Firstly, we look at the normal stress components. In order to have a direct comparison of their levels, all these normal stress components are plotted with the same scale. As shown in Fig.5.3 for $x = -20$ mm and Fig.5.5 for $x = 2$ mm, a good agreement is achieved between the ZLES and the experiment. There are globally two regions of high turbulent intensity. One is the tip-leakage vortex center ($40 \text{ mm} \leq y \leq 45 \text{ mm}$, $5 \text{ mm} \leq z \leq 15 \text{ mm}$), and a particularly high level is reached for the vertical fluctuations $w'w'$ in the experiment at the vortex center, but not in the simulation. This might be an experimental artefact due to the lack of particles

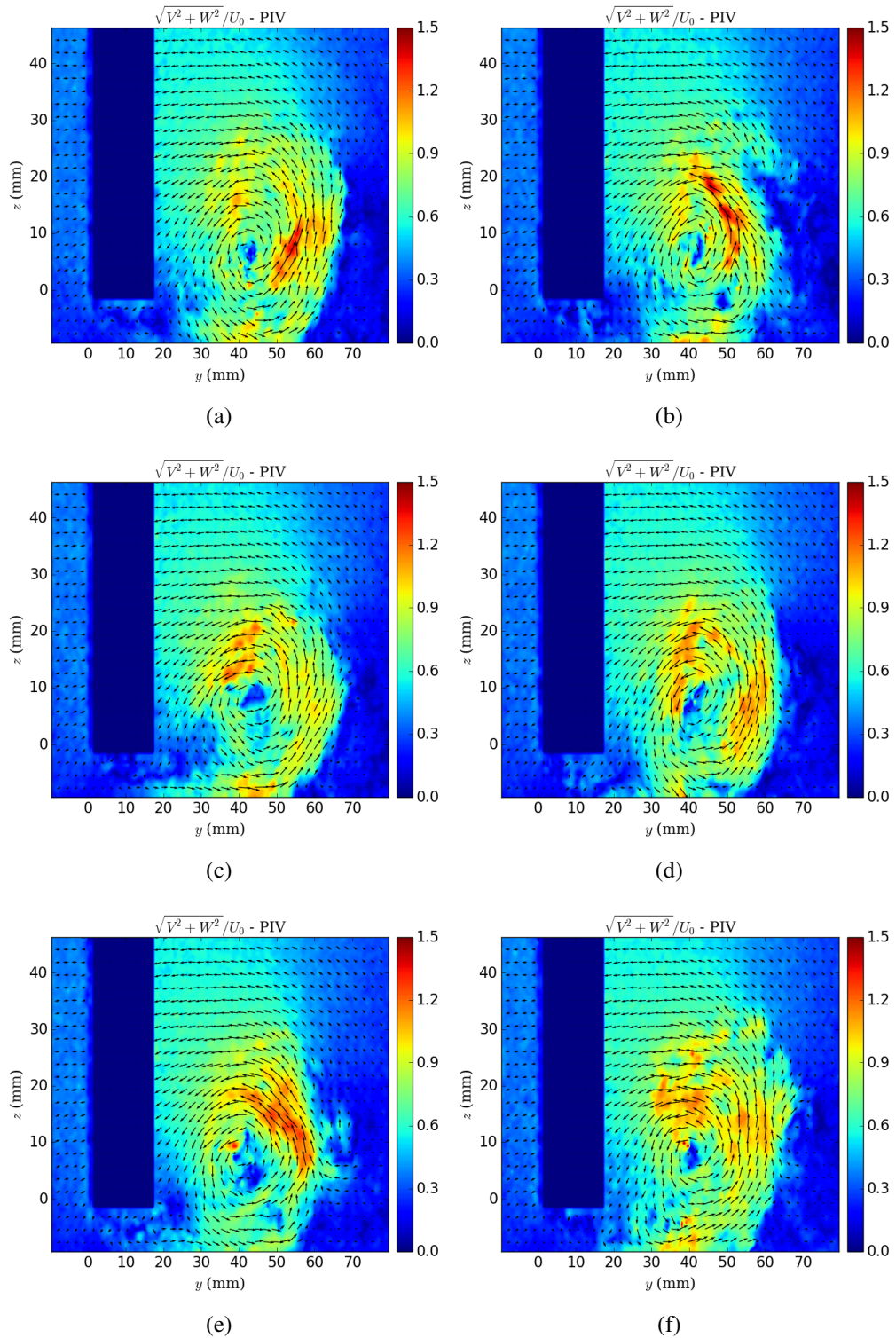


Fig. 5.2 PIV instantaneous flow fields at $x = 2\text{mm}$.

The background is coloured by the normalized circumferential velocity magnitude $\sqrt{V^2 + W^2}/U_0$ in the plane. The arrows represent the 2D instantaneous velocity vectors. From left to right and from top to bottom: $t, t + \Delta t, t + 2\Delta t, t + 3\Delta t, t + 4\Delta t, t + 5\Delta t$, with $\Delta t = 0.33\text{ms}$.

in the vortex centre and the vanishing mean velocity. Another region is the tip leakage jet ($10 \text{ mm} \leq y \leq 40 \text{ mm}$, $z \leq 0 \text{ mm}$), where the mean shear is intense. Besides these two regions, a relatively high level is also reached for $v'v'$ in the simulation at the place where the end-plate boundary layer is dragged up by the tip-leakage vortex and form the induced vortex. This region is also visible in the experiment, but the intensity is lower (about 3 times). At the right-hand side of the tip-leakage vortex, the turbulent intensity is over-estimated by the simulation. The patterns of the normal stress components at $x = 2 \text{ mm}$ (Fig.5.5) are similar to those observed at $x = -20 \text{ mm}$ (Fig.5.3), but the levels are smaller, since the plane is located downstream of the airfoil where the TLV is not fed anymore by the tip clearance flow.

As for the shear stress components, they are also plotted with the same scale. As shown in Fig.5.4 for $x = -20 \text{ mm}$ and Fig.5.6 for $x = 2 \text{ mm}$, the shear stresses are not negligible compared to the normal stresses. This demonstrates the anisotropy of the flow. The highest levels are found in the tip leakage jet and on the right-hand side of the TLV. The anisotropy on the right-hand side of the TLV is remarkable, especially for the ZLES, because it is probably reinforced by the dragging of the end-plate boundary layer. Globally, a good agreement is observed between the experiment and the ZLES. The ZLES is found to predict a little higher level of anisotropy on the right-hand side of the TLV.

5.3 Near-field energy spectrum

The wall pressure spectra are compared at three probe locations around $77.5\%c$ between the ZLES and the experiment. As shown in Fig.5.7 (a), the probe B is located on the blade tip. The probe 21 is located on the suction side, 1.5 mm above the suction edge. The probe 46 is located on the pressure side, 1.5 mm above the tip edge. At probe B, as shown in Fig.5.7 (b), we can say that the shape of the spectrum is well captured by the ZLES, considering the central frequency of the hump and the spectrum slope in the higher frequency range. The energy level is slightly over-estimated. At probe 21, as shown in Fig.5.7 (c), the shape of the spectrum is also captured, but the energy level is over-estimated by 5dB. Especially in the higher frequency range, the discrepancy increases up to 15 dB as the experimental spectrum decays more rapidly than the numerical one. This seems to indicate that the interaction between the airfoil boundary layer and the TLV is different in the simulation. Indeed, it was found by Grilliat [50] that most of the TLV is fed by the gap between $x = c/4$ and $x = 3c/4$, whereas in Fig.5.1 the TLV forms along the whole airfoil suction side edge. At probe 46, there is a remarkable agreement between the experiment and the simulation. In all pressure spectra, the medium frequency hump (0.7 - 3 kHz) that is typical for the tip leakage flow (as already reported by Jacob *et al.* [59]), is well simulated by the computation. When

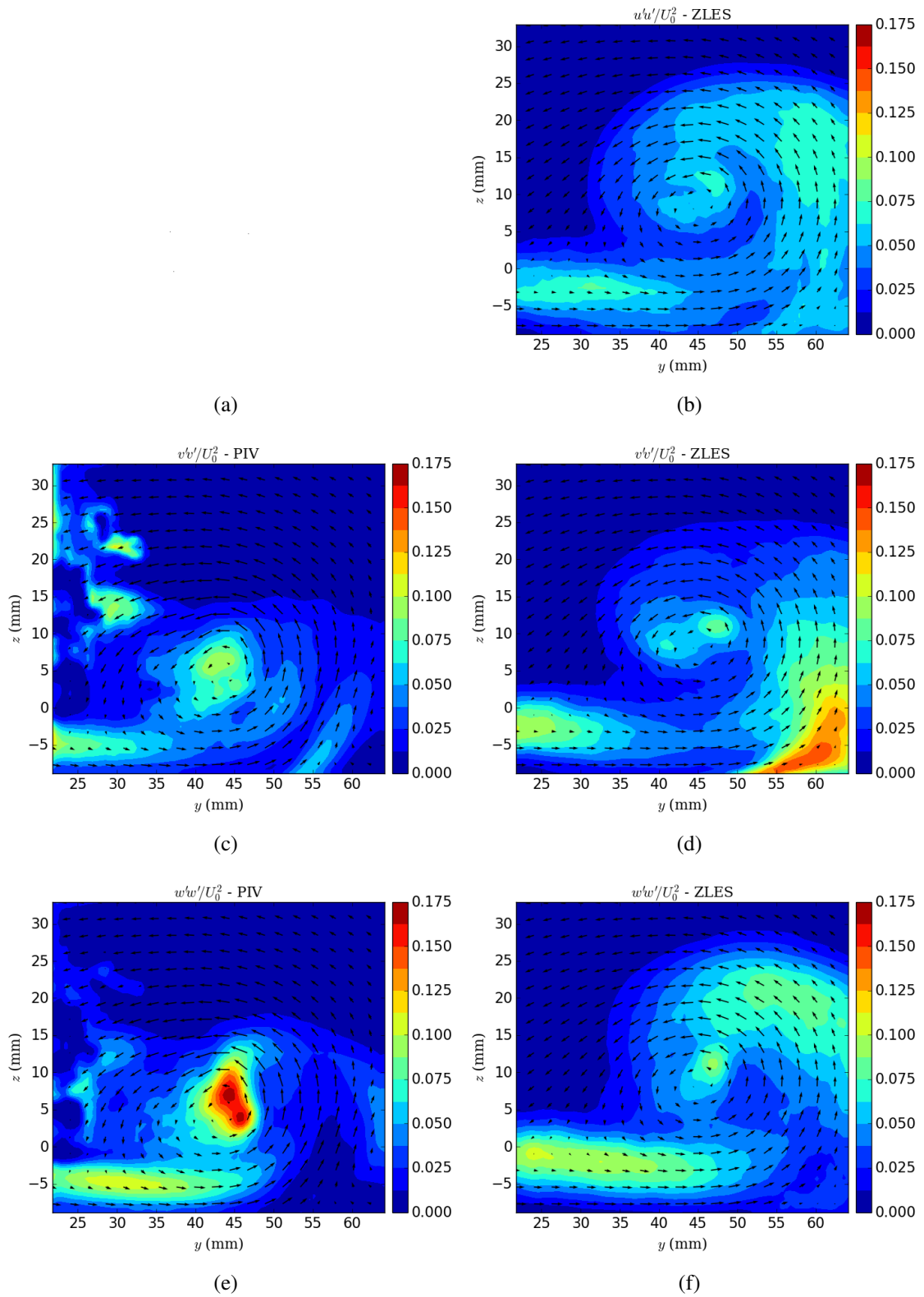


Fig. 5.3 Normalized normal Reynolds stresses at $x = -20$ mm.
 The arrows represent the 2D mean velocity vectors.
 Left: PIV, right: ZLES, top to bottom: $u'u'/U_0^2$, $v'v'/U_0^2$, $w'w'/U_0^2$

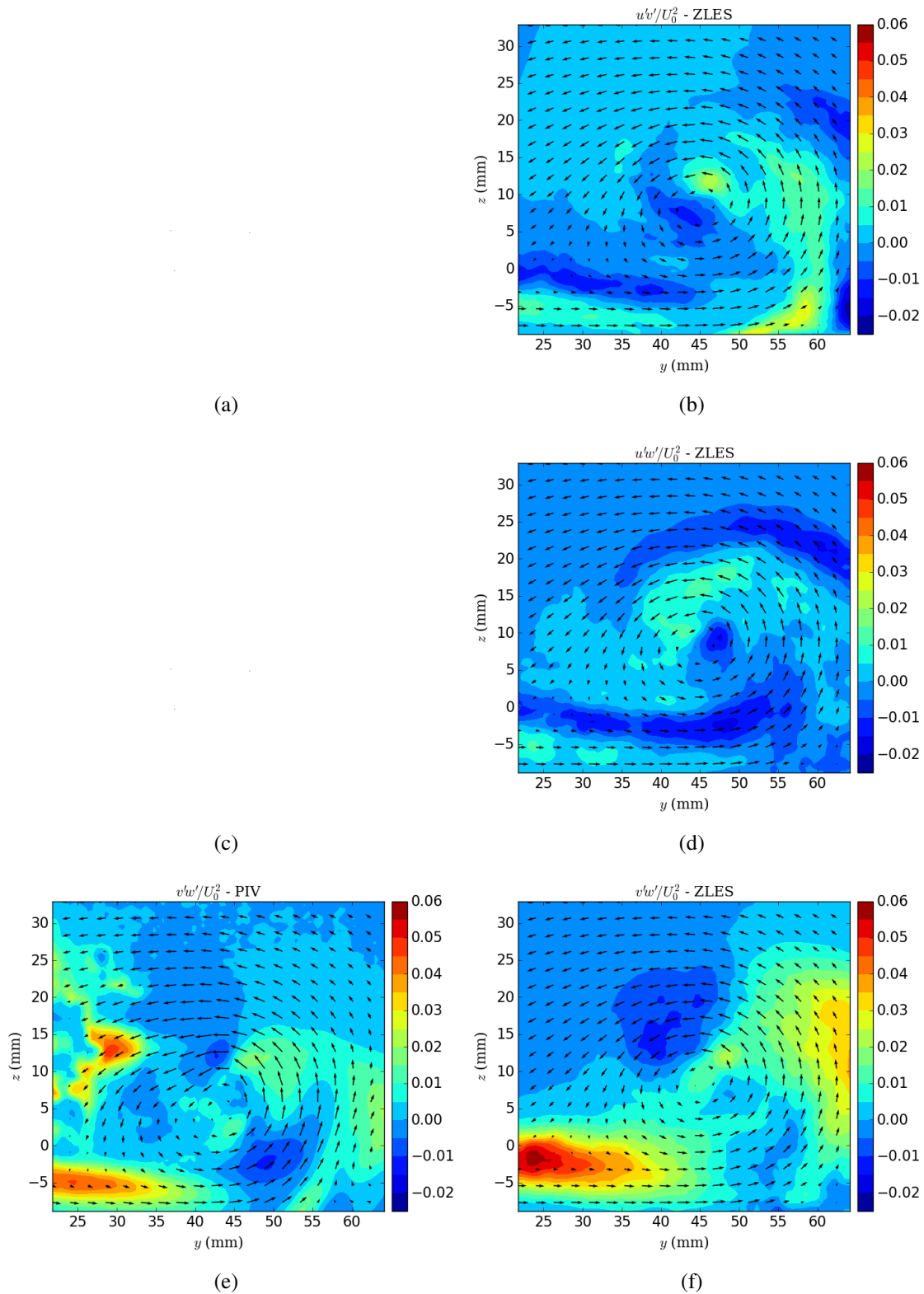


Fig. 5.4 Normalized shear Reynolds stresses at $x = -20$ mm.

The arrows represent the 2D mean velocity vectors.

Left: PIV, right: ZLES, top to bottom: $u'v'/U_0^2$, $u'w'/U_0^2$, $v'w'/U_0^2$

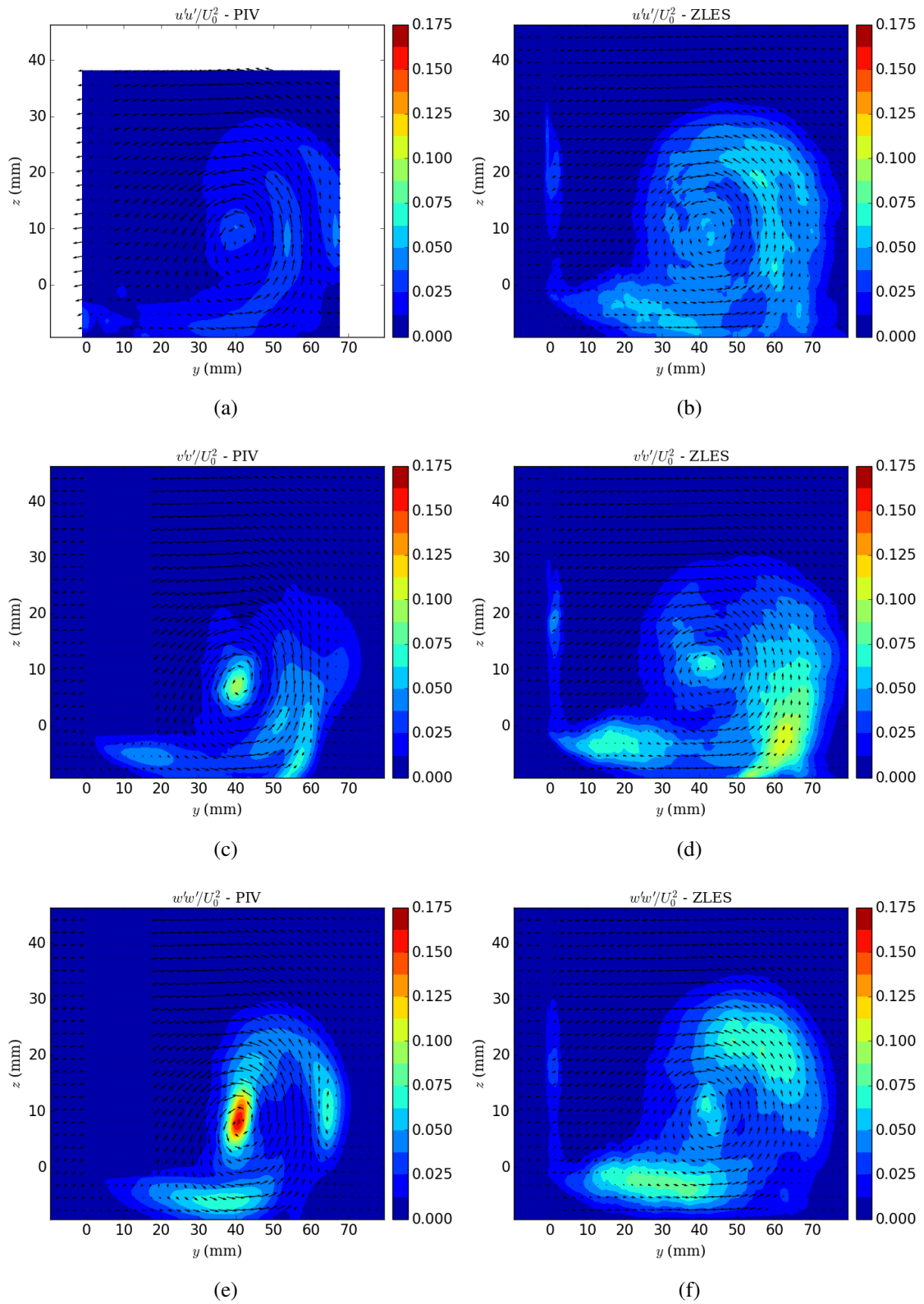


Fig. 5.5 Normalized normal Reynolds stresses at $x = 2$ mm.
 The arrows represent the 2D mean velocity vectors.
 Left: PIV, right: ZLES, top to bottom: $u'u'/U_0^2$, $v'v'/U_0^2$, $w'w'/U_0^2$

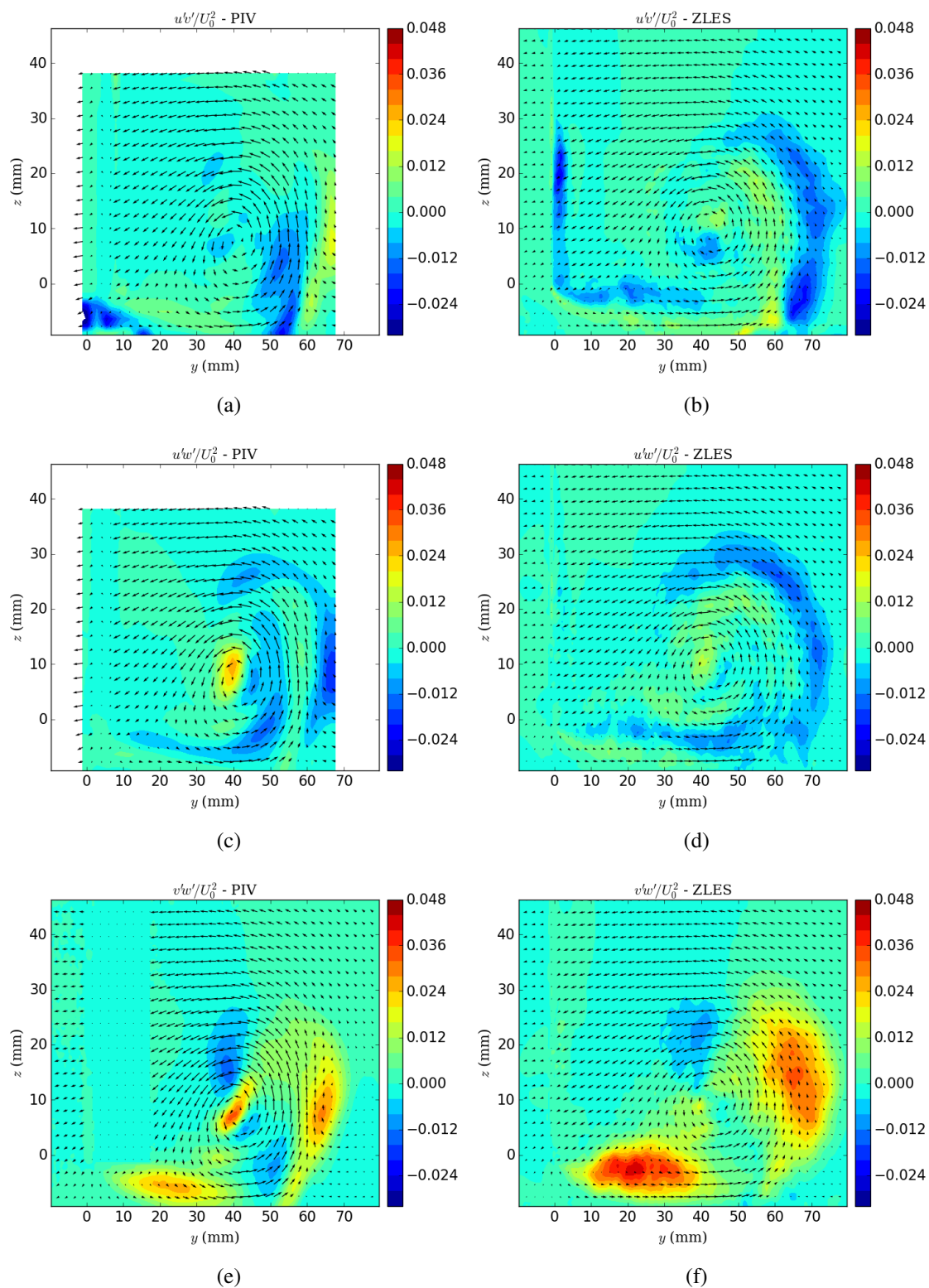


Fig. 5.6 Normalized shear Reynolds stresses at $x = 2$ mm.

The arrows represent the 2D mean velocity vectors.

Left: PIV, right: ZLES, top to bottom: $u'v'/U_0^2$, $u'w'/U_0^2$, $v'w'/U_0^2$

this frequency is normalized by the free-stream velocity U_0 and the clearance height h , we obtain a Strouhal number $St = f \cdot h / U_0 = 0.18$. Although this value is close to that obtained for the vortex shedding behind a circular cylinder of diameter h , the physical mechanism must be different, as the shedding can only be one-sided in the present case. Nevertheless, this strongly suggests that there is a vortex cross-stream shedding along the suction side edge where the tip leakage flow is expelled from the gap in a jet-like manner, as modelled by Dunne and Howe [35] in their simplified tip-leakage noise model. Globally, a good agreement is achieved between the experiment and the simulation over the experimental frequency range [0, 10kHz]. Higher frequencies are only available from ZLES.

In the previous section, we found that high velocity fluctuations appear around the tip-leakage vortex and in the tip-leakage jet. Here we choose two velocity probes (106 and 102) close to the two regions, respectively, to investigate their spectral contents. The positions of the two probes are indicated in Fig.5.7 (a). The probe 106 is located at the edge of the tip-leakage vortex, 5 mm above the lower end-plate. LDV measurements data are available at this point for comparison. As shown in Fig.5.7 (d), the experimental data describe the spectral content in the low-frequency range, while ZLES offers the description up to much higher frequencies. In the intermediate range [2kHz, 4kHz], a good agreement is achieved. The energy level and the slope of the spectrum are well captured by the ZLES. Besides, the numerical spectrum is found to damp below 2kHz and deviate from the experimental spectrum, which may be caused by the limited time duration (poor convergence at low frequencies) and to the limited spatial extent of the LES zone (the very large eddies are not described by the simulation). The probe 102 is located 5 mm above the lower end-plate and inside the tip-leakage jet. The energy level at this point is found to be lower than at probe 106, which is consistent with the observations on the normal Reynolds stress component $w'w'$ shown in Fig.5.5 (f): near the trailing edge, the tip-leakage jet is weakened, while the TLV is sustained. The shape of the spectrum at the probe 102 is a little similar to that of probe 106, but decays less rapidly at high frequencies.

More spectral information in the tip-leakage vortex region are offered by LDV and PIV measurements at $x = 2\text{mm}$. The location of the measurement points, as well as iso-contours of the spanwise velocity, are plotted in Fig.5.8. LDV spectra are plotted with solid lines in Fig.5.9, and PIV spectra with dashed lines. Most of the spectra are dominated by a broad peak around 50Hz and its level increases as the measurement point approaches the vortex core. This broad peak may be associated with the vortex wandering. Another possible explanation would be a more global resonance of the flow, but this latter scenario is discarded by the fact that the 50 Hz peak is not observed on all velocity spectra. PIV spectra and LDV spectra have almost the same shape and energy level in the low frequency range (up to 0.5kHz), but

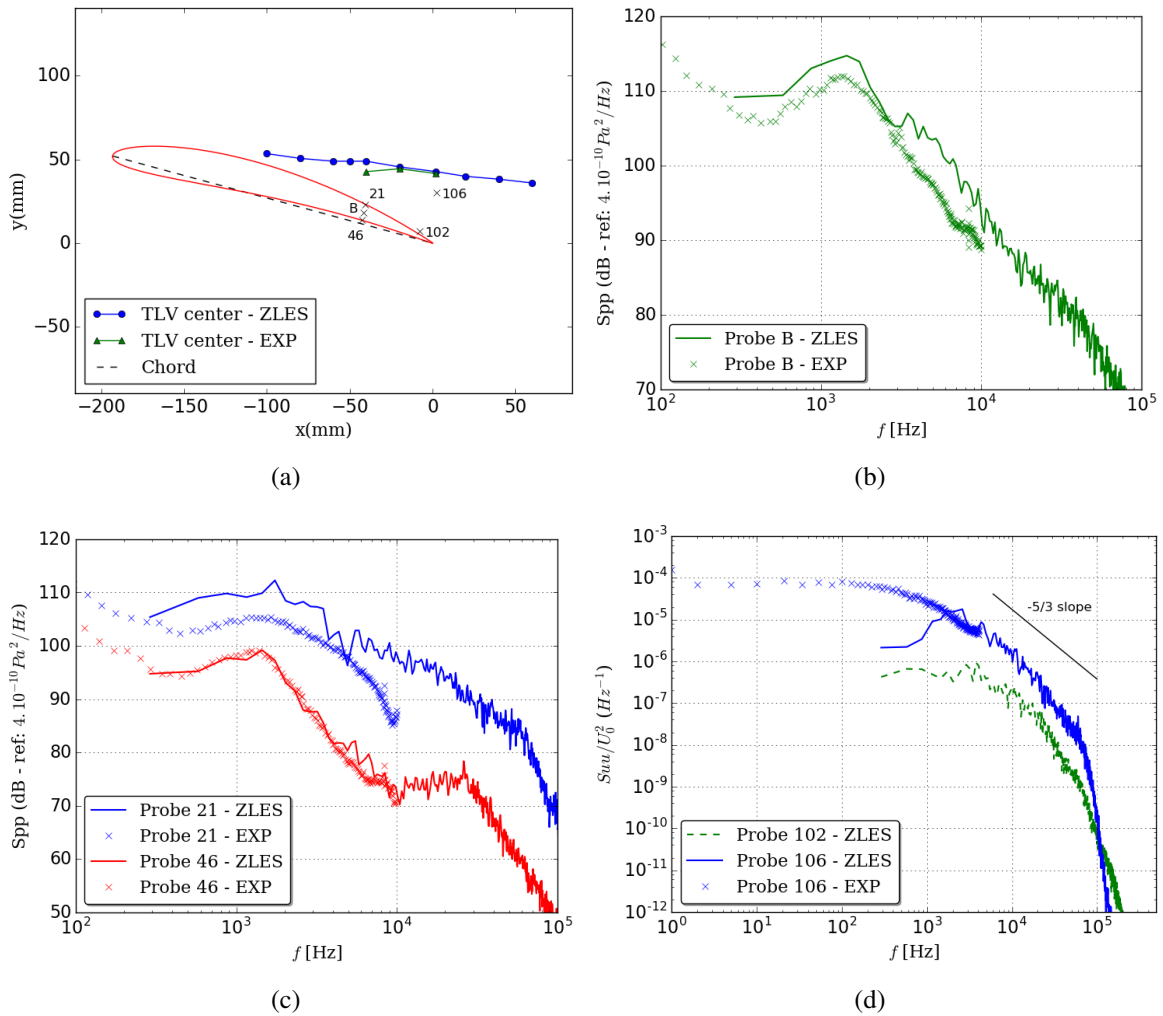


Fig. 5.7 Probe locations and corresponding pressure (B, 21, 46) and velocity (102, 106) power spectral densities.

PIV spectra do not decay at higher frequencies. Aliasing can only partly account for this discrepancy since the trend remains if the sampling frequency is doubled (see Figs. 5.9 (a) and (b), obtained for 3kHz and 7 kHz, respectively). Besides, this may also be explained by the fact that, in the current case the high-speed smoke particles cross the PIV plane in a very short time and the rapid low-amplitude flow changes are difficult to capture using PIV. Thus, TR PIV appears to be useful for the characterisation of the largest eddies, whereas the smaller high-frequency eddies remain under-resolved.

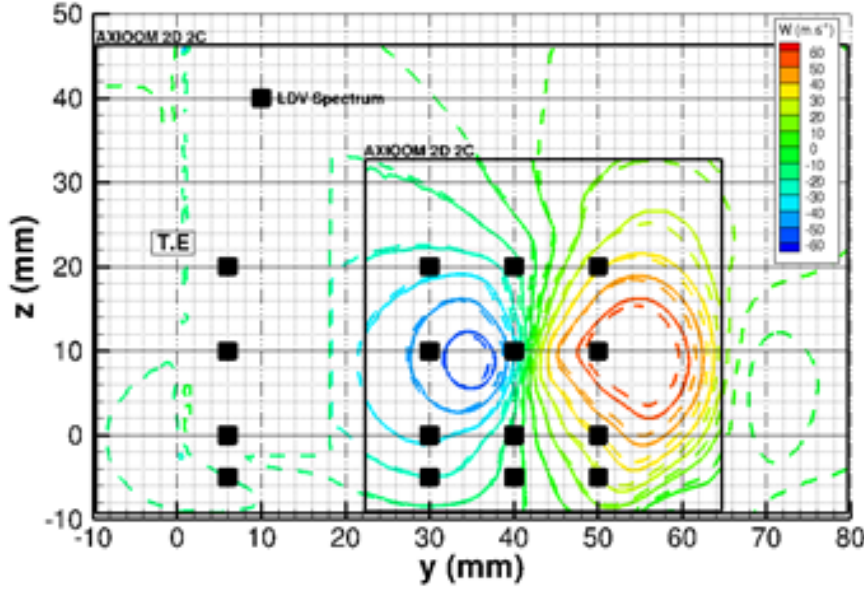


Fig. 5.8 Locations of the LDV measurement points at $x = 2$ mm.

5.4 Space-time correlations

The space-time correlations measure the scales of the turbulent structures, regardless of the surrounding surfaces. In the current study, the space-time correlations are calculated for a few correlation points at several correlation times, using 2D-3C TR PIV database AXIOOM-10 and the ZLES results.

5.4.1 Space-time correlations in the experiment

In the experiment, the sampling frequency of AXIOOM-10 is 7 kHz, corresponding to $\Delta t_{PIV} = 0.143$ ms.

The statistical error of the space-time correlations is firstly investigated. According to Bendat *et al.* [12, 13], the normalized random error of the space-time correlations can be estimated by:

$$\varepsilon [\hat{R}_{xy}(\tau)] = \left[\frac{1 + \rho_{xy}^{-2}(\tau)}{2BT} \right]^{1/2} \quad (5.1)$$

where

$$\rho_{xy}(\tau) = \frac{R_{xy}(\tau)}{[R_{xy}(0)R_{xy}(0)]^{1/2}} \quad (5.2)$$

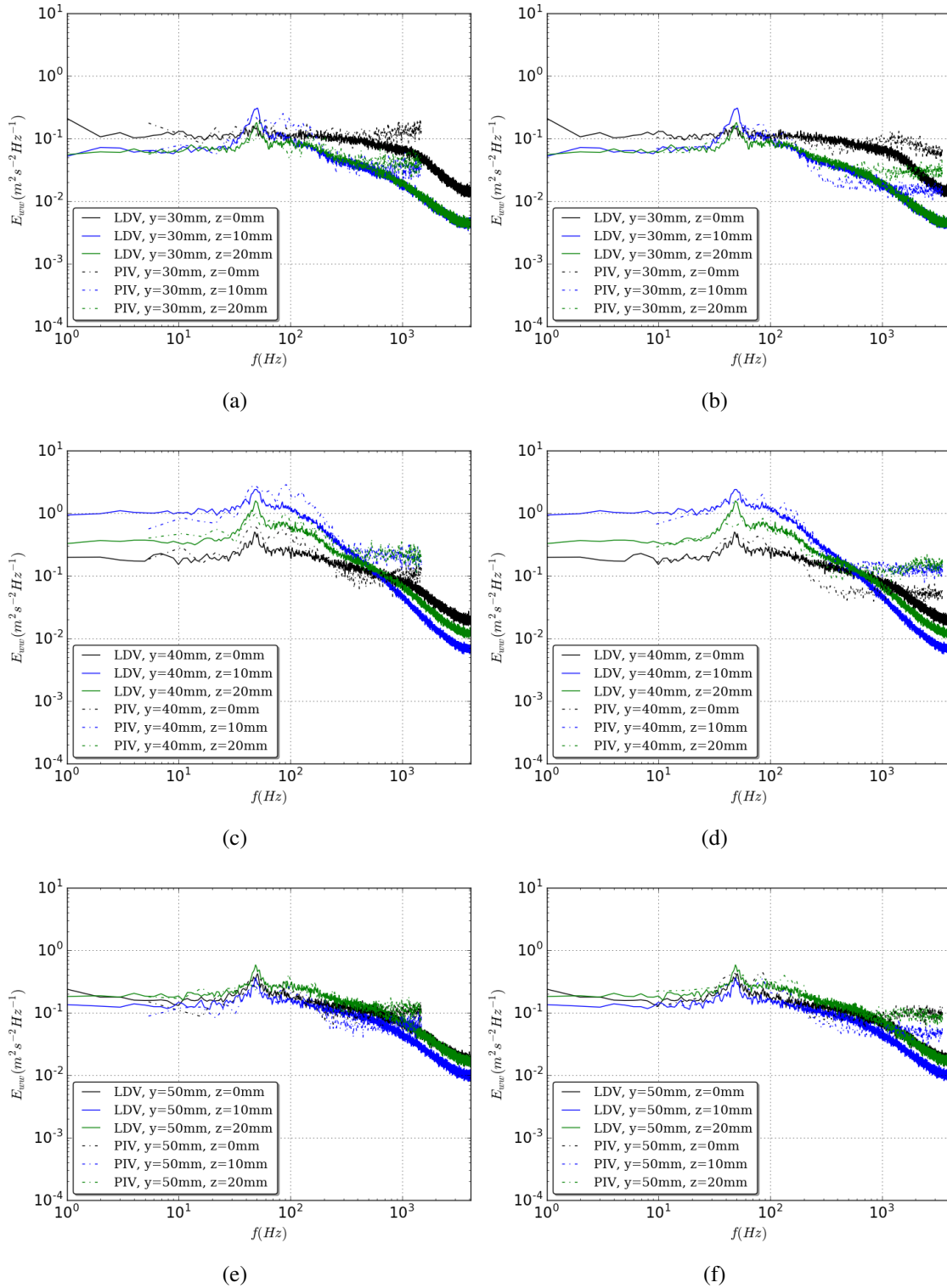


Fig. 5.9 Velocity spectra obtained from LDV (solid line) and 2D-2C PIV measurements (dashed line) at $x=2mm$.

Left: PIV AXIOM-2, 3000Hz, right: PIV AXIOM-3, 7000Hz

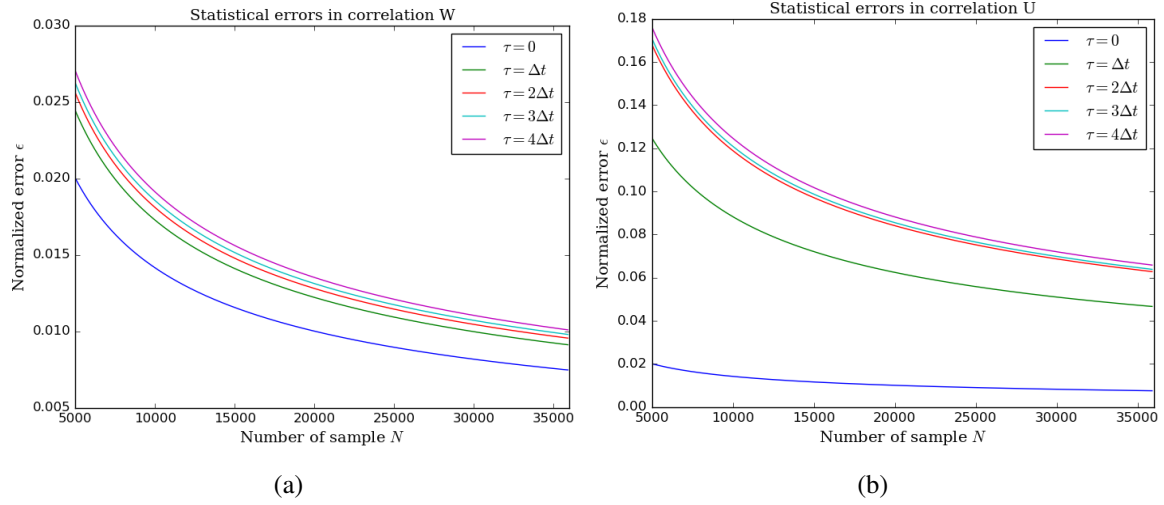


Fig. 5.10 Statistical error for the space-time velocity correlations at the vortex center.
(a) R_{ww} (b) R_{uu}

and $BT = N/2$. N is the number of samples, and for AXIOOM-10, $N = 36000$.

The statistical errors of the spanwise- and streamwise-velocity correlations are shown in Fig.5.10. For the spanwise-velocity correlations, the statistical error is about 1.5% or less up to $4\Delta t_{PIV}$, and remains far below 2% or 3% during the acquisition time. The statistical error of the streamwise-velocity correlations is found to be much higher than that of the spanwise-velocity correlations, but lies below 7% for $N = 36000$. For both components, the statistical error increases with the correlation time. The correlation uncertainty is thus essentially governed by the velocity estimates using the PIV technique.

Figs.5.11 and 5.12 show respectively the time evolution of the spanwise- and streamwise-velocity correlations for a point located at the vortex center marked with a cross. Given the correlation uncertainty discussed above, the contours of correlation levels ± 0.1 are also plotted on the correlation maps, indicating that the correlation values between -0.1 and 0.1 are not necessarily meaningful. A strong correlation can be observed for both the spanwise- and streamwise- velocity fluctuations at $\tau = 0$. However, the streamwise-velocity correlation decays much faster than the spanwise-velocity correlation. This phenomenon can be partly explained by the strong cross-stream motion of the tip-leakage flow. As shown in section 4.3.3, the cross-stream velocity components V and W have almost the same magnitude as the streamwise velocity component U . This is also consistent with the wider extent of the spanwise-velocity correlations, which develops along z .

According to the visual observation during the experiment, the vortex centre appeared to be a region containing less smoke particles than the surrounding flow, due to centrifugal forces.

Consequently, the vortex centre may be a singular point regarding the PIV measurements, and a bias might occur. So the space-time correlations are also calculated for another point located 3.5 mm left of the vortex center. The spanwise- and streamwise-velocity correlation maps for this point are shown in Figs.5.13 and 5.14, respectively. Unlike the correlations for the vortex center, a similar decay is observed for both components, which is consistent with the fact that the three velocity fluctuation components have almost the same magnitude.

5.4.2 Space-time correlations in the ZLES

The ZLES results are sampled every 3000 time steps. The corresponding sampling frequency is 20.8kHz and $\Delta t_{ZLES} = 0.048 \text{ ms} \approx 1/3\Delta t_{PIV}$.

Figs.5.15 and 5.16 show respectively the time evolution of the spanwise- and streamwise-velocity correlations for a point located at the vortex center, marked with a cross. At $\tau = 0$, a strong correlation can be observed for both the spanwise- and streamwise- velocity fluctuations. Similarly to the experimental results shown in Figs.5.11 and 5.12, the strong-correlation zone for R_{ww} is stretched along the z direction, and it is circular for R_{uu} . The strong-correlation zone for R_{ww} in the ZLES is smaller than that in the experiment, which could indicate an under-estimation of the turbulent scales in the ZLES. The ZLES appears poorer in large-scale eddies, which could be due to the limited spatial extent of the LES zone, compared with the whole experimental set-up. Besides, the measurement errors around the vortex center due to the lack of smoke particles, as discussed in section 5.4.1, may also contribute to this difference. With the increase of τ , the spanwise- and streamwise- velocity correlations decay almost at the same rate in the ZLES. The temporal decay of the correlation in the ZLES is faster than that in the experiment, especially for R_{ww} , which may be explained by the high sensitivity of the correlation to the velocity fluctuations. In the other words, a small difference in the velocity fluctuations may lead to a large difference in the global behaviour of the space-time correlations.

The spanwise- and streamwise- velocity correlations for another point located 3.5 mm left of the vortex center are also calculated and shown in Fig.5.17 and 5.18. Unlike the experiment, there is little difference that can be observed for the two different correlation points in the ZLES. This observation could substantiate that there are possibly some measurement errors around the vortex center in the experiment.

The space-time correlation for the normal-velocity fluctuations R_{vv} is not shown here, since it has a very similar behaviour as R_{ww} .

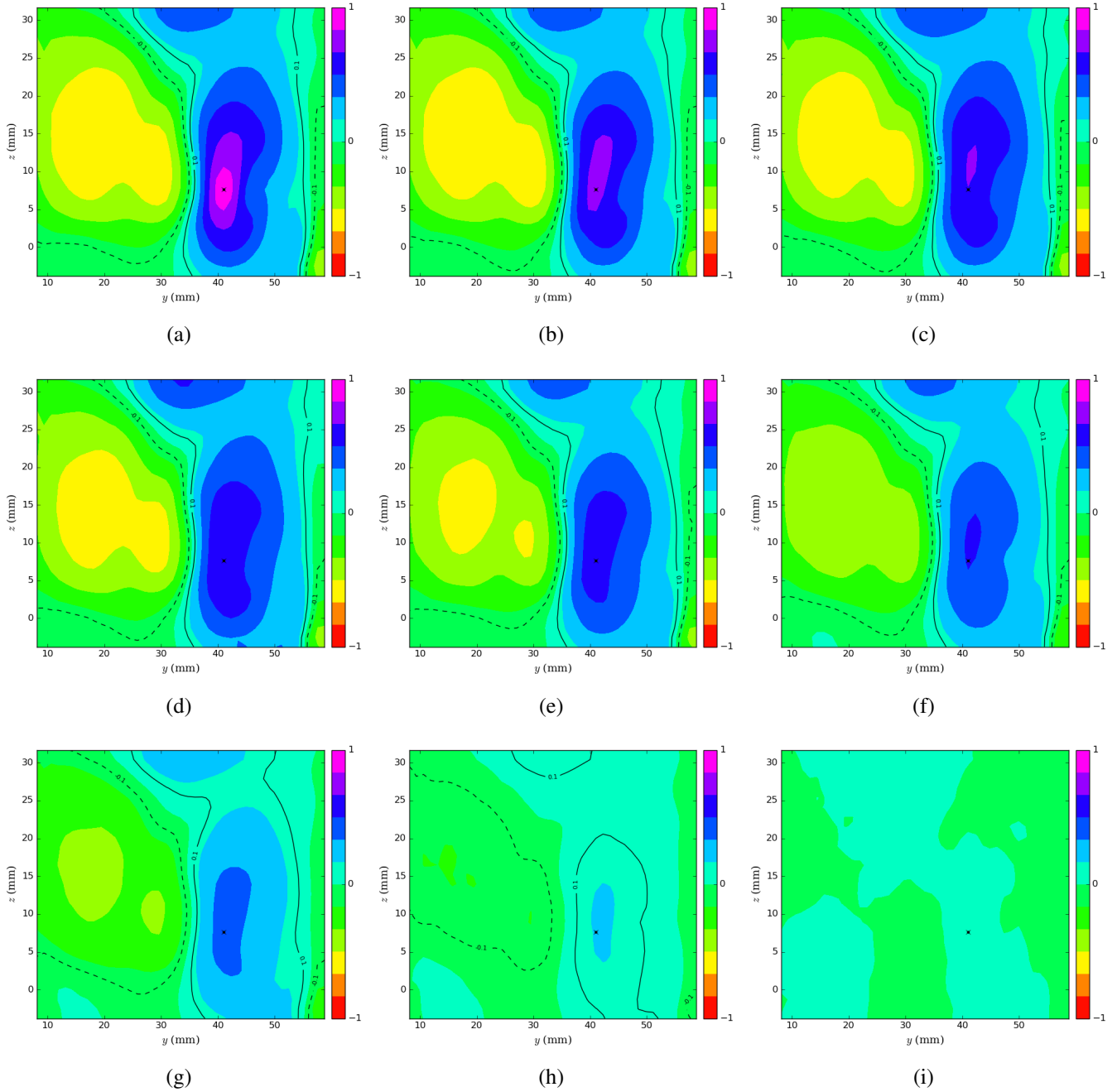


Fig. 5.11 Two-point two-time correlation map for the spanwise velocity fluctuations R_{ww} , for a point (\cdot) located at the vortex center (x). PIV AXIOOM-10.

From left to right and top to bottom: $\tau = 0, \Delta t_{PIV}, 2\Delta t_{PIV}, 3\Delta t_{PIV}, 5\Delta t_{PIV}, 7\Delta t_{PIV}, 10\Delta t_{PIV}, 15\Delta t_{PIV}, 20\Delta t_{PIV}$.

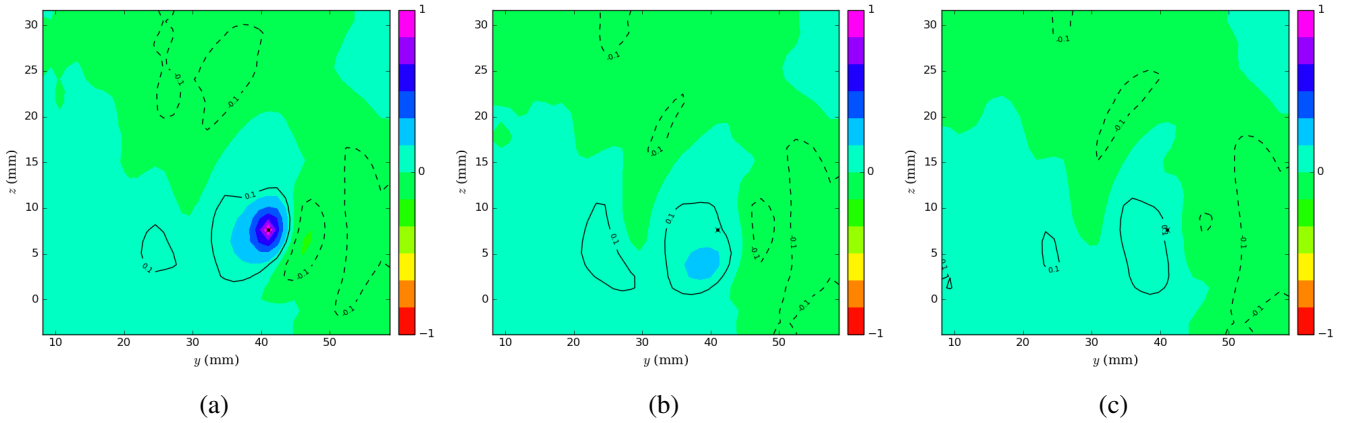


Fig. 5.12 Two-point two-time correlation map for the streamwise velocity fluctuations R_{uu} , for a point (\cdot) located at the vortex center (x). PIV AXIOOM-10.
From left to right: $\tau = 0, \Delta t_{PIV}, 2\Delta t_{PIV}$.

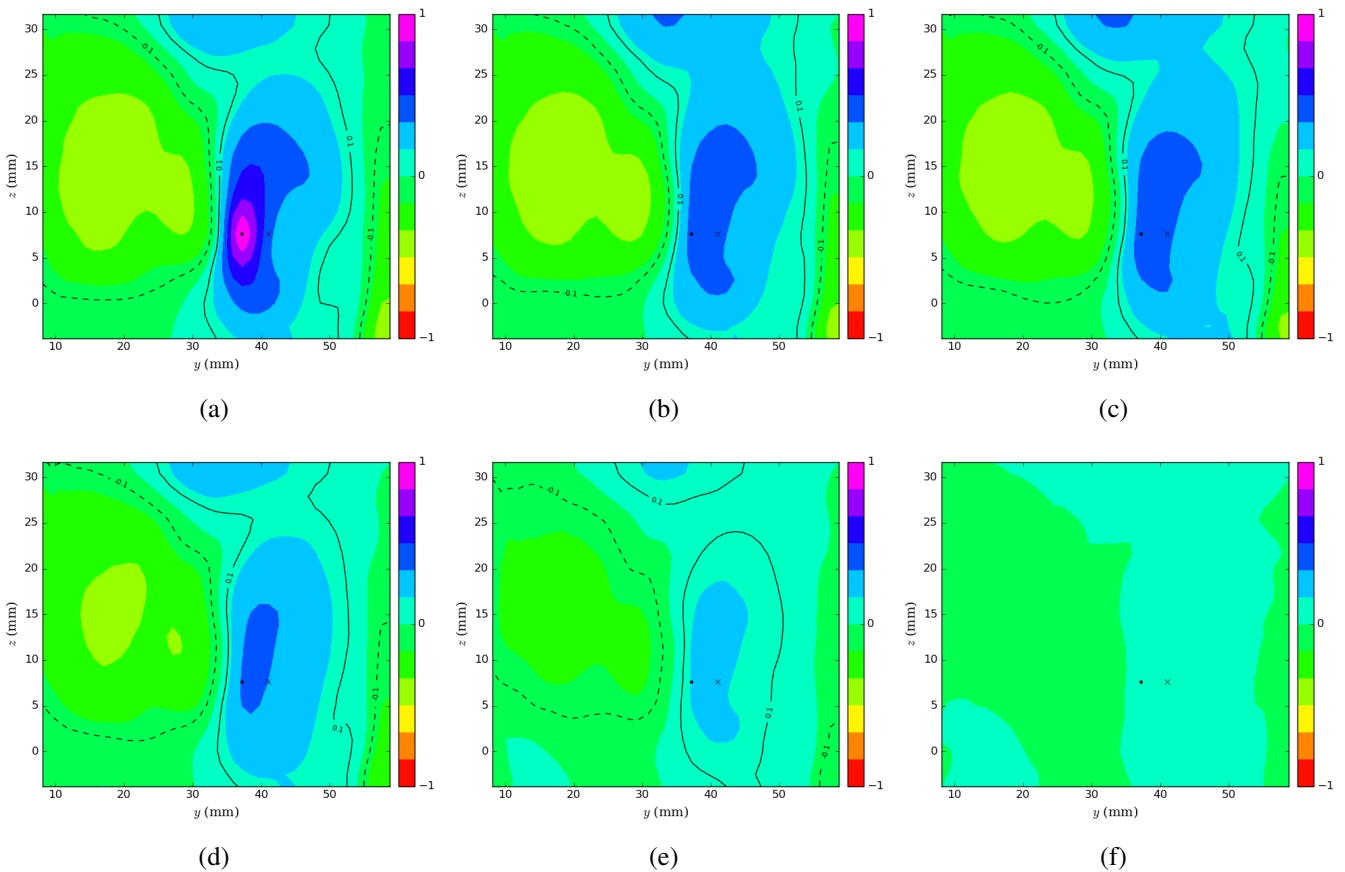


Fig. 5.13 Two-point two-time correlation map for the spanwise velocity fluctuations R_{ww} , for a point (\cdot) located 3.5 mm left of the vortex centre (x). PIV AXIOOM-10.
From left to right and top to bottom: $\tau = 0, \Delta t_{PIV}, 2\Delta t_{PIV}, 5\Delta t_{PIV}, 10\Delta t_{PIV}, 15\Delta t_{PIV}$.

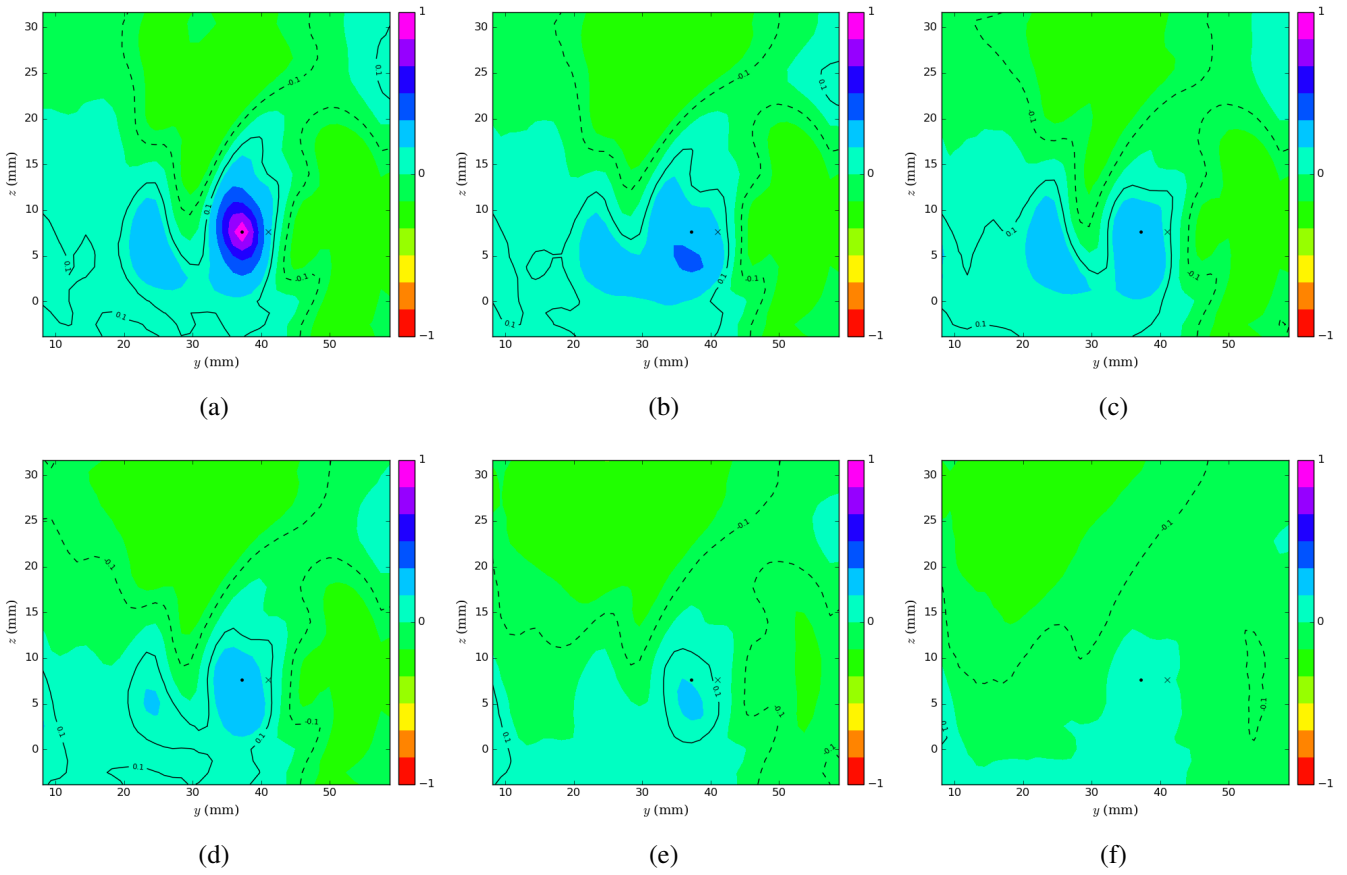


Fig. 5.14 Two-point two-time correlation map for the streamwise velocity fluctuations R_{uu} , for a point (·) located 3.5 mm left of the vortex centre (x). PIV AXIOOM-10. From left to right and top to bottom: $\tau = 0, \Delta t_{PIV}, 2\Delta t_{PIV}, 5\Delta t_{PIV}, 10\Delta t_{PIV}, 15\Delta t_{PIV}$.

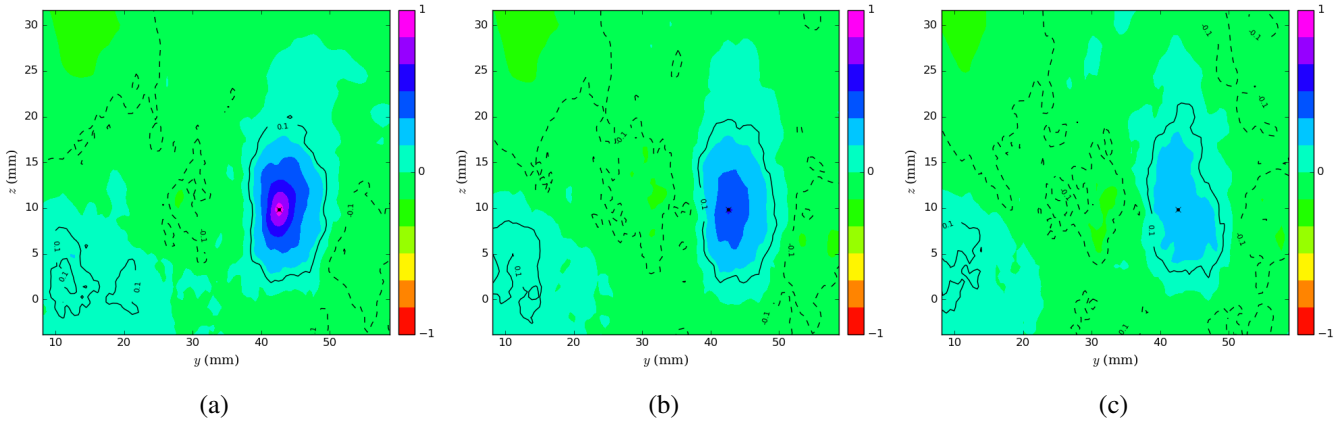


Fig. 5.15 Two-point two-time correlation map for the spanwise velocity fluctuations R_{ww} , for a point (\cdot) located at the vortex center (x). ZLES results. From left to right and top to bottom: $\tau = 0, \Delta t_{ZLES}, 2\Delta t_{ZLES}$.

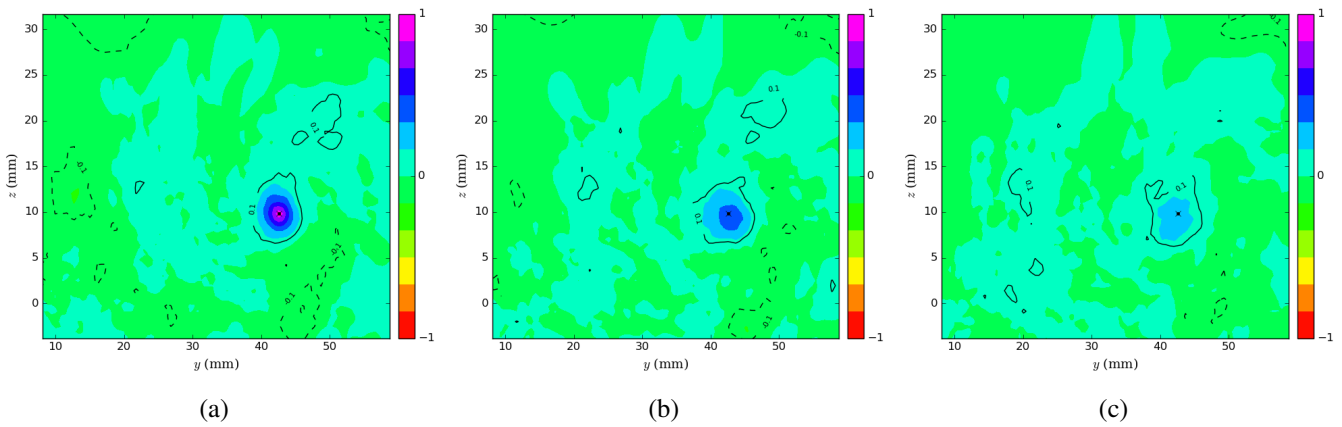


Fig. 5.16 Two-point two-time correlation map for the streamwise velocity fluctuations R_{uu} , for a point (\cdot) located at the vortex center (x). ZLES results. From left to right and top to bottom: $\tau = 0, \Delta t_{ZLES}, 2\Delta t_{ZLES}$.

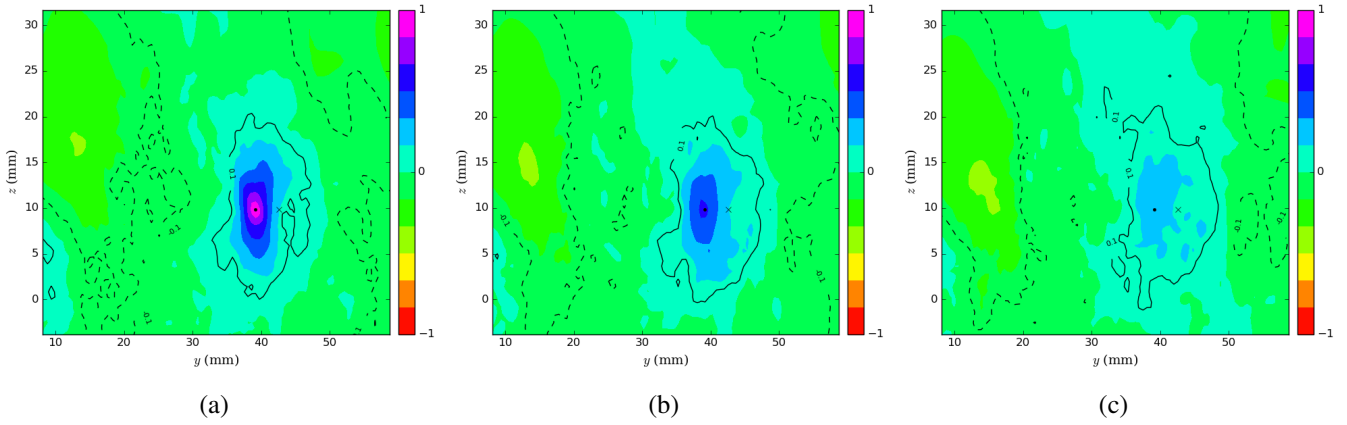


Fig. 5.17 Two-point two-time correlation map for the spanwise velocity fluctuations R_{ww} , for a point (\cdot) located 3.5 mm left of the vortex centre (x). ZLES results. From left to right and top to bottom: $\tau = 0, \Delta t_{ZLES}, 2\Delta t_{ZLES}$.

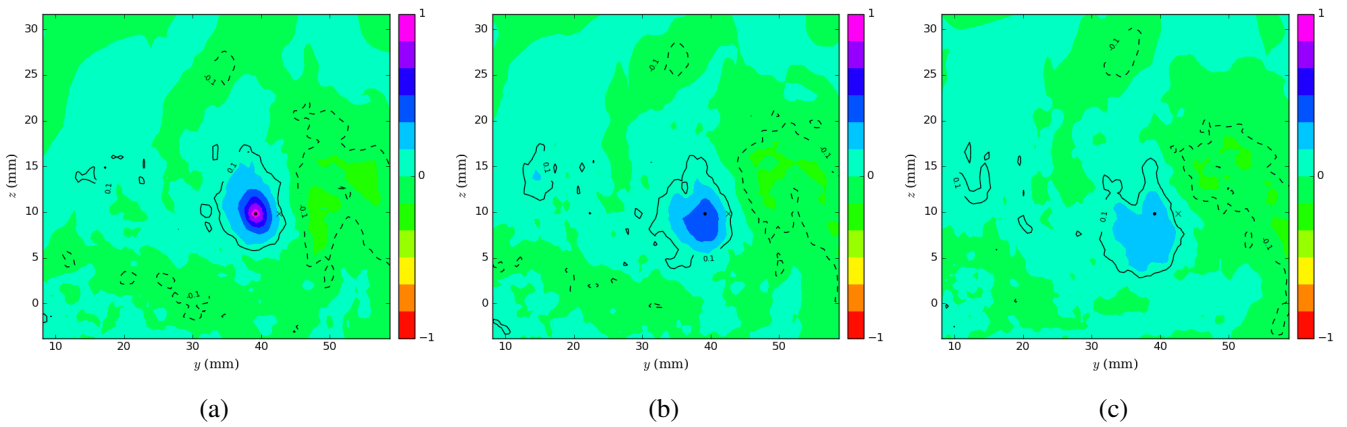


Fig. 5.18 Two-point two-time correlation map for the streamwise velocity fluctuations R_{uu} , for a point (\cdot) located 3.5 mm left of the vortex centre (x). ZLES results. From left to right and top to bottom: $\tau = 0, \Delta t_{ZLES}, 2\Delta t_{ZLES}$.

5.5 Tip-leakage vortex wandering

The phenomenon of vortex wandering corresponds to a movement of the vortex core in an apparently random fashion relative to the blade. This prevents reliable conclusions from being drawn from temporally averaged measurements [52]. In the current research, the tip-leakage vortex wandering is investigated using the PIV database and the ZLES instantaneous fields, based on Bailey and Tavoularis's method [5]. The wandering amplitude is estimated by the standard deviation of the vortex center evolution for a series of instantaneous fields.

5.5.1 Tip-leakage vortex wandering in the experiment

In the experiment, the function Γ_1 is used to determine the instantaneous vortex center with an integration domain of 11×11 points. Results for different PIV datasets are shown in Tab.5.1. The half vortex wandering amplitudes in the horizontal (y) and vertical (z) directions are reported in the two right columns, σ_y and σ_z , respectively.

Table 5.1 Half vortex wandering amplitudes in y and z directions.

PIV database	axial position (mm)	sampling frequency (HZ)	σ_y (mm)	σ_z (mm)
AXIOOM-2	2	3000	1.53	1.02
AXIOOM-3	2	7000	1.53	1.15
AXIOOM-5	-20	7000	1.34	1.14
AXIOOM-6	-40	7000	1.24	0.96
AXIOOM-7	2	3000	1.67	0.88
AXIOOM-10	2	7000	1.60	0.85

Table 5.2 Vortex wandering amplitudes in y and z directions.

PIV database	axial position (mm)	$2\sigma_y$ (mm)	$2\sigma_z$ (mm)
AXIOOM-6	-40	2.48	1.92
AXIOOM-5	-20	2.68	2.28
AXIOOM-3	2	3.06	2.30

For all the PIV series, the wandering amplitude in the horizontal direction is always a little larger than that in the vertical direction. This result is also demonstrated by the probability density function (PDF) of the tip-leakage vortex centre distribution, as shown

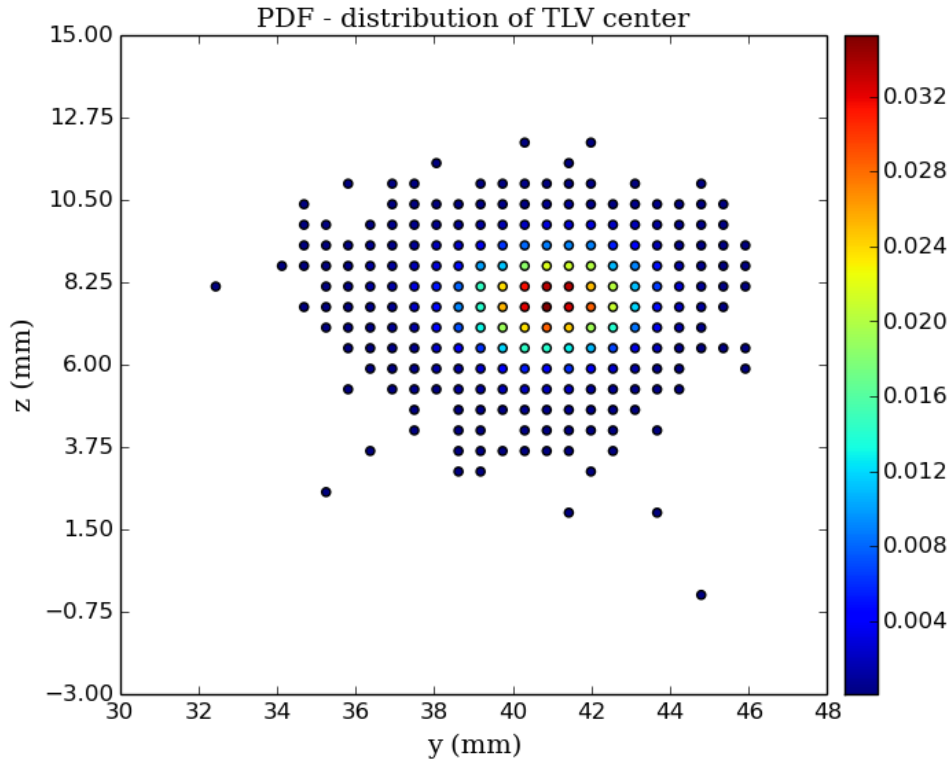


Fig. 5.19 Probability density function (PDF) of the tip-leakage vortex centre distribution at $x = 2\text{mm}$, PIV AXIOOM-2.

in Fig.5.19. The total width of wandering (2σ) is about 3mm in the horizontal direction and 2mm in the vertical direction. Both are above the PIV resolutions, which proves that this oscillation is not a sampling artefact. From the comparison between AXIOOM-3, 5 and 6, which have the same PIV grids but different axial positions, the wandering amplitude is found to increase with the streamwise distance. The four PIV series measured at 2mm downstream of the trailing edge show different results, probably because of their different measurement accuracy. Besides, the size of the integration domain for the calculation of Γ_1 is found to have a little effect on the calculated wandering amplitude. Results with different integration domain sizes for AXIOOM-2 are presented in Tab.5.3 and in Fig.5.20. With the increase of the integration domain size, the vortex wandering amplitude in both the horizontal and vertical directions slightly decreases, which is probably due to the influence of the neighbouring vortical structures (secondary vortex etc.). We did not further increase the integration domain to verify if the result could reach a convergence, because the largest integration domain 25×25 points is already a very high-cost calculation.

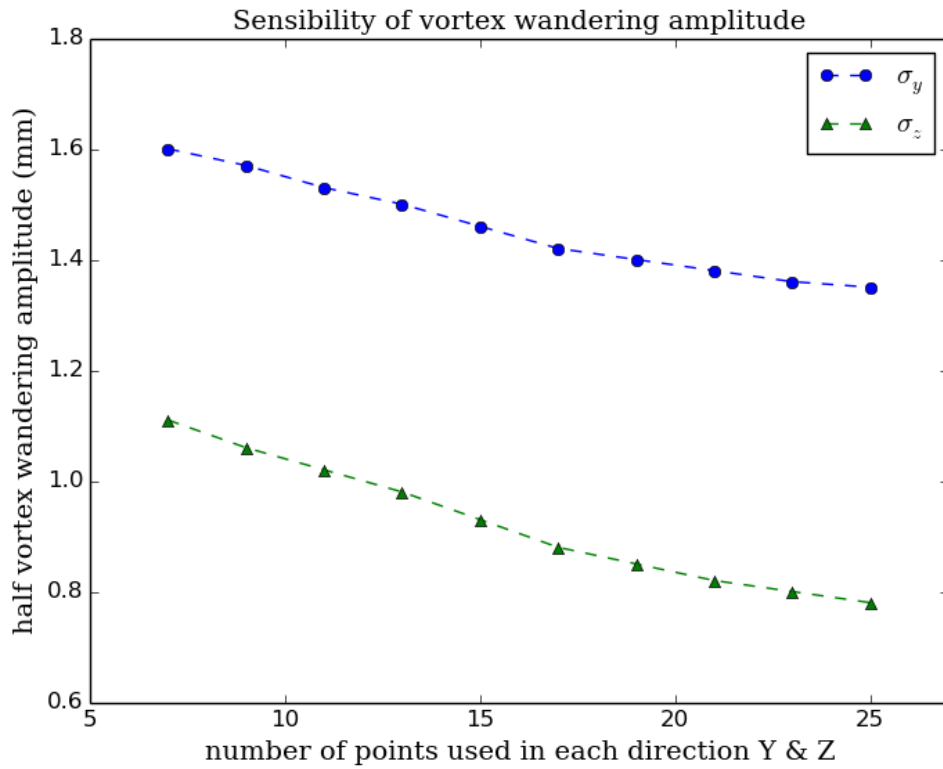


Fig. 5.20 Evolution of the half vortex wandering amplitudes σ_y and σ_z , with different integration domain sizes, PIV AXIOM-2.

Table 5.3 Half vortex wandering amplitudes with different integration domain sizes, PIV AXIOM-2.

integration domain size (points number)	σ_y (mm)	σ_z (mm)
7×7	1.60	1.11
9×9	1.57	1.06
11×11	1.53	1.02
13×13	1.50	0.98
15×15	1.46	0.93
17×17	1.42	0.88
19×19	1.40	0.85
21×21	1.38	0.82
23×23	1.36	0.80
25×25	1.35	0.78

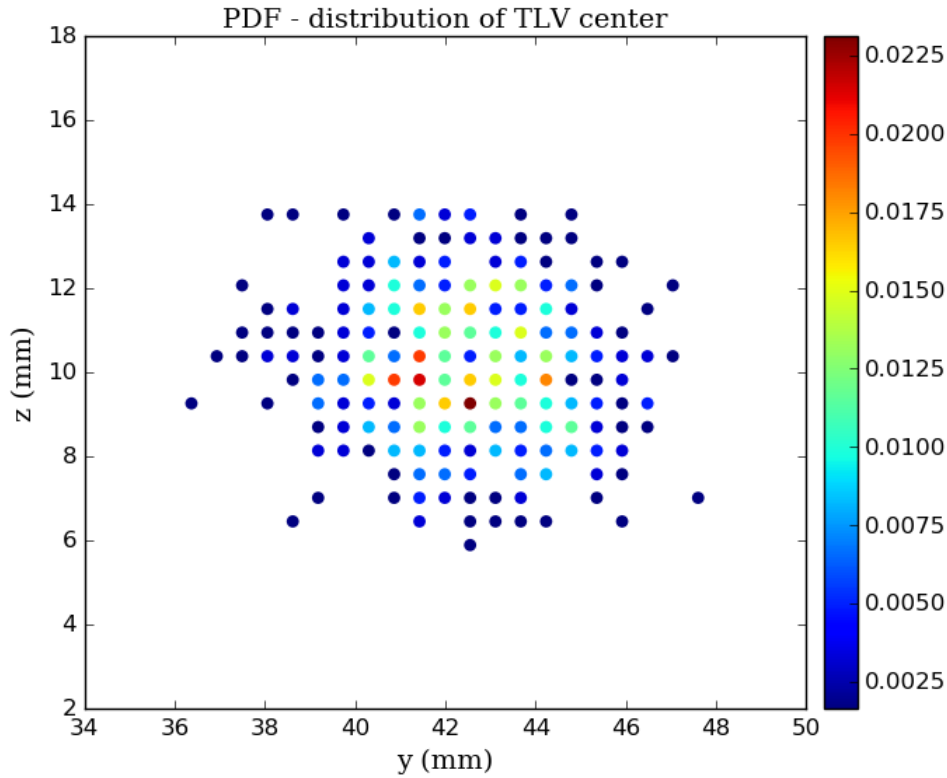


Fig. 5.21 Probability density function (PDF) of the tip-leakage vortex centre distribution at $x = 2\text{mm}$, ZLES.

5.5.2 Tip-leakage vortex wandering in the ZLES

The ZLES instantaneous fields are firstly interpolated on the same grid as PIV AXIOM-2. Then, the function Γ_1 is used to determine the instantaneous vortex center with an integration domain of 11×11 points. The probability density function (PDF) of the tip-leakage vortex centre distribution in the ZLES is shown in Fig.5.21, to compare with the experimental results in Fig.5.19. A comparison of the wandering amplitudes between the experimental and the ZLES results is shown in Tab.5.4.

We can observe a similar vortex centre distribution in the ZLES and the experiment: an elliptical distribution with larger extent in the y direction. In the experiment, the instantaneous vortex centers are more concentrated around the mean vortex center. In the ZLES, the PDF is more wiggly. In addition, the ZLES produces larger oscillatory amplitudes of the tip-leakage vortex in both y and z directions (cf. Tab.5.4). One possible explanation for these differences is that the number of samples in the ZLES (606 samples) is not sufficient to reach the same level of statistical convergence as in the experiment (13900 samples). Overall, the ZLES

compares well with the experiment. The TLV in this configuration shows a mild oscillation with $2\sigma_y$ and $2\sigma_z$ smaller than $2\%c$.

Table 5.4 Half vortex-wandering amplitudes in y and z directions, ZLES & PIV AXIOOM-2.

	σ_y (mm)	σ_z (mm)
ZLES	1.84	1.60
PIV AXIOOM-2	1.53	1.02

Table 5.5 Vortex-wandering amplitudes in y and z directions, ZLES & PIV AXIOOM-2.

	axial position (mm)	$2\sigma_y$ (mm)	$2\sigma_z$ (mm)
ZLES	2	3.68	3.20
PIV AXIOOM-3	2	3.06	2.30

5.6 An exploration of vortex wandering using URANS

In this section, URANS computations are employed to investigate the oscillatory motion of the tip-leakage vortex with excitation. The URANS computations are initiated by the converged RANS results. In order to introduce the unsteadiness into the flow field, inflow angle fluctuations are added at the inlet of the computational domain. The amplitude of the velocity fluctuations is computed from the inlet turbulent intensity measured in the experiment, and three frequencies, 1kHz, 3kHz and 5kHz, are chosen within the frequency range attributed to the tip clearance noise. More details can be found in Chapter 3.

5.6.1 Effects of grid coarsening

As presented in Chapter 3, the URANS computation grid is a coarsened version of the RANS grid by taking every second point in each direction, in order to reduce the computational needs. Before presenting the URANS results, the effects of grid coarsening in the URANS computations are firstly investigated by comparing the flow fields of the time-averaged URANS computation with 1kHz inflow angle fluctuations and the RANS results. The vortex identification functions Γ_1 and Γ_2 are shown in Fig.5.22 and the velocity components are shown in Fig.5.23.

The grid coarsening and the inlet forcing result in a larger diffusion in the URANS computations: the stronger deficit of axial velocity around the vortex center and the weaker cross-stream velocity components both indicate a less intense tip-leakage vortex. Compared with the RANS results, the vortex region detected by Γ_2 is also wider in the URANS computations. This increased diffusion may be a consequence of the grid coarsening or corresponds to a movement of the vortex. However, the TLV center determined by Γ_1 is well reproduced, which gives us confidence to investigate the vortex wandering with the URANS results.

5.6.2 URANS convergence

The convergence of the URANS computations is checked at a position close to the blade tip - trailing edge corner and within the tip-leakage vortex, where the flow state is highly unsteady. The transverse velocity (V) time histories for the three cases are shown in Fig. 5.24. For the cases with 1kHz and 3kHz inflow angle fluctuations, both a high-frequency oscillation and a low-frequency oscillation are observed. The high-frequency oscillation results from the inflow angle fluctuations. The constant amplitudes and periods of these fluctuations indicate the convergence of the computations. The high-frequency oscillation vanishes for the case with 5kHz inflow angle fluctuations, probably due to the low-pass-filter nature of the coarse grid. The low-frequency oscillation plays an important role in the formation of the vortex wandering in the URANS computations. Unlike the high-frequency oscillations, it does not show a constant frequency.

5.6.3 Vortex wandering amplitude

In order to maintain the same post-processing accuracy as the experiment, the URANS instantaneous flow fields are interpolated on the PIV AXIOOM-2 grid, and the vortex wandering amplitude is evaluated by the standard deviation of the vortex center evolution. Again, the function Γ_1 is used to determine the vortex center for each moment with an integration domain of 11×11 points. The half vortex wandering amplitudes σ_y and σ_z are shown in Tab. 5.6.

In the horizontal direction y , all the three URANS cases yield almost the same wandering amplitude as the experiment. Considering the different velocity histories reported in Fig. 5.24, the vortex wandering in URANS is definitely a result of the low-frequency oscillation of the flow fields, and the high-frequency oscillation has little contribution. In the spanwise direction z , the wandering amplitude predicted by URANS is much smaller than in the experiment, which may be due to the lack of the inflow angle fluctuations in this direction.

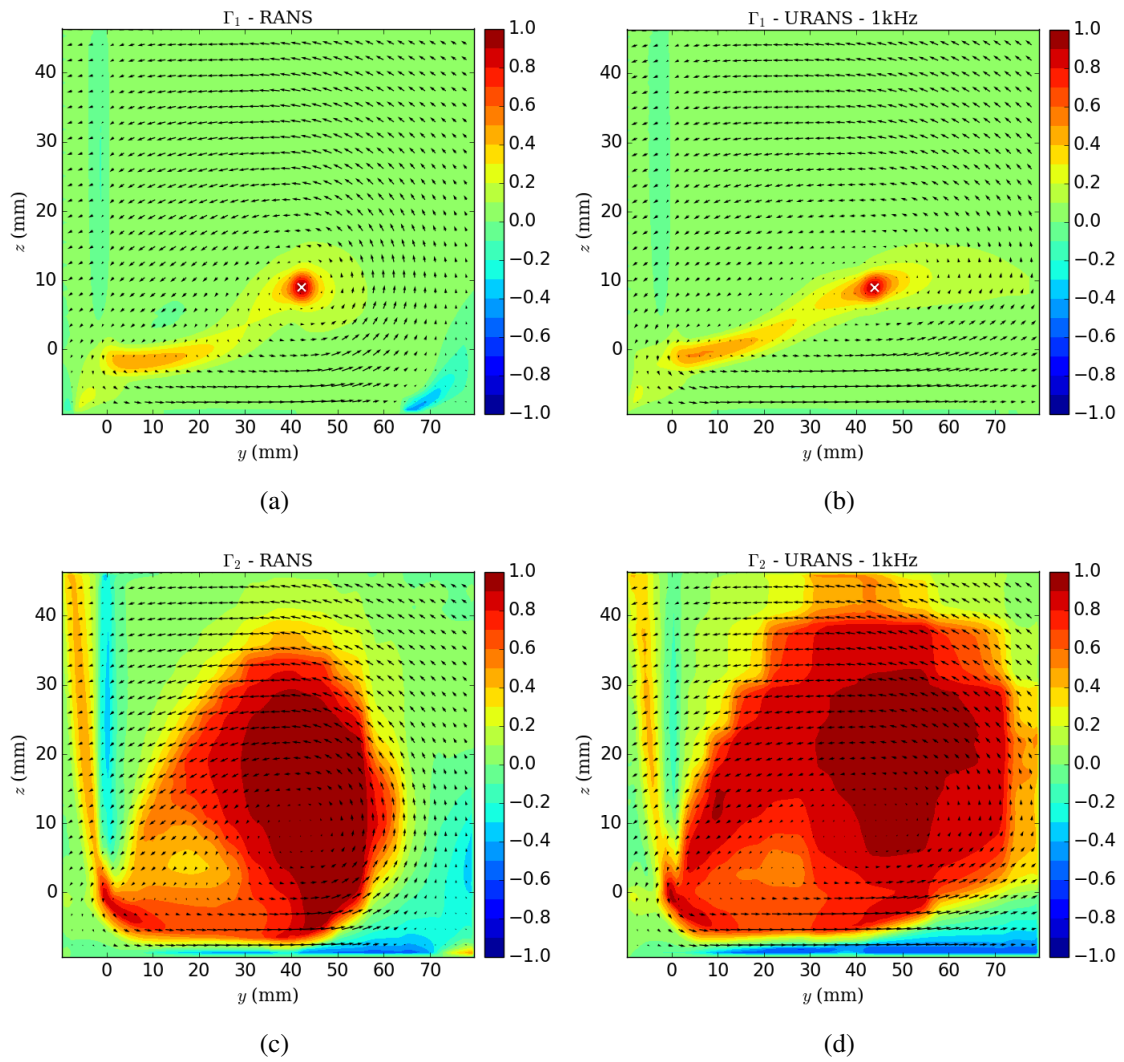


Fig. 5.22 Comparison of Γ_1 and Γ_2 between RANS (left) and time-averaged URANS (right) results, 2mm downstream of the trailing edge.

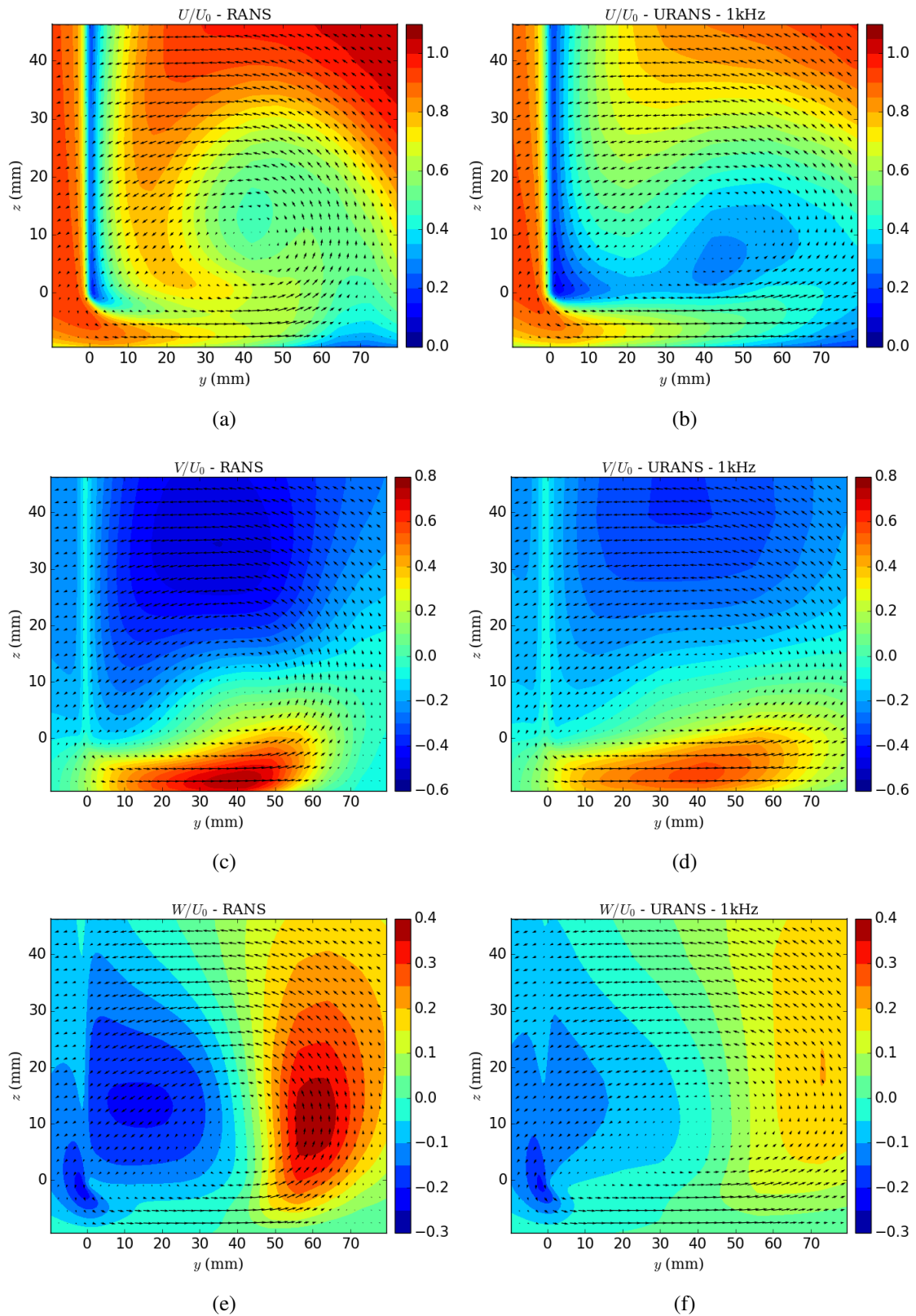


Fig. 5.23 Comparison of velocity components U , V and W between RANS (left) and time-averaged URANS (right) results, 2mm downstream of the trailing edge.

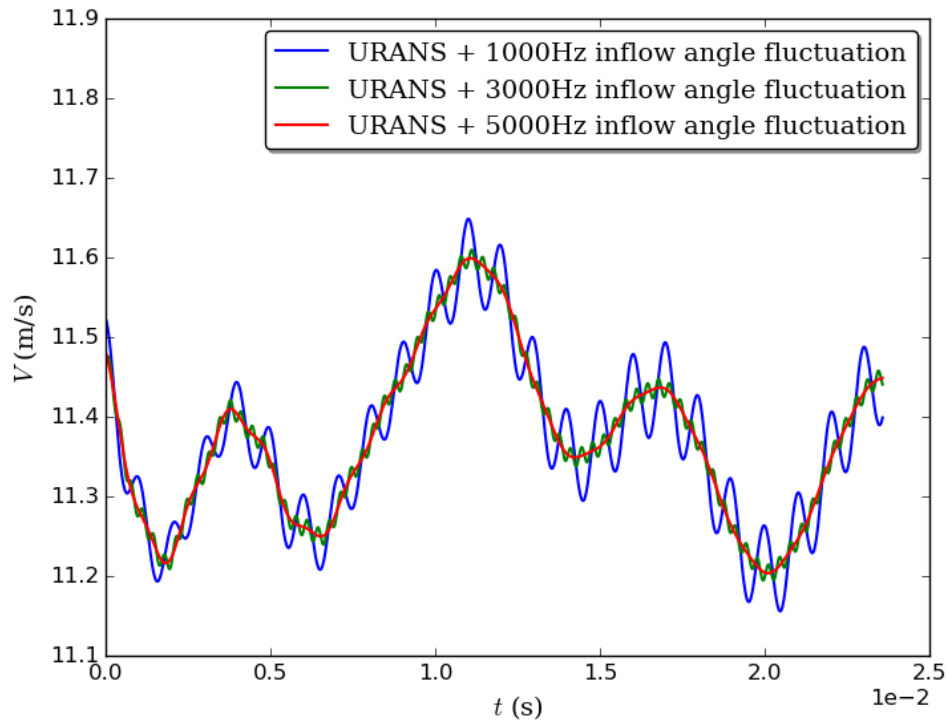


Fig. 5.24 Transverse velocity time histories close to the blade tip - trailing edge corner, from URANS computations.

Table 5.6 Calculated vortex wandering amplitudes for PIV and URANS.

case	σ_y (mm)	σ_z (mm)
PIV AXIOOM-2	1.53	1.02
URANS 1kHz	1.46	0.31
URANS 3kHz	1.46	0.31
URANS 5kHz	1.46	0.31

5.6.4 Discussion

Although the URANS computations reproduce the correct oscillation amplitude of the tip-leakage vortex in the horizontal direction, whether it is physical still needs to be discussed. There is a possibility that the low-frequency oscillation of the velocity field results from sound waves reflecting between the numerical boundaries, which does not exist in the real experiment. Further investigation are required to answer this question.

5.7 Conclusions

In this chapter, the turbulent characteristics of the tip-leakage flow and the relevant flow features have been discussed. The main conclusions of this chapter are drawn below:

1. Globally, high turbulent intensity is observed at the tip-leakage vortex center and in the tip-leakage jet. The dragging of the end-plate boundary layer by the vortex results in fluctuations and anisotropy on the border of the vortex. Compared with the experiment, ZLES is found to be a little more diffusive and predict a higher level of anisotropy.
2. For the pressure spectra, a good agreement is achieved between the experiment and the ZLES over the experimental frequency range [0, 10kHz]. Moreover, the ZLES provides the spectral information at higher frequencies. All the pressure spectra are characterized by an energy hump around 1.3 kHz, and this frequency should be associated with the tip-leakage flow .
3. A broad peak around 50Hz is observed in the experimental velocity spectra, and its level increases as the measurement point approaches the vortex core. This broad peak may be associated with the vortex wandering. Another possible explanation would be a more global resonance of the flow, but this latter scenario is discarded by the fact that the 50 Hz peak is not observed on all velocity spectra.
4. The space-time correlations have been calculated for a few correlation points at several correlation times. In the experiment, the streamwise-velocity fluctuation correlation decays much faster than the spanwise-velocity fluctuation correlation, for the correlation point located at the vortex center. This different decay between R_{uu} and R_{ww} can be explained partly by the strong cross-stream entrainment of the tip-leakage flow, partly by the measurement errors possibly existing around the vortex center, due to the lack of smoke particles. For the correlation point located 3.5 mm left of the vortex center, the correlations undergo a similar decay for both components, resulting from the same magnitude of the velocity components. The ZLES produces a very similar shape of the correlation zone as the experiment. The strong-correlation zone for R_{ww} in the ZLES is, however, smaller than that in the experiment and its decay is faster, probably because the scale of the turbulent structures is under-predicted in the ZLES. This could be due to the limited spatial extent of the LES zone.
5. A mild oscillatory motion of the TLV is observed in both the experiment and the ZLES. In the experiment, the TLV oscillation amplitudes are estimated to be 3mm in the horizontal direction and 2mm in the vertical direction, at 2mm downstream of the

trailing edge. By measuring its axial evolution, the wandering amplitude is found to increase with the streamwise distance. The ZLES agrees well with the experiment for the elliptical distribution of the instantaneous TLV centers, but produces larger oscillatory amplitudes. The PDF is more wiggly in the ZLES, probably because of the imperfect statistical convergence.

6. URANS computations have been employed to analyse the response of the tip-leakage vortex to inflow fluctuations. A correct wandering amplitude in the horizontal direction is obtained. However, the physical validity of this numerical observation is still to be confirmed.

Chapter 6

Far-Field Noise Prediction

In this chapter, a far-field noise prediction is derived from a limited set of near-field data. Such a modelling can help to analyze the physical mechanisms, and could be later used for the design of quieter blades. The far-field noise contributions from the blade-tip and the trailing-edge will be predicted using the blade-tip self-noise model [50, 51, 80] and the trailing-edge noise model [85, 93, 96], respectively. Firstly, the blade-tip self-noise model will be reformulated. Secondly, the blade-tip self-noise model will be applied to the ZLES near-field data. Thirdly, the trailing-edge noise model will be reformulated and tested using both RANS and ZLES data. Results will be compared against the experimental measurements.

6.1 Blade-Tip Self-Noise Model

The blade-tip self-noise model is an extension of Amiet's trailing-edge noise model [3] to the blade-tip with reflecting end-wall. The reflecting effect of the end-wall is accounted for by an imaginary blade created through the mirror reflection. The model is based on several assumptions with respect to the sound radiation:

- the relative thickness of the blade is small, $e/c \ll 1$, so that the blade could be assimilated to a zero-thickness, rigid, flat plate;
- the tip gap h is small compared with the chord and thickness, $h \ll c$ and $h \ll e$, so that the gap could be ignored without significant error when computing the far-field sound radiation.

The model is derived in the coordinate system shown in Fig.6.1. The space is described by the chordwise coordinate x , spanwise coordinate y and normal-to-wall coordinate z . The origin is located at the blade-tip/trailing edge corner and the reflecting end-wall is the $y = 0$ plane. Since the gap is ignored, the real blade ($y < 0$) of length $L/2$ and the image blade

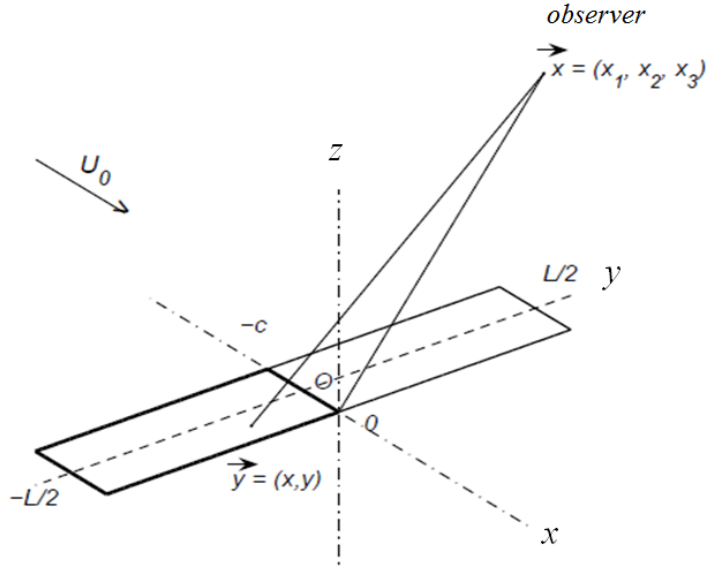


Fig. 6.1 Coordinate system for the blade-tip self-noise model [80].

($y > 0$) are considered together as a continuous blade of length L . The blade is unswept with zero angle of attack, so the incident mean flow speed U_0 is parallel to the chord line.

When the turbulent flow convects past the blade, a disturbance wall pressure p' is generated and acts as the equivalent acoustic source. The three-dimensional convected wave equation of the disturbance pressure reads

$$\frac{\partial^2 p'}{\partial x^2} + \frac{\partial^2 p'}{\partial y^2} + \frac{\partial^2 p'}{\partial z^2} - \frac{1}{c_0^2} \left(\frac{\partial}{\partial t} + U \frac{\partial}{\partial x} \right)^2 p' = 0 \quad (6.1)$$

With $p'(x, y, z, t) = P(x, y, z)e^{i\omega t}$, we obtain

$$\beta^2 \frac{\partial^2 P}{\partial x^2} + \frac{\partial^2 P}{\partial y^2} + \frac{\partial^2 P}{\partial z^2} - 2ikM \frac{\partial P}{\partial x} + k^2 P = 0 \quad (6.2)$$

where $k = \omega/c_0$ is the acoustic wavenumber, $M = U_0/c_0$ is the Mach number and $\beta^2 = 1 - M^2$. Since the model addresses a subsonic problem, M is lower than unity.

In order to further simplify the convected wave equation, a change of variable is proposed as

$$P(x, y, z) = p(x, z)e^{ikMx/\beta^2} e^{\gamma Y} \quad (6.3)$$

where $\gamma = \alpha - iK_2$. α is the non-dimensional damping factor. It describes the attenuation rate of the pressure gust when moving away from the blade-tip along the spanwise direction. K_2 is the spanwise wavenumber. $Y = y/b$ is the normalized spanwise coordinate.

By inserting Eq.6.3 into Eq.6.2, we obtain

$$\beta^2 \frac{\partial^2 p}{\partial x^2} + \frac{\partial^2 p}{\partial z^2} + \left(\frac{\gamma^2}{b^2} + \frac{k^2}{\beta^2} \right) p = 0 \quad (6.4)$$

We then normalize the coordinates as $X = x/b$ and $Z = \beta z/b$ and we obtain

$$\frac{\partial^2 p}{\partial X^2} + \frac{\partial^2 p}{\partial Z^2} + \left(\frac{\gamma^2}{\beta^2} + \mu^2 \right) p = 0 \quad (6.5)$$

where $\mu = \frac{kb}{\beta^2}$. With $\Gamma^2 = \frac{\gamma^2}{\beta^2} + \mu^2$, we have

$$\frac{\partial^2 p}{\partial X^2} + \frac{\partial^2 p}{\partial Z^2} + \Gamma^2 p = 0 \quad (6.6)$$

Since this equation is the same for both the physical half-space ($y < 0$) and image half-space ($y > 0$), it holds in full space.

Let us assume that p_1 is a solution of Eq.6.6 and its corresponding pressure gust is P_1 . The problem solution must satisfy a boundary condition, which is here the unsteady Kutta condition, requiring the pressure to vanish in the wake. As a result, for a given incident pressure gust $P_g = P_0 e^{-iK_1 X} e^{\gamma|Y|}$, a correction P_1 must be added such that $P_1 + P_g = 0$ for $X \geq 0$. So we have

$$\begin{aligned} P_1 + P_g &= p_1 e^{ikMx/\beta^2} e^{\gamma|Y|} + P_0 e^{-iK_1 X} e^{\gamma|Y|} \\ &= p_1 e^{i\bar{k}MX/\beta^2} e^{\gamma|Y|} + P_0 e^{-iK_1 X} e^{\gamma|Y|} \\ &= 0 \end{aligned} \quad (6.7)$$

where $\bar{k} = kb$ is the normalized acoustic wavenumber. On the surface of the blade, $Z = 0$, we have

$$\begin{aligned} \frac{p_1(X, 0)}{P_0} &= -e^{-iK_1 X} e^{-i\bar{k}MX/\beta^2} \\ &= -e^{-i(K_1 + M\mu)X}, X \geq 0 \end{aligned} \quad (6.8)$$

In addition, the blade is assimilated to a rigid flat plate, which imposes

$$\frac{\partial p_1}{\partial Z}(X, 0) = 0, X < 0 \quad (6.9)$$

Eqs.6.6, 6.8 and 6.9 form a Schwarzschild's problem. A standard Schwarzschild's problem can be described as

$$\frac{\partial^2 \Phi}{\partial x^2} + \frac{\partial^2 \Phi}{\partial z^2} + \lambda^2 \Phi = 0 \quad (6.10)$$

$$\Phi(x, 0) = f(x), x \geq 0 \quad (6.11)$$

$$\frac{\partial \Phi}{\partial z}(x, 0) = 0, x < 0 \quad (6.12)$$

For $x < 0$ and $z = 0$, the scalar field solution of the above wave problem is

$$\Phi(x, 0) = \frac{1}{\pi} \int_0^\infty G(x, \xi, 0) f(\xi) d\xi \quad (6.13)$$

with

$$G(x, \xi, 0) = \sqrt{\frac{-x}{\xi}} \frac{e^{-i\lambda(\xi-x)}}{\xi-x} \quad (6.14)$$

So we obtain the solution of our problem (Eqs.6.6, 6.8 and 6.9) on the blade surface $Z = 0$ and for $X < 0$:

$$\begin{aligned} \frac{p_1(X, 0)}{P_0} &= -\frac{1}{\pi} \int_0^\infty \sqrt{\frac{-X}{\xi}} \frac{e^{-i\Gamma(\xi-X)}}{\xi-X} e^{-i(K_1+M\mu)\xi} d\xi \\ &= -\frac{\sqrt{-X}}{\pi} e^{i\Gamma X} \int_0^\infty \frac{e^{\mathbf{Im}(\Gamma)\xi}}{\xi^{1/2}(\xi-X)} e^{-i(\mathbf{Re}(\Gamma)+K_1+M\mu)\xi} d\xi \end{aligned} \quad (6.15)$$

Since $\mathbf{Re}(\Gamma) + K_1 + M\mu$ is real, the term $e^{-i(\mathbf{Re}(\Gamma)+K_1+M\mu)\xi}$ is bounded by -1 and 1 . To ensure the convergence of the integral, the term in the integral $\frac{e^{\mathbf{Im}(\Gamma)\xi}}{\xi^{1/2}(\xi-X)}$ must converge to 0 for $\xi \rightarrow \infty$, and this imposes that the imaginary part of Γ is negative.

The analytical calculation of the integral yields [80]:

$$\begin{aligned}\frac{p_1(X, 0)}{P_0} &= -e^{-i(K_1 + \mu M)X} \left[1 - \frac{1}{\sqrt{\pi}} \int_0^{-i(\Gamma + K_1 + \mu M)X} \frac{e^{-z}}{\sqrt{z}} dz \right] \\ &= -e^{-i(K_1 + \mu M)X} [1 - \Phi^0((-i(\Gamma + K_1 + \mu M)X)^{1/2})]\end{aligned}\quad (6.16)$$

where Φ_0 is the complex error function. So the complete disturbance pressure gust P_1 in full space reads

$$P_1(X, Y, 0) = -P_0 e^{-iK_1 X} e^{\gamma|Y|} [1 - \Phi^0((-i(\Gamma + K_1 + \mu M)X)^{1/2})] \quad (6.17)$$

For an observer at the position (x_1, x_2, x_3) , the far-field pressure produced by a given gust on the blade surface of wavenumber (K_1, K_2) is given by [93]:

$$\begin{aligned}\frac{p_{K_1, K_2}(x_1, x_2, x_3, \omega)}{P_0} &= \frac{ikx_3}{2\pi S_0^2} b^2 \int_{-2}^0 \int_{-L/c}^{L/c} e^{-iK_1 X} e^{-\gamma|Y|} [1 - \Phi^0((-i(\Gamma + K_1 + \mu M)X)^{1/2})] \\ &\quad \times e^{-i(k/\beta^2)[S_0 - b(x_1 X + \beta^2 x_2 Y)/S_0 - M(x_1 - bX)]} dY dX\end{aligned}\quad (6.18)$$

where $S_0^2 = x_1^2 + \beta^2(x_2^2 + x_3^2)$.

Since X and Y are independent, we notice that this integration can be calculated separately on X and Y :

$$\begin{aligned}\frac{p_{K_1, K_2}(x_1, x_2, x_3, \omega)}{P_0} &= \frac{i\bar{k}x_3}{2\pi S_0^2} \\ &\quad \times \left(b \int_{-L/c}^{L/c} e^{-\gamma|Y|} e^{i(\bar{k}x_2/S_0)Y} dY \right) \\ &\quad \times \left(e^{-ik(S_0 - Mx_1)/\beta^2} \int_{-2}^0 e^{-i(K_1 + \mu(M - x_1/S_0))X} [1 - \Phi^0((-i(\Gamma + K_1 + \mu M)X)^{1/2})] dX \right) \\ &= \frac{i\bar{k}x_3}{2\pi S_0^2} \times \Sigma_Y \times I_1\end{aligned}\quad (6.19)$$

where Σ_Y and I_1 denote the integration on Y and X , respectively.

The integration on Y gives, after some algebra (See Appendix A):

$$\Sigma_Y = b \frac{L}{c} \left[\text{sinc}\left(\zeta \frac{L}{2c}\right) e^{i\zeta \frac{L}{2c}} + \text{sinc}\left(\xi \frac{L}{2c}\right) e^{i\xi \frac{L}{2c}} \right] \quad (6.20)$$

where $\zeta = K_2 + i\alpha - \bar{k}x_2/S_0$, $\xi = K_2 + i\alpha + \bar{k}x_2/S_0$ and $\text{sinc}(x)$ denotes $\sin(x)/x$.

Introducing $C = K_1 + \mu(M - x_1/S_0)$ and $B = K_1 + \mu M + \Gamma$, we obtain from the integration on X :

$$I_1 = e^{-ik(S_0 - Mx_1)/\beta^2} \frac{e^{2iC}}{iC} \left[1 - \Phi^0((2iB)^{1/2}) + e^{-2iC} \sqrt{\frac{B}{B-C}} \Phi^0((2i(B-C))^{1/2}) \right] \quad (6.21)$$

So the contribution of the elementary pressure gust of wavenumber (K_1, K_2) to the far-field pressure finally reads

$$\frac{p_{K_1, K_2}(x_1, x_2, x_3, \omega)}{P_0} = \frac{i\bar{k}x_3}{2\pi S_0^2} \times \Sigma_Y \times I_1 \quad (6.22)$$

The power spectral density (PSD) of the far-field sound is obtained by integration of all the gusts. Following Amiet's method [3], we obtain:

$$S_{pp}(\vec{x}, \omega) = \left(\frac{\bar{k}x_3 L}{4\pi S_0^2} \right)^2 \frac{1}{b} \int_{-\infty}^{\infty} \Pi_0\left(\frac{\omega}{U_c}, K_2\right) |I_1(K_2)|^2 \times \left| e^{i\zeta L/(4b)} \text{sinc}\left(\zeta \frac{L}{4b}\right) + e^{i\xi L/(4b)} \text{sinc}\left(\xi \frac{L}{4b}\right) \right|^2 dK_2 \quad (6.23)$$

where $\Pi_0 = \frac{1}{\pi} \Phi_{pp}(\omega) l_y(K_2, \omega)$. Φ_{pp} is the wall pressure spectrum near the trailing edge/blade-tip corner, and l_y is the corresponding spanwise coherence length.

6.2 Tip noise modelling from near-field ZLES data

In order to predict the power spectral density (PSD) of the far-field pressure with the blade-tip self-noise model, four important flow field characteristics must be provided:

- the non-dimensional damping factor α . It describes the attenuation rate of the incident pressure gust when moving away from the blade-tip along the spanwise direction.
- the wall pressure spectrum Φ_{pp} near the trailing edge / blade-tip corner.
- the spanwise coherence length l_y , with respect to the measurement point of the wall pressure spectrum.
- the longitudinal convection speed of the pressure disturbances U_c in the blade-tip region.

In the present section, these characteristics are extracted from the ZLES. Several numerical probes in the blade-tip region are used to collect the unsteady pressure signals. Their positions are shown in Fig.6.2.

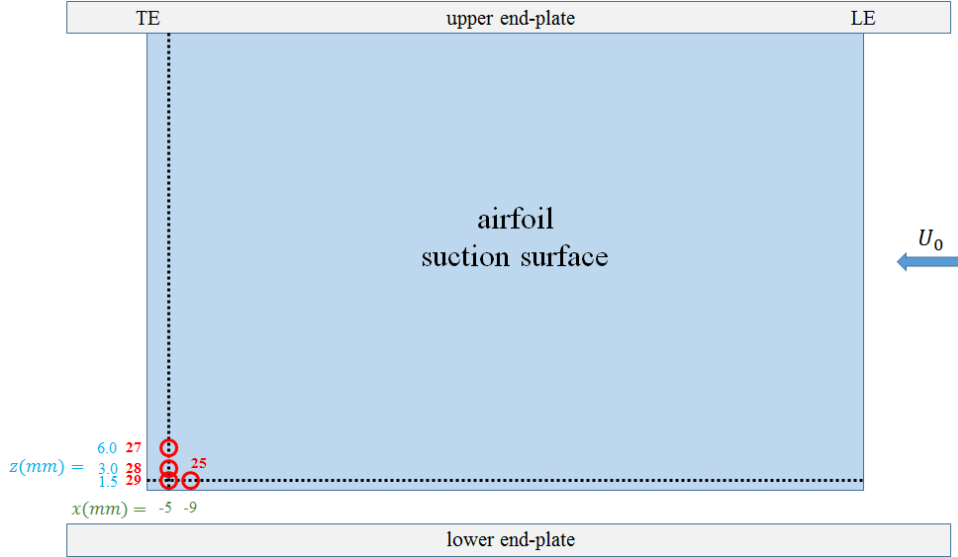


Fig. 6.2 Numerical probes on the suction surface.

6.2.1 Damping factor α

The damping factor α can be deduced by calculating the attenuation rate of the wall pressure spectrum along the spanwise direction at trailing edge and close to the blade-tip.

The model assumes that the incident pressure gust at given X reads:

$$p' = p'_0 e^{-\alpha Y} \quad (6.24)$$

where $Y = y/b$ is the spanwise distance between the measurement point and the blade-tip, normalized by the half-chord b . So the wall pressure spectrum $\Phi_{pp} \sim p'^2$ could be written as:

$$\Phi_{pp} = \Phi_0 e^{-2\alpha Y} \quad (6.25)$$

For two measurement points at positions y_1 and y_2 , their difference of spectrum level Δ_{12} in dB reads:

$$\Delta_{12} = 10 \log_{10} \left(\frac{\Phi_0 e^{-2\alpha Y_1}}{p'^2_{ref}} \right) - 10 \log_{10} \left(\frac{\Phi_0 e^{-2\alpha Y_2}}{p'^2_{ref}} \right) \quad (6.26)$$

and α could be calculated by:

$$\alpha = \frac{b}{2(y_2 - y_1)} \ln(10^{\Delta_{12}/10}) = \frac{b \ln(10)}{20} \frac{\Delta_{12}}{y_2 - y_1} \quad (6.27)$$

In this study, three probes, labelled 29, 28 and 27, at positions $y = 1.5\text{mm}$, 3mm and 6mm , respectively, are chosen to calculate α by measuring their spectrum decay. The pressure spectra measured in the experiment at the three probes are shown in Fig.6.4. Similarly to the section 5.3, all the pressure spectra in the region of the tip-leakage flow are featured by an energy hump around 1.3 kHz, by which frequency the tip-leakage flow is characterized. So the averaged value of α around this characteristic frequency should be a good estimate of the damping factor. With the experimental spectra, we obtain:

$$\bar{\alpha}_{EXP} \approx 15 \quad (6.28)$$

With the ZLES data, the PSD of the wall pressure is computed with Welch's method and the results at the three probes are shown in Fig.6.3. Although the energy hump is less visible in the ZLES spectra, the same method for extracting the dumping factor α can be employed. Here we use the averaged value of α between 1000Hz and 2000Hz:

$$\bar{\alpha}_{ZLES} \approx 12.4 \quad (6.29)$$

Compared to the experiment, the energy decay along the spanwise direction is underestimated by the ZLES.

6.2.2 Wall pressure spectrum Φ_{pp}

The original and modelled wall pressure spectra Φ_{pp} , for the experiment [50], are displayed in Fig.6.4. The shape of the modelled curve is controlled by a energy hump between 700Hz and 3000Hz, which can be clearly observed from the original spectrum. This energy hump is associated with tip clearance noise, as will be shown later. Here we propose a model function of the wall pressure spectrum:

$$\Phi_{pp} = 10 \frac{a_1 f^2 + b_1 f + c_1}{a_2 f^2 + b_2 f + c_2} \quad (6.30)$$

By fitting this model into the experimental spectrum at $z = 1.5\text{mm}$ with the Curve Fitting app *cftool* in MATLAB, we obtain $a_1 = -9.4$, $b_1 = 32090$, $c_1 = -13819670$, $a_2 = 1$, $b_2 = 9416$, $c_2 = 1470000$. The spectra at $z = 3.0\text{mm}$ and 6.0mm are simply obtained by Eq.6.25.

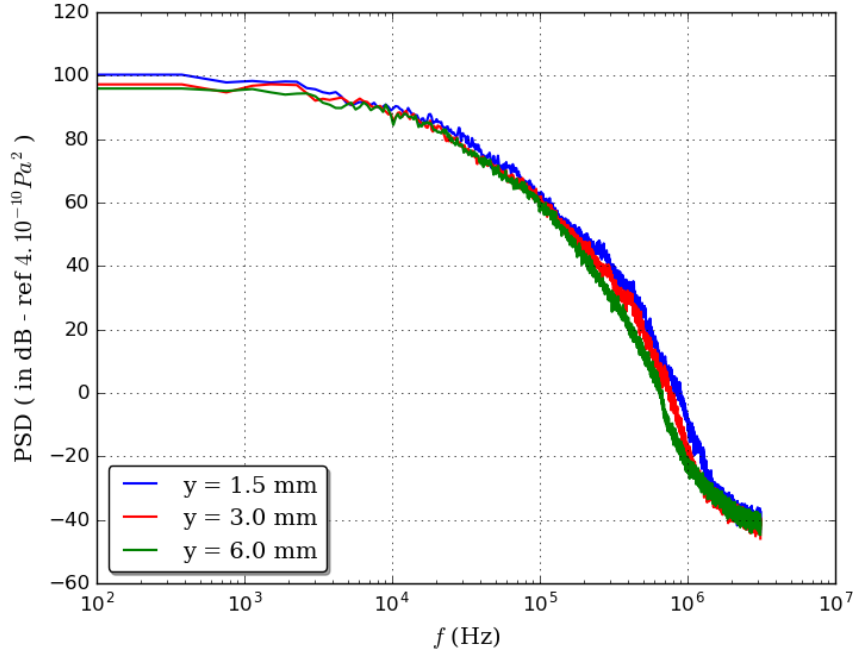


Fig. 6.3 PSD of wall pressure at probes 29 ($y = 1.5\text{mm}$), 28 ($y = 3\text{mm}$) and 27 ($y = 6\text{mm}$).

For the ZLES results shown in Fig.6.5, the energy hump is under-estimated. It is much less visible for $z = 1.5\text{mm}$ and 6.0mm and only the spectrum at $z = 3.0\text{mm}$ can be employed to determine the shape of the modelled spectrum. Again, by fitting Eq.6.30 into the spectrum, we get $a'_1 = -6.07$, $b'_1 = 23834$, $c'_1 = -14143070$, $a'_2 = 0.63$, $b'_2 = 7476$, $c'_2 = 1470000$ at $z = 1.5\text{mm}$. And this is the modelled spectrum Φ_{pp} that will be used in the blade-tip self-noise model.

The modelled EXP spectrum at $z = 1.5\text{mm}$ is also plotted with a black dot-dashed line in Fig.6.5. A small shift of central frequency between the modelled EXP spectrum and the modelled ZLES spectrum can be observed. Besides, the peak is a little under-estimated ($\sim 3\text{dB}$) by the ZLES.

It should be emphasized that, the wall pressure spectrum used here only describes the energy hump, consequently, the blade-tip self-noise model will only predict the noise contribution within the frequency range of the hump.

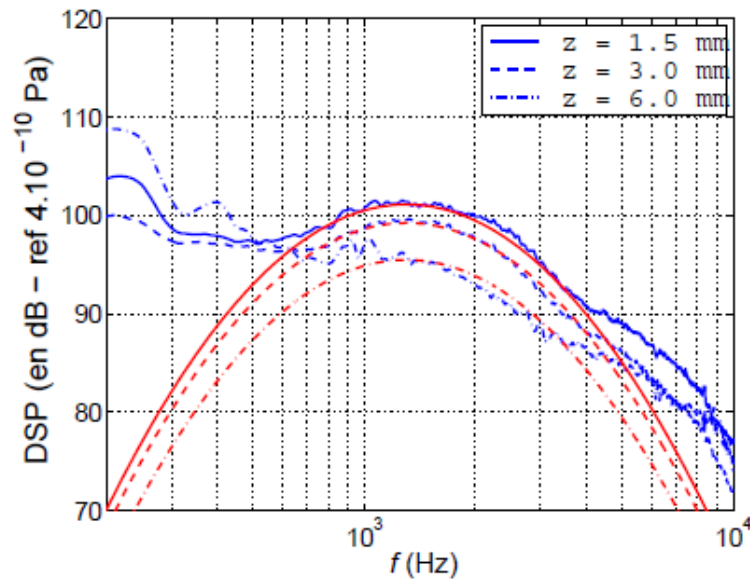


Fig. 6.4 Original and modelled PSD of wall pressure [50], blue lines: original EXP results; red lines: modelled EXP results (Eq.6.30).

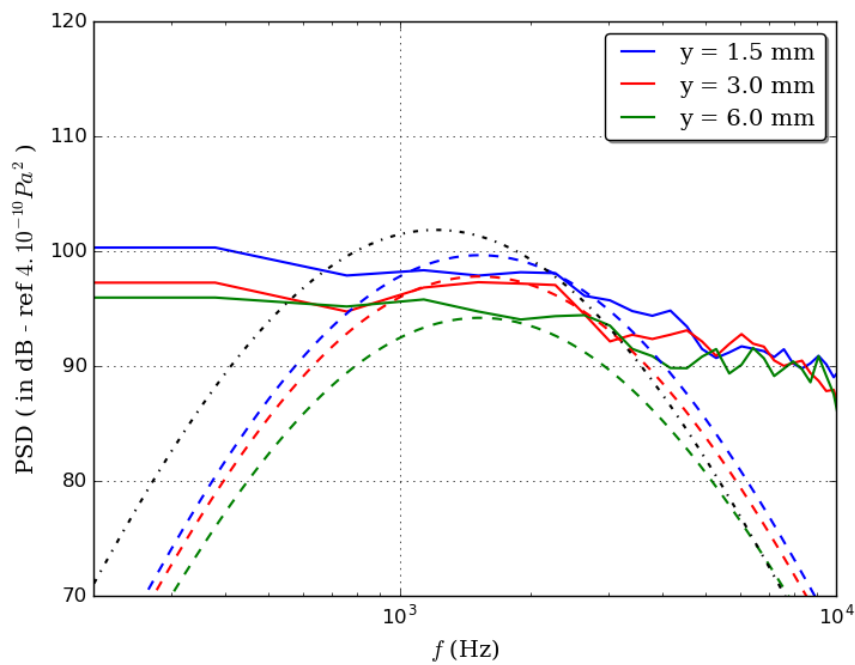


Fig. 6.5 Original and modelled PSD of wall pressure, solid lines: original ZLES results; dashed lines: modelled ZLES results; dot-dashed line: modelled EXP result for $z = 1.5$ mm.

6.2.3 Spanwise coherence length l_y

The coherence length l_y can be computed through the coherence function γ as:

$$l_y(K_2, \alpha, \omega) = \int_0^{\infty} \gamma(\omega, \eta) \cos(K_2 \eta / b) e^{-\alpha \eta / b} d\eta \quad (6.31)$$

where $\eta = |y_1 - y_2|$ is the two-point distance and the coherence function γ is defined as the normalized cross-power spectral density between the two points [91]:

$$\gamma^2(\omega, \eta) = \frac{|\Phi(\omega, z_1, z_2)|^2}{|\Phi(\omega, z_1, z_1)| |\Phi(\omega, z_2, z_2)|} \quad (6.32)$$

where Φ denotes the cross-power spectral density.

In this study, the probes 27, 28 and 29 are chosen to evaluate the function γ for $\eta = 1.5\text{mm}$, 3mm and 4.5mm . The cross-correlation between the pressure signals is firstly computed, and then Welch's method is employed to calculate their PSD. The results are showed in Fig.6.6.

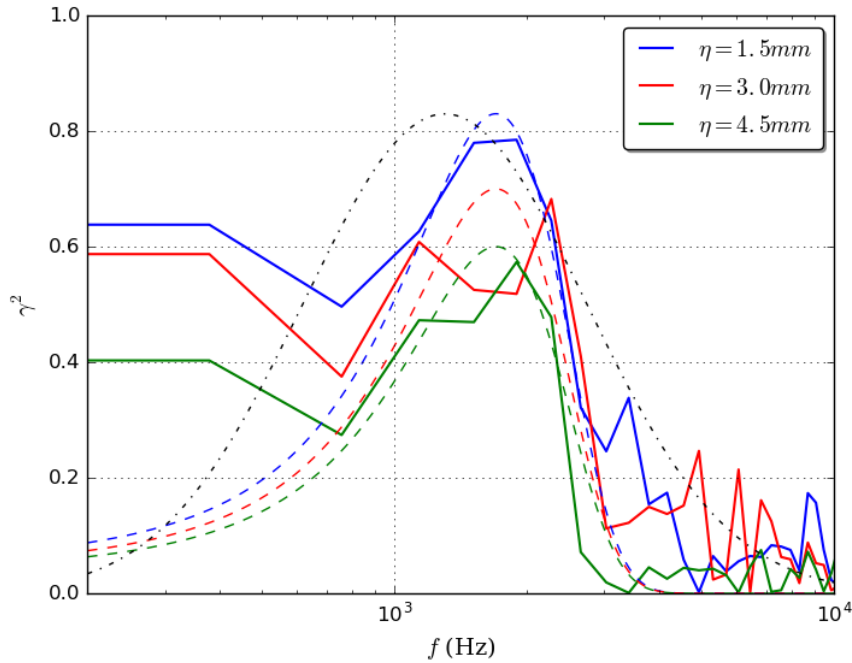


Fig. 6.6 Original and modelled coherence function γ^2 , solid lines: original ZLES results; dashed lines: modelled ZLES results; dot-dashed line: modelled EXP results for $\eta = 1.5\text{mm}$.

The coherence function γ is modelled before Eq.6.31 is used to estimate the coherence length. Here we propose a model function of γ as:

$$\gamma^2(f, \eta) = e^{-\left(\frac{f-f_{coh}}{a_{coh}}\right)^2} 10^{-2\eta/L_{coh}} \quad (6.33)$$

The first term of the model function defines the shape and magnitude, and the second term describes the decay with η . By fitting the model function into the real curves for $\eta = 1.5\text{mm}$, 3mm and 4.5mm , we obtain: $f_{coh} \approx 1700$, $a_{coh} \approx 1000$ and $L_{coh} \approx 38.4 \cdot 10^{-3}$. The fitted curves are displayed in Fig.6.6 with dashed lines.

The modelled experimental (EXP) coherence function for $\eta = 1.5\text{mm}$ is also plotted with a black dot-dashed line in Fig.6.6. The amplitude of the peak is well captured by the ZLES, but a small shift of central frequency is observed.

By inserting Eq.6.33 into Eq.6.31, we have:

$$l_y(K_2, \alpha, f) = \frac{L_{coh}}{\ln(10)} \frac{1 + \frac{\alpha L_{coh}}{\ln(10)b}}{\left(1 + \frac{\alpha L_{coh}}{\ln(10)b}\right)^2 + \left(\frac{K_2 L_{coh}}{\ln(10)b}\right)^2} e^{-\frac{1}{2}\left(\frac{f-f_{coh}}{a_{coh}}\right)^2} \quad (6.34)$$

Fig.6.7 shows the coherence length l_y of the ZLES, computed with the modelled function γ for different values of K_2 , in comparison with the experimental results. The ZLES gives a good description of the position and amplitude of the coherence length peak, but it drops more rapidly at higher and lower frequencies than the experimental results.

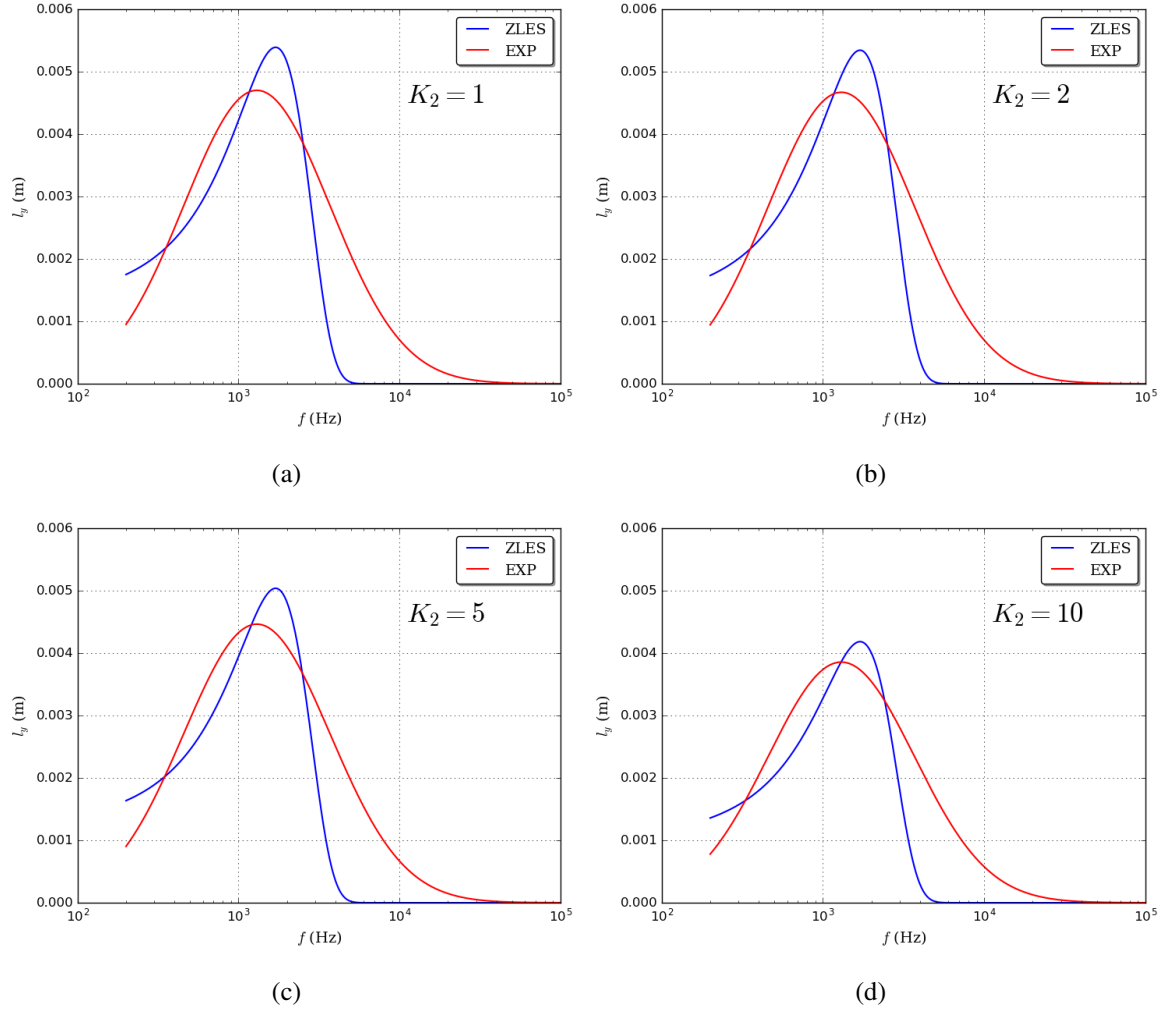


Fig. 6.7 Comparison of coherence length l_y between ZLES and EXP, for different values of K_2 .

6.2.4 Longitudinal convection velocity U_c

U_c is defined as the convection speed of the pressure gust in the chordwise direction. It is usually different from the free-stream velocity U_0 . We suppose there are two probes i and j separated by a chordwise distance ξ . The pressure gust is convected past i and j with a time delay $\tau = \xi/U_c$, and the corresponding phase shift is $\phi_{ij} = \omega\xi/U_c = 2\pi f\xi/U_c$. Thus the convection velocity U_c can be related to the slope of the phase spectrum $s = \phi_{ij}/f = 2\pi\xi/U_c$, and U_c can be calculated by:

$$U_c = 2\pi\xi/s \quad (6.35)$$

It is much more difficult to extract U_c from the ZLES data than from the experimental data. The total sampling time $T = 10 \cdot c/U_0$ in ZLES is not long, so that $\Delta f = 1/T$ in the phase spectrum is quite large. In our case, $\Delta f \sim 35\text{Hz}$.

In this study, the pressure signals collected at probes 25 and 29 with a chordwise distance $\xi \approx 4\text{mm}$ are employed to compute the longitudinal convection velocity. The procedure of data-processing is:

1. Firstly, the cross-correlation of the two pressure signals is computed.
2. Secondly, the phase spectrum of the cross-correlation is computed, with a Welch-type smoothing algorithm.
3. Thirdly, the Savitzky-Golay filter is employed to the phase spectrum to eliminate the noise and smooth the curve.
4. Finally, the slope s of the phase spectrum is calculated, and U_c is obtained from Eq.6.35.

The computed U_c is displayed in Fig.6.8 with a solid blue line. Again, the convection velocity U_c is modelled before putting it into the tip-noise model. A Gaussian distribution is used:

$$U_c(f) = A_c e^{-\left(\frac{f-f_c}{a_c}\right)^2} \quad (6.36)$$

and by fitting Eq.6.36 into the calculated U_c curve, we obtain $A_c = 80\text{m/s}$, $f_c = 1400\text{Hz}$ and $a_c = 300\text{Hz}$. The modelled convection velocity U_c for ZLES is shown in Fig.6.8, along with the experimental (EXP) result. Here again, the ZLES yields a good prediction of the peak position and amplitude, but its width is narrower.

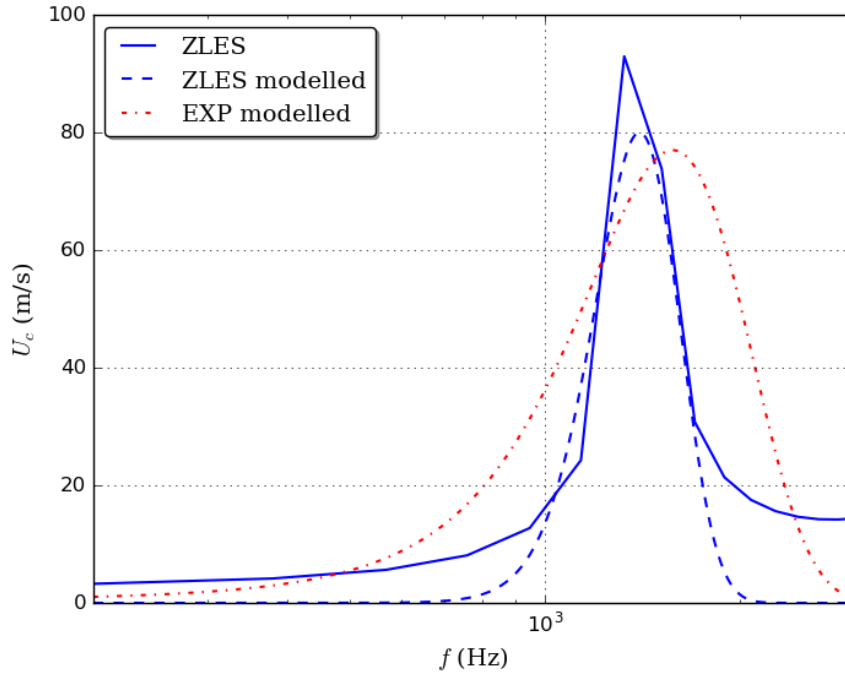


Fig. 6.8 Original and modelled convection velocity U_c , solid blue line: original ZLES results; dashed blue line: modelled ZLES results; dot-dashed red line: modelled EXP results.

6.2.5 Far-field noise prediction with ZLES data

With the damping factor α , the wall pressure spectrum Φ_{pp} , the spanwise coherence length l_y and the longitudinal convection velocity U_c calculated and modelled as above, we can predict the power spectral density of the far-field pressure with the blade-tip self-noise model. The prediction with the ZLES data is displayed in Fig.6.9, in comparison with the experimental (EXP) results.

The predictions from both EXP and ZLES drop rapidly at low and high frequencies. This is due to the bandwidth of the wall pressure spectrum Φ_{pp} and the longitudinal convection velocity U_c at low and high frequencies. The modelled Φ_{pp} and U_c are restricted to the bandwidth of the tip-leakage hump found in the experiment. They are forced to go to zero at low and high frequencies, for an easier fit over the frequency range of the hump. This artificial limit should have little influence on the prediction of the tip clearance noise, because the noise contributions outside this frequency range mostly come from other noise generation mechanisms. As shown in Fig.6.9, within the frequency range attributed to the tip clearance noise, from 0.7kHz to 7kHz as reported by Jacob *et al.*[60], the prediction based upon the ZLES data over-estimates by about 5dB. Compared to the prediction from the experimental

(EXP) data, the ZLES results reproduce the same peak, but the spectrum decays more rapidly at lower and higher frequencies. The similar decays previously observed on both l_y and U_c are probably at the origin of this phenomenon. Besides the analytical model, the PSD of the far-field pressure is also computed with the Ffowcs-Williams and Hawkings (FWH) acoustic analogy from the ZLES data, with the pressure fluctuations all over the blade surface as input. Since ZLES only describes the flow in the blade tip region and RANS has no contribution to the FWH computation, it is reasonable to think that the computed noise mostly comes from the tip-leakage noise. As shown in Fig. 6.9, the FWH prediction provides a very good description of the noise in the frequency range [0.7kHz, 7kHz]. This range of prediction is much larger than that for the blade-tip self-noise model, and the levels are also better predicted. This suggests the near-field data are appropriate, and more efforts should be put on the parameterization of the blade-tip self-noise model.

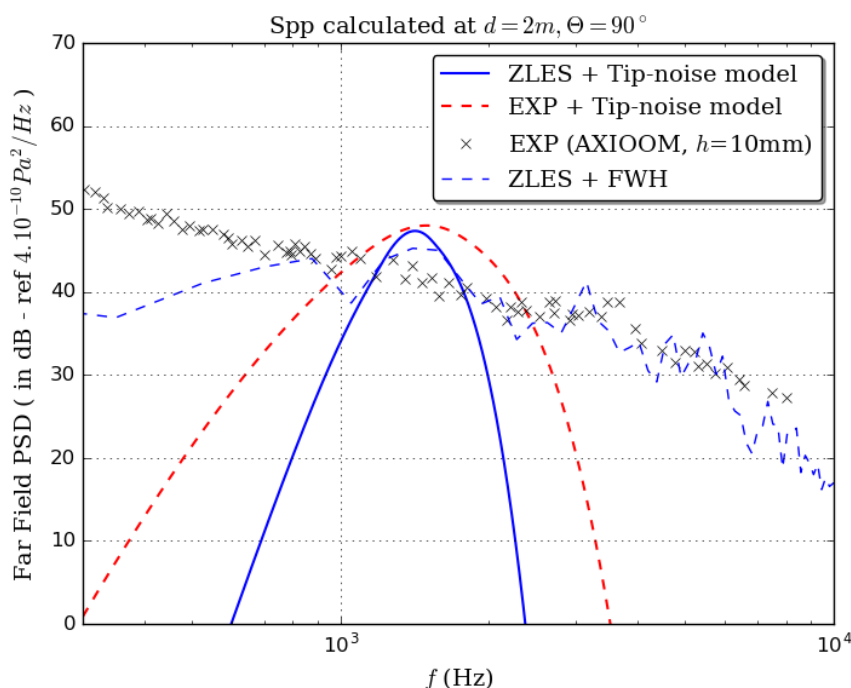


Fig. 6.9 Power spectral density of the far-field pressure.

6.2.6 Sensitivity of the blade-tip self-noise model

The sensitivity of the blade-tip self-noise model to the four input parameters α , U_c , Φ_{pp} and l_y is tested here. The ZLES result is used as the reference case. Each individual input parameter is given an artificial variation of $\pm 10\%$ from the ZLES result and the others remain

unchanged. Results of eight possible variations are plotted and compared to the reference case (“REF”) in Fig.6.10.

The computed far-field noise will increase with larger U_c , Φ_{pp} , l_y or smaller α , vice versa. According to the formula of the model (section 6.1), the computed far-field noise is proportional to Φ_{pp} and l_y . Consequently, a $\pm 10\%$ variation to Φ_{pp} and l_y leads to exactly $\pm 10\%$ variation to the far-field noise, which is about 0.4 dB in Fig.6.10. However, a $\pm 10\%$ variation to α and U_c leads to more than $\pm 10\%$ variation to the far-field noise. Thus, the blade-tip self-noise model is relatively more sensible to α and U_c . For all the cases considered in the test, the maximal variation to the far-field noise is about 1 dB. From this point of view, we can conclude that the blade-tip self-noise model is not very sensible to the input parameters.

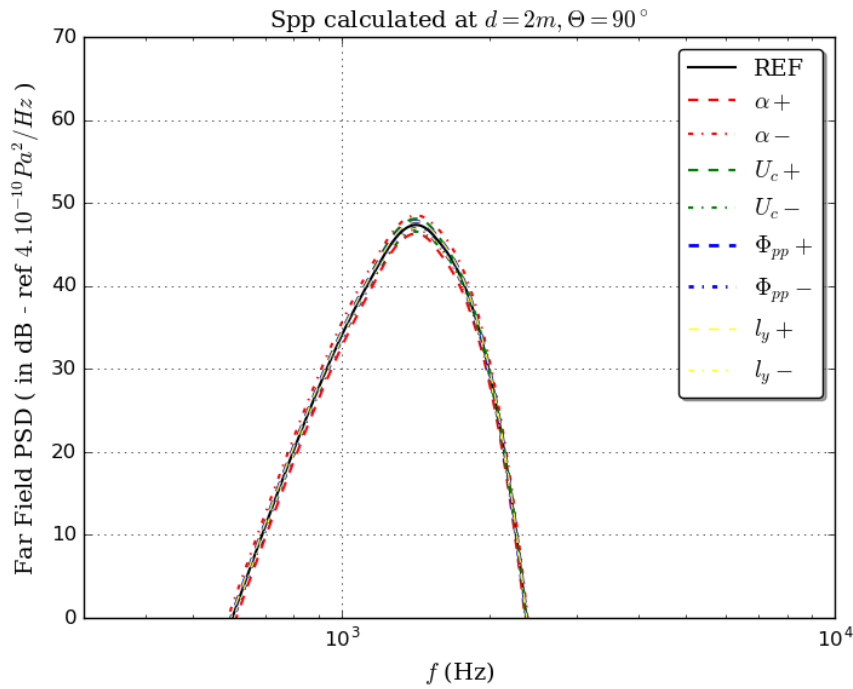


Fig. 6.10 The sensitivity of the blade-tip self-noise model to α , U_c , Φ_{pp} and l_y . “+” denotes +10% and “-” denotes -10% to each individual input parameter.

6.3 Trailing-edge noise model

Roger and Moreau [93] have extended Amiet’s trailing-edge noise model by taking into account the effects due to the limited chord length. The solution is derived for arbitrary oblique pressure gusts, and not only for parallel pressure gusts as in the original model,

which allows calculating the radiation integral with no restriction on the aspect ratio and for any observer location, including off mid-span.

The extended model is again deduced in the coordinate system shown in Fig.6.1. Differently from the blade-tip self-noise model, both the regions $y < 0$ and $y > 0$ represent the real blade. The blade is assimilated to a zero-thickness, rigid, flat plate. The spanwise extent is first assumed to be infinite, but the real span is then re-introduced when computing the far-field noise radiation from the unsteady lift, considered as the source of sound. The blade is assumed to have zero angle of attack, so the incident mean flow is parallel to the blade chord.

The final expression for the PSD of the far-field pressure reads

$$S_{pp}(\vec{x}, \omega) = \left(\frac{\omega x_3 b}{2\pi c_0 S_0^2} \right)^2 2\pi L \left| I \left(\frac{\bar{\omega}}{U_c}, \bar{k} \frac{x_2}{S_0} \right) \right|^2 \Pi_0 \left(\frac{\omega}{U_c}, k \frac{x_2}{S_0} \right) \quad (6.37)$$

The blade response function I is the main factor relating the far-field sound to the aerodynamic wall pressure field. It is calculated by a radiation integral summing the dominant trailing-edge contribution f_1 and the leading-edge scattering correction f_2 :

$$I(K_1, K_2) = \int_{-2}^0 f_1(X) e^{-iCX} dX + \int_{-2}^0 f_2(X) e^{-iCX} dX \quad (6.38)$$

More details can be found in Appendix B.

Similarly to the blade-tip self-noise model, $\Pi_0 = \frac{1}{\pi} \Phi_{pp}(\omega) l_y \left(\bar{k} \frac{x_2}{S_0}, \omega \right)$. Φ_{pp} is the wall pressure spectrum at the trailing edge and l_y is the spanwise coherence length.

6.4 TE noise modelling from near-field ZLES and RANS data

For the sake of applying the trailing-edge noise model, the wall pressure spectrum Φ_{pp} , the convection velocity U_c and the spanwise coherence length l_y must be extracted, from ZLES or RANS. The position of extraction should be near the trailing edge and at the mid-span plane, in order to minimize the finite-span effects. Since the flow field at mid-span is simulated by RANS for both ZLES and RANS simulations, Φ_{pp} , U_c and l_y have to be modelled from some statistical quantities of RANS results:

- the wall pressure spectrum Φ_{pp} near the trailing edge can be evaluated by some wall-pressure model based on the boundary layer parameters.

- the convection velocity U_c is usually taken as $U_c = \alpha_{Uc} U_0$ with $0.6 < \alpha_{Uc} < 0.8$. An intermediate value $U_c = 0.7U_0$ should be acceptable for the input.

- the spanwise coherence length l_y can be estimated by Corcos's model [31], $l_y = b_c U_c / \omega$. The constant b is found to vary between 1.2 and 1.7 in several experiments. Here we take an intermediate value $b_c = 1.47$, as suggested by Rozenberg [94–96].

6.4.1 Wall pressure spectrum Φ_{pp}

Based on the boundary layer statistics, numerous semi-empirical models have been developed to estimate the wall pressure spectrum:

Schlinker & Amiet's model

Schlinker and Amiet proposed an analytical model [97] based on Willmarth and Roos's experimental data [108]:

$$\frac{\Phi_{pp}(\omega)}{\rho_0^2 \delta^* U_0^3} = 2.10^{-5} \frac{F(\tilde{\omega})}{2} \quad (6.39)$$

with $F(\tilde{\omega}) = (1 + \tilde{\omega} + 0.217\tilde{\omega}^2 + 0.00562\tilde{\omega}^4)^{-1}$ and $\tilde{\omega} = \omega \delta^* / U_0$.

This semi-empirical model uses the boundary layer displacement thickness δ^* as input. It is originally designed for the zero pressure gradient case.

Goody's model

Based on Chase-Howe's model [26, 53] and taking into account the effect of the Reynolds number, Goody proposed a semi-empirical model [48]:

$$\frac{\Phi_{pp}(\omega) U_0}{\tau_w^2 \delta} = \frac{C_2 (\omega \delta / U_0)^2}{[(\omega \delta / U_0)^{0.75} + C_1]^{3.7} + [C_3 (\omega \delta / U_0)]^7} \quad (6.40)$$

with $C_1 = 0.5$, $C_2 = 3$ and $C_3 = 1.1 R_T^{-0.57}$. $R_T = (\delta / U_0)(\nu / u_\tau^2)$ is the parameter involving the Reynolds number effect. This model uses the boundary layer thickness δ , the wall shear stress τ_w , and the friction velocity u_τ as inputs.

Adverse pressure gradient (APG) model

Based on Goody's model, Rozenberg proposed an improved model, taking into account the adverse pressure gradient [95]:

$$\frac{\Phi_{pp}(\omega) U_0}{\tau_w^2 \delta^*} = \frac{0.78(1.8\pi\beta_c + 6)(\omega \delta^* / U_0)^2}{[(\omega \delta^* / U_0)^{0.75} + C'_1]^{3.7} + [C'_3 (\omega \delta^* / U_0)]^7} \quad (6.41)$$

with $C'_1 = 0.105$ and $C'_3 = 3.76R_T^{-0.57}$. $\beta_c = (\theta/\tau_w)(dp/dx)$ is Clauser's parameter [29] and Π is the parameter of the wake's law [30], given by

$$2\Pi - \ln(1 + \Pi) = \frac{\kappa U_0}{u_\tau} - \ln\left(\frac{\delta^* U_0}{\nu}\right) - \kappa C - \ln \kappa \quad (6.42)$$

with $\kappa = 0.41$ and $C = 5.1$.

This empirical model takes the boundary layer displacement thickness δ^* , the momentum thickness θ , the wall shear stress τ_w , and the pressure gradient dp/dx as input data.

6.4.2 Far-field noise prediction with ZLES and RANS data

The boundary layer parameters should not be extracted at a position too close to the trailing edge, because they may be contaminated by the scattered field that is not part of the incident gust in this model. On the other hand, the extraction position should not be far away from the trailing edge either, since the flow over the curved surface of an airfoil significantly varies. Here, the streamwise position of 97.5% c is chosen as a compromise, as suggested by Rozenberg [94]. The boundary layer parameters at 97.5% c from ZLES and RANS are presented in Tab.6.1. As can be seen from this table, the RANS computation has a thicker boundary layer than the ZLES. The external boundary layer parameters of the RANS computation are about two times higher than those of the ZLES, whereas the inner parameters are quite similar.

Table 6.1 Boundary layer parameters at 97.5% c from ZLES and RANS.

simulation	ZLES	RANS
boundary layer thickness δ	0.0129m	0.0215m
boundary layer displacement thickness δ^*	0.0036m	0.0052m
boundary layer momentum thickness θ	0.0017m	0.0027m
free-stream velocity U_0	70.8m/s	71m/s
wall shear stress τ_w	2.23Pa	2.01Pa
friction velocity u_τ	1.36m/s	1.29m/s
pressure gradient dp/dx	3×10^4 Pa/m	2.7×10^4 Pa/m

Based on these boundary layer parameters, the trailing-edge noise radiated by the airfoil is predicted using the analytical model at a point 2m away from the blade suction side, where the noise is also measured in the experiment. The results for ZLES and RANS with the APG model are plotted in Fig.6.11, as well as the experimental measurements. With this

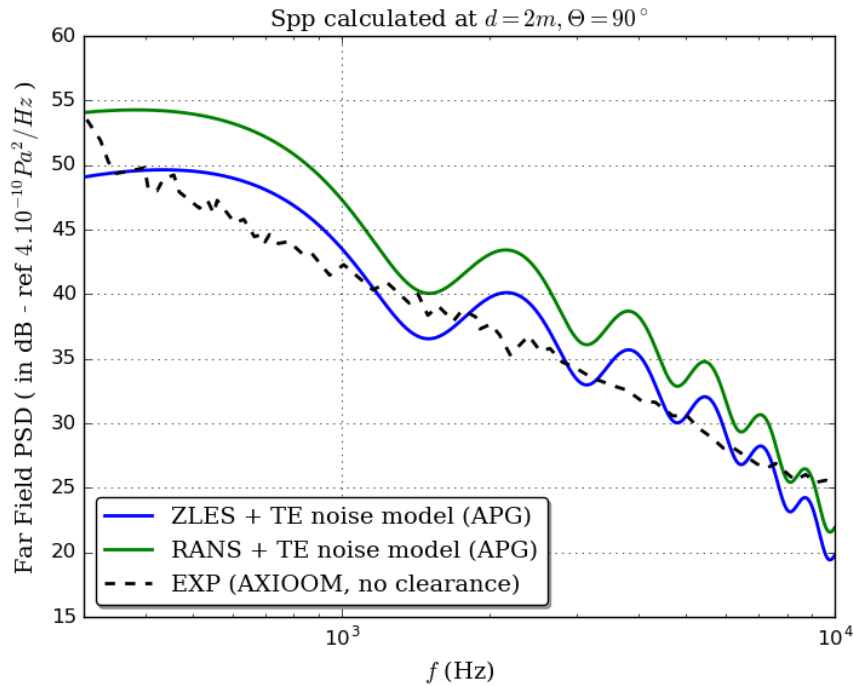


Fig. 6.11 Power spectral density of the far-field pressure.

analytical model, the ZLES yields a very good prediction within a broad frequency range. The oscillation results from the constructive and destructive interference between different acoustic sources distributed on the blade surface. The prediction with RANS boundary layer parameters is found to over-estimate the energy levels, especially at low frequencies. This over-estimate results from an over-prediction of the wall pressure spectrum Φ_{pp} by the model: since the RANS computation over-predicts the boundary layer thickness, the wall pressure estimated using the model is too high at low frequencies, and vice versa. Considering the fact that both the ZLES and the “pure” RANS computation simulate the flow field at mid-span with the RANS method, the better prediction from the ZLES results from its better mesh quality.

Fig.6.12 shows a comparison between the different wall pressure spectrum models from the ZLES data. Schlinker & Amiet’s model and Goody’s model yield very similar predictions, except at low frequencies. They both largely under-estimate the energy level of the spectrum. This under-estimate may be due to the pressure gradient effect, which neither of them takes into account. The APG model yields a much better prediction, compared with the measurements.

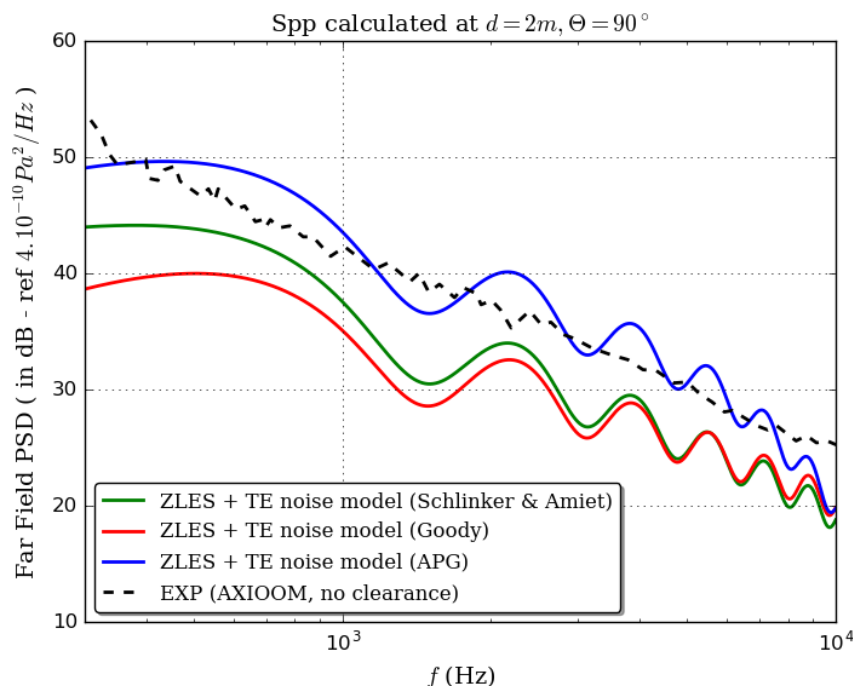


Fig. 6.12 Power spectral density of the far-field pressure.

6.5 Combined noise (TE+Tip) modelling from near-field ZLES data

In the last part of this chapter, the blade-tip self-noise model and the trailing-edge noise model are combined together to predict the far-field noise radiated by the airfoil in the current configuration. Using the ZLES data as inputs, the predicted noise, as well as the experimental measurements, are plotted in Fig.6.13. The measured spectrum with clearance is “above” the one without clearance in the frequency range [0.7kHz, 7kHz], thus the tip-leakage flow contributes essentially to the far-field noise in this frequency range. Similarly to the trailing-edge noise model, the combined model yields a good prediction within a broad frequency range. The only discrepancy between the numerical prediction and the experimental measurements is the energy hump around 1.3kHz, which corresponds to the tip clearance noise and results from the over-estimate of the blade-tip self-noise model, as shown in section 6.2. Compared with the trailing-edge noise, the tip clearance noise only contributes to the noise radiation within a narrow range of frequencies, that is, around the characteristic frequency of the tip-leakage flow.

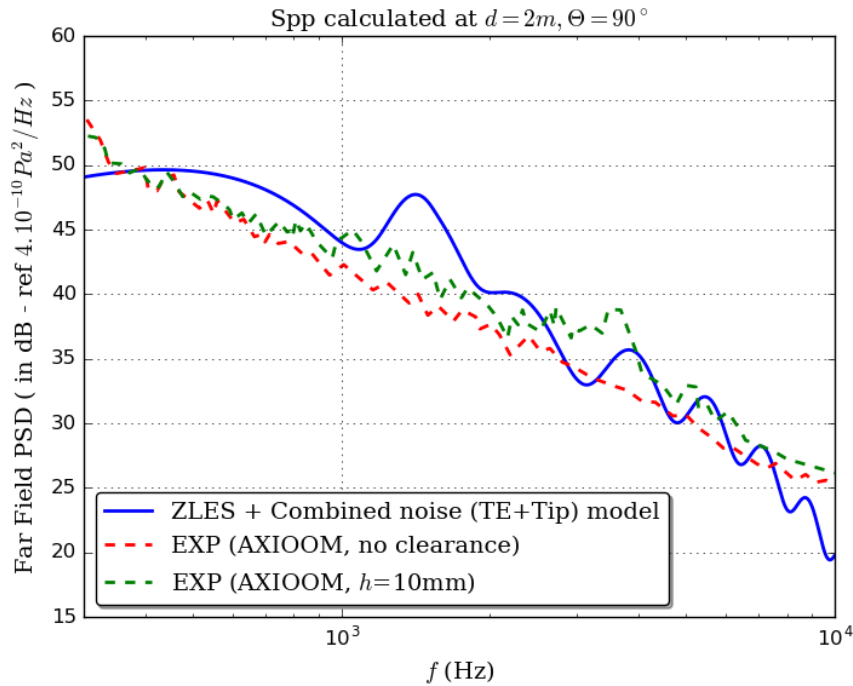


Fig. 6.13 Power spectral density of the far-field pressure.

6.6 Conclusions

In this chapter, two far-field noise prediction models are reformulated and implemented with the near-field data from the numerical simulations:

1. The blade-tip self-noise model is implemented with the ZLES near-field data. The four important flow field characteristics needed for the model are extracted and modelled: the damping factor α is deduced by calculating the attenuation rate of the wall pressure spectrum along the spanwise direction at trailing edge and close to the blade-tip; the wall pressure spectrum Φ_{pp} is extracted directly at the blade tip - trailing edge corner; the spanwise coherence length l_y is calculated from the spanwise coherence function for several two-point distances; the convection velocity U_c is calculated from the phase spectrum of the cross-correlation for two points along the streamwise direction. Within the frequency range attributed to the tip clearance noise, from 0.7kHz to 7kHz, the prediction from the ZLES is found to over-estimate by about 5dB. Since the FWH computation with the same ZLES near-field data provides a very good description of the noise, the near-field data are demonstrated to be appropriate, and more efforts should be put on the parameterization of the blade-tip self-noise model.

2. The trailing-edge noise model is implemented with the time-averaged ZLES and the RANS near-field data. The three important flow field characteristics needed for the model are extracted and modelled: the wall pressure spectrum Φ_{pp} is modelled based on the boundary layer statistics close to the trailing-edge; the spanwise coherence length l_y is evaluated using Corcos's model; the convection velocity U_c is evaluated from the free-stream velocity. With this analytical model, the ZLES yields a very good prediction within a broad frequency range. The prediction with RANS boundary layer parameters is found to over-estimate the energy levels, because of a thicker boundary layer.
3. The blade-tip self-noise model and the trailing-edge noise model are combined together to predict the far-field noise radiated by the airfoil in the current configuration. Using the ZLES data as inputs, the combined model yields a good prediction within a broad frequency range. Compared with the trailing-edge noise, the tip clearance noise only contributes to the noise radiation within a narrow range of frequency, that is, around the characteristic frequency of the tip-leakage flow.

Chapter 7

Conclusions and perspectives

7.1 Conclusions

The work of this thesis is in the frame of the Sino-French project AXIOOM. During this thesis, a tip-leakage flow in a single-airfoil configuration at low Mach number has been considered. This configuration is the simplest tip-leakage flow configuration, where there are neither cascade nor end-wall motion effects. Nevertheless, this simplest configuration does have some practical applications in real life: for instance, the flow past the slat fuselage junction is very similar to that in the current configuration. In the future, by comparing the current results and those in a more complex configuration, it will be possible to estimate the cascade effect or the influence of the end-wall motion. Moreover, numerical simulations, especially LES, have to be validated in a simple configuration such as the one examined in the present thesis, so that we can have confidence to use it in a more complex configuration in the future. Results from an experiment and a ZLES computation have been analysed systematically and thoroughly, and additionally a series of RANS/URANS computations have been carried out in order to investigate the TLV susceptibility to isolated flow disturbances at moderate computational cost. The random oscillation of the tip-leakage vortex, referred to as “vortex wandering”, has been investigated using the time-resolved PIV database and the URANS results. Based on the experimental and numerical near-field data, two far-field noise prediction models, corresponding to two different acoustic sources, have been adapted to the present flow conditions and implemented.

1. Both the Two-Component (2C) and Three-Component (3C) time-resolved PIV are successfully applied to capture the characteristics of the tip-leakage flow. Along with the cross-stream velocity components v and w , 3C TR PIV is shown to yield a description of the streamwise velocity component u , normal to the measurement plane,

in good agreement with LDV. 2C and 3C TR PIV both provide an insight into the low-frequency content of the velocity field, which is an important asset for the study of large scale structures and flow intermittency. However, the high-frequency content is under-resolved by PIV in the present experiment.

2. Various analyses of the flow characteristics have been carried out, including the inflow conditions, blade loading, tip-leakage vortex characteristics and the mean flow field in Chapter 4, the Reynolds stresses and the spectral contents in Chapter 5. They all show a good agreement between the experiment and the ZLES in the blade tip region. The zonal (RANS-LES) approach proves itself to be a powerful tool to provide a detailed description of the tip-leakage flow, with a limited computational cost.
3. The RANS and URANS computations are more diffusive and globally under-estimate the intensity of the tip-leakage vortex, which is partly due to the fact that turbulence is treated as steady in both RANS and URANS computations and subsequently the unsteady feature of turbulence, which plays an important role in the TLV dynamics, is not taken into account in the RANS and URANS computations. However, the TLV center and its streamwise evolution (trajectory) are well reproduced by the RANS and URANS computations. Thus it can be considered to investigate the vortex wandering using URANS simulation with appropriate forcing.
4. A multi-vortex system can be observed from the experiment and the simulations. This system consists of one large tip-leakage vortex, one small tip-separation vortex and one or several small induced vortices.
5. A mild oscillatory motion of the TLV is observed in both the experiment and the ZLES. In the experiment, the TLV oscillation amplitudes are estimated to be 3mm in the horizontal direction and 2mm in the vertical direction, at 2mm downstream of the trailing edge. By measuring its axial evolution, the wandering amplitude is found to increase with the streamwise distance. The ZLES agrees well with the experiment for the elliptical distribution of the instantaneous TLV centers, but produces larger oscillatory amplitudes. The PDF is more wiggly in the ZLES, probably because of the imperfect statistical convergence. It should be emphasized that the instability of the jet may also contribute to the vortex wandering in the experiment, though no clear evidence of this instability is found. However, the reproduced wandering motion in the ZLES has nothing to do with the instability of the jet, because the jet layer is simulated by RANS in the ZLES.

6. URANS computations have been employed to analyse the response of the tip-leakage vortex to inflow fluctuations. A correct wandering amplitude in the horizontal direction is obtained. However, the physical validity of this numerical observation is still to be confirmed.
7. The tip-leakage flow is confirmed to contribute essentially to the far-field noise in the frequency range [0.7kHz, 7kHz]. Within this frequency range, the blade-tip self-noise model using the ZLES near-field data is found to yield a good trend around the central frequency (1.3kHz) corresponding to the energy hump observed in the pressure spectra, but the energy level is over-estimated. Since the FWH computation with the same ZLES near-field data provides a very good description of the noise, the near-field data are demonstrated to be appropriate, and more efforts should be put on the parameterization of the blade-tip self-noise model.
8. With the trailing-edge noise model, the ZLES yields a very good prediction within a broad frequency range. The prediction with the RANS results is found to slightly over-estimate the energy levels, because of a thicker boundary layer.

7.2 Perspectives

The perspectives after this thesis are:

1. For ZLES:

With a better convergence of the statistics and a longer sampling time of the ZLES computation, more detailed analyses may be possible for the spectral contents, and a parameterization of better accuracy for the acoustic models can be expected. Besides, there are still many analyses that can be made with the ZLES results, such as the turbulent kinetic energy budget.

2. For experiment:

There are some potential improvements for the experiment of the present configuration: (i) more pressure probes can be used in the blade-tip region, in order to track the formation of the TLV and to determine the parameters for the blade-tip self-noise model with better accuracy; (ii) the end-plate boundary layer parameters can be measured with better accuracy, in order to investigate its role in the TLV evolution; (iii) PIV measurements can be made upstream of the present measurement planes, in order to investigate the tip-leakage jet (around $c/2$).

Other configurations, such as different shape of airfoil and different clearance height, can also be considered in the future.

3. For URANS:

The present URANS computations can be improved by correcting the pressure at inlet with the Poisson equation when the velocity fluctuations are added. More investigations, such as changing the size of the computational domain and using non-reflection boundary condition at lateral boundaries, are still needed for a better explanation and understanding of the vortex wandering observed in the URANS computations.

The objective of the URANS computations is to investigate the vortex wandering at moderate computational cost. However, by comparing the URANS results to the ZLES and experimental results, we find that the URANS mesh is too coarse and the computations are too dissipative and diffusive. This, along with the fact that turbulence is treated as steady in the URANS computation, makes it difficult to reproduce the natural instability of the tip-leakage flow. As a result, URANS may not be the appropriate tool to study the vortex wandering. For such a study, a much finer grid would be required, and a better compromise between the accuracy and the computational cost would be expected for URANS. Other types of numerical simulation can also be considered, such as ZLES (in progress), DES/IDDES and LBM.

4. For the blade-tip self-noise model:

In addition to a better parameterization, the model itself can perhaps be improved by (i) adding acoustic sources distributed along the suction side edge, since there may be noise generated along the suction side edge where the flow escapes from the gap and the TLV licks the airfoil edge; (ii) reformulating the model based on the vortex, instead of the pressure gust on the blade surface, which would be more faithful to the topology (3D) of the tip-leakage flow.

Appendix A

Blade-tip self-noise model - integration of Σ_Y

$$\begin{aligned}
 \frac{p_{K_1, K_2}(x_1, x_2, x_3, \omega)}{P_0} &= \frac{i\bar{k}x_3}{2\pi S_0^2} \\
 &\times \left(b \int_{-L/c}^{L/c} e^{-\gamma|Y|} e^{i(\bar{k}x_2/S_0)Y} dY \right) \\
 &\times \left(e^{-ik(S_0 - Mx_1)/\beta^2} \int_{-2}^0 e^{-i(K_1 + \mu(M - x_1/S_0))X} [1 - \Phi^0((-i(\Gamma + K_1 + \mu M)X)^{1/2})] dX \right)
 \end{aligned} \tag{A.1}$$

For the integration on Y , we have

$$\begin{aligned}
 b \int_{-L/c}^{L/c} e^{-\gamma|Y|} e^{i(\bar{k}x_2/S_0)Y} dY &= b \int_{-L/c}^0 e^{\gamma Y} e^{i(\bar{k}x_2/S_0)Y} dY + b \int_0^{L/c} e^{-\gamma Y} e^{i(\bar{k}x_2/S_0)Y} dY \\
 &= b \frac{1 - e^{-\frac{(\alpha - iK_2 + i\bar{k}x_2/S_0)L}{c}}}{\alpha - iK_2 + i\bar{k}x_2/S_0} + b \frac{e^{\frac{(-\alpha + iK_2 + i\bar{k}x_2/S_0)L}{c}} - 1}{-\alpha + iK_2 + i\bar{k}x_2/S_0} \\
 &= b \frac{e^{\frac{i(K_2 + i\alpha - \bar{k}x_2/S_0)L}{c}} - 1}{i(K_2 + i\alpha - \bar{k}x_2/S_0)} + b \frac{e^{\frac{i(K_2 + i\alpha + \bar{k}x_2/S_0)L}{c}} - 1}{i(K_2 + i\alpha + \bar{k}x_2/S_0)}
 \end{aligned} \tag{A.2}$$

With $\zeta = K_2 + i\alpha - \bar{k}x_2/S_0$ and $\xi = K_2 + i\alpha + \bar{k}x_2/S_0$, we obtain:

$$\begin{aligned}
b \int_{-L/c}^{L/c} e^{-\gamma|Y|} e^{i(\bar{k}x_2/S_0)Y} dY &= b \frac{e^{i\zeta \frac{L}{c}} - 1}{i\zeta} + b \frac{e^{i\xi \frac{L}{c}} - 1}{i\xi} \\
&= b \frac{\sin(\zeta \frac{L}{c}) + i(1 - \cos(\zeta \frac{L}{c}))}{\zeta} + b \frac{\sin(\xi \frac{L}{c}) + i(1 - \cos(\xi \frac{L}{c}))}{\xi} \\
&= (b \frac{L}{2c}) \frac{2\sin(\zeta \frac{L}{2c})\cos(\zeta \frac{L}{2c}) + i(2\sin^2(\zeta \frac{L}{2c}))}{\zeta(\frac{L}{2c})} \\
&\quad + (b \frac{L}{2c}) \frac{2\sin(\xi \frac{L}{2c})\cos(\xi \frac{L}{2c}) + i(2\sin^2(\xi \frac{L}{2c}))}{\xi(\frac{L}{2c})} \\
&= b \frac{L}{c} \left[\text{sinc}(\zeta \frac{L}{2c}) e^{i\zeta \frac{L}{2c}} + \text{sinc}(\xi \frac{L}{2c}) e^{i\xi \frac{L}{2c}} \right] \\
&= \Sigma_Y \tag{A.3}
\end{aligned}$$

where $\text{sinc}(x)$ denotes $\sin(x)/x$.

Appendix B

Trailing-edge noise model

For the trailing-edge noise model, the final expression for the PSD of the far-field pressure reads

$$S_{pp}(\vec{x}, \omega) = \left(\frac{\omega x_3 b}{2\pi c_0 S_0^2} \right)^2 2\pi L \left| I \left(\frac{\bar{\omega}}{U_c}, \bar{k} \frac{x_2}{S_0} \right) \right|^2 \Pi_0 \left(\frac{\omega}{U_c}, k \frac{x_2}{S_0} \right) \quad (\text{B.1})$$

The blade response function I is the main factor relating the far-field sound to the aerodynamic wall pressure field. It is calculated by a radiation integral summing the dominant trailing-edge contribution f_1 and the leading-edge scattering correction f_2 :

$$I(K_1, K_2) = \int_{-2}^0 f_1(X) e^{-iCX} dX + \int_{-2}^0 f_2(X) e^{-iCX} dX \quad (\text{B.2})$$

$$\begin{aligned} & \int_{-2}^0 f_1(X) e^{-iCX} dX \\ = & -\frac{e^{2iC}}{iC} \left\{ (1+i)e^{-2iC} \sqrt{\frac{B}{B-C}} E^*[2(B-C)] - (1+i)E^*[2B] + 1 - e^{-2iC} \right\} \quad (\text{B.3}) \end{aligned}$$

$$\begin{aligned} & \frac{1}{H} \int_{-2}^0 f_2(X) e^{-iCX} dX \\ = & e^{4i\bar{k}} [1 - (1+i)E^*(4\bar{k})]^c - e^{2iD} + i[D + \bar{K} + M\mu - \bar{k}]G \quad (\text{B.4}) \end{aligned}$$

where the notation $\{\cdot\}^c$ stands for an imaginary part multiplied by the correcting factor $\varepsilon = \left(1 + \frac{1}{4\mu}\right)^{-1/2}$ and $E^*(x) = \int_0^x \frac{e^{-it}}{\sqrt{2\pi t}} dt = C_2(x) - iS_2(x)$, C_2 and S_2 are Fresnel integrals [1].

$$B = K_1 + M\mu + \bar{k} \quad (\text{B.5})$$

$$\bar{k}^2 = \mu^2 - \frac{K_2^2}{\beta^2} \quad (\text{B.6})$$

$$C = K_1 - \mu\left(\frac{x_1}{S_0} - M\right) \quad (\text{B.7})$$

$$D = \bar{k} - \mu x_1/S_0 \quad (\text{B.8})$$

$$\begin{aligned} G = & (1 + \varepsilon)e^{i(2\bar{k}+D)} \frac{\sin(D - 2\bar{k})}{D - 2\bar{k}} + (1 - \varepsilon)e^{i(-2\bar{k}+D)} \frac{\sin(D + 2\bar{k})}{D + 2\bar{k}} \\ & + \frac{(1 + \varepsilon)(1 - i)}{2(D - 2\bar{k})} e^{4i\bar{k}} E^*(4\bar{k}) - \frac{(1 - \varepsilon)(1 + i)}{2(D + 2\bar{k})} e^{-4i\bar{k}} E(4\bar{k}) \\ & + \frac{e^{2iD}}{2} \sqrt{\frac{2\bar{k}}{D}} E^*(2D) \left[\frac{(1 + i)(1 - \varepsilon)}{D + 2\bar{k}} - \frac{(1 - i)(1 + \varepsilon)}{D - 2\bar{k}} \right] \end{aligned} \quad (\text{B.9})$$

$$H = \frac{(1 + i)e^{-4i\bar{k}}(1 - \Theta^2)}{2\sqrt{\pi}(\alpha - 1)\bar{K}\sqrt{B}} \quad (\text{B.10})$$

$$\bar{K} = Kb = \frac{\omega}{U_0} b \quad (\text{B.11})$$

Similarly to the blade-tip self-noise model, $\Pi_0 = \frac{1}{\pi} \Phi_{pp}(\omega) l_y \left(\bar{k} \frac{x_2}{S_0}, \omega\right)$. Φ_{pp} is the wall pressure spectrum at the trailing edge and l_y is the spanwise coherence length.

Appendix C

Published papers

The published papers during this thesis include:

1. Fang, L., **Li, B.**, and Lu, L.-P. (2014). Scaling law of resolved-scale isotropic turbulence and its application in large-eddy simulation. *Acta Mechanica Sinica*, 30(3):339–350.
2. Boudet, J., Caro, J., **Li, B.**, Jondeau, E., and Jacob, M. C. (2016a). Zonal large-eddy simulation of a tip leakage flow. *International Journal of Aeroacoustics*, 15(6-7):646–661.
3. Jacob, M. C., Jondeau, E., and **Li, B.** (2016a). Time-resolved PIV measurements of a tip leakage flow. *International Journal of Aeroacoustics*, page 1475472X16659384.
4. Boudet, J., **Li, B.**, Caro, J., Jondeau, E., and Jacob, M. C. (2016b). Tip-leakage flow: a detailed simulation with a zonal approach. In *22nd AIAA/CEAS Aeroacoustics Conference*, page 2824.
5. Jacob, M. C., Jondeau, E., **Li, B.**, and Boudet, J. (2016b). Tip leakage flow: Advanced measurements and analysis. In *22nd AIAA/CEAS Aeroacoustics Conference*, page 2823.

References

- [1] Abramowitz, M., Stegun, I. A., et al. (1966). Handbook of mathematical functions. *Applied mathematics series*, 55:62.
- [2] Amiet, R. (1975). Acoustic radiation from an airfoil in a turbulent stream. *Journal of Sound and vibration*, 41(4):407–420.
- [3] Amiet, R. (1976). Noise due to turbulent flow past a trailing edge. *Journal of sound and vibration*, 47(3):387–393.
- [4] Arguillat, B. (2006). Etude expérimentale et numérique de champs de pression pariétale dans l'espace des nombres d'onde, avec application aux vitrages automobiles. *Ecole Centrale de Lyon*.
- [5] Bailey, S. and Tavoularis, S. (2008). Measurements of the velocity field of a wing-tip vortex, wandering in grid turbulence. *Journal of Fluid Mechanics*, 601:281–315.
- [6] Bailly, C. and Juve, D. (1999). A stochastic approach to compute subsonic-noise using linearized euler's equations.
- [7] Bailly, C. and Juve, D. (2000). Numerical solution of acoustic propagation problems using linearized euler equations. *AIAA journal*, 38(1):22–29.
- [8] Bailly, C., Lafon, P., and Candel, S. (1995). A stochastic approach to compute noise generation and radiation of free turbulent flows. *DGLR BERICHT*, pages 669–669.
- [9] Bailly, C., Lafon, P., and Candel, S. (1996). Computation of noise generation and propagation for free and confined turbulent flows. *AIAA Paper*, 1732.
- [10] Baldwin, B. S. and Lomax, H. (1978). *Thin layer approximation and algebraic model for separated turbulent flows*, volume 257. American Institute of Aeronautics and Astronautics.
- [11] Bauer, M., Zeibig, A., and Költzsch, P. (2006). Application of the sngr-model to compute trailing edge noise. *Research Report, Institute of Acoustics and Speech Communication*.
- [12] Bendat, J. S. and Piersol, A. G. (1980). Engineering applications of correlation and spectral analysis. *New York, Wiley-Interscience, 1980. 315 p., 1*.
- [13] Bendat, J. S. and Piersol, A. G. (2011). *Random data: analysis and measurement procedures*, volume 729. John Wiley & Sons.

- [14] Betz, A. (1925). The phenomena at the tips of kaplan turbines. *Hydraulische Probleme*.
- [15] Bindon, J. (1989). The measurement and formation of tip clearance loss. *Journal of turbomachinery*, 111(3):257–263.
- [16] Boudet, J., Cahuzac, A., Kausche, P., and Jacob, M. C. (2015a). Zonal large-eddy simulation of a fan tip-clearance flow, with evidence of vortex wandering. *Journal of Turbomachinery*, 137(6):061001.
- [17] Boudet, J., Grilliat, J., Caro, J., and Jacob, M. (2009). *Combined experimental/computational study of tip clearance flow and acoustics*. European Turbomachinery Conference, Graz.
- [18] Boudet, J., Monier, J.-F., and Gao, F. (2015b). Implementation of a roughness element to trip transition in large-eddy simulation. *Journal of Thermal Science*, 24(1):30–36.
- [19] Brooks, T. F. and Hodgson, T. (1981). Trailing edge noise prediction from measured surface pressures. *Journal of sound and vibration*, 78(1):69–117.
- [20] Brooks, T. F., Pope, D. S., and Marcolini, M. A. (1989). *Airfoil self-noise and prediction*, volume 1218. National Aeronautics and Space Administration, Office of Management, Scientific and Technical Information Division.
- [21] Cahuzac, A., Boudet, J., Borgnat, P., and L ev eque, E. (2010). Smoothing algorithms for mean-flow extraction in large-eddy simulation of complex turbulent flows. *Physics of Fluids (1994-present)*, 22(12):125104.
- [22] Cahuzac, A., Boudet, J., Jacob, M., and Kausche, P. (2011). Large-eddy simulation of a rotor tip-clearance flow. *AIAA Paper*, (2011-2947).
- [23] Camussi, R., Grilliat, J., Caputi-Gennaro, G., and Jacob, M. C. (2010). Experimental study of a tip leakage flow: wavelet analysis of pressure fluctuations. *Journal of Fluid Mechanics*, 660:87–113.
- [24] Casalino, D. (2003). An advanced time approach for acoustic analogy predictions. *Journal of Sound and Vibration*, 261(4):583–612.
- [25] Ce, Y., Chaochen, M., Yansheng, W., and Dazhong, L. (2001). A review of studies on turbomachinery tip gap leakage flow [j]. *Advances In Mechanics*, 1:006.
- [26] Chase, D. M. (1980). Modeling the wavevector-frequency spectrum of turbulent boundary layer wall pressure. *Journal of Sound and Vibration*, 70(1):29–67.
- [27] Chen, G., Greitzer, E., Tan, C., and Marble, F. (1991). Similarity analysis of compressor tip clearance flow structure. *Journal of Turbomachinery*, 113(2):260–269.
- [28] Chen, G.-T. (1991). *Vortical structures in turbomachinery tip clearance flows*. PhD thesis, Massachusetts Institute of Technology.
- [29] Clauser, F. H. (2012). Turbulent boundary layers in adverse pressure gradients. *Journal of the Aeronautical Sciences*.

- [30] Coles, D. (1956). The law of the wake in the turbulent boundary layer. *Journal of Fluid Mechanics*, 1(02):191–226.
- [31] Corcos, G. (1964). The structure of the turbulent pressure field in boundary-layer flows. *Journal of Fluid Mechanics*, 18(03):353–378.
- [32] De Graaff, D. B. and Eaton, J. K. (2000). Reynolds-number scaling of the flat-plate turbulent boundary layer. *Journal of Fluid Mechanics*, 422:319–346.
- [33] Decaix, J., Balarac, G., Dreyer, M., Farhat, M., and Münch, C. (2015). Rans and les computations of the tip-leakage vortex for different gap widths. *Journal of Turbulence*, 16(4):309–341.
- [34] Dieste, M. and Gabard, G. (2012). Random particle methods applied to broadband fan interaction noise. *Journal of Computational Physics*, 231(24):8133–8151.
- [35] Dunne, R. and Howe, M. (1997). Wall-bounded blade-tip vortex interaction noise. *Journal of sound and vibration*, 202(5):605–618.
- [36] Ewert, R. (2007). Rpm—the fast random particle-mesh method to realize unsteady turbulent sound sources and velocity fields for caa applications. *parameters*, 4:1.
- [37] Ewert, R. (2008). Broadband slat noise prediction based on caa and stochastic sound sources from a fast random particle-mesh (rpm) method. *Computers & Fluids*, 37(4):369–387.
- [38] Ewert, R., Appel, C., Dierke, J., and Herr, M. (2009). Rans/caa based prediction of naca 0012 broadband trailing edge noise and experimental validation. *AIAA Paper*, 3269:2009.
- [39] Ewert, R. and Bauer, M. (2004). Towards the prediction of broadband trailing edge noise via stochastic surface sources. *AIAA Paper*, 2861:2004.
- [40] Ewert, R., Dierke, J., Siebert, J., Neifeld, A., Appel, C., Siefert, M., and Kornow, O. (2011). Caa broadband noise prediction for aeroacoustic design. *Journal of sound and vibration*, 330(17):4139–4160.
- [41] Foley, A. C. and Ivey, P. C. (1996). Measurement of tip-clearance flow in a multistage, axial flow compressor. *Journal of turbomachinery*, 118(2):211–217.
- [42] Fukano, T. and Jang, C.-M. (2004). Tip clearance noise of axial flow fans operating at design and off-design condition. *Journal of sound and vibration*, 275(3):1027–1050.
- [43] Fukano, T., Takamatsu, Y., and Kodama, Y. (1986). The effects of tip clearance on the noise of low pressure axial and mixed flow fans. *Journal of Sound and Vibration*, 105(2):291–308.
- [44] Furukawa, M., Inoue, M., Saiki, K., and Yamada, K. (1998). The role of tip leakage vortex breakdown in compressor rotor aerodynamics. In *ASME 1998 International Gas Turbine and Aeroengine Congress and Exhibition*, pages V001T01A054–V001T01A054. American Society of Mechanical Engineers.
- [45] Gao, F. (2014). *Advanced numerical simulation of corner separation in a linear compressor cascade*. PhD thesis, Ecole Centrale de Lyon.

- [46] Gao, F., Ma, W., Zambonini, G., Boudet, J., Ottavy, X., Lu, L., and Shao, L. (2015). Large-eddy simulation of 3-d corner separation in a linear compressor cascade. *Physics of Fluids (1994-present)*, 27(8):085105.
- [47] Germano, M., Piomelli, U., Moin, P., and Cabot, W. H. (1991). A dynamic subgrid-scale eddy viscosity model. *Physics of Fluids A: Fluid Dynamics (1989-1993)*, 3(7):1760–1765.
- [48] Goody, M. (2004). Empirical spectral model of surface pressure fluctuations. *AIAA journal*, 42(9):1788–1794.
- [49] Graftieaux, L., Michard, M., and Grosjean, N. (2001). Combining piv, pod and vortex identification algorithms for the study of unsteady turbulent swirling flows. *Measurement Science and Technology*, 12(9):1422.
- [50] Grilliat, J. (2009). *Contribution à l'étude aéroacoustique des écoulements de jeu*. PhD thesis, Ecully, Ecole centrale de Lyon.
- [51] Grilliat, J., Jondeau, E., Jacob, M., Roger, M., and Camussi, R. (2008). Broadband noise prediction models and measurements of tip leakage flows. In *14th AIAA/CEAS Aeroacoustics Conference*.
- [52] Heyes, A., Jones, R., and Smith, D. (2004). Wandering of wing-tip vortices. In *Proceedings of 12th international symposium on the applications of laser techniques to fluid mechanics. Lisbon, Portugal*.
- [53] Howe, M. S. (1998). *Acoustics of fluid-structure interactions*. Cambridge university press.
- [54] Hughes, C. E., Jeracki, R. J., Woodward, R., and Miller, C. (2002). Fan noise source diagnostic test—rotor alone aerodynamic performance results. In *8th AIAA/CEAS Aeroacoustics Conference, Breckenridge, CO, June*, pages 17–19.
- [55] Hughes, C. E., Woodward, R. P., and Podboy, G. G. (2005). Effect of tip clearance on fan noise and aerodynamic performance. In *11th AIAA/CEAS Aeroacoustics Conference (26th AIAA Aeroacoustics Conference)*.
- [56] Inoue, M., Furukawa, M., Saiki, K., and Yamada, K. (1998). Physical explanations of tip leakage flow field in an axial compressor rotor. In *ASME 1998 International Gas Turbine and Aeroengine Congress and Exhibition*, pages V001T01A027–V001T01A027. American Society of Mechanical Engineers.
- [57] Inoue, M., Kuroamaru, M., and Fukuhara, M. (1986). Behavior of tip leakage flow behind an axial compressor rotor. *Journal of Engineering for Gas Turbines and Power*, 108(1):7–14.
- [58] Intaratep, N. (2006). *Formation and development of the tip leakage vortex in a simulated axial compressor with unsteady inflow*.
- [59] Jacob, M., Grilliat, J., Camussi, R., and Gennaro, G. (2010). Aeroacoustic investigation of a single airfoil tip leakage flow. *International Journal of Aeroacoustics*, 9(3):253–272.

- [60] Jacob, M. C., Jondeau, E., and Li, B. (2016). Time-resolved piv measurements of a tip leakage flow. *International Journal of Aeroacoustics*, page 1475472X16659384.
- [61] Jameson, A., Schmidt, W., Turkel, E., et al. (1981). Numerical solutions of the euler equations by finite volume methods using runge-kutta time-stepping schemes. *AIAA paper*, 1259:1981.
- [62] Jang, C.-M., Fukano, T., and Furukawa, M. (2003). Effects of the tip clearance on vortical flow and its relation to noise in an axial flow fan. *JSME International Journal Series B*, 46(3):356–365.
- [63] Kalitzin, G., Kalitzin, N., and Wilde, A. (2000). A factorization scheme for rans turbulence models and sngr predictions of trailing edge noise. In *6th Aeroacoustics Conference and Exhibit*, page 1982.
- [64] Kameier, F. and Neise, W. (1997a). Experimental study of tip clearance losses and noise in axial turbomachines and their reduction. *Journal of Turbomachinery*, 119(3):460–471.
- [65] Kameier, F. and Neise, W. (1997b). Rotating blade flow instability as a source of noise in axial turbomachines. *Journal of Sound and Vibration*, 203(5):833–853.
- [66] Kang, S. and Hirsch, C. (1993a). Experimental study on the three-dimensional flow within a compressor cascade with tip clearance: Part ii—the tip leakage vortex. *Journal of Turbomachinery*, 115(3):444–452.
- [67] Kang, S. and Hirsch, C. (1993b). Experimental study on the three-dimensional flow within a compressor cascade with tip clearance: Part i—velocity and pressure fields. *Journal of Turbomachinery*, 115(3):435–443.
- [68] Kang, S. and Hirsch, C. (1994). Tip leakage flow in linear compressor cascade. *Journal of turbomachinery*, 116(4):657–664.
- [69] Karstadt, S., Hess, M., Matyschok, B., and Pelz, P. F. (2010). The influence of tip clearance on the acoustic and aerodynamic characteristics of fans. In *ASME Turbo Expo 2010: Power for Land, Sea, and Air*, pages 39–47. American Society of Mechanical Engineers.
- [70] Knacke, T. and Thiele, F. (2014). Numerical simulation of broadband noise from low-speed flows with separation. *The 21st International Congress on Sound and Vibration*.
- [71] Lakshminarayana, B. (1970). Methods of predicting the tip clearance effects in axial flow turbomachinery. *Journal of Basic Engineering*, 92(3):467–480.
- [72] Lakshminarayana, B. and Horlock, J. (1963). Tip-clearance flow and losses for an isolated compressor blade. Technical report, DTIC Document.
- [73] Lakshminarayana, B. and Horlock, J. t. (1967). *Leakage and secondary flows in compressor cascades*. HM Stationery Office.
- [74] Lakshminarayana, B., Zaccaria, M., and Marathe, B. (1995). The structure of tip clearance flow in axial flow compressors. *TRANSACTIONS-AMERICAN SOCIETY OF MECHANICAL ENGINEERS JOURNAL OF TURBOMACHINERY*, 117:336–336.

- [75] Lévêque, E., Toschi, F., Shao, L., and Bertoglio, J. P. (2007). Shear-improved smagorinsky model for large-eddy simulation of wall-bounded turbulent flows. In *TSFP DIGITAL LIBRARY ONLINE*. Begel House Inc.
- [76] Lewin, E., Kozulovic, D., and Stark, U. (2010). Experimental and numerical analysis of hub-corner stall in compressor cascades. In *ASME Turbo Expo 2010: Power for Land, Sea, and Air*, pages 289–299. American Society of Mechanical Engineers.
- [77] Lighthill, M. J. (1952). On sound generated aerodynamically. i. general theory. In *Proceedings of the Royal Society of London A: Mathematical, Physical and Engineering Sciences*, volume 211, pages 564–587. The Royal Society.
- [78] Lighthill, M. J. (1954). On sound generated aerodynamically. ii. turbulence as a source of sound. In *Proceedings of the Royal Society of London A: Mathematical, Physical and Engineering Sciences*, volume 222, pages 1–32. The Royal Society.
- [79] Longhouse, R. (1978). Control of tip-vortex noise of axial flow fans by rotating shrouds. *Journal of sound and vibration*, 58(2):201–214.
- [80] M Roger, J. G. and Jacob, M. (2008). Improvement of fan broadband noise prediction: Experimental investigation and computational modelling. deliverable d2.10: Final report on improved fan tip source model. *PROBAND Deliverable*.
- [81] Ma, R. (2003). *Unsteady turbulence interaction in a tip leakage flow downstream of a simulated axial compressor rotor*. PhD thesis, Virginia Polytechnic Institute and State University.
- [82] Marz, J., Hah, C., and Neise, W. (2002). An experimental and numerical investigation into the mechanisms of rotating instability. *Journal of turbomachinery*, 124(3):367–374.
- [83] Meneveau, C., Lund, T. S., and Cabot, W. H. (1996). A lagrangian dynamic subgrid-scale model of turbulence. *Journal of Fluid Mechanics*, 319:353–385.
- [84] Menter, F. R. (1994). Two-equation eddy-viscosity turbulence models for engineering applications. *AIAA journal*, 32(8):1598–1605.
- [85] Moreau, S. and Roger, M. (2009). Back-scattering correction and further extensions of amiet’s trailing-edge noise model. part ii: Application. *Journal of Sound and Vibration*, 323(1):397–425.
- [86] Mugridge, B. and Morfey, C. (1972). Sources of noise in axial flow fans. *The Journal of the Acoustical Society of America*, 51(5A):1411–1426.
- [87] Muthanna, C. and Devenport, W. J. (2004). Wake of a compressor cascade with tip gap, part 1: Mean flow and turbulence structure. *AIAA journal*, 42(11):2320–2331.
- [88] Nikolos, I., Douvikas, D., and Papailiou, K. (1995). Theoretical modelling of relative wall motion effects in tip leakage flow. In *ASME 1995 International Gas Turbine and Aeroengine Congress and Exposition*, pages V001T01A017–V001T01A017. American Society of Mechanical Engineers.

- [89] Nikolos, J., Douvilcas, D., and Papailiou, K. (1993). A method for the calculation of the tip clearance flow effects in axial flow compressors. part i: Description of basic models, part ii: Calculation procedure. *7aper ASME*.
- [90] Perennes, S. and Roger, M. (1998). Aerodynamic noise of a two-dimensional wing with high-lift devices. In *4th AIAA/CEAS Aeroacoustics Conference*, page 2338.
- [91] Pröbsting, S., Scarano, F., Bernardini, M., and Pirozzoli, S. (2013). On the estimation of wall pressure coherence using time-resolved tomographic piv. *Experiments in fluids*, 54(7):1–15.
- [92] Rains, D. A. (1954). *Tip clearance flows in axial flow compressors and pumps*. PhD thesis, California Institute of Technology.
- [93] Roger, M. and Moreau, S. (2005). Back-scattering correction and further extensions of amiet’s trailing-edge noise model. part 1: theory. *Journal of Sound and Vibration*, 286(3):477–506.
- [94] Rozenberg, Y. (2007). *Modélisation analytique du bruit aérodynamique à large bande des machines tournantes: utilisation de calculs moyennés de mécanique des fluides*. PhD thesis, Ecole Centrale de Lyon.
- [95] Rozenberg, Y., Robert, G., and Moreau, S. (2012). Wall-pressure spectral model including the adverse pressure gradient effects. *AIAA journal*, 50(10):2168–2179.
- [96] Rozenberg, Y., Roger, M., and Moreau, S. (2008). Fan blade trailing-edge noise prediction using rans simulations. *Journal of the Acoustical Society of America*, 123(5):3688.
- [97] Schlinker, R. H. and Amiet, R. K. (1981). Helicopter rotor trailing edge noise. In *AIAA, Astrodynamics Specialist Conference*, volume 1.
- [98] Sharland, I. (1964). Sources of noise in axial flow fans. *Journal of Sound and Vibration*, 1(3):302–322.
- [99] Siefert, M. and Ewert, R. (2009). Sweeping sound generation in jets realized with a random particle-mesh method. *AIAA Pap*, 3369.
- [100] Song, S. and Martinez-Sanchez, M. (1997). Rotordynamic forces due to turbine tip leakage: Part i—blade scale effects. *Journal of turbomachinery*, 119(4):695–703.
- [101] Stauter, R. (1993). Measurement of the three-dimensional tip region flow field in an axial compressor. *Journal of turbomachinery*, 115(3):468–476.
- [102] Storer, J. and Cumpsty, N. (1991). Tip leakage flow in axial compressors. *Journal of Turbomachinery*, 113(2):252–259.
- [103] Toschi, F., Amati, G., Succi, S., Benzi, R., and Piva, R. (1999). Intermittency and structure functions in channel flow turbulence. *Physical review letters*, 82(25):5044.
- [104] Wang, Y. and Devenport, W. J. (2004). Wake of a compressor cascade with tip gap, part 2: effects of endwall motion. *AIAA journal*, 42(11):2332–2340.

- [105] Wilcox, D. C. (1988). Reassessment of the scale-determining equation for advanced turbulence models. *AIAA journal*, 26(11):1299–1310.
- [106] Wilcox, D. C. et al. (1998). *Turbulence modeling for CFD*, volume 2. DCW industries La Canada, CA.
- [107] Williams, J. F. and Hawkings, D. L. (1969). Sound generation by turbulence and surfaces in arbitrary motion. *Philosophical Transactions of the Royal Society of London A: Mathematical, Physical and Engineering Sciences*, 264(1151):321–342.
- [108] Willmarth, W. and Roos, F. (1965). Resolution and structure of the wall pressure field beneath a turbulent boundary layer. *Journal of Fluid Mechanics*, 22(01):81–94.
- [109] Woodward, R. P., Hughes, C. E., Jeracki, R. J., and Miller, C. J. (2002). Fan noise source diagnostic test—far-field acoustic results. *AIAA paper*, 2427:2002.
- [110] Wright, S. (1976). The acoustic spectrum of axial flow machines. *Journal of Sound and Vibration*, 45(2):165–223.
- [111] Wu, Y. and Chu, W. (2007). Behaviour of tip-leakage flow in an axial flow compressor rotor. *Proceedings of the Institution of Mechanical Engineers, Part A: Journal of Power and Energy*, 221(1):99–110.
- [112] You, D., Mittal, R., Wang, M., and Moin, P. (2002). Progress in large-eddy simulation of a rotor tip-clearance flow. In *12th Annual DoD HPCMP User Group Conference*. Austin, TX. Citeseer.
- [113] You, D., Wang, M., Moin, P., and Mittal, R. (2006). Effects of tip-gap size on the tip-leakage flow in a turbomachinery cascade. *Physics of Fluids (1994-present)*, 18(10):105102.
- [114] You, D., Wang, M., Moin, P., and Mittal, R. (2007a). Large-eddy simulation analysis of mechanisms for viscous losses in a turbomachinery tip-clearance flow. *Journal of Fluid Mechanics*, 586:177–204.
- [115] You, D., Wang, M., Moin, P., and Mittal, R. (2007b). Vortex dynamics and low-pressure fluctuations in the tip-clearance flow. *Journal of Fluids Engineering*, 129(8):1002–1014.
- [116] Zhang, H., Deng, X., Lin, F., Chen, J., and Huang, W. (2006). A study on the mechanism of tip leakage flow unsteadiness in an isolated compressor rotor. In *ASME Turbo Expo 2006: Power for Land, Sea, and Air*, pages 435–445. American Society of Mechanical Engineers.
- [117] Zhu, T. and Carolus, T. H. (2013). Experimental and unsteady numerical investigation of the tip clearance noise of an axial fan. In *ASME 2013 Turbine Blade Tip Symposium*, pages V001T04A001–V001T04A001. American Society of Mechanical Engineers.